

The ${}^2H(e, e'p)n$ reaction at large energy transfers

H.W. Willering

ISBN: 90-393-3309-2

Printed by: Ponsen & Looijen bv, Wageningen

The $^2H(e, e' p)n$ reaction at large energy transfers

De $^2H(e, e' p)n$ reactie bij hoge waarden van de energieoverdracht

(met een samenvatting in het Nederlands)

Proefschrift ter verkrijging van de graad van doctor
aan de Universiteit Utrecht
op gezag van de Rector Magnificus, prof. dr. W.H. Gispen,
ingevolge het besluit van het College voor Promoties
in het openbaar te verdedigen
op maandag 7 april 2003 des middags te 12:45 uur

door

Hendrik Willem Willering

geboren op 21 juli 1968 te Groningen

Promotor: prof. dr. P.K.A. de Witt Huberts
Faculteit der Natuur- en Sterrenkunde
Copromotor: dr. Th.S. Bauer
Nationaal Instituut voor Kernfysica en Hoge-energiefysica

ISBN 90-393-3309-2

The work described in this thesis is part of the research program of the “Stichting voor Fundamenteel Onderzoek der Materie” (FOM) which is financially supported by the “Nederlandse organisatie voor Wetenschappelijk Onderzoek” (NWO).

All's well that ends well...

Contents

1	Introduction	1
1.1	Electron scattering off the deuteron	1
1.2	Existing ${}^2H(e, e'p)n$ results	3
1.3	Objectives of the current experiment	6
1.4	Organisation of the thesis	7
2	Formalism of the ${}^2H(e, e'p)n$ reaction	9
2.1	Kinematical definitions	9
2.2	General cross section formalism	12
2.2.1	Form factors	12
2.2.2	Differential cross section	14
2.2.3	Observables	15
2.3	Model calculations	17
2.3.1	Basic model	17
2.3.2	Meson exchange currents, isobar configurations	18
2.3.3	Relativistic corrections	19
2.3.4	Results	19
3	Experimental setup	23
3.1	The ELSA accelerator facility	23
3.2	Layout of the experiment	24
3.2.1	Target	25
3.2.2	ELAN spectrometer	26
3.2.3	TOF-walls	26
3.2.4	Telescopes	28
3.3	Electronics and data acquisition	29
3.3.1	Spectrometer electronics and readout trigger	30
3.3.2	TOF-wall electronics	30
3.3.3	Telescope electronics	31
3.4	Kinematics of the experiment	32

4	Data analysis	35
4.1	Electron spectrometer	35
4.1.1	Wire chamber hits	35
4.1.2	Scintillator hits	36
4.1.3	Efficiencies	39
4.1.4	Stability of the beam	40
4.1.5	Energy transfer bins	41
4.2	TOF-walls	42
4.2.1	TDC values	44
4.2.2	ADC values	48
4.2.3	Proton identification	52
4.2.4	Protons from deuteron breakup	55
4.2.5	Proton detection efficiency	58
4.3	Telescopes	62
4.3.1	TDC values	62
4.3.2	ADC values	63
4.3.3	Walk effects	65
4.3.4	Simulations	67
4.3.5	Proton identification	67
4.3.6	Protons from deuteron breakup	70
4.3.7	Proton detection efficiency	72
4.4	Other corrections	74
4.4.1	Accumulated charge	75
4.4.2	Deuterium target	76
4.4.3	Detection volume	77
4.4.4	Multiple scattering	79
4.4.5	Radiative effects	80
5	Results and interpretation	85
5.1	Data representation	85
5.1.1	Choice of variables	85
5.1.2	Integration over the electron quantities	86
5.1.3	Extrapolation in the angles	88
5.1.4	In-plane and out-of-plane	88
5.2	Data selection	89
5.2.1	Contributions to the error	89
5.2.2	Selection criteria	91
5.2.3	<i>Passing</i> and <i>stopping</i> results	92
5.3	Result of the experiment	93
5.3.1	TOF-walls	95
5.3.2	Telescopes	97
5.4	Consistency of the results	97
5.4.1	Telescopes and TOF-walls	98

5.4.2	Two data sets	98
5.4.3	Comparison with other experiments	100
5.4.4	Comparison with quasilastic model calculations	101
5.4.5	Inclusive rates	105
5.4.6	Other possible explanantions	105
5.4.7	Which data set should be chosen?	106
5.5	Model calculations	107
5.5.1	Overall strength	107
5.5.2	Out-of-plane effects	109
5.6	Form factors	115
5.7	Conclusions and outlook	120
6	Summary	125
	References	127
	Appendix – Numerical results	131
	Samenvatting	155
	Nawoord	159
	Levensloop	163

Chapter 1

Introduction

1.1 Electron scattering off the deuteron

Protons and neutrons belong to the main building blocks of matter. The interaction between these *nucleons*, as they are generally known, is dominated by the strong interaction, one of the four fundamental forces of nature. It is generally assumed that this strong interaction is governed by the theory called quantum chromodynamics (QCD), which is expressed in terms of quarks and gluons. However, since it is difficult (in the energy domain we are interested in) to describe the nucleonic interaction directly in these terms, one mostly relies on effective models, which employ empirical nucleon-nucleon(NN)-potentials to describe the dynamics of the interaction. The subnuclear degrees of freedom – in QCD, the effects of the substructure of a nucleon – enter the effective models as virtual mesons exchanged by the nucleons or as virtual excitations of the nucleons (“isobar configurations”).

The most simple nucleonic bound system is the deuteron, consisting of only one proton and one neutron. It therefore represents a good testing ground for our knowledge of the strong interaction, even more so since it is a two-body system, for which in principle exact calculations are possible. Models describing the deuteron can either be based on the non-relativistic Schrödinger equation or start with the Lorentz-covariant Bethe-Salpeter equation. In the latter case it has (so far) not been possible to include the isobar currents in the models.

In the context of such models, there are many interesting topics, such as the choice of the NN-potential, the admixture of D-state components in the deuteron wave function, the possibility of tensor forces, the contribution of the isobar degrees of freedom – especially the $\Delta(1232)$ -resonance – or the need for a relativistic treatment of the various elements of the model. Of specific interest is the short-range structure of the NN-interaction – or, equivalently, the high-momentum components of the nucleon wave function – which is difficult to access experimentally

and is therefore less well known.

In order to gauge the models, they need to be compared to experimental observables. The electron scattering reaction is well suited for this purpose for several reasons: (1) The electromagnetic nature of the probe is described by quantum electrodynamics (QED), so that the experimental results can be directly related to the hadronic (deuteron) structure under investigation. (2) The weakness of the interaction allows it to be approximated by the exchange of only one photon (OPE), thus simplifying the theoretical model. (3) The virtuality of the exchanged photon allows an independent variation of the amount of energy and momentum transferred to the deuteron, so that a large kinematical range becomes experimentally accessible.

In order to distinguish between different reaction channels, in some of which extra particles (e.g. pions) may be created, it is necessary to detect one or more of the final state particles in addition to the scattered electron. Much work has been done in this field using the electron accelerators of Saclay, Amsterdam (MEA) and MIT/Bates. Since the advent of accelerators with higher duty-cycles, such as AmPS (Amsterdam), MAMI (Mainz), TJNAF and ELSA (Bonn), it has also become feasible to access the much lower cross sections at higher energies or momenta, or to use detectors with relatively large opening angles. In addition, modern data acquisition systems allow for the correspondingly high event rates, and the rapid advance in computing power facilitates the analysis of large data sets.

Through such ($e, e'N$) experiments a large amount of data has been accumulated on the deuteron (and also on larger nuclei). However, in many cases the kinematics indicate that the detected nucleon has absorbed most of the transferred energy and momentum, so that subnuclear degrees of freedom do not play an important role. In order to observe effects related to those degrees of freedom, higher momenta or higher energy transfers are needed (not necessarily together), or one can focus on out-of-plane and/or polarization observables.

The experiment described in this thesis concerns the “breakup” of the deuteron into a proton and a neutron through electron scattering *without* the creation of any other particles. By extending our measurement to high energy transfers and by measuring out-of-plane, we will be sensitive to the influence of the subnuclear degrees of freedom, especially the Δ -isobar, and also to the need for a relativistic treatment of the model components.

Knowledge of the response of the deuteron to electron scattering also benefits another type of experiment. In the absence of free neutron sources the deuteron is often used to investigate the properties of the neutron like the neutron magnetic and electric form factors, G_M^n and G_E^n . In order to obtain reliable values for the neutron, such measurements must be corrected for nuclear effects, e.g. final state interactions involving a “charge exchange” of protons from the much stronger proton reaction channel, which must therefore also be well known.

1.2 Existing ${}^2H(e, e'p)n$ results

Before explaining the objectives of our experiment, we will first discuss some previous ${}^2H(e, e'p)n$ results, specifically recent data from Bonn, Mainz, NIKHEF.

Relevant quantities in comparing the kinematics of these experiments are the four-momentum transfer Q^2 , the invariant mass W_{np} of the np -system, the “missing momentum” p_m and the angle Θ_{pn}^{CM} of the knocked-out proton with respect to (w.r.t.) the momentum transfer. These quantities will be defined in the next chapter. Here it is sufficient to note that Q^2 represents the transfer of energy and momentum from the electron to the deuteron, W_{np} is related to the excitation of the nucleus, and p_m and/or the proton angle Θ_{pn}^{CM} concern the relative motion of the proton and the neutron within the nucleus. Instead of W_{np} many authors quote the “relative energy” E_{np} which is obtained by subtracting the proton and neutron mass, i.e. it is the total kinetic energy available in the center-of-momentum system if no extra particles are created in the reaction.

The kinematic region where only one of the nucleons absorbs (nearly) all the energy and momentum transferred to the deuteron system¹ is often referred to as the “quasielastic region”. Although this often corresponds to small values for E_{np} , this is not necessarily the case, because only the combination of the energy and the momentum of the np -system determines if the kinematics are quasielastic. Probing beyond the quasielastic region by increasing the energy and/or momentum transfer to the np -system may result in the creation of extra particles such as pions – which is not of interest to us here – or in the virtual excitation of nucleon resonances, e.g. the $\Delta(1232)$ -resonance.

Apart from measuring the total cross section, many experiments also extract some of the four so-called form factors – f_L , f_T , f_{LT} , f_{TT} , also defined in the next chapter – which contain all the physics of an unpolarized ($e, e'N$) cross section.

Quasielastic results

Quite a number of experiments have been performed in the quasielastic region, e.g. at Saclay [Ber81, Duc94], at SLAC [Bul95], in Japan [Tam87] and at Bates [Jor96]. Both the ${}^2H(e, e'p)$ and the complementary ${}^2H(e, e'n)$ cross sections have been determined, and in many cases form factors have been extracted from the results. Some measurements extend to high four-momentum transfers, especially those from SLAC – up to $Q^2 = -6.8$ (GeV/c)² – but kinematically they are still quasielastic because the knocked-out proton absorbs nearly all the transferred energy and momentum.

In the neutron form factor experiments by Joosse *et al.* [Joo93] and Reike, Bruins *et al.* [Rei93, Bru95b] both the ${}^2H(e, e'n)$ and ${}^2H(e, e'p)$ reactions were

¹In a non-relativistic approximation: $\omega \approx q^2/2m$, where (ω, q) are the energy and momentum transfer, respectively, and m is the nucleon mass.

measured simultaneously. However, the results have no absolute normalization, because only the *ratio* of the two is needed (together with values for the proton form factors) to extract G_M^n .

Previous quasielastic experiments at NIKHEF include those by Van der Schaar *et al.* [Sch91]. In this experiment the f_{LT} form factor was determined for missing momenta in the range 35-180 MeV/c at a four-momentum transfer $Q^2 = -0.21$ (GeV/c) 2 . The data demonstrated the relevance of a relativistic approach to the model calculations.

Beyond the quasielastic region

One experiment probing beyond the quasielastic region was reported by Turck-Chieze *et al.* [Tur84], at $Q^2 = -0.038$ (GeV/c) 2 and $E_{np} = 179$ MeV, i.e. at kinematics centered at the Δ -resonance. The missing momentum range from 300 to 500 MeV/c was sampled using a two-spectrometer setup at Saclay. The results were reproduced within less than 10% by non-relativistic model calculations including subnuclear degrees of freedom.

There are also some ${}^2H(e, e'p)n$ data from Bonn dating from before the addition of the ELSA stretcher ring to the accelerator, e.g. Breuker *et al.* [Bre86]. In this experiment the cross section was measured as a function of the invariant mass in the Δ -resonance region at $Q^2 = -0.23$ (GeV/c) 2 and $\Theta_{pn}^{CM} = 80^\circ$. Generally, the (non-relativistic) model calculations available at that time overestimated the results by up to 30%, again indicative of Δ degrees of freedom.

Recent results from Bonn

In the first experiments taking advantage of the much higher duty cycle delivered by ELSA, Boden *et al.* [Bod90] measured the ${}^2H(e, e'p)n$ cross section at $Q^2 = -0.12$ (GeV/c) 2 for energy transfers in the region of the Δ -resonance. Two magnetic spectrometers were used, one for the electron and one for the proton. The conclusions were that the available model calculations could not completely describe the excess strength due to the Δ -resonance. Also, the experimental cross section seemed to be lower than expected at smaller proton angles.

Frommberger *et al.* [Fro94] used the same magnetic electron spectrometer, but non-magnetic detectors for the proton. This experiment was performed at $Q^2 = -0.144$ (GeV/c) 2 with missing momenta ranging up to 100 MeV/c, but in the quasielastic region ($E_{np} = 38$ MeV). The cross section was measured in-plane on either side of the momentum transfer, so that the f_{LT} form factor could be determined by considering the asymmetry between the two. A comparison of the experimental results with model calculations indicated that relativistic corrections to the electromagnetic operators and the deuteron wave function were necessary to reproduce the data.

Recent results from NIKHEF

In recent years there have been two ${}^2H(e, e'p)n$ experiments probing beyond the quasielastic region. The two NIKHEF spectrometers [Vri84] were used, and/or the HADRON-4 detector [Pel96]. This implies that the angular range was not extremely large, but the energy resolution was high.

The first experiment, by Kasdorp *et al.* [Kas97], measured the ${}^2H(e, e'p)n$ cross section at $Q^2 = -0.1, -0.2$ and -0.3 (GeV/c)², still close to quasielastic energies ($E_{np} = 160$ MeV), but extending up to large missing momenta ($p_m < 700$ MeV/c). At $Q^2 = -0.20$ (GeV/c)² the f_{LT} form factor was determined in the missing momentum range 145–215 MeV/c, also by considering the asymmetry between experimental results on either side of the momentum transfer. Again, the main conclusion was that relativistic corrections to the nuclear current operator were necessary to obtain agreement with the data.

The second experiment, by Pellegrino *et al.* [Pel97], was performed approximately at the mass of the Δ -resonance ($E_{np} = 282$ MeV), but at the small four-momentum transfer $Q^2 = -0.029$ (GeV/c)². The cross section and the f_{TT} form factor were determined for Θ_{pn}^{CM} angles in the range 100–135°. The experiment confirmed the dominant role of the Δ -resonance at high energy transfers. No conclusions were drawn about other contributions to the cross section due to the size of the statistical and systematical uncertainties.

Recent results from Mainz

In the experiment by Blomqvist *et al.* [Blo98, Böh01] at the MAMI accelerator facility the ${}^2H(e, e'p)n$ cross section was measured for missing momenta up to 950 MeV/c and energy transfers up to the Δ -resonance region. Also, an L/T-separation was performed, i.e. the f_L and f_T form factors were extracted, in parallel kinematics² for $p_m \leq 350$ MeV/c. A two-spectrometer setup was used.

For missing momenta below 200 MeV/c the data could be reproduced to 10–15% by model calculations including a dynamical excitation of the Δ -resonance. For higher missing momenta (up to 350 MeV/c) the model was more compatible with the data measured in parallel kinematics than with the other results. According to the authors this might be due to the contributions of the interference form factors [Böh01]. At the highest missing momenta the model could not really reproduce the data in a satisfactory way, although the general trend was comparable.

Recent results from MIT/Bates

No unpolarized experiments comparable to ours have been reported, only one ${}^2H(\vec{e}, e'p)n$ experiment using the OHIPS-OOPS spectrometer system [Zho01].

²“Parallel kinematics”: the proton is detected in the direction of the momentum transfer.

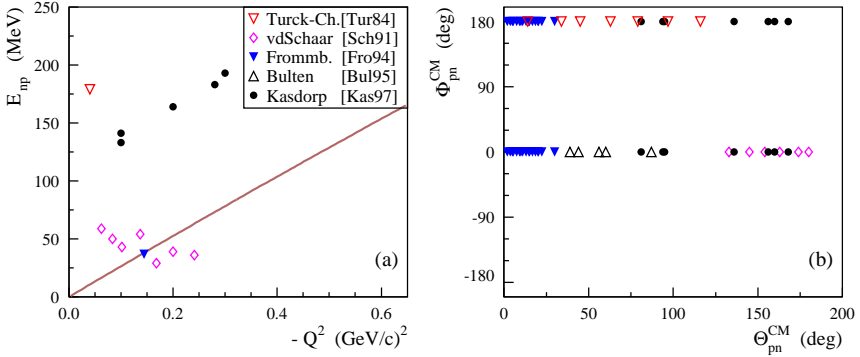


Figure 1.1: Kinematics of previous ${}^2\text{H}(e, e'p)n$ experiments in or close to the quasielastic region (a) in the E_{np} vs Q^2 plane, and (b) in the Φ_{pn}^{CM} vs Θ_{pn}^{CM} plane. The line in (a) corresponds to quasielastic kinematics. The data by Bulten et al. are on this line, but at $-Q^2 = 1.2 \dots 6.8$ (GeV/c)².

In this experiment a few values for the f_{LT} , f_{TT} and f'_{LT} form factors were determined in quasielastic and ‘‘dip’’ kinematics for missing momenta around $p_m = 200$ MeV/c. It was concluded that relativistic corrections were necessary to describe the f_{LT} data, whereas the subnuclear degrees of freedom were important for the f_{TT} data. No results were given for the cross section.

1.3 Objectives of the current experiment

The kinematics of the various experiments discussed above are compared in Figures 1.1 and 1.2. In both figures (a) shows the location of the experiments in the (E_{np}, Q^2) plane. This representation, also used in e.g. [Fab79], indicates how far the various results are from quasielastic kinematics (represented by the line). In part (b) of the figures the center-of-momentum angles (Θ_p^{CM} , Φ_p^{CM}) of the data are given. Nearly all results are located in-plane, i.e. at $\Phi_{pn}^{CM} = 0^\circ$ or 180° . Only Pellegrino *et al.* measured out-of-plane and therefore could extract the f_{TT} form factor.

The first objective of our experiment is to obtain ${}^2\text{H}(e, e'p)n$ cross section data for energies from the quasielastic region to beyond the Δ -resonance while covering as much as possible of the proton solid angle, both in-plane and out-of-plane. By covering such a large kinematical range in one experiment we hope to obtain a good overview, in order to determine regions of interest for further, more detailed investigation. At low energy transfers our results complement existing (in-plane) data by adding out-of-plane results, and we also extend the experimental data set to kinematics, for which results do not yet exist. Our second objective is to extract

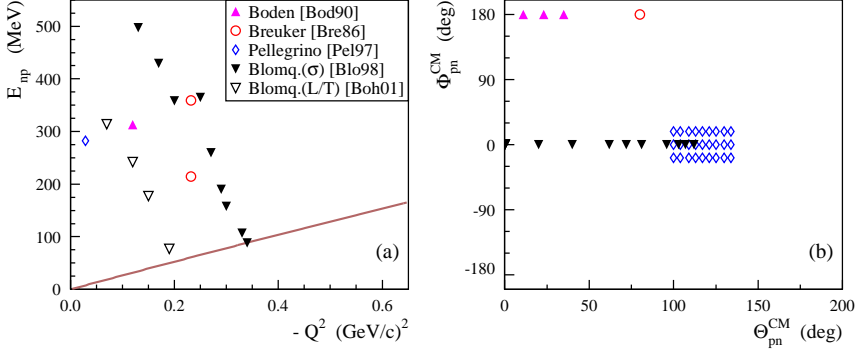


Figure 1.2: Kinematics of previous ${}^2\text{H}(e, e'p)n$ experiments probing beyond the quasielastic region (a) in the E_{np} vs Q^2 plane, and (b) in the Φ_{pn}^{CM} vs Θ_{pn}^{CM} plane. The line in (a) corresponds to quasielastic kinematics. Note that the scale is different from that of Figure 1.1a. The LT-separation results by Blomqvist et al. (open triangles) are all located at $\Theta_{pn}^{\text{CM}} = 0^\circ$. As far as their cross section results are concerned, the largest proton angles in (b) correspond to the largest values for E_{np} in (a).

the longitudinal-transverse interference form factor, f_{LT} , in as much of the same kinematical region as possible. Making use of a large out-of-plane acceptance, we can do this by fitting the dependence of the cross section on the proton azimuthal angle. This procedure will be explained in a later chapter.

The results described in this thesis are limited to the ${}^2\text{H}(e, e'p)n$ reaction channel. The complementary ${}^2\text{H}(e, e'N)N\pi$ reaction channels of this experiment – seen as “background” in our analysis! – in combination with more experiments aimed specifically at those reaction channels, are the subject of several other theses [Wac98, Hai00, Lan00, Bru01, Mas01, Ban03].

1.4 Organisation of the thesis

This thesis is organized as follows. In chapter 2 the relevant formalism for the ${}^2\text{H}(e, e'p)n$ reaction is given, along with an outline of the available model calculations. The experimental setup at the ELSA accelerator facility is described in chapter 3, together with details of the kinematics of the measurement. In chapter 4 the offline analysis for the various detectors is discussed, as well as several general correction factors needed to obtain absolute cross section values. The final data points and the extracted values for the f_{LT} form factor are given in chapter 5, together with a discussion of the internal consistency of the results and a comparison to the model calculations. The thesis is summarized in chapter 6. Numerical values for all the experimental results are given in an Appendix.

Chapter 2

Formalism of the ${}^2H(e, e'p)n$ reaction

In this chapter the formalism for the electro-disintegration of the deuteron is introduced, including the relevant kinematical variables, and a description is given of the available model calculations.

2.1 Kinematical definitions

The geometry of the ${}^2H(e, e'p)n$ reaction is displayed in Figure 2.1. The main kinematical variables are:

$$\begin{aligned}
 K_\mu &= (E_0, \mathbf{k}) : \text{the four-vector of the initial electron,} \\
 K'_\mu &= (E_{e'}, \mathbf{k}') : \text{the four-vector of the scattered electron,} \\
 Q_\mu &= (\omega, \mathbf{q}) : \text{the four-momentum transfer,} \\
 P_\mu^T &= (E_T, \mathbf{p}_T) : \text{the four-vector of the target,} \\
 P_\mu^p &= (E_p, \mathbf{p}_p) : \text{the four-vector of the final proton,} \\
 P_\mu^n &= (E_n, \mathbf{p}_n) : \text{the four-vector of the final neutron.}
 \end{aligned}$$

Bold symbols indicate three-vectors. In the Laboratory (L) reference frame, which is also the deuteron rest frame, we have $E_T = M_d$ and $\mathbf{p}_T = \mathbf{0}$. In the Extreme Relativistic Limit (ERL), which is appropriate here, the mass of the electron is neglected w.r.t. its energy, so that $k = E_0$ and $k' = E_{e'}$.

In the laboratory frame the *scattering plane* is defined by the incoming and scattered electron, where the z -axis is chosen in the direction of the momentum transfer \mathbf{q} and the y -axis lies along $\mathbf{k} \times \mathbf{k}'$. Thus the *reaction plane*, defined by the proton and neutron, is tilted w.r.t. the scattering plane by the azimuthal angle Φ_p of the scattered proton.

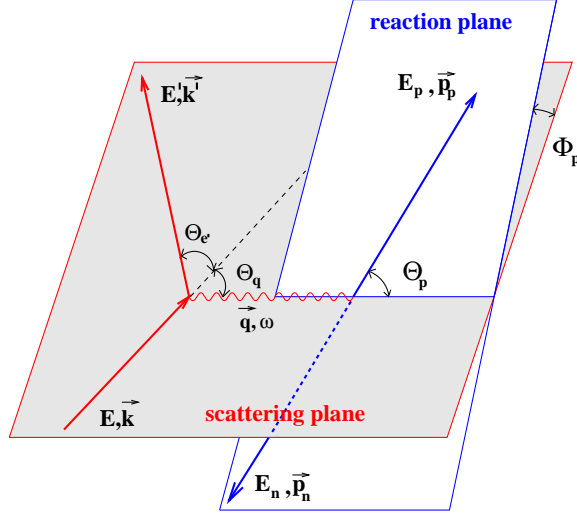


Figure 2.1: Geometry of the ${}^2\text{H}(e, e'p)n$ reaction in the laboratory frame. The various symbols are discussed in the text.

The four-momentum transferred by the electron is

$$Q_\mu \equiv K_\mu - K'_\mu \quad (2.1)$$

which in the One Photon Exchange (OPE) approximation corresponds to the energy and momentum of the virtual photon emitted by the electron and absorbed by the deuteron. Four-momentum conservation at the photon-deuteron vertex is expressed by

$$Q_\mu + P_\mu^T = P_\mu \quad (2.2)$$

where

$$P_\mu = P_\mu^p + P_\mu^n \quad (2.3)$$

is the total four-momentum in the case of the ${}^2\text{H}(e, e'p)n$ “breakup” process. At higher energy transfers an additional pion can be created. For such a ${}^2\text{H}(e, e'p)n\pi$ reaction the total four-momentum is

$$P_\mu = P_\mu^p + P_\mu^n + P_\mu^\pi . \quad (2.4)$$

For kinematical reasons this competing ${}^2\text{H}(e, e'p)n\pi$ reaction is only possible at (laboratory) energy transfers of at least 300 MeV.

The *invariant mass* of the system, conveniently evaluated in the laboratory frame, is independent of the final state of the reaction:

$$W_{np}^2 \equiv P_\mu P^\mu = (\omega + M_d)^2 - q^2 . \quad (2.5)$$

If only the proton is detected, the *missing energy* and *missing momentum* are defined, in the L frame, as

$$\begin{aligned} E_m &\equiv \omega + M_d - E_p \\ \mathbf{p}_m &\equiv \mathbf{q} - \mathbf{p}_p \end{aligned} \quad (2.6)$$

Combining these two quantities one has the *missing mass*

$$M_m = \sqrt{E_m^2 - p_m^2} \quad (2.7)$$

which for the ${}^2H(e, e'p)n$ reaction is the mass m_n of the undetected neutron.

The other useful reference frame is the Centre-of-Momentum (CM) frame, in which the scattered proton and neutron have equal but opposite momenta:

$$\mathbf{p}_p^{\text{CM}} = -\mathbf{p}_n^{\text{CM}}. \quad (2.8)$$

The relevant quantities are the relative momentum of the np -pair

$$\mathbf{p}_{pn}^{\text{CM}} = \frac{1}{2}(\mathbf{p}_p^{\text{CM}} - \mathbf{p}_n^{\text{CM}}) \quad (2.9)$$

with polar angle Θ_{pn}^{CM} and azimuthal angle Φ_{pn}^{CM} and the *relative energy*

$$E_{np}^{\text{CM}} = W_{np} - m_p - m_n \quad (2.10)$$

which is the kinetic energy available for the np -pair in the CM frame.

The CM frame is moving with momentum \mathbf{q} w.r.t. the L frame, so that a transformation from L to CM simply corresponds to a boost along the z -axis. The orientation of the three axes is the same for both reference frames.

Finally, an important kinematical observation is that for the ${}^2H(e, e'p)n$ reaction the proton kinematics are fully determined by the scattered electron vector and the proton *direction*. Therefore the proton *energy* is redundant, a fact which we will use in the analysis to separate “breakup” results (equation 2.3) from events in which an additional pion is created (equation 2.4). The following formula can be derived for the momentum of the knocked-out proton in the laboratory frame (assuming equal masses for proton and neutron):

$$p_p^{\text{L}} = \frac{-B + \sqrt{B^2 - 4AC}}{2A} \quad (2.11)$$

$$\begin{aligned} A &= (\omega + M_d)^2 - q^2 \cos^2 \Theta_{pq} & C &= (\omega + M_d)^2 m_p^2 - D^2/4 \\ B &= -Dq \cos \Theta_{pq} & D &= (\omega + M_d)^2 - q^2 \end{aligned}$$

using only energy and momentum conservation and the assumption that the scattering centre is a deuteron.

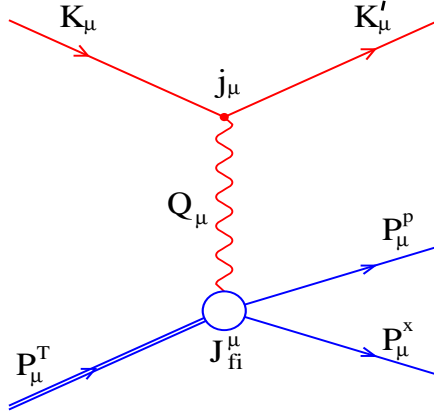


Figure 2.2: Diagram representing the $A(e, e' p)$ reaction in the OPE approximation.

2.2 General cross section formalism

In this section the general formalism of the ${}^2H(e, e' p)n$ cross section is described. We follow the approach by e.g. Donnelly [Don94], which we find appealing because it clearly introduces – to the experimentalist – the available degrees of freedom and the various possible observables.

2.2.1 Form factors

In the OPE approximation the cross section of the reaction in which one proton is knocked out of a nucleus, $A(e, e' p)$, follows from the diagram in Figure 2.2. The four-vectors used have been defined in the previous section, except P_x , which is the four-momentum of the undetected residual ($A-1$) nucleus, including any possible excitation energy. In the case of the ${}^2H(e, e' p)n$ reaction this is simply the neutron four-momentum P_n with no excitation.

The cross section for this process is proportional to the square of the invariant matrix element \mathcal{M}_{fi} , which is itself the product of the electron current j_μ , the photon propagator and the nuclear current J_{fi}^μ :

$$|\mathcal{M}_{fi}|^2 \sim \left| j_\mu \frac{1}{Q^2} J_{fi}^\mu \right|^2 = \frac{1}{Q^4} J_\mu^* J_\nu \cdot J_{fi}^{\mu*} J_{fi}^\nu. \quad (2.12)$$

In order to obtain the full cross section the average must be taken of the initial (spin) states i and the sum of the final states f , according to the experimental conditions. This leads to

$$d\sigma \sim \frac{1}{Q^4} \eta_{\mu\nu} W^{\mu\nu} \quad (2.13)$$

where the leptonic and hadronic tensors are related to the electron current and nuclear current terms, respectively:

$$\eta_{\mu\nu} \sim \overline{\sum} j_\mu^* j_\nu \quad W^{\mu\nu} \sim \overline{\sum} J_{fi}^{\mu*} J_{fi}^\nu. \quad (2.14)$$

The symbol $\overline{\sum}$ indicates the average or sum mentioned above.

The *leptonic tensor* is readily evaluated using standard techniques [Hal84]:

$$\eta_{\mu\nu} = \frac{1}{2m_e^2} [K_\mu K'_\nu + K'_\mu K_\nu - g_{\mu\nu} K \cdot K'] \quad (2.15)$$

for unpolarised electron scattering.

The *hadronic tensor* is less straightforward, since it involves the nuclear structure and the reaction mechanism. In Donnelly's approach it is constructed as the most general form based on the available four-vectors, to which the relevant conservation laws are applied. At the hadronic vertex in Figure 2.2 four four-vectors are involved: $\{Q, P_T, P_p, P_x\}$. Only three of these are independent due to momentum conservation:

$$Q + P_T = P_p + P_x \quad (2.16)$$

so that the building blocks for the hadronic tensor are e.g. $\{Q, P_T, P_p\}$. Since the leptonic tensor is symmetric for unpolarised electron scattering, only symmetric combinations of these four-vectors have to be considered. The general form is

$$\begin{aligned} W^{\mu\nu} = & X_1 g^{\mu\nu} + X_2 Q^\mu Q^\nu + X_3 V_T^\mu V_T^\nu + X_4 V_p^\mu V_p^\nu \\ & + X_5 (Q^\mu V_T^\nu + V_T^\mu Q^\nu) + X_6 (Q^\mu V_p^\nu + V_p^\mu Q^\nu) + X_7 (V_T^\mu V_p^\nu + V_p^\mu V_T^\nu) \end{aligned} \quad (2.17)$$

where the structure functions X_i contain all the physics. For later convenience the four-vector P_p^μ has been replaced by the following linear combination:

$$V_p^\mu \equiv \left\{ P_p^\mu - \left(\frac{Q \cdot P_p}{Q^2} \right) Q^\mu \right\} \quad (2.18)$$

and in a similar way P_T^μ has been replaced by V_T^μ . In this way, by construction $Q \cdot V_T = Q \cdot V_p = 0$. Using the condition for (hadronic) current conservation, $Q_\mu W^{\mu\nu} = 0$, it can be deduced that $X_1 + X_2 Q^2 = X_5 = X_6 = 0$. Therefore, there are only four independent structure functions in the hadronic tensor and hence in the cross section.

Contracting the leptonic and hadronic tensors in terms of their spherical components yields

$$\eta_{\mu\nu} W^{\mu\nu} \sim \rho_L f_L + \rho_T f_T + \rho_{LT} f_{LT} \cos \Phi_p + \rho_{TT} f_{TT} \cos 2\Phi_p \quad (2.19)$$

where the structure functions f_x are linear combinations of the X_i in equation 2.17. The *only* dependence of the cross section on the azimuthal angle Φ_p is given explicitly. In the laboratory system the four electron kinematical factors – often

referred to as the *virtual photon matrix* – are

$$\begin{aligned}\rho_L &= \rho_{00} = Q^2 \frac{\xi^2}{2\eta} & \rho_T &= \rho_{11} = \frac{1}{2} Q^2 \left(1 + \frac{\xi}{2\eta}\right) \\ \rho_{LT} &= \rho_{10} = Q^2 \frac{\xi}{\eta} \sqrt{\frac{\xi+\eta}{8}} & \rho_{TT} &= \rho_{-11} = -Q^2 \frac{\xi}{4\eta}.\end{aligned}\quad (2.20)$$

The following dimensionless variables have been introduced [Are88]:

$$\xi \equiv \frac{Q^2}{q^2} \quad \eta \equiv \tan^2 \frac{\Theta_{e'}}{2}.\quad (2.21)$$

2.2.2 Differential cross section

To obtain the complete formula for the cross section the invariant flux factor and phase space elements – assuming covariant normalization – are combined with the square of the matrix element. For the knock-out of one proton from a nucleus A in the ERL this is

$$d\sigma = \frac{1}{(2\pi)^5} \frac{e^4}{Q^4} \left(\frac{d^3\mathbf{k}'}{4M_T k k'} \right) \eta_{\mu\nu} W^{\mu\nu} \left(\frac{m_p M_x d^3\mathbf{p}_p d^3\mathbf{p}_x}{E_p E_x} \right) \times \delta^{(4)}(Q + P_T - P_p - P_x) \quad (2.22)$$

so that integrating over the variables for the unobserved (A-1) nucleus leads to

$$\frac{d^6\sigma}{dE_{e'} d\Omega_{e'} dE_p d\Omega_p} \sim \frac{2\alpha^2}{Q^4} \left(\frac{k'}{k} \right) \eta_{\mu\nu} W^{\mu\nu} \delta(E_p + E_x - M_T - \omega). \quad (2.23)$$

In the case of the ${}^2H(e, e' p)n$ reaction the proton energy and direction are not independent, so that one can integrate out the remaining delta function to achieve the five-fold differential cross section

$$\frac{d^5\sigma}{dE_{e'} d\Omega_{e'} d\Omega_p} \sim \frac{2\alpha^2}{Q^4} \left(\frac{k'}{k} \right) \eta_{\mu\nu} W^{\mu\nu}. \quad (2.24)$$

Equation 2.24 is expressed in terms of quantities in the L frame. However, for the model calculations it is more convenient to evaluate the hadronic tensor in the CM frame, where the trivial center-of-momentum motion can be eliminated from the wave functions. Expressing (only) the hadronic part of equation 2.22 in the CM frame yields

$$d\sigma = \frac{1}{(2\pi)^5} \frac{e^4}{Q^4} \left(\frac{d^3\mathbf{k}'}{4M_d k k'} \right) \eta_{\mu\nu}^{\text{CM}} W^{\mu\nu}_{\text{CM}} \left(\frac{4m_p m_n d^3\mathbf{p}_{\text{tot}}^{\text{CM}} d^3\mathbf{p}_{pn}^{\text{CM}}}{E_p^{\text{CM}} E_n^{\text{CM}}} \right) \times \delta^{(4)}(Q^{\text{CM}} + P_T^{\text{CM}} - P_p^{\text{CM}} - P_n^{\text{CM}}) \quad (2.25)$$

and eventually for the ${}^2H(e, e'p)n$ reaction:

$$\frac{d^5\sigma}{dE_{e'}d\Omega_{e'}d\Omega_{pn}^{\text{CM}}} = \frac{2\alpha^2}{Q^4} \left(\frac{k'}{k}\right) \eta_{\mu\nu}^{\text{CM}} W_{\text{CM}}^{\mu\nu}. \quad (2.26)$$

Note that in this case the virtual photon matrix elements must be evaluated in the CM frame too, because only $|\mathcal{M}_{fi}|^2 = \eta_{\mu\nu} W^{\mu\nu}$ is a Lorentz scalar and therefore invariant under Lorentz transformations. In the CM frame the *longitudinal* ρ_L and ρ_{LT} acquire extra boost factors $\beta = \frac{q^L}{q^{\text{CM}}}$:

$$\rho_L = \beta^2 Q^2 \frac{\xi^2}{2\eta} \quad \rho_{LT} = \beta Q^2 \frac{\xi}{\eta} \sqrt{\frac{\xi+\eta}{8}}, \quad (2.27)$$

while the *transverse* ρ_T and ρ_{TT} remain unchanged (see equation 2.20).

The differential cross sections in the L frame and in the CM frame are related through a Jacobian [Are93]:

$$\mathcal{J} \equiv \frac{\partial\Omega_{pn}^{\text{CM}}}{\partial\Omega_p} = \frac{1}{\gamma} \left(\frac{p_p^L}{p_p^{\text{CM}}}\right)^3 \left(1 + \beta \frac{E_p^{\text{CM}} \cos\Theta_{pn}^{\text{CM}}}{p_p^{\text{CM}}}\right)^{-1} \quad (2.28)$$

where β and γ are the boost parameters for the transformation between the L and CM frames ($\gamma = \frac{1}{\sqrt{1-\beta^2}}$).

2.2.3 Observables

To determine the observables on which the four structure functions depend, one has to consider – in Donnelly’s approach – all independent Lorentz scalars which can be constructed from the available four-vectors.

Again starting with the four-vectors $\{Q, P_T, P_p\}$ for the general $A(e, e'p)$ case, there are six independent scalars:

$$\{P_T^2, P_p^2, Q^2, (Q \cdot P_T), (P_p \cdot P_T), (Q \cdot P_p)\} \quad (2.29)$$

of which two simply represent the target or proton mass ($P_T^2 = M_T^2$, $P_p^2 = m_p^2$). For the ${}^2H(e, e'p)n$ reaction the mass of the residual (A-1) target is also fixed, so that there is an extra relationship between the four remaining scalars:

$$\begin{aligned} m_n^2 \equiv P_x^2 &= (Q + P_T - P_p)^2 \\ &= Q^2 + M_T^2 + m_p^2 + 2(Q \cdot P_T) - 2(P_p \cdot P_T) - 2(Q \cdot P_p). \end{aligned} \quad (2.30)$$

Therefore in this specific case there are only *three* independent scalars.

There are several ways to relate these scalars to observables. For example, in the L frame one has:

$$\begin{aligned} Q^2 &= \omega^2 - q^2 & (Q \cdot P_T) &= \omega M_T \\ (P_p \cdot P_T) &= E_p M_T & (Q \cdot P_p) &= \omega E_p - qp_p \cos\Theta_{pq}. \end{aligned} \quad (2.31)$$

A possible choice of observables for the ${}^2H(e, e'p)n$ reaction is $\{Q^2, \omega, E_p\}$, approximately corresponding to the first three scalars. An alternative choice is $\{Q^2, \omega, \Theta_{pq}\}$, obtained by eliminating the third scalar in favour of the fourth.

On the other hand, if equation 2.16 is used to eliminate the proton four-vector P_p instead of the undetected P_x , we again find four independent scalars for the $A(e, e'p)$ reaction, for example:

$$\{Q^2, (Q \cdot P_T), (Q \cdot P_x), (P_x \cdot P_T)\}. \quad (2.32)$$

In the laboratory frame the last two evaluate to:

$$\begin{aligned} (Q \cdot P_x) &= \omega E_x - qp_x \cos \Theta_{xq} = \omega E_m - qp_m \cos \Theta_{xq} \\ (P_x \cdot P_T) &= E_x M_T = E_m M_T \end{aligned} \quad (2.33)$$

leading to the four observables $\{Q^2, \omega, p_m, E_m\}$. This set of observables is often used for $A(e, e'p)$ experiments, especially in the quasielastic region, because – assuming the $(A-1)$ nucleus acts as a spectator – one can relate p_m to the momentum of the knocked-out proton *before* the interaction. For the ${}^2H(e, e'p)n$ reaction again only three are independent, so that the relevant observables are $\{Q^2, \omega, p_m\}$, where p_m is of course equal to the momentum of the undetected neutron.

A third possibility – especially convenient for the ${}^2H(e, e'p)n$ reaction – is to separate the relative motion of the np -pair from the total motion of the system, i.e. to start out with the four-vectors

$$\{Q, P_T, (P_p + P_x), (P_p - P_x)\} \quad (2.34)$$

and eliminate $(P_p + P_x)$ using equation 2.16. Again, only three of the resulting scalars are independent, for example

$$\{Q^2, (Q \cdot P_T), (P_p - P_x)^2\} \quad (2.35)$$

which leads to the observables $\{Q^2, \omega, p_p^{\text{CM}}\}$ by evaluating the third scalar in the CM frame:

$$(P_p - P_x)^2 = -4(p_p^{\text{CM}})^2. \quad (2.36)$$

In a similar manner the scalars

$$\{Q^2, (Q \cdot P_T), (Q \cdot (P_p - P_x))\} \quad (2.37)$$

yield the observables $\{Q^2, \omega, \Theta_{pn}^{\text{CM}}\}$ since

$$(Q \cdot (P_p - P_x)) = -2q^{\text{CM}} p_p^{\text{CM}} \cos \Theta_{pn}^{\text{CM}}. \quad (2.38)$$

This last set of observables is quite convenient for model calculations.

Evidently, the various sets of observables are completely equivalent – they are just different representations of the three degrees of freedom available for the hadronic form factors. The choice which observables are actually used can be based on what is convenient for the experiment.

One appealing aspect of using the CM observable(s) for the ${}^2H(e, e' p)n$ reaction is that they focus on the *complete* two-body system, whereas a quantity like p_m suggests “free”, single-particle behaviour. It is already known that beyond the quasielastic region the proton cannot be considered really “free” anymore, as effects like Δ -excitation or MEC become important. Also, the CM variables can be seen as more natural than quantities in the laboratory reference frame, but this is more a matter of taste.

Note that, although the four structure functions depend only on three observables, the actual differential cross section also explicitly depends on the proton azimuthal angle Φ_p (equation 2.19) and on the electron variables in the virtual photon matrix elements (equation 2.20). These dependencies are purely kinematical, whereas all dynamics of the system are contained in the structure functions.

2.3 Model calculations

The main theoretical calculations for deuterium that extend beyond the quasielastic region are those by Arenhövel *et al.*, in which several subnucleonic processes are added to the original quasielastic model and a correction for relativistic effects is also included. Other models – e.g. by Tjon [Hum94], who takes a completely covariant approach – presently restrict themselves to the quasielastic region. Since the goal of our experiment is to probe beyond the quasielastic region, the discussion in this section will be limited to the calculations of Arenhövel *et al.*

The model was originally developed more than twenty years ago [Fab79] and has since been improved and extended [Are88, Lei91, Are92, Wil93]. A major extension has been the inclusion of electron or proton polarization in the calculations, but since this is not relevant for our unpolarized experiment it is not discussed here.

2.3.1 Basic model

The basic model (labeled “NORMAL”) is a non-relativistic description of the two-nucleon system, in which the contracted tensors $\eta_{\mu\nu}W^{\mu\nu}$ are expressed in terms of the spherical components

$$\begin{aligned} \eta_{\mu\nu}W^{\mu\nu} &\sim \sum_{\lambda\lambda', sm_s, m_d} \langle sm_s | T | \lambda m_d \rangle \rho_{\lambda\lambda'} \langle sm_s | T | \lambda' m_d \rangle^* & (2.39) \\ &= \sum_{\lambda\lambda', sm_s, m_d} t_{sm_s\lambda m_d} e^{i(\lambda+m_d)\Phi_{pn}^{\text{CM}}} \rho_{\lambda\lambda'} t_{sm_s\lambda' m_d}^* e^{-i(\lambda'+m_d)\Phi_{pn}^{\text{CM}}} \end{aligned}$$

and the corresponding (reduced) transition matrix elements are calculated in a non-relativistic approximation. The quantum numbers (sm_s) characterize the spin of the final np -state, m_d is the projection of the initial deuteron spin w.r.t. the direction of the momentum transfer \mathbf{q} and $(\lambda\lambda')$ characterizes the spherical components. These (reduced) transition matrix elements are related to the hadronic current elements in equation 2.14 by a kinematical factor [Are88].

In the evaluation of the transition matrix elements $\langle sm_s | T | \lambda m_d \rangle$ a realistic NN-potential is used to calculate the initial-state wave function of the deuteron, and non-relativistic one-body charge and current densities including nucleon form factors are employed. In the calculations shown in this thesis these are the Paris potential and the so-called dipole model for the Sachs form factors of the nucleon with a non-vanishing neutron electric form factor.

The transition matrix elements are evaluated in the CM frame, since this allows the elimination of the trivial center-of-momentum motion. In order to do this the wave functions are first transformed into this frame.

For practical purposes the multipole expansion of equation 2.39 is truncated at a certain L_{\max} (usually 6), but since the higher partial waves are necessary for the convergence of the multipole expansion, they are included using the Born Approximation [Are82] for the final state, i.e. assuming plane waves. For details see [Fab79]. This truncation of the full t-matrix expansion implies that *final state interactions* (FSI) are included in the model for the lowest $L_{\max}+1$ partial waves.

2.3.2 Meson exchange currents, isobar configurations

The model also takes into account subnuclear degrees of freedom, namely *meson exchange currents* (MEC) and *isobar configurations* (IC). The former represent the coupling of the virtual photon to a (virtual) meson exchanged within the deuteron, the latter describe the (temporary) excitation of one of the nucleons.

The IC – usually restricted to the $\Delta(1232)$ and perhaps the $N(1470)$ isobar – are included in the two-body wave functions describing the initial and/or final state. Therefore expressions are needed for the transition NN^* and diagonal N^*N^* densities and currents, e.g. $\rho^{\Delta N}$ and $\mathbf{J}^{\Delta N}$. In analogy to the nucleon density and current, these (non-relativistic) expressions contain form factors, such as $G_M^{\Delta N}$, for which a specific description is chosen. Details are given in [Fab79] and [Lei87].

For the MEC only the dominant terms are considered, arising from the long ranged π -meson two-body exchange currents $\mathbf{J}_{(2)}^\pi$ and occasionally the shorter ranged ρ - and ω -meson currents $\mathbf{J}_{(2)}^\rho$, $\mathbf{J}_{(2)}^\omega$. The expressions for these currents [Fab79] again contain form factors, e.g. G_E^v , and coupling constants, e.g. f_π .

2.3.3 Relativistic corrections

At higher energies and momentum transfers the non-relativistic (NR) treatment is not sufficient [Fro94, Sch91, Kas97]. Therefore *relativistic corrections* (REL) are applied to the model [Wil88, Wil93, Bec92], consisting of lowest order expansions in $(p/M)^2$ of the various components of the t-matrix.

The first relativistic correction J_λ^R is an expansion of the one-body charge and current operators themselves by retaining more terms in the usual NR reduction of the relativistic current of a Dirac particle. These extra terms are the so-called Darwin-Foldy and spin-orbit currents and some additional higher-order one-body currents. The second correction J_λ^B is due to the transformation of the wave functions into the CM frame, originating in the relativistic expansion of the boost operator (hence the “B”) for this transformation. No relativistic corrections are applied to the internal deuteron dynamics since the potential used is already a realistic one. The new hadronic current including relativistic corrections is:

$$J_\lambda = J_\lambda^{NR} + J_\lambda^R + J_\lambda^B . \quad (2.40)$$

Also, in the various kinematical factors in the t-matrix the *relativistic* expressions are retained, i.e. not approximated by the non-relativistic version [Are88].

A bonus of including relativistic corrections in the model is that the dependence of the non-relativistic results on the choice of the form factor parametrization – Dirac-Pauli or Sachs – is largely eliminated [Bec92].

2.3.4 Results

Figure 2.3 shows calculations using the model described above at the kinematics of our experiment [Are98]. The influence of the various model components is illustrated by the different curves in the figure. For comparison, equivalent results for the simple PWBA case are also shown.

At low energy transfers adding the subnuclear degrees of freedom does not alter the results, but beyond $\omega \approx 250$ MeV they become the dominant contribution, especially the Δ -isobar configurations. The strongest effects of the subnuclear degrees of freedom occur at large proton angles ($\Theta_{pn}^{\text{CM}} > 40^\circ$), whereas at forward ($\Theta_{pn}^{\text{CM}} = 0^\circ$) and backward ($\Theta_{pn}^{\text{CM}} = 180^\circ$) angles the cross section is insensitive to the interaction between the proton and the neutron. The relativistic corrections seem to reduce the cross section by some 40% at small proton angles.

Since our experiment aims to cover a large part of the proton solid angle, the dominant component of the out-of-plane effects – the f_{LT} form factor – is also interesting. Model calculations for this quantity are shown in Figure 2.4. Again, the most interesting region is at higher energy transfers, although the relativistic corrections also have a 40% effect in the quasielastic region. Beyond $\omega \approx 250$ MeV the effect of adding the Δ -isobar configurations is of the same order of magnitude, but including the MEC has nearly no influence at all.

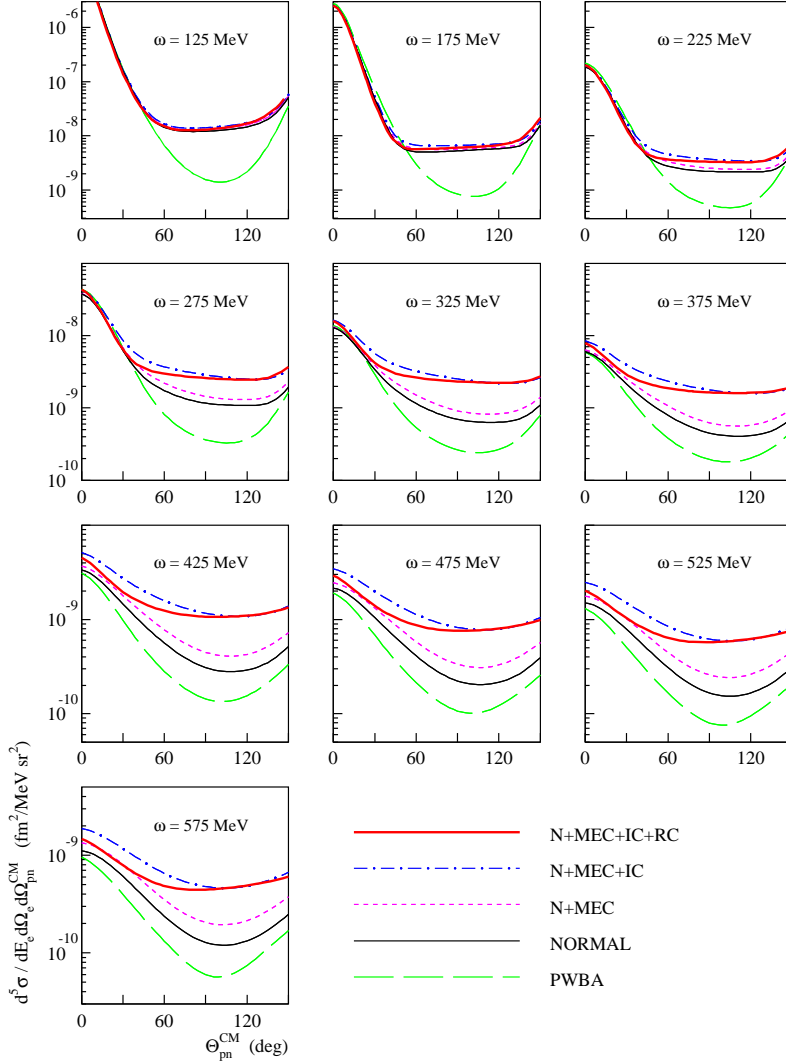


Figure 2.3: Model calculations by Arenhövel et al. [Are98] for the in-plane cross section at $Q^2 \approx -0.2 \text{ (GeV/c)}^2$. The thin solid curves represent the basic, non-relativistic part of the model including FSI. For the short dashed curves MEC have been added and for the dash-dotted curves the Δ -isobar configurations are taken into account as well. The "full" model including relativistic corrections is represented by the thick solid line. The PWBA results (long dashes) are shown for comparison.

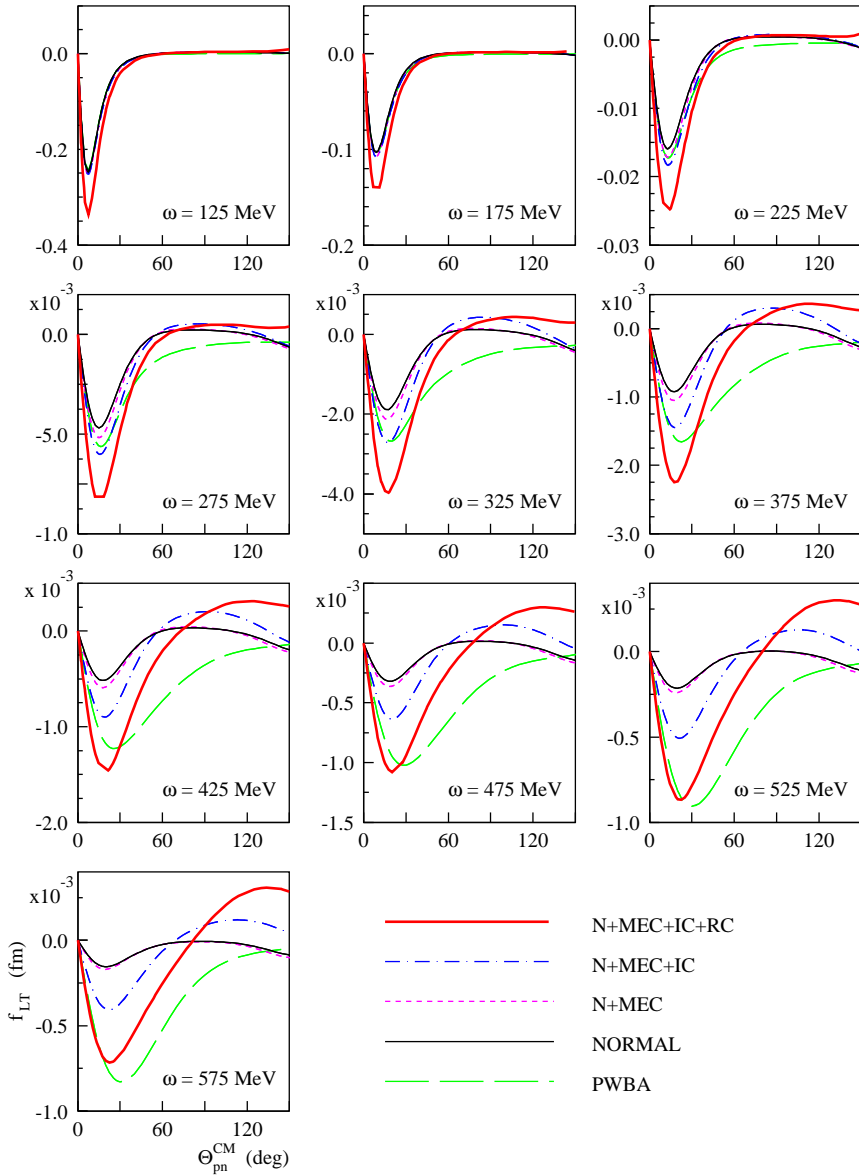


Figure 2.4: Model calculations by Arenhövel et al. [Are98] for the f_{LT} form factor at $Q^2 \approx -0.2$ (GeV/c) 2 . The curves have the same meaning as in Figure 2.3.

Chapter 3

Experimental setup

The experiment described in this thesis was performed at the ELSA¹ electron accelerator facility of the Universität Bonn, Germany, in collaboration with the ELAN² experimental group of this university. The various components of the setup are described in this chapter: the ELSA facility in section 3.1, the detectors in section 3.2, the front-end electronics and data acquisition system in section 3.3.

There were two periods of measurements, in January 1996 (*jan96*) and in February 1997 (*feb97*). After the first period the detector configuration was modified to accommodate a pion calorimeter not relevant to the present work. Also, an error in one part of the data acquisition electronics was corrected at this time. Throughout the experiment several settings of the ELAN spectrometer have been used – details are given in the discussion of the kinematics in section 3.4.

3.1 The ELSA accelerator facility

The general layout of the ELSA accelerator is shown in Figure 3.1. A linear accelerator serves as the injector for a synchrotron, which can boost electrons to energies up to 2.5 GeV. The pulsed electron beam is injected into the ELSA ring, where it is stored and continuously extracted to one of several experimental areas, which receive a nearly continuous beam. During our experiment the extracted beam was approximately 10–15 nA with a macroscopic duty cycle of 40–70%.

The ELSA ring has several operating modes. In the *jan96* measurement the pure *stretcher mode* was used. In this mode the synchrotron boosts the electrons to their final energy (1.6 GeV) and ELSA serves only to “stretch” the beam packets into a continuous beam. In the *feb97* measurement the electrons were accelerated

¹ELektronen Stretcher Anlage, or ELectron Stretcher and Accelerator.

²ELektronenstreuung An Nukleonen (electron scattering off nucleons).

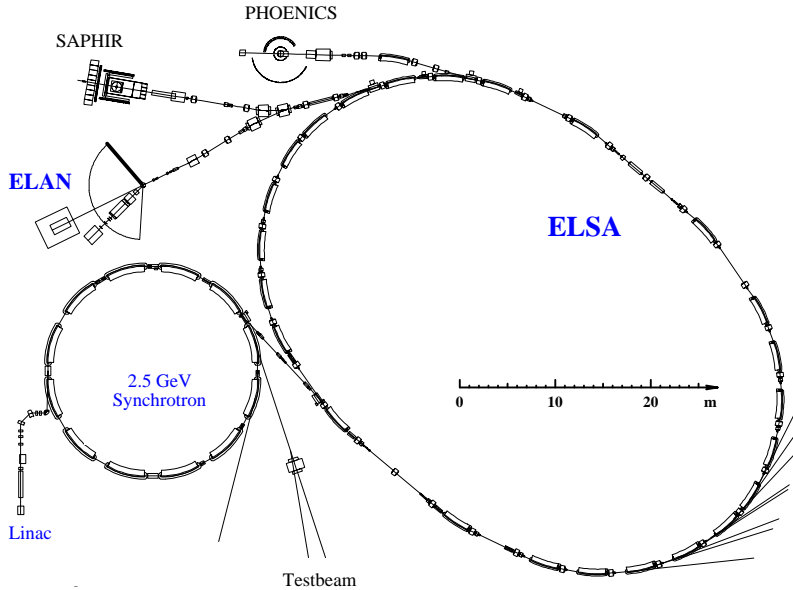


Figure 3.1: The Bonn accelerator facility consisting of a Linac, the booster Synchrotron and the ELSA stretcher ring. The various experimental areas are indicated.

to 1.5 GeV in the synchrotron, and the final boost to 1.6 GeV was given in ELSA by ramping the magnets. This mode of operation is called *post-accelerator mode*. The third option, *storage mode*, was not used for our experiment. In this mode the beam is stored in the ELSA ring for as long as one hour and serves primarily as a source of synchrotron radiation.

3.2 Layout of the experiment

In the ELAN experimental area several detectors were installed in addition to the ELAN spectrometer, notably the four time-of-flight-walls (TOF-walls) with a vertex detector and twelve scintillator telescopes. Two walls of concrete blocks were used to shield the TOF-walls from background radiation coming from the electron beam or from other detectors. Figure 3.2 shows a schematic top view of the entire setup for the *jan96* measurement. The vertex detector, which was only present in the *feb97* measurement, is also shown. The various detectors and the deuterium target are discussed in subsequent sections.

In the *feb97* measurement two of the telescopes on the spectrometer side of the beam were removed and a leadglass calorimeter was installed (not shown in the figure). Also, the telescopes on the left side of the beam were moved further

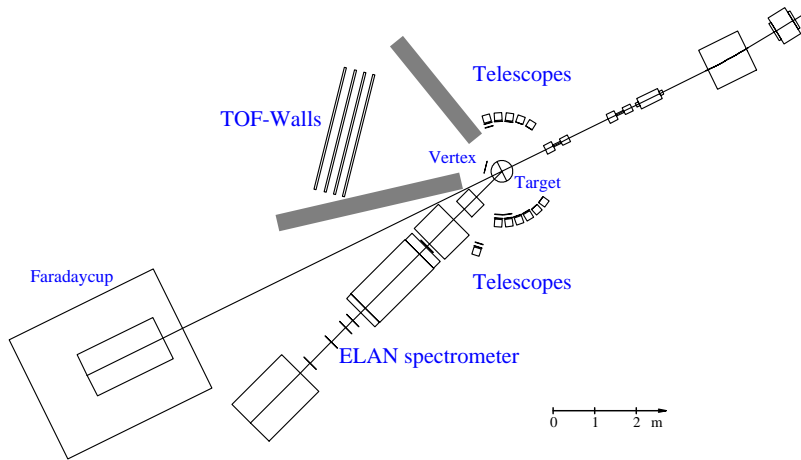


Figure 3.2: Layout of the detectors: ELAN spectrometer, four TOF-walls, vertex detector (not yet for jan96) and twelve telescopes (T1–T4, S1–S4, D1–D4). Note that in the feb97 measurement two telescopes were replaced by a leadglass calorimeter. The two grey boxes indicate the concrete shielding for the TOF-walls.

away from the target. Details are given in section 3.2.4. Also, in order to reduce the background from the diverging beam, in this measurement the beamline downstream from the target was replaced by a bag filled with helium.

3.2.1 Target

The target is a cylindrical cell of liquid deuterium, 6 cm long and 3 cm in diameter. The beam is focused approximately along the axis of the cell. The deuterium is surrounded by a vacuum defined by two Kapton foils with a total thickness of $250\ \mu\text{m}$. All the gas handling and cooling equipment is located on top of the target, so that the target has an almost 360° window in the horizontal plane. The only limitation is the support connecting the top and bottom parts of the apparatus, which is positioned at an angle where it does not hinder any detector. The out-of-plane window of the target is larger than the acceptance of the detectors.

For the feb97 measurement a magnet with a 5 cm radius was installed above and below the liquid deuterium, creating a magnetic field of the order of 0.5 T [Ban96]. The purpose of this field was to reduce the low energy electromagnetic background in the vertex detector. This was accomplished, but at the cost of a strongly increased background in the telescopes on the left side of the beam.

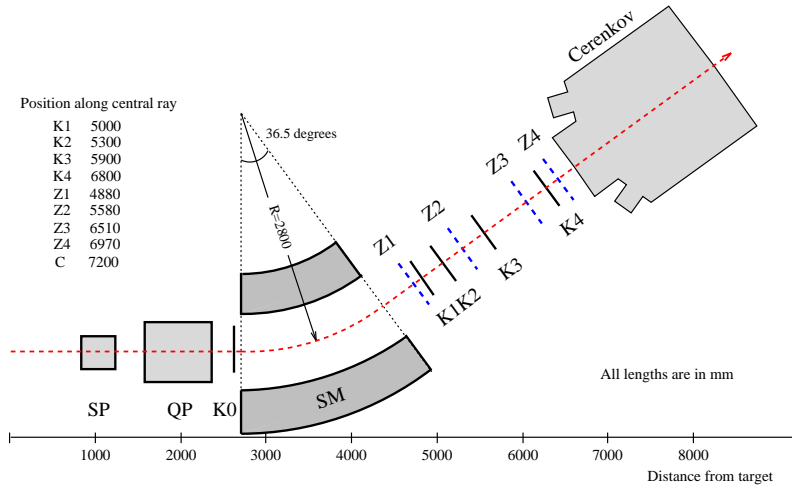


Figure 3.3: The components of the ELAN spectrometer: a bending dipole magnet (Sektor Magnet), two focusing magnets (QuadruPole and SextuPole), fi ve wire chambers (Kammer 0–4), four scintillators (Z1–Z4) and a Čerenkov counter. The distances from the target are indicated, measured along the central ray.

3.2.2 ELAN spectrometer

The ELAN spectrometer consists of one bending magnet, two focusing magnets, four wire chambers for tracking, four scintillators for time and pulse height measurements and a Čerenkov counter to distinguish electrons from pions. A fifth wire chamber, “Kammer 0” [Mas96], in front of the bending magnet helps to improve the resolution at the target. The various components of the spectrometer are shown in Figure 3.3. An extensive description of this detector can be found in [Rit74].

The spectrometer has a momentum acceptance of $\pm 12\%$ with a resolution of 3 MeV. The angular acceptance is 1.8 msr: 22 mrad in the horizontal plane and 80 mrad out-of-plane. At the angle used in our experiment ($\Theta_{e'} = 19^\circ$) the out-of-plane acceptance corresponds to a range $|\Phi_{e'}| < 7^\circ$ in the azimuthal angle.

3.2.3 TOF-walls

The four TOF-walls, developed and built by the Universität Bonn [Got98], each consist of 15 scintillator bars with two-sided photomultiplier readout. Each scintillator bar is 20 cm wide, 300 cm long and 5 cm thick, so that the total active area is $300 \times 300 \text{ cm}^2$. The primary signal processing electronics is incorporated in the frame of the TOF-walls. Each TOF-wall is also equipped with a movable thin scintillator attached to the rear of the wall, perpendicular to the 15 bars, which can

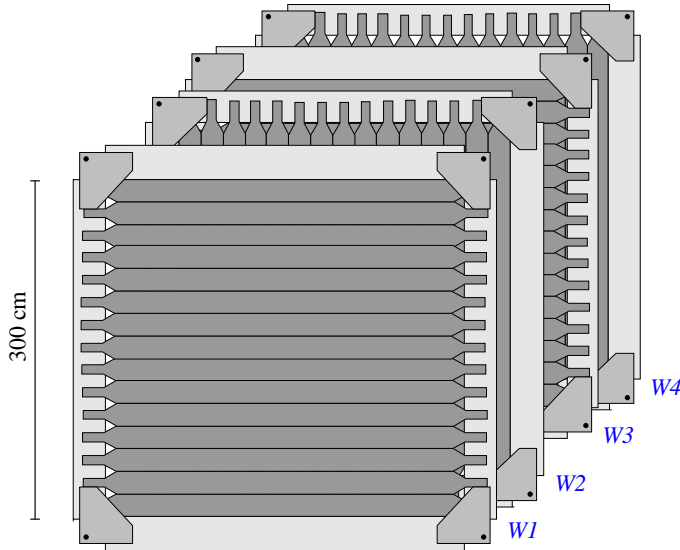


Figure 3.4: The four TOF-walls, consisting of fifteen 300 cm long scintillator bars with photomultipliers on both sides and signal processing electronics in the frame.

Wall	distance	angle	middle bar	
	d (m)	θ (deg)	j_{mid}	y_{shift} (m)
1	3.5	-40.	11	
2	3.706	-40.35	24	+0.012
3	3.952	-40.37	43	-0.019
4	5.1	-40.	55	

Table 3.1: Position of the four TOF-walls. The angle θ is for a line perpendicular to the wall and through the centre of the target. The intersection of this line with Wall 2 lies in the “middle bar” j_{mid} at an offset y_{shift} from the centre of the bar.

be used to investigate the position dependence of measured quantities. These thin scintillators are not used in the experiment discussed in this thesis.

The four TOF-walls are placed behind each other as shown in Figure 3.4, approximately 4 m from the target at an angle of 40° w.r.t. the beam. The perpendicular placement of two consecutive walls allows a segmentation of (charged) particle hits into $15 \times 15 = 225$ bins. The position of the second and third wall has been determined accurately (see Table 3.1), other positions can be inferred using coincident events. A 5 mm aluminum shield placed in front of Wall 1 suppresses the background of low energy electromagnetic radiation from the target or from the beamline. A 5 cm thick iron shield inserted between Wall 3 and Wall 4 prevents protons from reaching Wall 4. This is only necessary for neutron detection.

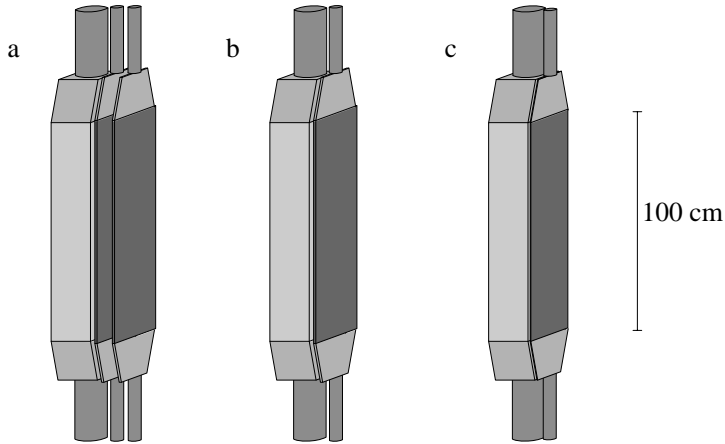


Figure 3.5: The three kinds of scintillator telescopes: (a) double: one thick bar and two thin bars, (b) single: one thick bar and one thin bar, and (c) thin: one thick bar and one very thin bar. Each scintillator is equipped with two photomultipliers.

Vertex detector

In the *feb97* measurement an additional detector was installed close to the target in order to better discriminate between charged and neutral particles in the TOF-walls and to improve the determination of the (charged) particle angle. This “vertex detector” [Ban96] consists of two layers of fifteen 1 mm thick scintillator strips. The solid angle covered by the vertex detector is approximately equal to that of the TOF-walls. This detector is not used in our analysis.

3.2.4 Telescopes

Twelve scintillator telescopes were placed at larger angles w.r.t. the momentum transfer. Each of these telescopes consists of a thick “E-bar” and one or two thin “ ΔE -bars”. Three different configurations were available (see Figure 3.5):

D(ouble): one E-bar with two 1 cm thick ΔE -bars, F(ront) and R(ear),

S(ingle): one E-bar with one 1 cm thick ΔE -bar,

T(hin): one E-bar with one 3 mm thick ΔE -bar.

The E-bars and the *thin* ΔE -bars are 18 cm wide and 100 cm long, whereas the other ΔE -bars are 20 cm wide and 102 cm long. The E-bar is 18 cm thick. All bars are equipped with photomultipliers on both ends and are mounted on magnetic feet. There are four telescopes of each type.

Telescope	height (m)	jan96		feb97	
		Θ (deg)	distance (m)	Θ (deg)	distance (m)
D1	-0.138	+45.0	1.6	+46.5	1.92
D2	-0.143	+60.0	1.1	+54.5	1.92
D3	-0.143	+71.8	1.1	+61.9	1.92
S1	-0.143	+83.3	1.1	+69.7	1.92
S2	-0.143	+94.8	1.1	+76.3	1.92
T3	-0.128	+106.3	1.1		
T1	-0.153	+118.0	1.1		
D4	-0.143	-95.0	1.0	-100.0	1.22
S4	-0.143	-108.0	1.0	-112.1	1.22
S3	-0.143	-122.5	1.0	-124.0	1.22
T4	-0.123	-137.0	1.0	-135.8	1.22
T2	-0.123	-150.0	1.0	-147.9	1.22

Table 3.2: Position of the twelve telescopes during the two measurements. Angles are given w.r.t. the beam, positive on the spectrometer side and negative on the TOF-wall side. The height is the vertical position of the telescope centre w.r.t. the beamheight. The distance is measured from the centre of the target to the front face of the E-bar.

The three types were employed according to the different experimental conditions expected. At the most forward angles w.r.t. the beam the *double* telescopes (D1-D4) were used, in order to better distinguish interesting particles from the stronger background. At backward angles w.r.t. the momentum transfer the four *thin* telescopes (T1-T4) were used, because at these angles the energy of the protons is so low that they cannot pass through the 1 cm ΔE -bars. The remaining positions were occupied by the four *single* detectors (S1-S4). In the *feb97* measurement the telescopes were shielded from the low energy electromagnetic background by various sheets of iron (all approximately 1 mm thick); in the *jan96* measurement only telescope D1 was shielded.

In the *feb97* measurement a leadglass calorimeter was installed, replacing telescopes T1 and T3 and forcing the other telescopes on the left side of the beam to more forward angles and a larger distance from the target. The exact position of the twelve telescopes in the two measurements is given in Table 3.2.

3.3 Electronics and data acquisition

The front end electronics [Noe92] are based on a CAMAC system for the spectrometer data and on a FastBus system for the other detectors. Pre-processing of the data – discrimination, coincidences – is performed by NIM modules for the spectrometer and telescopes. For the TOF-walls dedicated electronics have been designed and built by D. Jakob [Jak96]. The vertex detector data are also discriminated inside the detector [Ban96] but no further pre-processing is performed.

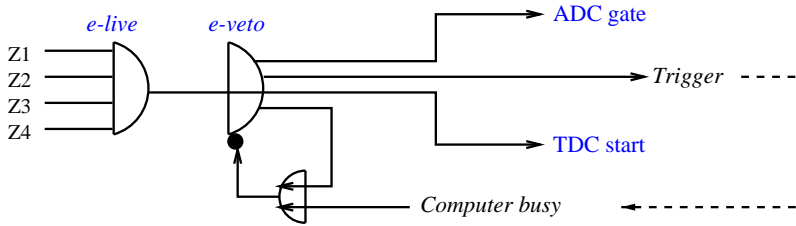


Figure 3.6: The spectrometer hardware trigger of the experiment. Only the essential elements are shown.

The primary interface to the electronics is the MECDAS³ system, running on a VME processor⁴. The data are retrieved from MECDAS and stored on disk by the GOOSY⁵ software. In the *jan96* measurement the VAX version was used, whereas in the *feb97* measurement the AXP version was available. The data files are transferred from the VAX or AXP to other computers and stored on exabyte tapes by dedicated software developed in Bonn.

3.3.1 Spectrometer electronics and readout trigger

The trigger for the data acquisition system to read out the front-end electronics is given by the “e-live” signal (see Figure 3.6). This signal – indicating an electron hit – is the coincidence between the four scintillators *Z1–Z4* in the spectrometer, of which *Z1* always defines the timing. The data acquisition electronics also provides a more complicated (electron-hadron coincidence) trigger, which was used in previous experiments [Bru95b]. For our experiment it was not required, because the single arm countrates could be handled adequately.

In order to ensure that data from two events are not mixed, the “e-live” signal is inhibited, or “vetoed”, during the readout of the electronics by MECDAS. The “e-veto” signal is also used as the *start* for the TOF-wall TDC modules and as the gate for all ADC modules, except the telescope ADCs in the *jan96* measurement (see section 3.3.3).

3.3.2 TOF-wall electronics

The 30 photomultiplier signals of the 15 bars in one Wall are processed by dedicated electronics, built into the frame of the Wall. The signals are split in three: one is delayed and then integrated by a FastBus ADC module, one is fed into discriminator chips with a low threshold and the third triggers discriminator chips with a

³Mainz Experiment Control and Data Acquisition System

⁴ELTEC E6 M68030

⁵GSI Online and Offine SYstem

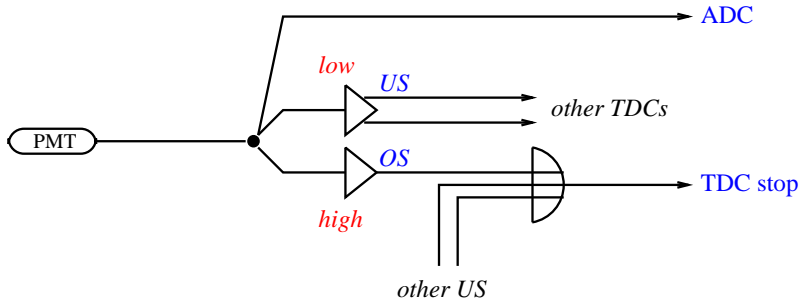


Figure 3.7: Simplified scheme of the electronics used for the TOF-walls. Note the two TDC-signals, Obere Schwelle (OS) and Untere Schwelle (US).

high(er) threshold. The two discriminators – referred to as *Untere Schwelle (US)* and *Obere Schwelle (OS)*⁶ – generate the *stop* for the FastBus TDC-modules. The *OS* is the main TDC signal for a photomultiplier, the *US* is meant for very small energy deposits, but is also more sensitive to low energy background. In order to reduce the amount of TDC-channels needed, an *US* does not have its own TDC, but is delayed by approximately 65 ns and then uses the TDC of a different photomultiplier (the “host”). Obviously, the *US* TDC signal is only available if the host photomultiplier has not fired, but thanks to the shielding the countrates in the individual photomultipliers were low enough to ensure that this was usually the case. To be on the safe side, each *US* is fed into *two* host TDC-channels. Therefore, a value in a given TDC-channel may belong to any one of three photomultipliers – in the analysis we must determine the correct one. The essential features of the TOF-wall electronics are shown in Figure 3.7, details can be found in [Jak96].

There is one common low threshold and one common high threshold for each TOF-wall. In our experiment they were all set to comparable low values.

3.3.3 Telescope electronics

The signals from the telescope photomultipliers are split into two equal parts, one of which is delayed and passed on to the ADC module, while the other triggers a discriminator module. The NIM level output of the discriminator is converted to an ECL signal and passed to the TDC module. The coincidence of the signals from the two ends of the E-bar constitutes the “telescope triggers”. The logical OR of all twelve of such telescope signals was used in combination with the electron signal as a gate for the telescope ADC modules during the *jan96* measurement. The goal was to allow a narrower ADC gate, but due to the large differences in proton energies between the twelve telescopes, or even within one telescope, the gate

⁶German for *lower* and *higher threshold*

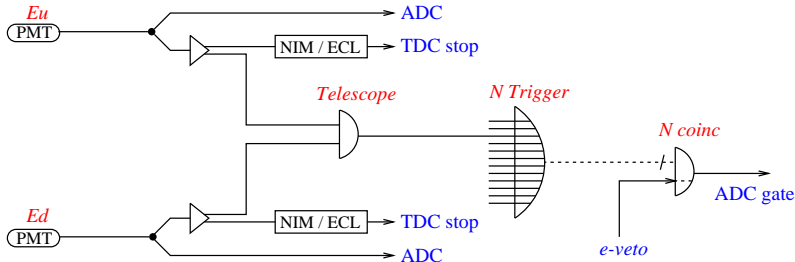


Figure 3.8: Scheme of the telescopes E-bar and coincidence electronics. In the *jan96* measurement the ADC gate for the telescopes consisted of the coincidence between “e-veto” and “N Trigger”, in the *feb97* measurement only “e-veto” was used. The electronics for the ΔE -bars is similar, but without the coincidence part.

still needed to be quite wide. Therefore, in the *feb97* measurement, the electron signal “e-veto” was simply used for the ADC gate, just as for the TOF-walls. The electronics scheme for the telescopes is shown in Figure 3.8.

Unfortunately, in the analysis it turned out that during the *jan96* measurement the ADC gate came a little too late, so that only the final part of the ADC signals was integrated. As a result the telescope data of that measurement cannot be analyzed in a reliable way. This problem was solved before the *feb97* measurement.

3.4 Kinematics of the experiment

The kinematics were chosen with the following points in mind:

- In order to maximize the countrate and to leave as much space as possible for the telescopes, the ELAN spectrometer was put at its most forward angle, 19° w.r.t. to the beam.
- The beam energy of 1.6 GeV was – at the time – the highest energy for which a reasonably high intensity beam was available.
- Two kinematical settings of the ELAN spectrometer are needed to cover the complete energy transfer range from below quasielastic scattering ($\omega \approx 140$ MeV) to beyond the Δ -resonance ($\omega \approx 450$ MeV). By creating some overlap in the energy transfer range of the two settings, and by measuring at an intermediate energy transfer for a short period of time, the consistency of the different parts was ensured.

Details of the different settings are given in Table 3.3. There were four settings, $\mathcal{J}1$ – $\mathcal{J}4$, during the *jan96* measurement and three, $\mathcal{F}1$ – $\mathcal{F}3$, during the *feb97* measurement. The majority of the data was taken at settings $\mathcal{J}1$, $\mathcal{J}4$ and $\mathcal{F}1$.

	$E_{e'}$ (GeV) central	ω (GeV) central range	q (GeV/c) central range	Θ_q (deg) central range
<i>January 1996</i>				
$\mathcal{J}1$	1.154	0.446 0.31 – 0.58	0.629 0.56 – 0.71	-36 -47 – -27
$\mathcal{J}2$	1.214	0.386 0.24 – 0.53	0.596 0.54 – 0.68	-41 -54 – -30
$\mathcal{J}3$	1.275	0.325 0.17 – 0.48	0.568 0.52 – 0.65	-46 -62 – -34
$\mathcal{J}4$	1.325	0.275 0.12 – 0.43	0.549 0.52 – 0.62	-51 -67 – -37
<i>February 1997</i>				
$\mathcal{F}1$	1.154	0.446 0.31 – 0.58	0.629 0.56 – 0.71	-36 -47 – -27
$\mathcal{F}2$	1.325	0.275 0.12 – 0.43	0.549 0.52 – 0.62	-51 -67 – -37
$\mathcal{F}3$	1.410	0.190 0.02 – 0.36	0.525 0.52 – 0.58	-60 -78 – -43
<i>all</i>	$E_0 = 1.6$ GeV	$\Theta_{e'} = 18.95$ deg	$-Q^2 = 0.19 - 0.26$ (GeV/c) ²	

Table 3.3: Details of the different kinematical settings during the experiment: $\mathcal{J}1$ – $\mathcal{J}4$ for the jan96 measurement and $\mathcal{F}1$ – $\mathcal{F}3$ for the feb97 measurement.

In addition, for each kinematical setting a measurement was performed without any deuterium in the target, in order to be able to subtract the contribution of the target walls from the results.

Chapter 4

Data analysis

In order to obtain the final cross section results from the original experimental values, many different analysis steps are necessary, such as various calibrations, the proton identification, the selection of ${}^2H(e, e'p)n$ “breakup” protons and the estimation of some correction factors and scaling factors.

All analysis steps related to the electron spectrometer are described in section 4.1, those specific for the TOF-walls in section 4.2 and those for the telescopes in section 4.3. Finally, the overall correction and scaling factors are given in section 4.4.

4.1 Electron spectrometer

This section describes the analysis of the information obtained from the ELAN spectrometer. The four-vector of the scattered electron is reconstructed from the signals in the *wire chambers*, including the extra wire chamber “Kammer 0”. The four *scintillators* in the spectrometer are used to improve all recorded TDC signals by eliminating variations in the “start time”. The detection efficiency follows from the wire chamber analysis and the dead time of the electronics is calculated using the *scalers* recorded for every event. Finally, the stability of the position of the electron beam on the target is investigated by considering variations in the reconstructed interaction point.

The last subsection introduces the electron energy binning, which will be used throughout the remainder of the thesis.

4.1.1 Wire chamber hits

To interpret the hits in the five wire chambers, $K0-K4$, the existing ELAN analysis software has been used, of which the main features are described here.

A least-squares fit is performed to all possible hit combinations in wire chambers $K1$ – $K4$. If one of the wire chambers does not have a hit – or if the four wire chamber fit does not yield a valid result – any “dead” wires in the missing wire chambers are used instead. If this still does not yield a valid result, the chamber is ignored. The quality of a fit is determined by the standard deviation of the slope. Not more than ten fits are considered for either direction perpendicular to the central ray (“radial” and “axial”).

The information from the extra wire chamber $K0$ is used to improve the track reconstruction. The wires in the three planes of $K0$ are rotated by 60 degrees w.r.t. one another. The best hits in this chamber are defined as the hit combinations which enclose the smallest triangle. If one of the planes has not fired, the coordinates of any “dead” wires are inserted, or else the plane is ignored and the intersection point of the wires in the other two planes is used. Again, only the ten best hits are considered.

For each combination of radial and axial fits, the angles and momentum of the electron and the interaction point in the target along the beam are calculated from the four fit parameters (two slopes and two offsets) with third order polynomials. It is assumed that the interaction took place on the target axis, i.e. the vertical and horizontal position are set to zero. From these quantities the intersection point of the track with $K0$ is determined, again using third order polynomials. The final “quality” of such a track is determined from the standard deviations of the axial and radial fits and the distance of the intersection point from the center of gravity of the nearest $K0$ hit, and the highest quality hit is selected.

The final values for the angles and momentum of the electron and the interaction point in the target are calculated from the radial and axial offsets and the $K0$ hit using Chebychev polynomials. The inclusion of the $K0$ information improves the resolution of the interaction point by a factor 5 [Mas96].

4.1.2 Scintillator hits

The hardware trigger of the spectrometer consists of a fourfold coincidence between the four scintillators $Z1$ – $Z4$, so that these signals exist in every recorded event. The position of the hit in these scintillators is calculated from the track obtained in the wire chamber fit, so that the TDC values can be corrected for the light propagation time within the scintillator. In addition, walk effects are removed using the ADC signals.

The $Z1$ signal always defines the time of the trigger and therefore the TDC-start for all detectors in the experiment. However, this signal is not at a fixed offset w.r.t. the interaction time in the deuterium target, e.g. due to different paths of the electrons through the spectrometer. In order to eliminate these variations and thus obtain a more accurate value for the time-of-flight of the particle, the following procedure [Rei93, Jak96] is applied (the symbols are explained in Figure 4.1).

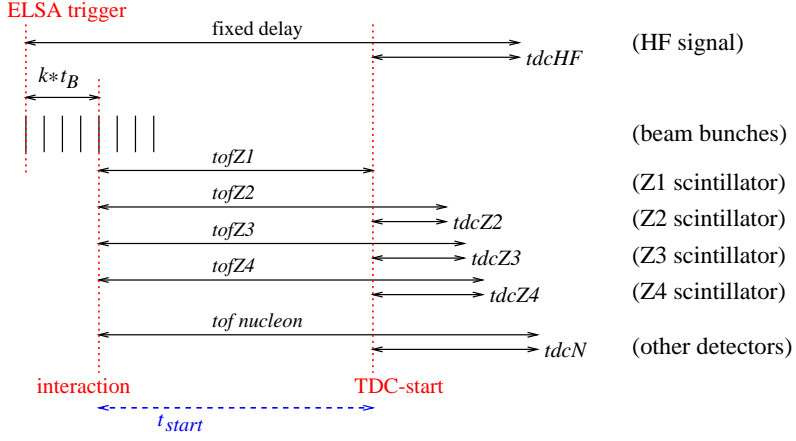


Figure 4.1: Definition of the various times involved in the HF correction. Note that times called $tofZ$ are actually the sum of the time-of-flight, the light propagation time and the resolution of the corresponding photomultiplier. t_B is the time between two bunches (2 ns).

The method relates the TDC-start to a fixed point in time – the trigger of the high frequency (500 MHz) microwaves used within the ELSA ring – by also recording a TDC value ($tdcHF$) for this signal. Any variations in the TDC-start will be visible as deviations from the constant in the $tdcHF$ spectrum. However, the procedure is complicated by the high frequency structure of the electron beam, which arrives at the target in small bunches 2 ns apart. Each bunch corresponds to one extraction of electrons from the ELSA ring and the fixed point in time is the extraction of the first bunch. Therefore the actual $tdcHF$ spectrum does not consist of only one constant value with deviations, but several – just as many as there are bunches. Unfortunately, the variation in TDC-start is so large that it is not clear in this spectrum where the constant values are and thus what the deviation from the relevant constant value is for a specific event (see Figure 4.2a). The solution is to compare the $tdcHF$ value to the TDC of another scintillator, e.g. Z2. One can write

$$\begin{aligned} tdcZ2 &= tofZ2 - tofZ1 + \text{offset} \\ tdcHF &= \text{constant} - k * t_B - tofZ1 \end{aligned} \quad (4.1)$$

and it follows that the difference

$$tdcHF - tdcZ2 = -k * t_B - tofZ2 + \text{offset} \quad (4.2)$$

eliminates the TDC-start variation and is directly related to the correct bunch k . An example of such a $tdcHF - tdcZ$ spectrum for Z2 is given in Figure 4.2b. Scintillators Z3 and Z4 yield similar spectra.

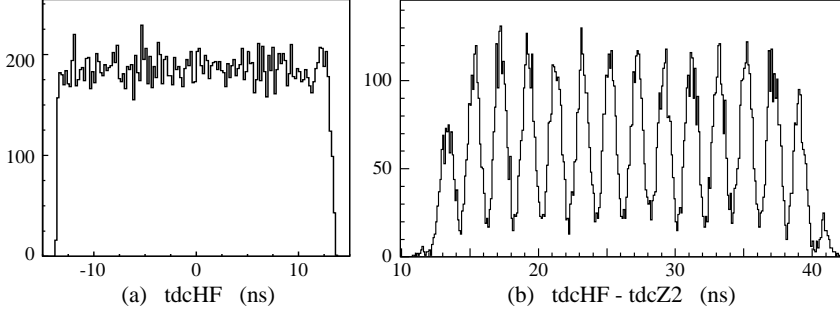


Figure 4.2: (a) The TDC value of the ELSA trigger signal. (b) The spectrum used to determine the most probable bunch for the Z2 scintillator. The order of the bunches is from right to left: for events from a “later” bunch the TDC-start is later and hence $tdcHF$ is smaller.

The remaining uncertainty in the $tdcHF - tdcZ$ spectrum (due to variations in $tofZ2$) is sufficiently smaller than the time between two bunches t_B , so that the bunch b , in which the interaction most probably took place, can be determined as follows. First, the position of the peaks and their width σ is determined for all three scintillators Z2–Z4. Next, a Gaussian weight factor

$$w_Z = e^{-d_{Z,i}^2/2\sigma^2} \quad (4.3)$$

is assigned to each bunch (per event), where $d_{Z,i}$ is the distance of the event from the center of bunch i . The bunch with the largest weight in all three spectra simultaneously ($w_{Z2} + w_{Z3} + w_{Z4}$) is chosen as the most probable bunch for that event.

When the most probable bunch b is known, the correction for the elimination of the TDC-start variations is defined as

$$t_{start} \equiv tdcHF + b * t_B \approx \text{constant} - tofZ1 \quad (4.4)$$

which only depends on the variations in $tofZ1$, apart from a constant offset. Indeed, applying this correction to e.g. scintillator Z2 and assuming $b = k$ (the bunch assignment is correct) yields:

$$tdcZ2 - t_{start} \approx tofZ2 + \text{offset} \quad (4.5)$$

which corresponds to the actual¹ time-of-flight for scintillator Z2.

Figure 4.3 shows the effect of this correction on scintillators Z1–Z4. In addition, all peaks have been moved to a common value. When the variation in the TDC-start is eliminated, the peak becomes sharper, except for Z1 which always defines its own TDC-start. Similar improvements are obtained for the other detectors.

¹Walk and light propagation effects have already been eliminated.

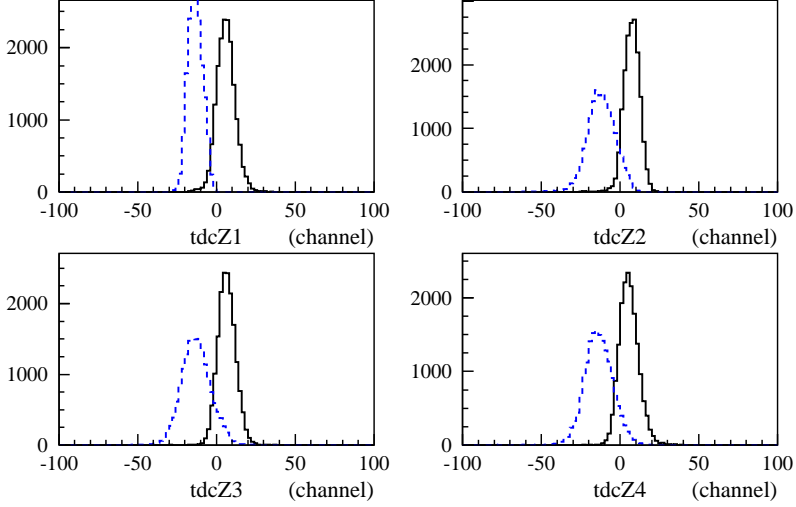


Figure 4.3: TDC spectra for the four spectrometer scintillators Z1 – Z4 before (dashed line) and after (solid line) correcting for t_{start} .

4.1.3 Efficiencies

The *electron detection efficiency* η_e is the product of the hardware trigger efficiency, $\eta_Z = 99\%$ [Fro93], and the wire chamber efficiencies η_{radial} and η_{axial} ². The wire chamber efficiencies are calculated by comparing the number of good wire chamber fits (i.e. both axial *and* radial fit) to the number of axial fits or the number of radial fits, respectively:

$$\eta_{\text{WC}} = \eta_{\text{radial}} \times \eta_{\text{axial}} = \frac{N_{\text{goodfit}}}{N_{\text{ax.fit}}} \times \frac{N_{\text{goodfit}}}{N_{\text{rad.fit}}}. \quad (4.6)$$

When the data acquisition system is triggered by a valid hit, the input channels are disabled until the event has been completely processed. Therefore any valid events occurring before this “veto” is removed are ignored. The correction for this *dead time* of the data acquisition system is found by comparing the number of events in a datafile to the the actual number of valid hits (“e-live” signals) in the same period:

$$\eta_{\text{live}} = \frac{N_{\text{file}}}{N_{\text{e-live}}}. \quad (4.7)$$

The number of “e-live” signals is counted by a scaler which is *not* disabled during event processing and is also recorded in the datafile.

²“Radial” and “axial” are the two directions perpendicular to the central ray of the spectrometer, see section 4.1.1.

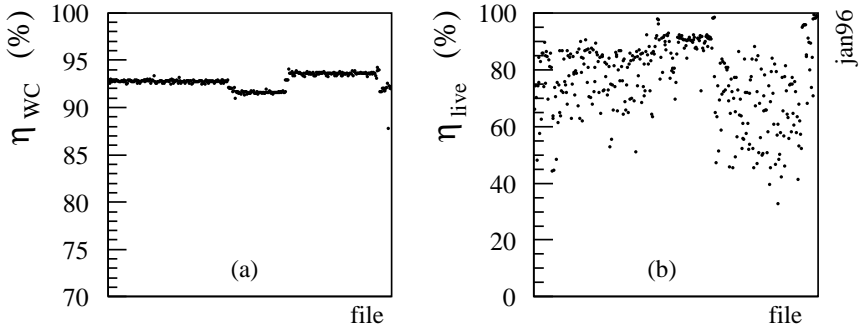


Figure 4.4: (a) The spectrometer wire chamber efficiency η_{WC} and (b) the correction for the dead time of the data acquisition system η_{live} during the jan96 experiment. Note the different scales.

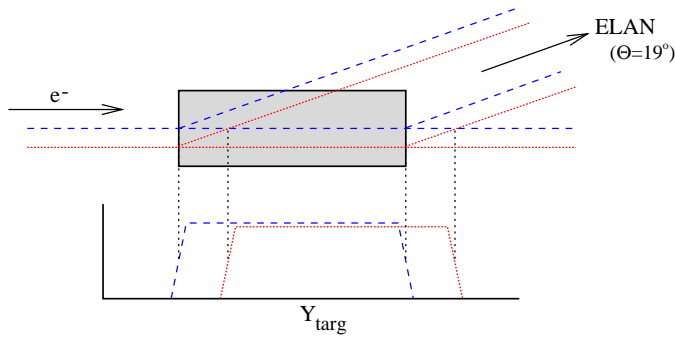


Figure 4.5: Top view of the target and the corresponding spectrum of the calculated target position Y_{targ} . The effect on the Y_{targ} spectrum of a change in the position of the beam on the target is illustrated by the dashed and solid lines.

The wire chamber efficiency and the dead time correction have been determined separately for every datafile. Figure 4.4 shows the variation of these quantities during the *jan96* experiment. The rather abrupt changes in (a) correspond to the changes in the kinematical setting of the spectrometer and are probably related to the different instantaneous countrates.

4.1.4 Stability of the beam

Throughout the experiment the position of the beam on the deuterium target varied a little in the direction perpendicular to the target axis. This is observed as a shift in the spectrum of Y_{targ} , the calculated intersection of the scattered electron track with the axis of the target (see Figure 4.5).

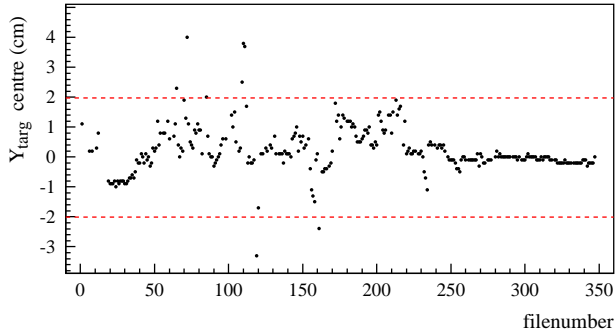


Figure 4.6: Stability of the center of gravity of the Y_{targ} spectrum during one of the experiments. The lines indicate the limits of acceptable values.

bin	ω (MeV)	$E_{e'}$ (MeV)	bin	ω (MeV)	$E_{e'}$ (MeV)
E1	100 – 150	1450 – 1500	E6	350 – 400	1200 – 1250
E2	150 – 200	1400 – 1450	E7	400 – 450	1150 – 1200
E3	200 – 250	1350 – 1400	E8	450 – 500	1100 – 1150
E4	250 – 300	1300 – 1350	E9	500 – 550	1050 – 1100
E5	300 – 350	1250 – 1300	E10	550 – 600	1000 – 1050

Table 4.1: Limits of the ten energy transfer bins in terms of the transferred energy ω and (equivalently) the scattered electron energy $E_{e'}$.

To investigate if a correction is needed, the variation of the center of gravity of this Y_{targ} spectrum is given in Figure 4.6. For most files the variation is less than 1 cm, which is small compared to the distance of the detectors from the target (approximately 1 and 4 m) and can therefore be neglected. Or, from a different perspective, a 1 cm Y_{targ} shift corresponds to a 3.5 mm perpendicular shift of the beam, which is well within the 1.5 cm target radius. Files for which the Y_{targ} shift is more than 2 cm have been rejected.

4.1.5 Energy transfer bins

In the remainder of the analysis the events will be separated into ten energy transfer bins, in order to obtain sufficient statistics, especially at large energy transfers. Each bin is 50 MeV wide and together the ten bins cover the complete energy range of the experiment. The bins are labeled E1–E10, where bin E1 corresponds to the lowest energy transfers (the quasielastic region) and bin E10 lies beyond the Δ -resonance. See Table 4.1 and Figure 4.7.

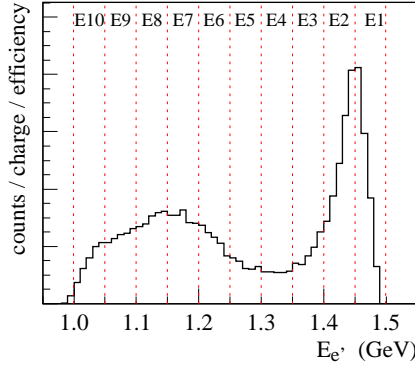


Figure 4.7: The ten energy transfer bins superposed on a spectrum of the scattered electron energy $E_{e'}$ for the jan96 measurement.

4.2 TOF-walls

The analysis of the TOF-walls consists of the calibration of the ADC and TDC values to obtain the deposited energy, position and time-of-flight, subsequently the identification of protons, and finally the selection of events from the ${}^2\text{H}(e, e'p)n$ reaction. The proton detection efficiency is determined from the data in such a way that it includes the corrections for proton losses in all these analysis steps. Only the data from the second and third TOF-wall are analyzed, because Wall 1 suffered from too high background radiation and Wall 4 was – intentionally! – shielded from protons by 5 cm of iron.

The scintillator bars in the four TOF-walls are numbered continuously³ as shown in Figure 4.8. The individual TOF-wall bars are usually referred to as e.g. “L23” (for the seventh bar in Wall 2) where the L stands for *Latte*, which is German for *bar*. When dealing with the individual photomultipliers, the two sides of a vertical bar are labeled “U” (up) and “D” (down) and the two sides of a horizontal bar “L” (left) and “R” (right). When the orientation of the bar is not relevant, the two sides are simply referred to as “A” and “B”.

Since both TOF-walls consist of 15 bars and the two walls were placed orthogonally, the results of the experiment are separated into 225 so-called segments, each corresponding to the $20 \times 20 \text{ cm}^2$ intersection of a vertical bar in Wall 2 and a horizontal bar in Wall 3.

Most of the other geometrical quantities defined in Figure 4.8 are used in the position calibration (section 4.2.1). Some values are given in Table 3.1.

³The omitted number 32 is used for the thin scintillator on the rear of Wall 2 and is not relevant for our analysis (see section 3.2.3).

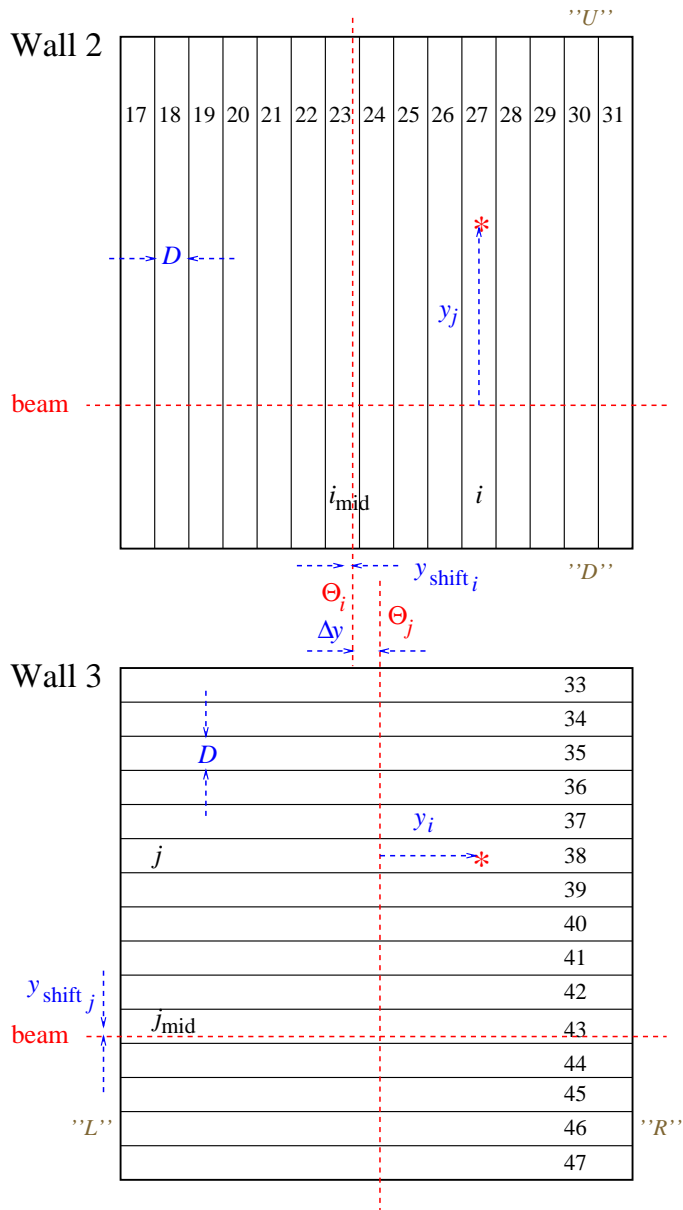


Figure 4.8: Numbering of the TOF-wall bars (as seen from the direction of the target) and some other geometrical quantities relevant to the analysis. The dashed lines indicate the beam height and the angle of the wall.

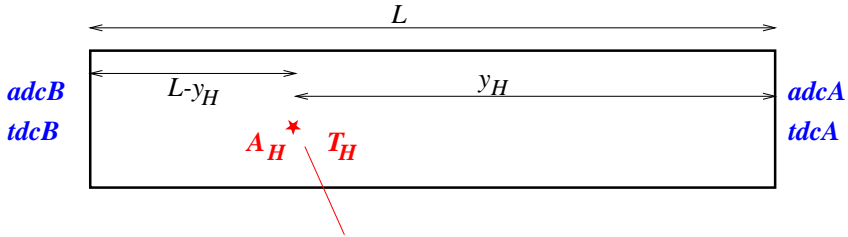


Figure 4.9: Definition of quantities related to a hit in a scintillator bar. (A_H, T_H) represent the actual energy deposit and time of the hit at position y_H , while ($tdcA, adcA$) and ($tdcB, adcB$) are the TDC and ADC values recorded by the electronics. L is the length of the bar.

4.2.1 TDC values

Several quantities related to a hit in a scintillator bar and the corresponding ADC and TDC values at both ends of the bar are defined in Figure 4.9. Using these definitions the TDC values at the two ends of a scintillator bar can be written as

$$\begin{aligned} tdcA &= T_H + (L - y_H)/c_n \\ tdcB &= T_H + y_H/c_n \end{aligned} \quad (4.8)$$

where c_n is the effective propagation speed of the signals in the scintillator material (about 0.13 m/ns). Adding and subtracting the TDC values of the two ends of a bar yields quantities proportional to the time and the position of the hit, respectively:

$$\begin{aligned} T_{\text{sum}} &\equiv (tdcA + tdcB)/2 = T_H + (L/c_n) \\ T_{\text{dif}} &\equiv (tdcA - tdcB) = (2y_H - L)/c_n . \end{aligned} \quad (4.9)$$

The measured time-of-flight and position of the hit is then defined as

$$\begin{aligned} t_{\text{hit}} &\equiv T_{\text{sum}} - t_0 \\ y_{\text{hit}} &\equiv (T_{\text{dif}} - y_0) \times y_C . \end{aligned} \quad (4.10)$$

The calibration factor y_C and the offsets t_0 and y_0 are determined below, and we have assumed that the individual TDC values are already expressed in nanoseconds. These TDC calibration factors, approximately 50 ps per channel, have been determined separately for every TDC-channel before the experiment [Wac96].

OS and US

The time signal of each photomultiplier in the TOF-walls is recorded in *three* different TDC-channels, once with a high threshold, OS, and twice with a (common)

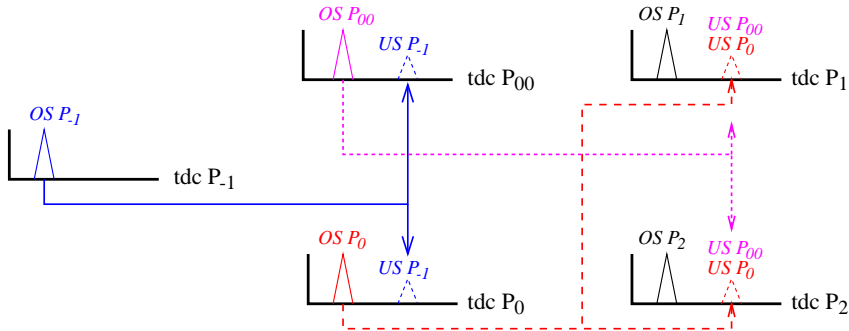


Figure 4.10: Relationships between the OS and US of the TOF-wall TDC channels. See the main text for explanation.

low threshold, $US1$ and $US2$, where the US signals are delayed by about 65 ns in the electronics (see section 3.3.2).

Several combinations of OS and US can be used to define t_{hit} and y_{hit} . Priority is given to the OS , because this is the “direct” TDC of the photomultiplier and is less sensitive to spurious low-energy background events, but when the OS of one of the photomultipliers (or both) is not available, one of the corresponding US is used instead⁴. The possibilities are, in order of decreasing priority:

- “P” : OS (A) and OS (B)
- “NA” : OS (A) and US (B)
- “NB” : US (A) and OS (B)
- “G” : US (A) and US (B)
- “A” : ADC (A) and ADC (B).

The labels “P”, “N” and “G” are derived from the words “proton”, “neutron” and “gamma”, respectively, as they reflect the kind of signals expected for those particles. The fifth possibility, “A” (derived from “ADC”) is explained below.

In the analysis the constant delay of an US w.r.t. its OS is subtracted from the recorded TDC value of the US :

$$tdcUS_{\text{corr}} = tdcUS - t_{US\text{off}} \quad (4.11)$$

so that the OS and US signals coincide and only one common set of calibration parameters is needed for all four possible combinations of TDC values. The correction factor $t_{US\text{off}}$ is determined for each US separately by considering events in which both OS and US are present, i.e. the majority of the events.

Two different US and one OS are multiplexed into a single TDC-channel. Therefore the US (or OS) of one photomultiplier can be mistaken for the OS (or US) of another photomultiplier, as illustrated in Figure 4.10.

⁴When both US are available for a certain photomultiplier, $US1$ is arbitrarily chosen.

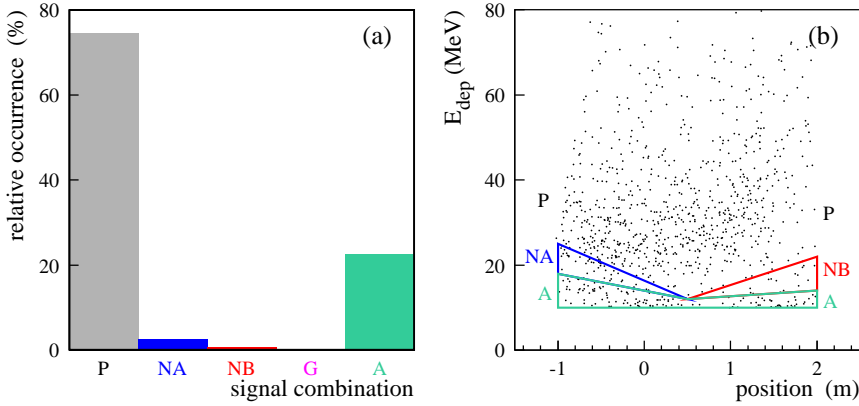


Figure 4.11: (a) Relative occurrence of the five possible combinations of TDC/ADC values for a bar in Wall 2. (b) Energy deposit versus position for the same bar. The contributions of the various signal combinations are indicated.

- What is presumed to be an *OS* in $tdcP_0$ can actually be the *US* of an early hit in photomultiplier P_{-1} . This case is identified by a corresponding value in $tdcP_{00}$ at a constant offset from $tdcP_0$. The offset, the difference in cable length for *US1* and *US2* of P_{-1} , is determined using certain *OS* hits in $tdcP_{-1}$.
- An *US* value in $tdcP_1$ or $tdcP_2$ may belong to either photomultiplier P_0 or P_{00} . In order to assign the signal to photomultiplier P_0 , there must *not* be a corresponding *OS* in $tdcP_{00}$, again at a constant offset from the *US*.

In principle this argument can be repeated for more layers of indirection, but thanks to the low multiplicity of hits in the TOF-walls, one step is sufficient.

When none of the TDC values is available, a possible hit is defined using only the ADC values. In this case, labeled “A”, the position of the hit in the bar is calculated from the ratio of the two ADC values (see below). As signal type “A” obviously is sensitive to low energy random signals in the bar, it is given lowest priority and a value above 50 channels is required for both ADCs.

In our experiment the high and low thresholds were both quite low and nearly equal, so that the majority of the recorded events have two *OS* signals. Only at the edges of some bars does the proton signal become so small that just the *US* is available. Figure 4.11a gives the relative contributions of the different signal types for a bar in Wall 2. Figure 4.11b illustrates the energy deposits and positions that typically lead to the various types of signals. For example, the “N” combinations are mainly from low energy deposits at the edges of the bar.

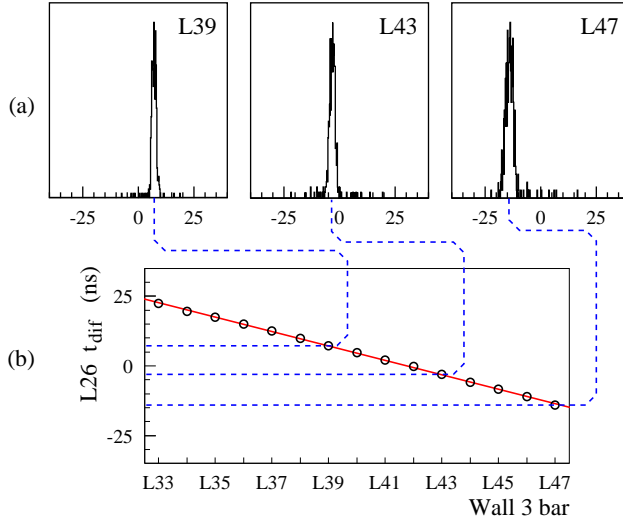


Figure 4.12: (a) T_{dif} spectra for bar L26 in Wall 2 with a coincident hit in the indicated bar in Wall 3. (b) Fit of the fifteen peak positions as a function of the Wall 3 bar number.

Position calibration

The position spectra of the TOF-wall bars are calibrated using coincident hits in the two Walls together with the known positions of Wall 2 and Wall 3. Figure 4.12a shows T_{dif} spectra of a bar in Wall 2, when there is also a hit in the indicated bar in Wall 3. The centres of all these peaks for a given bar i , corresponding to the fifteen bars j in the other wall, are parametrized by a straight line:

$$T_{\text{dif},i}(j) = A_i \times j + B_i \quad (4.12)$$

where A_i and B_i are the fit parameters. An example is given in Figure 4.12b.

Assuming the particles originate in the centre of the deuterium target and hit the centre of the bar j in the other wall, the position y_i of the hit in the wall under consideration can be calculated. In the case of a vertical bar i_V in Wall 2 one has:

$$y_i = ((j_{\text{mid}} - j) \times D + y_{\text{shift},j}) \times \left(\frac{d_i}{d_j}\right) \quad (4.13)$$

where D is the width of a bar and the factor $\left(\frac{d_i}{d_j}\right)$ projects the (vertical) position of the hit in Wall 2 onto Wall 3 by adjusting for the difference in the distance from the target. The beam height is taken as $y = 0$. Combining equations 4.11 and 4.13 and using equation 4.12 leads to expressions for the two calibration factors:

$$y_{C_i}^V = -\frac{d_i}{d_j} \times \frac{D}{A_i} \quad (4.14)$$

$$y_{0i}^V = A_i \times (j_{\text{mid}} + \frac{y_{\text{shift}j}}{D}) + B_i .$$

For a *horizontal* bar j_H in Wall 3 the position $y = 0$ is defined as the point where a line from the target intersects the wall perpendicularly⁵, so that

$$y_j = ((i - i_{\text{mid}}) \times D + y_{\text{shift}i}) \times (\frac{d_j}{d_i}) + \Delta y \quad (4.15)$$

$$\Delta y \equiv d_j \tan(\theta_j - \theta_i) .$$

The different in-plane angles of the two TOF-walls are taken into account in the projection of the hit in Wall 3 onto Wall 2 and the extra minus sign reflects the inverse numbering of the bars in Wall 3. Thus the calibration factors are:

$$y_{Cj}^H = \frac{d_j}{d_i} \times \frac{D}{A_j} \quad (4.16)$$

$$y_{0j}^H = A_j \times (i_{\text{mid}} - \frac{y_{\text{shift}i}}{D} - \frac{\Delta y}{D}) + B_j .$$

Time-of-flight calibration

The offset t_0 in equation 4.10 is determined by comparing the (calibrated) TDC values with the time-of-flight expected from the energy deposit in the bar. The relationship between the two is given in the lookup tables discussed in section 4.2.2.

4.2.2 ADC values

The ADC modules⁶ used in our experiment have two integration ranges in order to accommodate a large range of pulse heights while retaining a 12-bit accuracy for the smallest signals. This is achieved by splitting the incoming pulse and integrating the two parts separately. If the pulse is small, the low range result is used (channels 0 – 4095), otherwise the high range result (15 bits, channels 4096 – 32767) with the three least significant bits implicitly put to zero. However, since the high voltages of the photomultipliers were quite low during our experiment, the high range of the ADC module was not used for the TOF-walls.

For each ADC channel the position of the pedestal is determined separately by requiring no signal in the corresponding TDC. The pedestal is subtracted from the recorded value to obtain the actual ADC value. The pedestal can vary in time, for example due to temperature changes. To check if a correction is needed, the pedestals have been determined separately for every data file. Figure 4.13 shows the variation during the *feb97* measurement for a few typical ADCs. The variation is negligible compared to the typical proton signals of 200 – 600 channels.

⁵This is the vertical dashed line in Figure 4.8.

⁶LeCroy 2249.

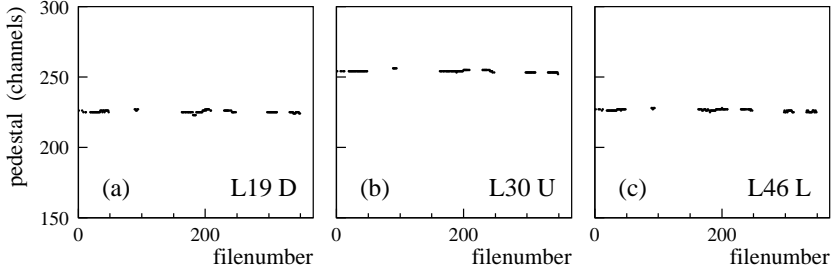


Figure 4.13: Stability of the TOF-wall pedestals throughout the feb97 measurement. Two bars in Wall 2 and one in Wall 3 are shown as typical examples.

Again using the definitions in Figure 4.9 the ADC values at the two ends of a scintillator bar can be written as:

$$adcA' = GA_H e^{-\alpha y_H} \quad (4.17)$$

$$adcB' = A_H e^{-\alpha(L-y_H)}$$

where α is an attenuation factor, indicating how fast a light signal decreases in a specific bar, and G is the gain ratio of the two photomultipliers of the bar. The accents indicate that the pedestals have already been subtracted from the raw ADC values. The product A_{pro} of the two ADCs (after subtracting the pedestals) is a position independent quantity proportional to the deposited energy A_H

$$A_{\text{pro}} \equiv \sqrt{adcA' \times adcB'} = A_H \sqrt{G} e^{-\alpha L/2} \quad (4.18)$$

so that we can define the measured energy deposit of a hit by

$$\Delta E_{\text{hit}} \equiv c_A A_{\text{pro}} \quad (4.19)$$

where only the calibration factor c_A has to be determined (see below).

Attenuation

The logarithm of the quotient A_{div} of the two ADCs is proportional to the position of the hit

$$\log(A_{\text{div}}) \equiv \log\left(\frac{adcA'}{adcB'}\right) = \log G - \alpha(2y_H - L) \quad (4.20)$$

as illustrated in Figure 4.14. This dependency is used to determine the position of hits without any TDC values (signal type ‘‘A’’ in section 4.2.1):

$$y_{\text{hit}} \equiv \log(A_{\text{div}}) \times y_{C_A} + y_{0_A} \quad (4.21)$$

The calibration parameters y_{C_A} and y_{0_A} are determined using events *with* TDC values and therefore a known position.

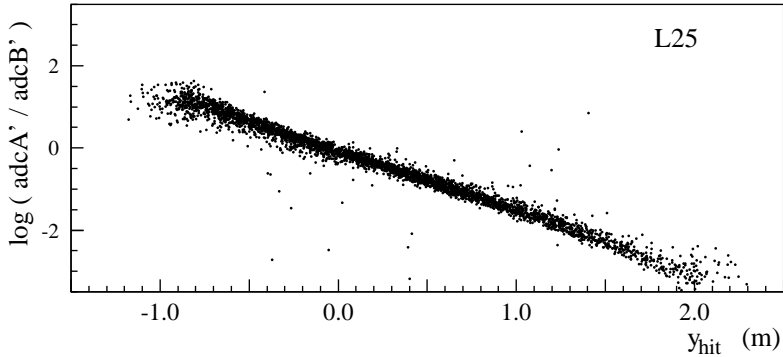


Figure 4.14: Ratio of the ADC values along a TOF-wall bar. The slope reflects the light attenuation factor α , the offset is related to the gain ratio G of the two photomultipliers.

Energy deposit calibration

In order to determine the calibration factor c_A for the energy deposit in a bar (equation 4.19) the measured values A_{pro} are compared to values based on the Bethe-Bloch formula (given in [Leo92]). A lookup table has been created⁷ containing the proton energy deposit $\Delta E_{\text{hit}}^{(i)}$ and time-of-flight for each of the four TOF-walls and the vertex detector as a function of the proton energy T_{kin} at the reaction vertex and its angle θ_S w.r.t. the normal to the wall. It is assumed that the ${}^2\text{H}(e, e'p)n$ reaction occurs in the centre of the target and all energy losses before the proton reaches Wall 2 are taken into account. The lookup table has 69 kinetic energy bins (10 – 350 MeV) and nine angular bins (0 – 40 degrees). For a given segment the angle θ_S is defined by the geometrical centre of the square formed by the two bars involved. Starting with an energy deposit ΔE_{hit} in one of the walls any of the other tabulated quantities is found by linear interpolation in energy deposit and angle.

Note that this lookup table, which assumes the proton also loses some energy in the vertex detector, has been used for both measurements whereas actually the vertex detector was not present in part of the *jan96* measurement. However, the energy loss of a proton in this thin piece of scintillator material is so small (less than 1 MeV at the relevant proton energies) that this does not influence the results.

The ADC calibration factors c_A are determined by scaling the punch-through point⁸ in the experimental ADC spectra to the energy deposit predicted by the Bethe-Bloch tables. This is done separately for every segment – instead of once per scintillator bar – because the measured ADC values seem to vary somewhat differently than is expected on the basis of the geometry alone, see Figure 4.15. The punch-through points exhibit a minimum in the center of the bar (part (a) of

⁷Using the TENERGY program [Pap87].

⁸This is the energy deposit of a proton *just passing through* the scintillator.

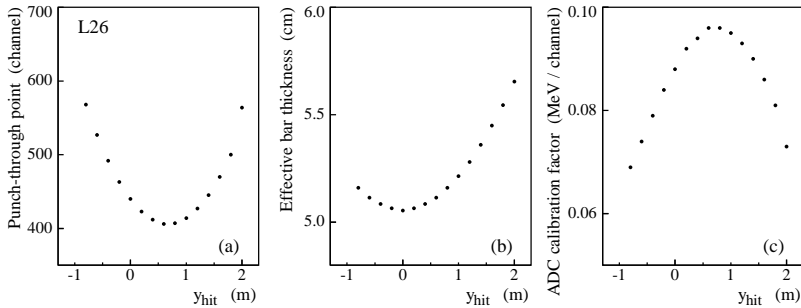


Figure 4.15: (a) Variation of the punch-through point for the fifteen segments of bar L26. (b) Effective thickness of the bar and (c) ADC calibration factor c_A for these segments.

the figure) whereas one would expect the minimum to be at the point where the protons encounter the least material, i.e. at beamheight for the vertical bars and at the intersection with the normal for the horizontal bars. This expected behaviour is illustrated in part (b) of the figure in terms of the effective thickness of the bar, i.e. the thickness of the bar times a factor reflecting the angle of the incident proton. In addition, the observed variation is much stronger than the 10% variation of this thickness. No explanation has been found, so we have used the calibration factors c_A to compensate. Part (c) of the figure gives an example of these factors.

Passing and stopping protons

The Bethe-Bloch tables are also used to relate the (calibrated) energy deposit of a proton to its kinetic energy (section 4.2.4). Unfortunately, for low proton energies this transformation is quite sensitive to details of the geometry and small variations in the proton energy deposit, especially for protons just reaching a scintillator without passing through. In order to obtain consistent results, the calibration factors for protons *stopping* in a bar need to be slightly different than for protons *passing* through. The following procedure has been applied. The missing mass M_{mis} is calculated using the energy deposit in Wall 3, the angle of the segment and the scattered electron quantities. The *stopping* calibration factors are determined by requiring M_{mis} to be at a constant value – the neutron mass m_n – for all scattered electron energies. Figure 4.16c gives an example for *stopping* protons and Figure 4.16b shows the equivalent for *passing* protons. For these plots most of the non- $^2\text{H}(e, e'p)n$ protons have been removed in order to enhance the band near $M_{\text{mis}} = m_n$. An example of the full missing mass spectrum is given in Figure 4.16a, but then using the energy deposit in Wall 2 to calculate M_{mis} .

The assignment of a proton as *passing* or *stopping* is done on the basis of its energy deposit in Wall 2: protons with an energy deposit above the value at the punch-through point are expected to stop in Wall 3. This separation is the cause of

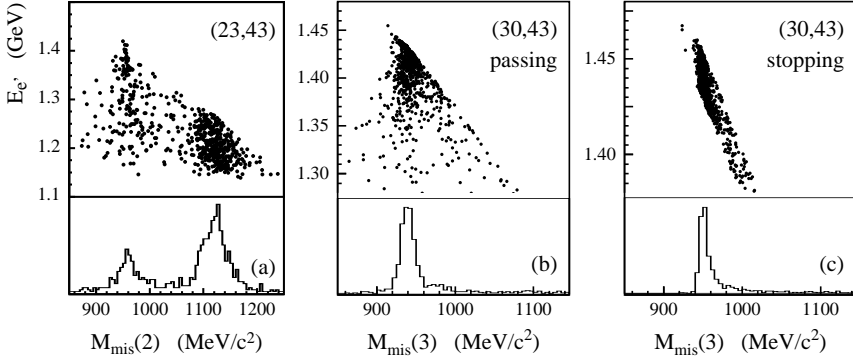


Figure 4.16: The missing mass M_{mis} calculated from the energy deposit in a TOF-wall for a range of scattered electron energies $E_{e'}$. (a) The full spectrum, using the energy deposit in Wall 2 in the calculation. (b) Analogous results, but using the energy deposit in Wall 3, for protons expected to pass through Wall 3. (c) The same, for protons expected to stop in Wall 3. The data shown are for two segments during kinematical setting J4. Note the different vertical and horizontal scales!

the sharp cutoff on the lower edge of the data in part (c) of the figure and on the upper edge in part (b).

4.2.3 Proton identification

Protons are identified by requiring a coincident hit in two TOF-walls. In our analysis, only coincidences between Wall 2 and Wall 3 are considered. The most important alternative – coincidences between Wall 2 and Wall 1 – suffers from the much higher background in Wall 1. By neglecting these alternative coincidences we fail to detect very low energy protons, which cannot reach Wall 3. However, since protons from the ${}^2\text{H}(e, e'p)n$ reaction beyond quasielastic energies have sufficient energy to reach Wall 3, this is not considered a limitation.

As each TOF-wall consists of fifteen bars, there are 225 different possible hit combinations or “segments”. The following procedure is used to determine which segments are relevant in a given event and to select the best segment candidate:

1. Candidates are identified separately for either wall, based on the information of that wall only.
2. Any candidates not found in *both* walls simultaneously are rejected, except when they belong to neighbouring segments in the two walls.
3. The best segment candidate is chosen on the basis of the signal type (as defined in section 4.2.1).

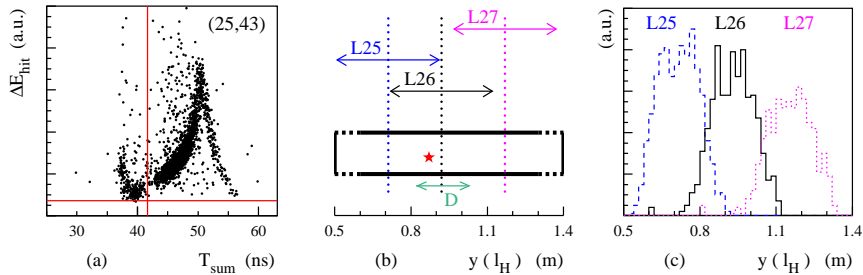


Figure 4.17: (a) Energy deposit versus time-of-flight for hits in Wall 3. The limits used to identify protons are indicated by the two lines. (b) An example of the procedure to determine the relevant bars in Wall 2 for a hit (star) in a bar (thick box) in Wall 3. The dotted lines indicate the $-$ projected $-$ centres $y_{\text{cen}}(l_V)$ of the perpendicular bars in the other wall, D is the width of a bar. The arrows give the region which is relevant for the bar mentioned above the arrow. (c) Assignment of the hits in Wall 3 to the various bars in Wall 2, based on the possibilities from part (b) and the coincident hit(s) in Wall 2.

Segment candidates in the two walls

A proton hit $H^{(p)}$ in a horizontal bar l_H in Wall 3 is defined as an energy deposit above the background level and a time-of-flight beyond the peak of minimum ionizing particles, if both are available for the bar (signal types “P”, “N” or “G”). These cuts are illustrated in Figure 4.17a. When only a type “A” signal is available for the bar the restraint on the time-of-flight is lifted.

Which bars l_V in Wall 2 are relevant for the hit in Wall 3 is determined from the position $y(l_H)$ measured in Wall 3 by requiring

$$-0.20 \text{ m} < y(l_H) - y_{\text{cen}}(l_V) < 0.20 \text{ m} \quad (4.22)$$

where $y_{\text{cen}}(l_V)$ – the projection of the centre of a bar l_V onto Wall 3 – is known from the geometry and the limits are wide enough to account for the resolution of the bars. For example, in Figure 4.17b the hit (star) in Wall 3 might be related to bars L25 or L26 in Wall 2, but not to bar L27.

A proton hit $V^{(p)}$ in a vertical bar l_V in Wall 2 is treated in a similar manner. Eventually, up to three segment candidates H are found for every Wall 3 hit and also up to three candidates V for every Wall 2 hit:

$$H_{i,j-1} \quad H_{i,j} \quad H_{i,j+1} \quad V_{k-1,l} \quad V_{k,l} \quad V_{k+1,l}$$

where i and k are in Wall 3 and j and l are in Wall 2.

Selecting the best segment candidate

The segment most probably corresponding to the actual hit is found by seeking combinations of $H^{(p)}$ and $V^{(p)}$ with the same bar numbers ($i = k$ and $j = l$).

In order to reduce the number of spurious segment candidates, only the following three signal type combinations are considered:

- “P”, “N” or “G” in Wall 3 and “P”, “N” or “G” in Wall 2
- “P”, “N” or “G” in Wall 3 and “A” in Wall 2
- “A” in Wall 3 and “P”, “N” or “G” in Wall 2

For most of the events only one segment candidate is found. For a small number of these candidates the measured energy deposit can be improved by including the energy deposit in the adjacent bar(s). This corresponds to events in which the proton lost most of its energy in one bar, but also just hit the next bar.

When more than one segment candidate is found, a further selection is needed to determine the best candidate. The following criteria are applied (in order of decreasing importance):

1. In most cases exactly *two* segment candidates are found with the same bar assignment in one Wall and adjacent bars in the other Wall. Such candidates are combined by adding the energy deposits from the two adjacent bars.
2. If the (two or more) segment candidates are not adjacent, a candidate with more “P”, “N” or “G” signals is favoured over one with “A” signals.
3. If there is still more than one candidate left, “P” signals are favoured over “N” signals and “N” over “G”.
4. If it is still impossible to select one segment candidate, the event is discarded.

For the example mentioned above, the final result of the assignment of the *segments* is illustrated in Figure 4.17c, in which the $y(l_H)$ distribution (in Wall 3) is given for *segments* involving each of the three bars in Wall 2.

Single hits

After the assignment of the segments the remaining events with only *single* hits in the two walls are considered, i.e. segment candidates for which no corresponding candidate was found in the other wall. These single hits are needed for the calculation of the proton efficiency (section 4.2.5). In our analysis we have retained *all* single hits from Wall 2 and Wall 3 for this purpose, although (in retrospect) it probably would have been advantageous to first determine the best “single candidate” – using criteria similar to those mentioned above for segment candidates – and then to use only this best candidate in the determination of the efficiency.

Bar L31 – at the far right of Wall 2 – constitutes a special case, because it is only partly in front of Wall 3. Many protons passing through this bar will miss Wall 3, so that bar L31 has relatively many single hits. Unfortunately, this means that it is not possible to determine the proton detection efficiency using the method described below. Therefore, all results for bar L31 have been discarded.

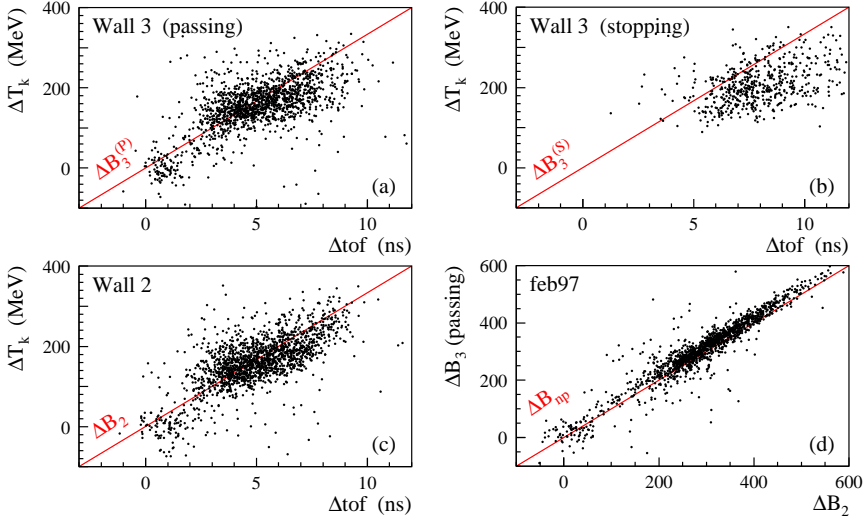


Figure 4.18: Selection of breakup protons in the higher energy transfer bins of the feb97 measurement: (a) The selection parameter ΔB_3 for protons passing through Wall 3. (b) The selection parameter ΔB_3 for protons stopping in Wall 3. (c) The selection parameter ΔB_2 for Wall 2. (d) Combination of the two selection parameters for passing protons to create the final breakup parameter B_{np} . In all four plots the relevant protons are located near (0, 0). The diagonal lines indicate the axis onto which the projection is made.

4.2.4 Protons from deuteron breakup

In order to distinguish the ${}^2\text{H}(e, e'p)n$ “breakup” protons from protons of the competing ${}^2\text{H}(e, e'p)n\pi$ reaction, the measured time-of-flight and kinetic energy are compared to the values fixed by the kinematics of the ${}^2\text{H}(e, e'p)n$ reaction. This is equivalent to selecting events with missing mass $M_{\text{mis}} = m_n$ (the neutron mass). The reason for not using the missing mass spectrum directly is that the calculation of M_{mis} involves the subtraction of two *measured* vectors, \mathbf{q} and \mathbf{p}_p , followed by yet another subtraction, $E_m^2 - p_m^2$. Therefore, the uncertainties of the measured quantities will propagate strongly in these calculations, so that the uncertainty in the resulting M_{mis} can be quite large and an accurate separation becomes difficult.

The breakup parameter

For each TOF-wall the difference Δt between the measured and calculated time-of-flight and the difference ΔT between the measured and calculated proton en-

ergy are combined in the *selection parameter* ΔB :

$$\begin{aligned}\Delta B &\equiv \frac{1}{2}(\Delta T + b \times \Delta t) \\ \Delta T &\equiv T_{\text{kin}} - T_{\text{kin}}^{(\text{np})} \\ \Delta t &\equiv t_{\text{hit}} - t^{(\text{np})}\end{aligned}\tag{4.23}$$

where $t^{(\text{np})}$ and $T_{\text{kin}}^{(\text{np})}$ are the values corresponding to ${}^2H(e, e'p)n$ kinematics and T_{kin} is calculated from the calibrated energy deposit ΔE_{hit} using the Bethe-Bloch tables described in section 4.2.2. The empirical factor b is introduced to make the scale of Δt of the same order of magnitude as that of ΔT . For Wall 2 and Wall 3 we use $b = 30$ and $b = 25$, respectively. For the “breakup” protons both Δt and ΔT should be (approximately) zero. The final selection of relevant protons is performed on the combination of the selection parameters from Wall 2 and Wall 3

$$B_{\text{np}} \equiv \frac{1}{2}(\Delta B_2 + \Delta B_3)\tag{4.24}$$

so that, again, the ${}^2H(e, e'p)n$ protons should be located near (0, 0).

The construction of the selection parameters is illustrated in Figure 4.18 for the higher energy transfer bins of the *feb97* measurement. Graphically ΔB corresponds to a projection onto the diagonal line in Figure 4.18*abc*. Note that protons *passing* through or *stopping* in Wall 3 are treated separately here, due to their slightly different calibration parameters (see section 4.2.2), but it is clear that there are no *stopping* ${}^2H(e, e'p)n$ protons anymore at these energies. That the selection parameters of Wall 2 and Wall 3 for *passing* protons agree well with each other is illustrated in Figure 4.18*d*. Again, the combined result B_{np} corresponds to the projection onto the diagonal line.

Several examples of the final *breakup parameter* B_{np} spectra are given in Figure 4.19. The spectra consist of a peak of ${}^2H(e, e'p)n$ protons near zero and the tail of the background from other reactions. As expected, the relative importance of this background increases strongly for the higher energy transfer bins (i.e. away from the quasielastic region). Also, the *stopping* protons occur mostly in energy transfer bin E2 and a little in E3.

Fit of the peak and the background

In order to determine the number of relevant protons, a Gaussian is fitted to the B_{np} peak near zero. Ideally, the width of this peak represents only the resolution of the detector, but in practice the peak is somewhat wider in the higher energy transfer bins. The position of the B_{np} peak also changes slightly from segment to segment, possibly due to small variations in the calibration enhanced by the non-linear transformation from energy deposit ΔE_{hit} to proton kinetic energy T_{kin} .

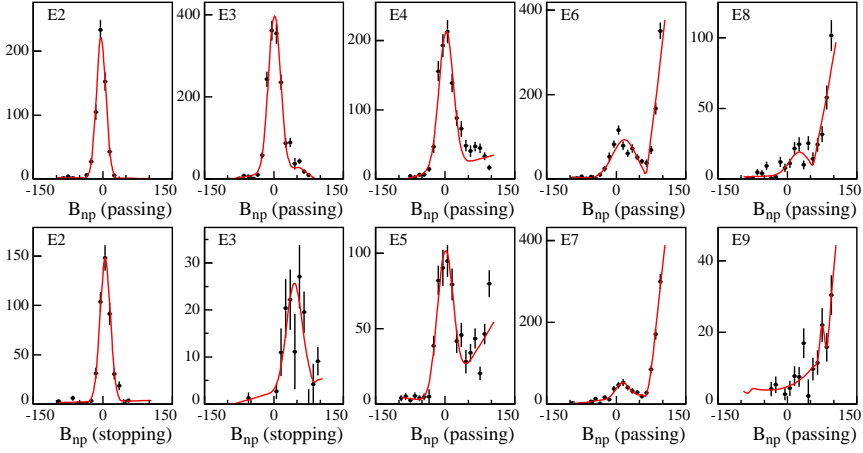


Figure 4.19: Spectra of the final TOF-wall breakup parameter B_{np} for segment (L26,L43) in the jan96 measurement. For energy transfer bins E2 and E3 two spectra are shown, one for protons passing through Wall 3, the other for protons stopping in Wall 3. The diagonal line indicates the result of the fit described in the text. Note the different vertical scales.

In most cases the tail of a Gaussian is used to describe the background, but when such a fit is too difficult, the background close to the ${}^2H(e, e'p)n$ peak is approximated by a simple straight line. Such cases occur mostly in the higher energy transfer bins, where the ${}^2H(e, e'p)n$ peak is very small and any slight irregularity on the tail tends to draw the – automatic – fit away from the actual ${}^2H(e, e'p)n$ peak. A more refined shape of the background is not necessary, because only the outermost part of the tail is needed and most tails are similar there. In addition, the influence of the tail is small in many cases, so that the even smaller effect of different shapes can be neglected w.r.t. the expected uncertainty of the result.

The final number of detected protons N_{wall} is found by integrating the Gaussian describing the B_{np} peak:

$$N_{wall} = 2\pi h\sigma/b \quad (4.25)$$

where h and σ are the (fitted) height and width of the peak, and b is the bin size of the histogram on which the fit is performed. Since a simultaneous fit of the peak and the background is performed, the errors obtained for the fit parameters for the peak also reflect the influence of the tail.

In cases where no (reliable) fit is possible, the number of events near zero is simply counted. This number serves as an upper limit for the actual countrate.

Since the strength of the B_{np} peak varies strongly with energy transfer and proton angle, a separate fit is performed for every segment in each energy transfer bin. Also, the B_{np} spectra for *passing* protons are *not* combined with the spectra for *stopping* protons. To minimize the statistical error, all data files from all con-

tributing kinematical settings of the spectrometer are combined in the spectrum to be fitted, but separately for the two measurements, *jan96* and *feb97* (see section 4.4.1 for details). Before the fits are performed, the “empty target” contribution (section 4.4.2) is subtracted and the spectra are corrected for the spectrometer efficiency η_e and dead time η_{live} (section 4.1.3). Note that for the calculation of the final countrates we have chosen to use only segments with “P”, “N” or “G” signals in both TOF-walls.

4.2.5 Proton detection efficiency

The proton detection efficiency η_p is needed to correct for any ${}^2\text{H}(e, e'p)n$ protons not included in the final number of detected protons N_{wall} . Note that it must not only correct for protons rejected by the electronics, but also for proton losses due to the calibration, the segment selection, the proton identification and the final selection of “breakup” protons.

Since we did not perform an independent efficiency measurement, the correction has been determined using the experimental data set itself. The method described below uses clearly identified proton hits in one wall to determine the efficiency of the other wall and vice versa. This is feasible as long as one can assume that the efficiencies of the two TOF-walls involved are independent, but it cannot account for proton signals lost simultaneously in *both* walls (e.g. due to a relatively high threshold in both bars). Fortunately, this problematic situation occurs for only six segments in some of the energy transfer bins up to bin E6. These specific cases have been excluded from the results.

The (in)efficiency is sensitive to the proton energy, since high energy protons with small energy deposits more often fail to reach the discriminator threshold than low energy protons. Therefore, only protons of approximately the energies relevant for the ${}^2\text{H}(e, e'p)n$ reaction are used in the determination of the efficiency. Obviously, this reduces the statistical accuracy of the calculation, especially in the higher energy transfer bins, where protons with the “wrong” energy dominate.

Method

The efficiency for a given segment in TOF-wall x is calculated using clearly identified protons in the other wall y . It is defined as

$$\eta_x \equiv \frac{N_{\text{OK}(y)}^{\text{ID}(x)}}{N_{\text{OK}(y)}} \quad (4.26)$$

where the label $\text{OK}(y)$ indicates that in wall y the event must satisfy more stringent criteria than those used for protons in the actual analysis (see below) and the label $\text{ID}(x)$ indicates that in wall x the same criteria as in the actual analysis are applied in deciding that a hit represents a ${}^2\text{H}(e, e'p)n$ proton.

The enumerator is easily determined by selecting all segment events which satisfy the more stringent criteria in wall y and the usual criteria in wall x . The denominator consists of the same events and in addition any events satisfying the criteria for wall y but not those for wall x . Since only events with “ P ”, “ N ” or “ G ” signals have been used to determine the final countrates (see section 4.2.4), the denominator must also contain any events without TDC values in wall x . Thus we have:

$$N_{\text{OK}(y)} = N_{\text{OK}(y)}^{\text{ID}(x)} + N_{\text{OK}(y)}^{\overline{\text{ID}}(x)} + N_{\text{OK}(y)}^{\overline{\text{TDC}}(x)} \quad (4.27)$$

where the label $\overline{\text{ID}}(x)$ indicates events rejected by the proton identification and/or “breakup” selection in wall x , and the label $\overline{\text{TDC}}(x)$ indicates events without TDC values in wall x . Finally, in order to obtain *all* events satisfying (only) the criteria in wall y , the number $N_{\text{OK}(y)}^{\overline{\text{TDC}}(x)}$ must also include any *single* hits satisfying the more stringent criteria for wall y .

The constraint for the identification of ${}^2\text{H}(e, e'p)n$ protons in wall x is applied only to the selection parameter of that wall:

$$|\Delta B(x)| < \Delta B_{\text{max}}(x) \quad (4.28)$$

where the limit ΔB_{max} is based on the width of the ΔB peaks. This constraint is slightly more lenient than the constraint in the actual analysis, which is applied to the combined *breakup parameter* B_{np} , but it is clear from Figure 4.18d that this is not a major difference. However, it must be noted that any background events below the ΔB peak are counted as correct hits by this simple constraint, in contrast to the fit in the analysis. The constraints for clearly identified protons in wall y are:

$$\begin{aligned} |\Delta E_{\text{hit}}(y) - \Delta E^{(\text{np})}| &< 8 \text{ MeV} \\ |t_{\text{hit}}(y) - t^{(\text{np})}| &< 2 \text{ ns} \end{aligned}$$

where $\Delta E^{(\text{np})}$ and $t^{(\text{np})}$ are the values for the energy deposit and time-of-flight in ${}^2\text{H}(e, e'p)n$ kinematics.

The distinction made in the analysis between protons *passing* through or *stopping* in Wall 3 is reflected in the calculation of the efficiency η_3 of that TOF-wall by splitting the number of events $N_{\text{OK}(2)}^{\text{ID}(3)}$ into two parts, $N^{\text{P}(3)}$ and $N^{\text{S}(3)}$. The assignment of an event to either of these two groups is based on the energy deposit in the other wall (Wall 2):

$$\Delta E_{\text{hit}}^{(2)} < \Delta E_{\text{ptp}}^{(2)} \text{ for } N^{\text{P}(3)} \quad \Delta E_{\text{hit}}^{(2)} > \Delta E_{\text{ptp}}^{(2)} \text{ for } N^{\text{S}(3)} \quad (4.29)$$

i.e. below or above the energy deposit ΔE_{ptp} at the punch-through point.

The complete proton efficiency for a given segment is found by multiplying the two efficiencies of the individual walls for that segment:

$$\eta_p(x, y) \equiv \eta_2(x, y) \times \eta_3(x, y) . \quad (4.30)$$

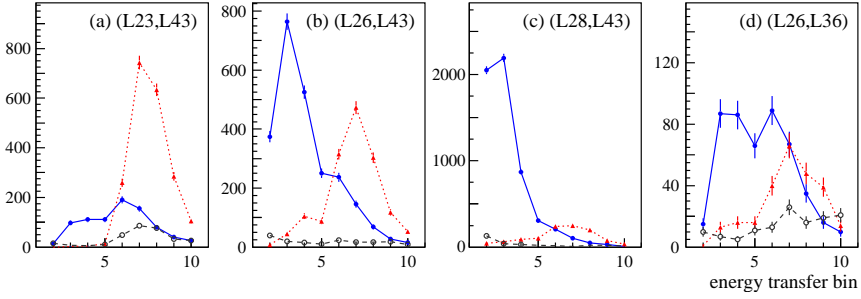


Figure 4.20: The main contributions to the TOF-wall efficiency η_{B} per energy transfer bin for some typical segments. Three in-plane segments and one out-of-plane segment are shown, identified by the two bars involved. Note the different vertical scales. The solid, dotted and dashed lines represent the major contributions: $N_{\text{OK}(2)}^{\text{ID}(3),\text{P}(3)}$, $N_{\text{OK}(2)}^{\overline{\text{ID}(3)}}$ and $N_{\text{OK}(2)}^{\overline{\text{TDC}(3)}}$.

Results

Using the method described above, the proton efficiency is calculated for every segment in each energy transfer bin. The resulting values are included in the Appendix, some typical examples are shown in Figures 4.20 and 4.21.

The different types of lines in the first figure (showing the countrates per energy transfer bin) correspond to the three major contributions:

- the solid line represents protons *passing* through Wall 3 which are correctly identified as ${}^2\text{H}(e, e'p)n$ protons,
- the dotted line represents protons rejected in one of the analysis steps,
- the dashed line represents protons without a TDC value in Wall 3.

The *stopping* protons not rejected in the analysis are not shown because they only contribute in energy transfer bins E2 and E3.

In the lower energy transfer bins the number of correctly identified “breakup” protons is highest near the direction of the momentum transfer, i.e. in the neighbourhood of segment (L30,L43). In the higher energy transfer bins the dominating contribution comes from protons rejected in the analysis, in most cases by the “breakup” selection, because here other reactions such as ${}^2\text{H}(e, e'p)n\pi$ are more important. Also the number of protons with no TDC value in Wall 3 increases in the higher energy transfer bins, since the proton energy is higher and therefore the energy deposit is lower.

In Figure 4.21 (showing the efficiency per Wall 3 bar) it is clear that the efficiency drops sharply in the energy transfer bins beyond E5. This is true for nearly all segments. The loss of efficiency usually starts at both ends of a bar: as the energy deposit becomes small, the light from one end of the bar is attenuated so

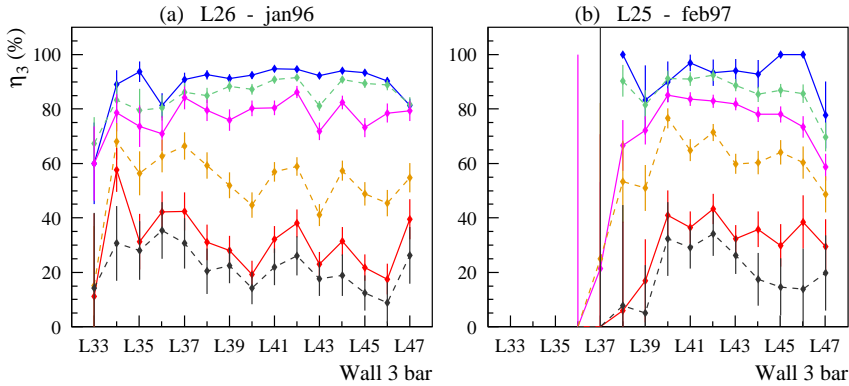


Figure 4.21: The efficiencies η_B (in percent) for the 15 segments (a) in a typical Wall 3 bar and (b) in a bar with an efficiency problem. The lines – from top to bottom – represent energy transfer bins E3 through E8.

much while travelling along the bar that on arrival at the far end it has fallen below the discriminator threshold. The second part of the figure illustrates this in an extreme manner: L25 is one of the bars for which the threshold was clearly too high during the *feb97* measurement, so that for several segments on one side of the bar the efficiency is practically zero.

In the highest energy transfer bins the efficiency still drops, while the energy deposit does not change much since it is already close to the minimum. Therefore this decrease of the efficiency cannot be attributed to discriminator threshold effects, but is probably explained by the following. The transformation of the energy deposit into the corresponding proton energy is quite non-linear, so that especially for low energy deposits a small error in the deposit corresponds to a large change in the calculated proton energy. Since the proton energy is an important part of the selection parameter ΔB , more protons will be rejected by the “breakup” selection in the higher energy transfer bins. In retrospect, it would have been profitable to use the energy deposit in the definition of the selection parameter ΔB instead of the kinetic energy. The transformation from the expected ${}^2H(e, e'p)n$ proton energy to an expected energy deposit – just as non-linear – would have led to much smaller deviations in ΔB for high energy protons with small energy deposits.

The large uncertainties in the higher energy transfer bins are of course related to the decreasing statistics in these bins. Remember that only protons with approximately the correct energy for the ${}^2H(e, e'p)n$ reaction are used to determine the efficiency and not the abundant protons from the ${}^2H(e, e'p)n\pi$ reaction. In practice, the conclusion must be that all efficiencies in energy transfer bins E7 and higher are too small or too uncertain to be used. Unfortunately, this means that a lot of data points have to be discarded.

4.3 Telescopes

The analysis of the telescope data also consists of several calibrations (position, time-of-flight, energy deposit), a few corrections (time walk, geometry, proton detection efficiency) and the identification of the relevant ${}^2\text{H}(e, e'p)n$ protons. All these steps are described in this section. Since the only reliable telescope results are from the *feb97* measurement, all data presented in this section are from that measurement. See Figure 4.9 for the definitions related to the calibration of a scintillator bar. For the telescopes the lower edge (labeled “d” for *down*) is side A and the upper edge (labeled “u” for *up*) is side B.

4.3.1 TDC values

Just as for the TOF-walls (section 4.2.1) the time-of-flight of a hit is obtained from the average of the TDC values from the two ends of the bar:

$$\begin{aligned} T_{\text{sum}} &\equiv (tdcA + tdcB)/2 \\ t_{\text{hit}} &\equiv T_{\text{sum}} - t_0 \end{aligned} \quad (4.31)$$

and the position of the hit along a telescope bar is given by the difference:

$$\begin{aligned} T_{\text{dif}} &\equiv tdcA - tdcB \\ y_{\text{hit}} &\equiv (T_{\text{dif}} - y_0) \times y_C . \end{aligned} \quad (4.32)$$

All TDC channels have been calibrated separately before the experiment, so that only the three factors y_C , y_0 and t_0 have to be determined.

Calibrations

The time-of-flight offset t_0 is found by comparing the measured spectra to the results of the GEANT simulations discussed in section 4.3.4. The position calibration factor y_C is found by fitting the T_{dif} spectrum (see Figure 4.22) with a block function and relating the FWHM to the length of the bar. The offset y_0 follows from the known vertical position of the bar given in section 3.2.4.

Geometry

Due to the length of the telescopes, there is a significant variation in the distance travelled by protons from the target to the detector:

$$d_{\text{hit}} = d_x \times \sqrt{1 + (y_{\text{hit}}/d_x)^2} \quad (4.33)$$

and a corresponding variation in the time-of-flight:

$$t_{\text{hit}} \approx t_x \times \sqrt{1 + (y_{\text{hit}}/d_x)^2} . \quad (4.34)$$

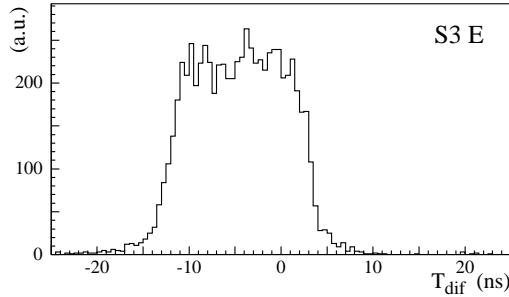


Figure 4.22: A typical position spectrum (T_{dif}) for a telescope.

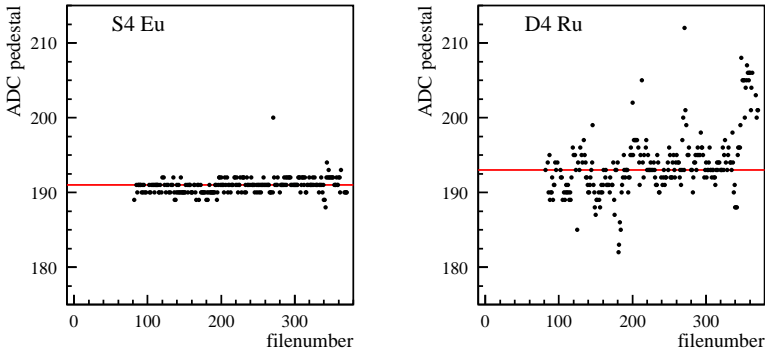


Figure 4.23: Typical variation of the pedestals during the feb97 measurement, for an E -bar and a ΔE -bar, respectively. The higher pedestals starting at file 347 correspond to the “empty target” situation. The lines have been added to guide the eye.

Here d_x is the horizontal distance of the telescope from the target, y_{hit} is the vertical position of the hit above or below the target plane, and t_x is the time-of-flight of a proton over the distance d_x .

Since in our final results we will combine all events from a telescope disregarding any effects along the length of the telescope bar, this variation in the proton time-of-flight is eliminated by dividing the measured (calibrated) t_{hit} by the geometrical factor $\sqrt{1 + (y_{\text{hit}}/d_x)^2}$.

4.3.2 ADC values

In contrast to the TOF-wall case, both integration ranges of the ADC modules (see section 4.2.2) were used for the ADC signals of the telescope photomultipliers. Therefore, two offsets have to be determined, one for each range. The offset or “pedestal” for the low range is found by requiring a timeout in the corresponding

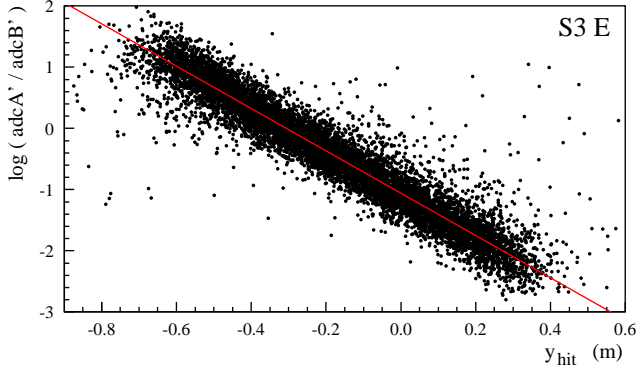


Figure 4.24: A typical $\log(\text{adcA}'/\text{adcB}')$ versus position spectrum for a telescope. The slope corresponds to the attenuation α , the offset is related to the gain ratio G .

TDC. The offset for the high range follows directly from the ADC spectra as there is a clearly visible gap between the two ranges. By moving the beginpoint of the high range to the endpoint of the low range (after correcting both for the pedestals), we can treat the results as one undivided range of ADC values, because according to previous tests [Got95] the gains of the two ranges are equal.

Again, the pedestals have been determined separately for every data file. A typical example is shown in Figure 4.23, both for a thick E-bar and a thinner Δ E-bar. The only significant change occurs for the “empty target” measurement (file 348 and onwards), probably due to the much lower instantaneous (background) rates in that situation [Leo92]. The shift of about 15 channels is negligible compared to the typical proton signals of 1000 – 6000 channels, so that no file-dependent correction of the pedestal is necessary.

Attenuation

Just as in the TOF-wall case, the logarithm of the ratio A_{div} of the two ADCs should be proportional to the position in the bar:

$$\log(A_{\text{div}}) \equiv \log\left(\frac{\text{adcA}'}{\text{adcB}'}\right) = \log G - \alpha(2y_H - L) \quad (4.35)$$

where the accents indicate that the pedestals have already been subtracted. In the *jan96* measurement equation 4.35 was not fulfilled, which led to the discovery that the telescope ADC gate was not correct in that measurement. In the *feb97* measurement the problem was solved, as illustrated in Figure 4.24 for a typical telescope. There is a clear linear correlation between the ratio and the position, so that the attenuation α and the gain ratio G can be determined from the slope and

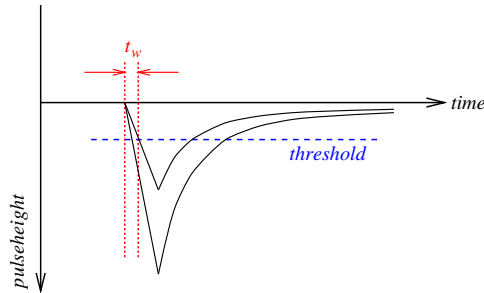


Figure 4.25: Walk effects in a photomultiplier: a large pulse triggers earlier than a small pulse of the same shape.

offset, respectively. These values are needed for the walk corrections described below and the GEANT simulations.

Energy deposit calibration

A position-independent value for the energy deposit in a bar, ΔE_{hit} , is again obtained by taking the product of the ADCs of the two sides of the telescope:

$$\Delta E_{\text{hit}} \equiv c_A A_{\text{pro}} \equiv c_A \sqrt{\text{adc}A' \times \text{adc}B'} . \quad (4.36)$$

The calibration factor c_A can be found by comparing the A_{pro} data to the results of the GEANT simulations (see section 4.3.4). This is not necessary, however, because in the particle identification procedure described below, a parametrization of the energy deposit is used for which the uncalibrated A_{pro} is just as useful.

4.3.3 Walk effects

The “leading edge” discriminators used for the experiment fire at the moment the incoming pulse exceeds a certain threshold. This leads to so-called “walk effects”: a large pulse crosses this threshold sooner than a small pulse and thus gives an earlier trigger (see Figure 4.25). The time difference t_w can be described by

$$t_w = \frac{w}{\sqrt{\text{adc}'}} \quad (4.37)$$

where adc' is the ADC value after subtracting the pedestal, i.e. the total charge deposited, equivalent to the area of the pulse in the figure; w is a scaling parameter. This relationship indicates that the measured TDC values can be further improved by correcting for the walk. We follow the procedure described in e.g. [Ham89].

Under the assumption that the corrections are smaller for a ΔE -bar than for an E-bar, since the variation in pulse heights is much less for the thin scintillator, the

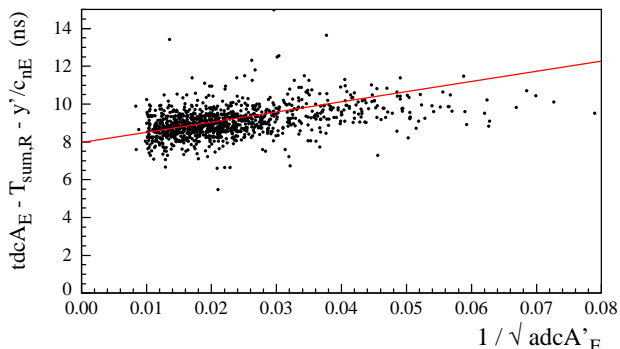


Figure 4.26: A typical walk correction for a telescope E-bar. The line represents the relationship in equation 4.39.

E-bar TDC values are corrected first. Including walk effects, the equations for the TDC values at the two ends of an E-bar are:

$$\begin{aligned} tdcA &= T_H + \frac{y_H}{c_n} + \frac{w_A}{\sqrt{adcA'}} \\ tdcB &= T_H + \frac{L - y_H}{c_n} + \frac{w_B}{\sqrt{adcB'}} \end{aligned} \quad (4.38)$$

where w_A and w_B are the walk parameters. To determine, for example, the walk in $tdcA$ of the E-bar, all other sources of variations in $tdcA_E$ are eliminated using the time and position information from the ΔR -bar and the remaining variation is fitted to equation 4.37:

$$tdcA_E - T_{\text{sum,R}} - \frac{y'_R}{c_{nE}} \propto \frac{w_{AE}}{\sqrt{adcA'_E}} \quad (4.39)$$

where $y'_R \equiv y_R \times (d_E/d_{\Delta R})$ is the position in the ΔR -bar projected onto the E-bar adjusting for the horizontal distances of the two bars from the target, d_E and $d_{\Delta R}$. A typical example is shown in Figure 4.26.

After determining the walk parameters w_{AE} and w_{BE} , the position and time-of-flight calibration (section 4.3.1) is repeated for the walk-corrected TDC values:

$$\begin{aligned} tdcA'_E &= tdcA_E - \frac{w_{AE}}{\sqrt{adcA'_E}} \\ tdcB'_E &= tdcB_E - \frac{w_{BE}}{\sqrt{adcB'_E}} \end{aligned} \quad (4.40)$$

Next, the walk correction procedure is applied to the ΔR -bars, using the *new* time and position in the E-bar to eliminate the non-walk related effects:

$$tdcA_R - T'_{\text{sum,E}} - \frac{y'_E}{c_{nR}} \propto \frac{w_{AR}}{\sqrt{adcA'_R}} \quad (4.41)$$

and a similar relationship for $tdcB_R$. Finally the time-of-flight and position calibration is repeated for the ΔR -bar as well using the walk-corrected values. In practice, no walk correction has been necessary for most ΔR -bars.

4.3.4 Simulations

The simulations mentioned throughout this section are performed with the GEANT package [GEA93]. The relevant parts of the experimental setup are defined in the program, including the target foils and the shielding of the various detectors. The GEANT package takes into account the interaction of the protons with the “dead” or “active” material encountered and thus generates energy deposit and time-of-flight information for every detector element. Realistic ADC and TDC values are approximated for all photomultipliers using the values for the attenuation found in section 4.3.2 and the various calibration factors. The ENIGMA event generator [Vis94] is used to obtain a reasonably realistic distribution of proton energies and angles for the ${}^2\text{H}(e, e'p)n$ reaction in the deuterium target. The events generated by ENIGMA serve as input for the GEANT simulations.

4.3.5 Proton identification

In order to separate protons from other particles, we first consider the E-bar, in which both charged and neutral particles can cause a hit. Figure 4.27 shows the uncalibrated energy deposit A_{pro} versus the time-of-flight T'_{sum} (corrected for walk effects and geometry) for the five telescopes on the right side of the beam, i.e. opposite the electron spectrometer. The last part of the figure schematically indicates the regions of interest in these plots.

The clear curving band of hits (region A) represents protons stopping in the E-bar. This region is described by the Bethe-Bloch formula (given in [Leo92]) for protons. For telescope $D4$ the highest energy protons are not stopped, so that the proton band curves back down below the punch-through point (region B). Also, some of the protons do not deposit all their energy in the scintillator as they scatter off other particles of the scintillator material. Such events will populate the area *below* region A. It may be necessary to correct for this effect (see section 4.3.7). Neutrons populate this same region, since they have approximately the same mass as protons and also lose only part of their energy by scattering off another particle in the scintillator.

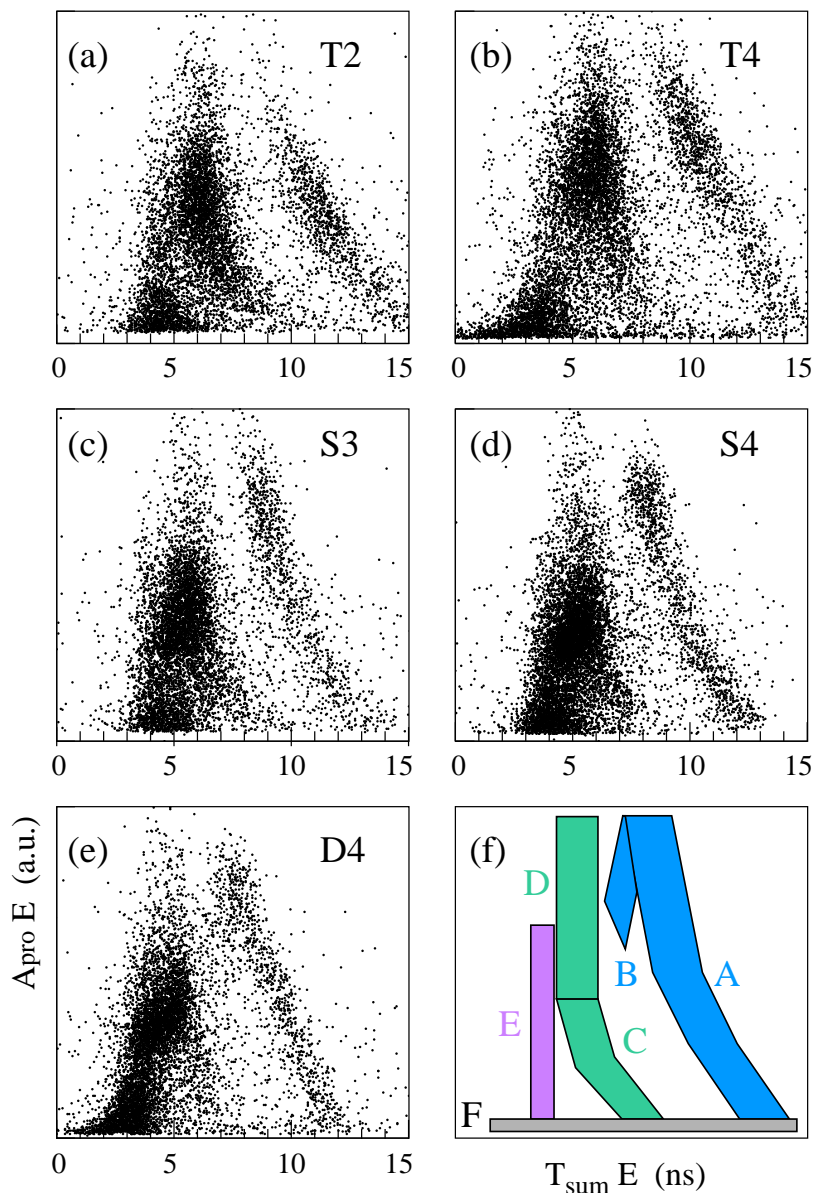


Figure 4.27: Plots of the uncalibrated energy deposit A_{pro} versus the time-of-flight T'_{sum} for the E-bar of the five telescopes on the right side of the beam. See the main text for an explanation of the areas indicated (f).

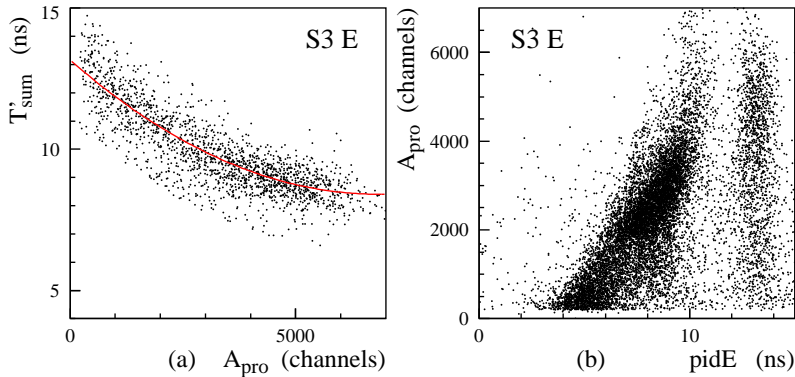


Figure 4.28: (a) Second order polynomial parametrization of the (projected) time-of-flight T'_{sum} as a function of the energy deposit A_{pro} for the E-bar of telescope S3. (b) The energy deposit A_{pro} versus the PID-parameter for the same bar.

Charged pions, which have a smaller mass, arrive earlier in the telescope and interact in various ways with the scintillator. If only energy loss through ionization is taken into account, the pions would populate a band (region C) similar to the proton band, or possibly end up below this band. However, the pion also has a reasonable chance to be absorbed in the scintillator. In such cases even more energy is deposited, so that these events populate the area *above* the pion band (region D).

Photons are the first particles to arrive, without much variation in their time-of-flight, and are therefore found in region E, while the low-energy electromagnetic background populates region F.

The PID-parameter

A “particle identification parameter”, or PID-parameter, is defined in such a way that the curved proton band (region A) in Figure 4.27 becomes a vertical band, thus enabling a simple separation of protons and (mostly) pions. In order to accomplish this the proton band is parametrized by a second order polynomial:

$$T'_{\text{sum,E}} = P_0 + P_1 \left(\frac{A_{\text{pro,E}}}{1000} \right) + P_2 \left(\frac{A_{\text{pro,E}}}{1000} \right)^2 \quad (4.42)$$

where $T'_{\text{sum}} = T_{\text{sum}} / \sqrt{1 + (y_{\text{hit}}/d_x)^2}$ is the projection of the time-of-flight onto the horizontal plane. The factors 1000 are inserted to keep the parameters P_1 and P_2 within a reasonable range. The PID-parameter $pidE$ is defined as

$$pidE \equiv T'_{\text{sum,E}} - P_1 \left(\frac{A_{\text{pro,E}}}{1000} \right) - P_2 \left(\frac{A_{\text{pro,E}}}{1000} \right)^2 \quad (4.43)$$

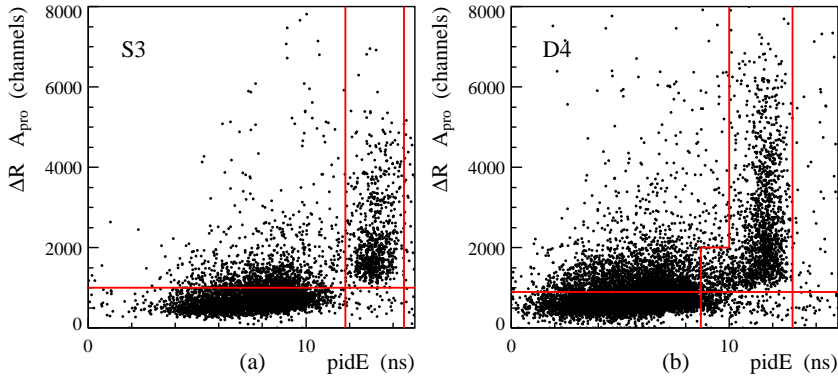


Figure 4.29: The proton definition used for the five telescopes on the right side of the beam: (a) telescope S3 as a typical example of the general case, (b) telescope D4.

where P_1 and P_2 are taken from the parametrization. Figure 4.28 shows the parametrization and the resulting PID-parameter for telescope S3 – compare this to the original in Figure 4.27c.

Identifying protons

The (rear) ΔE -bar is used to distinguish between charged and neutral particles. A *proton* is defined as a hit with the correct PID-parameter $pidE$ and an energy deposit $A_{pro,R}$ in the ΔE -bar above a certain minimum. In all cases except telescope D4 a clear separation between protons and other particles is achieved, as illustrated in Figure 4.29a.

For telescope D4 some protons are not stopped in the scintillator. These punch-through protons are *not* described by the parametrization, so that the calculated parametrization is too small. Therefore, the proton definition is extended for this telescope, as indicated in Figure 4.29b.

The random background in these plots is quite small, so that – in view of the expected accuracy of the final telescope results – no correction is applied.

4.3.6 Protons from deuteron breakup

For protons originating from the ${}^2H(e, e'p)n$ reaction (“breakup” protons) the kinematics are overdetermined, so that knowing the four-momentum transfer q_μ and the angle of the proton is sufficient to calculate the proton energy (see equation 2.11). For this purpose the proton angle Θ_{pq} can be calculated for a given hit using the measured vertical position of the hit together with the known horizontal position of the telescope.

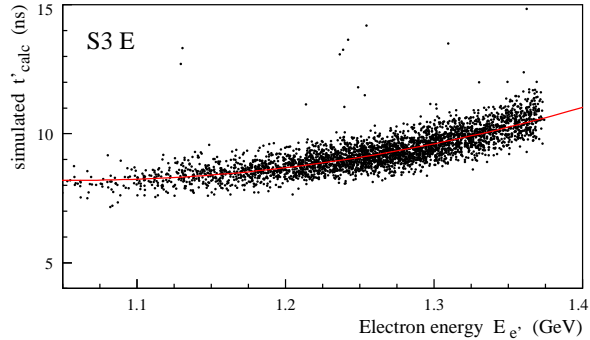


Figure 4.30: Simulations of the proton time-of-flight t'_{calc} as a function of the scattered electron energy $E_{e'}$ and the second order polynomial function used to describe the relationship. The results are for the E-bar of telescope S3.

In practice, it is more convenient to compare time signals. Therefore the time-of-flight⁹ $t'_{\text{calc},E}$ corresponding to these proton energies is determined from the simulations (section 4.3.4) and the resulting distribution is approximated by a second order polynomial in the scattered electron energy $E_{e'}$:

$$t'_{\text{calc},E} = p_0 + p_1 E_{e'} + p_2 E_{e'}^2. \quad (4.44)$$

An example is given in Figure 4.30.

To distinguish between “breakup” protons and protons from other reactions the measured time-of-flight $T'_{\text{sum},E}$ is compared to this $t'_{\text{calc},E}$ in the *breakup parameter*

$$B_{\text{np}} \equiv T'_{\text{sum},E} - t'_{\text{calc},E}. \quad (4.45)$$

In order to keep the statistical error small, especially in the lowest and highest energy transfer bins, the events from the complete telescope are combined, and thus any dependence on out-of-plane variables is lost. Figure 4.31 shows the resulting *breakup parameter* B_{np} for one telescope. The peak around zero – clearly visible in energy transfer bins E5 through E8 – corresponds to the ${}^2\text{H}(e, e'p)n$ protons; to the right one sees the tail of background protons which dominates in bins E9 and E10. The low statistics in bins E2 through E4 are due to the short period of time reserved for those energies in the *feb97* measurement.

Just as in the case of the TOF-walls, a simultaneous fit of the peak and the tail is performed in each energy transfer bin (see section 4.2.4), but here only a simple linear background is assumed, since the spectra do not show enough of the tail to allow a more complicated shape.

⁹The accent again indicates that $t_{\text{calc},E}$ has been divided by the geometrical factor $\sqrt{1 + (y_{\text{hit}}/d_x)^2}$.

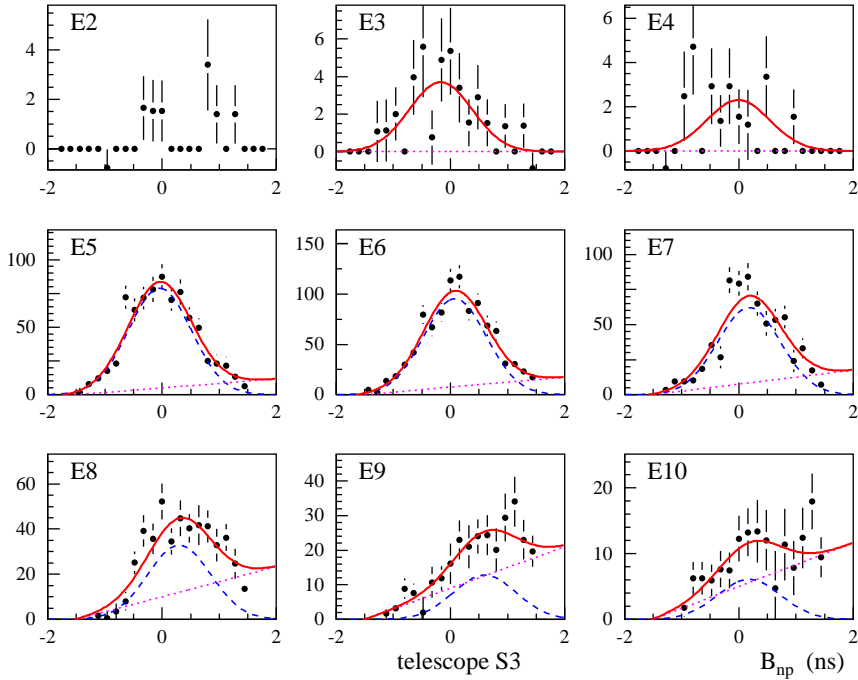


Figure 4.31: The breakup parameter B_{np} for telescope S3 in nine energy transfer bins. The simultaneous fit of the ‘breakup’ peak around zero and the background tail is indicated by the solid line; the two contributions are indicated by the dashed and dotted lines.

The final ‘number of detected protons’ N_{tele} is found – for each energy transfer bin – by integrating over the Gaussian peak:

$$N_{tele} = 2\pi h\sigma/b \quad (4.46)$$

where h is the fitted peak height, σ is the width and b is the histogram bin size.

4.3.7 Proton detection efficiency

The proton detection efficiency η_p must correct for any ${}^2H(e, e'p)n$ protons not included in the final number N_{tele} as they either failed to cross the discriminator threshold or were rejected in one of the analysis steps described above. Originally, we expected to determine this efficiency by detecting neutrons in the TOF-walls and checking for the corresponding proton in the telescopes. Unfortunately, this turned out to be not feasible, and therefore the efficiency has been estimated.

In a previous experiment [Bru95a] with the same telescopes and comparable

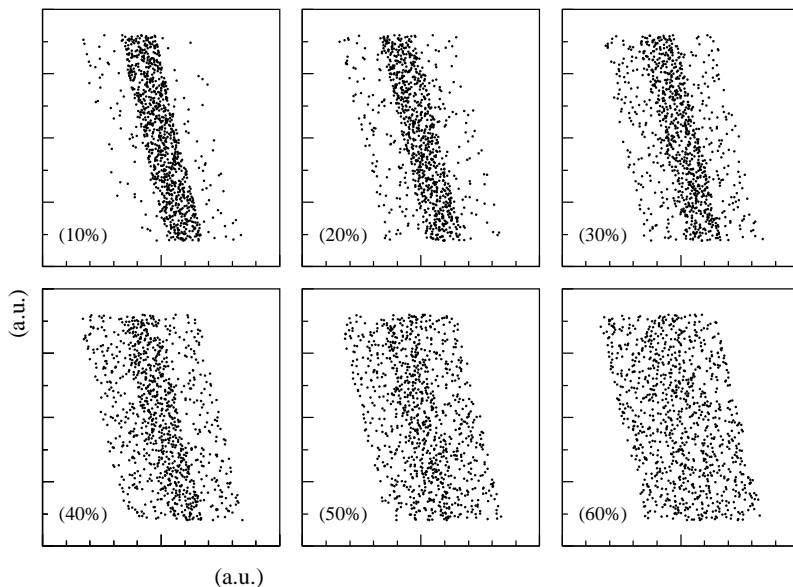


Figure 4.32: The effect of the proton detection efficiency on a two-dimensional spectrum like Figure 4.29. The percentage indicates the fraction of the events outside the band of correctly identified events.

discriminator modules the proton losses were found to be a few percent, which we take as an upper limit for the contribution of the electronics to the inefficiency.

An event representing a “breakup” proton is also lost when it does not have the expected time-of-flight, i.e. it disappears from the peak of ${}^2\text{H}(e, e'p)n$ protons in Figure 4.31. Since there are no events on the left side of the peak in all energy transfer bins and only very few on the side of the tail in the lower bins, we can assume that this contribution to the inefficiency is small, at most a few percent.

In the proton identification, losing a proton event means not finding it within the limits shown in Figure 4.29 or, equivalently, not in the proton band in Figure 4.27. Assuming that the removal of protons from this band is a continuous effect and that most of these events will not be far off the expected values, the amount of random hits in the area (closely) around the band is an indication of the amount of unidentified protons. This is of course an upper limit, since there may also be true random events in this area. In order to get some feeling for this process, it has been simulated using a simple model. A varying percentage of the events is removed from such a band and randomly placed in the surrounding area, which is (arbitrarily) taken to be about twice as large, see Figure 4.32. Comparing these results with the experimental values in Figures 4.27 and 4.29, the upper limit for proton losses is estimated to be $30 \pm 10\%$.

Adding up all contributions, the proton detection efficiency for the telescopes is estimated to be $80 \pm 20\%$, where we have taken slightly lower values for the actual proton losses than the upper limits mentioned above and we have increased the uncertainty to reflect that this is a crude estimate.

Specifically for telescope *D4* there is the additional problem, that some of the punch-through protons might not be included in the proton definition. From Figure 4.29*b* this effect is estimated to be less than 10%, and this upper limit is included in the proton detection efficiency and its error for this telescope. Note that the wider proton identification limits for telescope *D4* also allow some events *not* representing a proton to be incorrectly identified as protons. However, such events end up in the tail of background events in the B_{np} spectrum and are therefore still eliminated from the number of “breakup” protons by the fitting procedure.

4.4 Other corrections

The cross section is related to the electron-proton coincidence countrate by

$$\frac{d^5\sigma}{dE_e d\Omega_e d\Omega_{pn}^{CM}} \equiv \frac{N_{ep}}{N_{beam} N_{targ} \mathcal{V}_{CM}} \quad (4.47)$$

where

N_{ep} is the actual number of ${}^2H(e, e' p)n$ events,

$N_{beam} = \frac{Q_{tot}}{e}$ is the number of incident electrons, determined from the total accumulated charge Q_{tot} ,

$N_{targ} = \frac{\rho \ell N_A}{A}$ is the number of target nuclei, defined by the target thickness $\rho \ell$ in g/cm^2 and its atomic mass A , and

\mathcal{V}_{CM} is the detection volume for the ${}^2H(e, e' p)n$ reaction in the center-of-momentum system.

The actual number of ${}^2H(e, e' p)n$ events is defined by

$$N_{ep} = \frac{N_{meas}}{\eta_e \eta_p \eta_{live} \eta_{RAD}} \quad (4.48)$$

where

N_{meas} is the measured number of “breakup” events,

η_e and η_p are the electron and proton detection efficiencies,

η_{live} is the correction for the live time of the data acquisition system, and

η_{RAD} is the correction for radiative effects.

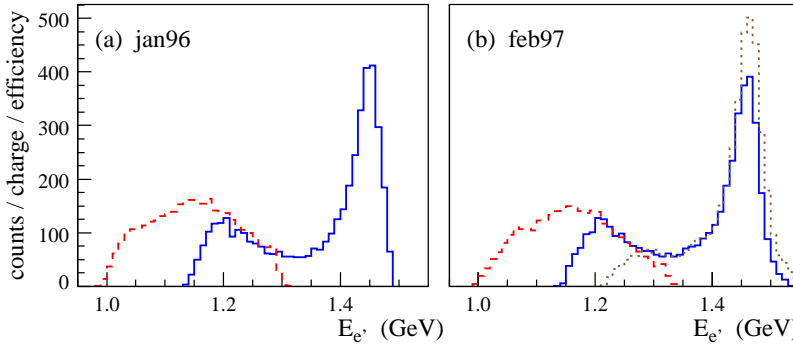


Figure 4.33: Inclusive ${}^2\text{H}(e, e')$ spectrum for (a) the jan96 and (b) the feb97 measurements. The lines correspond to different kinematical settings.

In the previous sections $N_{\text{meas}}/\eta_e\eta_{\text{live}}$ has been determined – referred to as N_{wall} and N_{tele} for the TOF-walls and telescopes, respectively – as well as the proton detection efficiency η_p . The remaining factors and corrections are discussed in the following subsections, together with the procedure to combine results from the different kinematical settings and the correction for the contribution of the target walls to the measured countrates.

4.4.1 Accumulated charge

The accumulated charge was recorded separately for every data file using a scaler in the Faraday cup. This apparatus was calibrated in Bonn [Ban98b]; the result is estimated to be accurate to 1.5%. The value Q_{tot} , needed to scale the measured countrate for a specific energy transfer bin, is found by adding the results from all contributing files, as explained below.

Combining kinematical settings

The results from all files in all relevant kinematical settings are combined to create the *breakup parameter* B_{np} spectra, on which the fits described in sections 4.2.4 and 4.3.6 are performed. However, since the limits of the spectrometer acceptance do not necessarily coincide with the edge of an energy transfer bin, in each setting the first and last energy transfer bin – which might not be completely used – are skipped. Table 4.2 shows to which of the ten energy transfer bins the kinematical settings contribute.

In three cases the inclusive ${}^2\text{H}(e, e')$ spectra¹⁰ indicate that also the second-

¹⁰The inclusive spectra are available, because the hardware trigger for the data acquisition system consists only of signals from the electron spectrometer (see section 3.3.1).

kinematical setting	$E_{e'}$ (GeV)		energy transfer bins		η_Q for the second-last bin
	central	range	available	used	
$\mathcal{J}1$	1.154	1.02 – 1.29	5 – 10	6 – 10	0.50
$\mathcal{J}2$	1.214	1.07 – 1.36	3 – 9	4 – 8	
$\mathcal{J}3$	1.275	1.12 – 1.43	2 – 9	3 – 8	
$\mathcal{J}4$	1.325	1.17 – 1.48	1 – 8	1 – 7*	
$\mathcal{F}1$	1.154	1.02 – 1.29	4 – 10	5* – 10	0.90
$\mathcal{F}2$	1.325	1.17 – 1.48	1 – 8	1 – 7	0.80
$\mathcal{F}3$	1.410	1.24 – 1.58	1 – 6	1 – 5*	

Table 4.2: Contributions of the seven kinematical settings to the ten energy transfer bins. The stars indicate the three cases where the correction factor η_Q is introduced for the second-last bin. The corresponding value for η_Q is given in the last column.

jan96	$Q_{\text{tot}}(D_2)$	$Q_{\text{tot}}(MT)$	feb97	$Q_{\text{tot}}(D_2)$	$Q_{\text{tot}}(MT)$
$\mathcal{J}1$	3771	1045	$\mathcal{F}1$	4558	1882
$\mathcal{J}2$	246	150	$\mathcal{F}2$	78	96
$\mathcal{J}3$	1269	394	$\mathcal{F}3$	32	46
$\mathcal{J}4$	2403	662			

Table 4.3: Total accumulated charge Q_{tot} (in μC) per kinematical setting for both the deuterium (D_2) and “empty target”(MT) measurements.

last energy transfer bin does not contribute completely to the results, see Figure 4.33 and the stars in Table 4.2. A correction factor η_Q – a kind of efficiency – is introduced to take this into account. It is determined by comparing the inclusive spectra for the extreme case to the corresponding spectra in a kinematical setting where the energy transfer bin is *not* near the edge of the acceptance. The values are given in Table 4.2.

4.4.2 Deuterium target

The length ℓ of the deuterium target is 6.05 ± 0.05 cm [Ban98a]. The target density is taken to be 175 ± 6 g/cm³, which corresponds to the range of deuterium densities from the boiling point (23.57 K) to the freezing point (18.72 K) [PDG96]. The whole range is taken, because the actual temperature of the liquid deuterium target was not fixed in the experiment.

“Empty target” correction

The contribution of the target walls to the measured countrates is taken into account by subtracting the “empty target” rate. This background is determined for every kinematical setting in a measurement with no deuterium in the target, which is analyzed in the same way as the actual data.

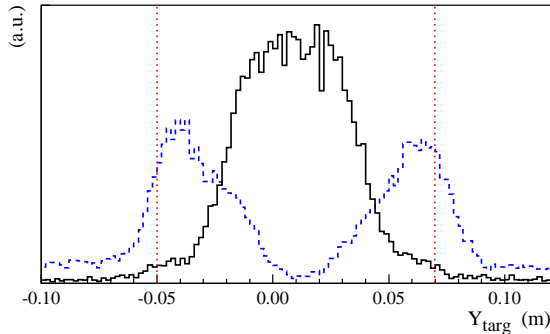


Figure 4.34: Reconstructed position of the interaction along the beam axis Y_{targ} for the ‘empty target’ measurement (dashed line) and for the deuterium measurement (solid line). Note that the relative vertical scale of two spectra is arbitrary; the ‘empty target’ results actually are much weaker than the deuterium results. The two vertical lines indicate the cut applied in the analysis.

Figure 4.34 shows the distribution of the reconstructed position of the interaction along the beam axis for the ‘empty target’ and for the deuterium measurements – note that the two are *not* to scale, since the ‘empty target’ results actually are much weaker than the deuterium results. On either side of the deuterium the contribution from the entrance and exit windows is visible. The Y_{targ} resolution does not allow a separation of the two foils on the downstream end of the target, nor of the two foils on the upstream side, although the spectra do suggest that there are two peaks there. The vertical lines indicate the cut applied to Y_{targ} in the analysis, thereby excluding part of the contribution of the outer foil, but not that of the inner foil. The cut is a little wider than perhaps seems necessary in the figure. This is necessary because of the shift in Y_{targ} mentioned in section 4.1.4.

The ‘empty target’ results are scaled to the Deuterium results using the total accumulated charge per kinematical setting, given in Table 4.3. The actual subtraction of the two rates is performed on the level of the spectra of the *breakup parameter* B_{np} , i.e. per segment or telescope, *after* correcting for the live time and the spectrometer efficiency and *before* performing the fits described in sections 4.2.4 and 4.3.6.

4.4.3 Detection volume

The detection volume \mathcal{V}_{CM} of the ${}^2\text{H}(e, e'p)n$ reaction has three components:

$$\mathcal{V}_{\text{CM}} = \Delta E_{e'} \Delta \Omega_{e'} \Delta \Omega_{\text{pn}}^{\text{CM}} \quad (4.49)$$

where the electron part is known to be

$$\Delta E_{e'} = 50 \pm 3 \text{ MeV}$$

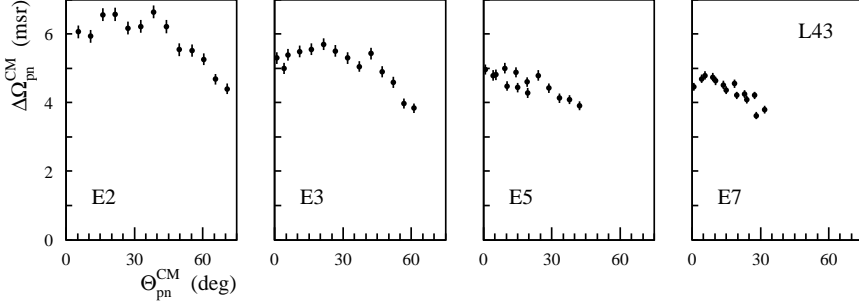


Figure 4.35: The TOF-wall proton solid angle $\Delta\Omega_{\text{pn}}^{\text{CM}}$ in several energy transfer bins. The values are for L43, the horizontal bar at beamheight.

$$\Delta\Omega_{e'} = 1.80 \pm 0.07 \text{ msr} .$$

The error in the scattered electron energy is based on the energy resolution of the ELAN spectrometer only.

The solid angle in the center-of-momentum system, $\Delta\Omega_{\text{pn}}^{\text{CM}}$, is calculated using simulations with the event generator ENIGMA [Vis94]. A flat center-of-momentum angular distribution and a constant matrix element are used. The complete spectrometer opening angle is taken into account as well as the 50 MeV energy acceptance of each energy transfer bin. The calculation is as follows. Based on the geometry of the TOF-walls (or telescopes) the number of particles N_{hit} aimed in the direction of each segment (or telescope) is determined and then scaled to obtain the solid angle for that segment (or telescope):

$$\Delta\Omega_{\text{pn}}^{\text{CM}} = \left(\frac{4\pi}{N_{\text{sim}}}\right)N_{\text{hit}} . \quad (4.50)$$

The scaling factor is the total simulated center-of-momentum solid angle 4π divided by the number of simulated events N_{sim} .

Examples of the TOF-wall proton solid angle in four energy transfer bins are shown in Figure 4.35. To check these results the solid angle has also been roughly estimated from the geometry:

$$\Delta\Omega_{\text{pn}}^{\text{CM}} \approx \frac{A}{r^2}\mathcal{J} \quad (4.51)$$

where A and r are the area and distance of a segment (in the laboratory frame) and the Jacobian \mathcal{J} transforms the laboratory solid angle into a center-of-momentum solid angle (see equation 2.28). The values obtained in this way are in the same order of magnitude.

	TOF-walls			telescopes		
	x	x/X_0	$\langle d \rangle$	x	x/X_0	$\langle d \rangle$
target (radius)	1.5 cm	0.002	3.7 m	1.5 cm	0.002	1.3 m
Vertex-detector	2 mm	0.005	3.5 m			
air	3.5 m	0.012	1.8 m	1.2 m	0.004	0.6 m
shielding	5 mm Al	0.06	25 cm	3 mm Fe	0.17	20 cm
Wall 1	5 cm	0.12	20 cm			

Table 4.4: Sources of multiple scattering effects for the TOF-walls and telescopes. Note that the Vertex detector was only present during the feb97 measurement.

$T_{\text{kin}} =$	50 MeV		100 MeV		200 MeV		300 MeV		500 MeV	
	$\Theta_{\text{RMS}} \langle \delta s \rangle$		$\Theta_{\text{RMS}} \langle \delta s \rangle$		$\Theta_{\text{RMS}} \langle \delta s \rangle$		$\Theta_{\text{RMS}} \langle \delta s \rangle$		$\Theta_{\text{RMS}} \langle \delta s \rangle$	
target			0.004	1.5	0.002	0.6	0.0012	0.4	0.0008	0.3
Vertex			0.006	2.1	0.003	1.0	0.002	0.7	0.0013	0.5
air			0.010	1.8	0.004	0.8	0.003	0.5	0.002	0.4
Al			0.02	0.6	0.011	0.3	0.008	0.2	0.005	0.1
Wall 1			0.04	0.7	0.016	0.3	0.012	0.2	0.008	0.2
<i>Total</i>			<i>0.05</i>	<i>3.3</i>	<i>0.02</i>	<i>1.5</i>	<i>0.015</i>	<i>1.0</i>	<i>0.010</i>	<i>0.7</i>
target	0.007	0.9	0.004	0.5	0.002	0.2				
air	0.01	0.6	0.005	0.3	0.002	0.1				
Fe	0.08	1.6	0.04	0.8	0.02	0.4				
<i>Total</i>	<i>0.08</i>	<i>1.9</i>	<i>0.04</i>	<i>1.0</i>	<i>0.02</i>	<i>0.5</i>				

Table 4.5: The effect of the sources of multiple scattering on protons, expressed as the RMS scattering angle Θ_{RMS} (in rad) or as the RMS offset $\langle \delta s \rangle$ (in cm). The top part concerns the TOF-walls, the bottom part is for the telescopes.

4.4.4 Multiple scattering

Before the scattered protons reach the active detector elements, they pass through several layers of “dead” material and suffer multiple scattering. In a Gaussian approximation the RMS multiple scattering angle for protons is [Leo92]:

$$\Theta_{\text{RMS}} = \sqrt{\langle \theta^2 \rangle} = \frac{20 \text{ MeV}/c}{p\beta} \sqrt{\frac{x}{X_0}} \left[1 + \frac{1}{9} {}^{10} \log\left(\frac{x}{X_0}\right) \right] \quad (4.52)$$

where p and β are the momentum and velocity of the proton, and x/X_0 is the thickness of the scattering material in radiation lengths.

Table 4.4 shows the values for x/X_0 in the current setup together with the average distance $\langle d \rangle$ of each material from the surface of the active detector material. Using these numbers the multiple scattering effects have been estimated for various proton energies, see Table 4.5. In order to reach Wall 3, a proton needs at least 125 MeV, but about 50 MeV is sufficient to reach a telescope E-bar. From this table it is clear that the average shift (< 3 cm) is much smaller than the typical size of the detector elements (20 cm), so that no correction is necessary.

4.4.5 Radiative effects

The emission of an extra (undetected!) real photon, due to the interaction of the electron with the target, influences the experimental countrates:

- by moving events from one energy transfer bin to another, due to changes in the measured energy transfer, or
- by preventing the identification of “breakup” protons because of changes in the measured or calculated energy or time-of-flight.

Since our energy transfer bins are necessarily wide, it is not possible to correct for the radiative tail by unfolding it from the missing energy spectrum as described in e.g. [MTs69]. Instead, the radiative effects have been simulated using the event generator ENIGMA [Vis94] and the results are compared to simulations *without* radiative effects to obtain a correction factor.

As the correction factors for the TOF-walls do not vary strongly from segment to segment, one common correction factor is used per energy transfer bin. The main advantage is the large reduction in the amount of simulations needed to obtain sufficiently accurate results. To account for the differences between the segments, the standard deviation of the variation is taken as the error for η_{RAD} . For the telescopes, too, one correction factor per energy transfer bin is sufficient, but it is *not* the same as the TOF-wall factor due to the different size of the telescope bars and the different kinematical conditions (large proton angles).

The same correction factor can be applied for both the *jan96* and *feb97* measurements, because the geometry of the setup was not changed. Radiative effects for the proton are not taken into account, since they are at least an order of magnitude smaller than the effects for the electron due to the factor $\log(\frac{2E}{m})$ in equation 4.56 below.

Event generator

The event generator has a built-in angular distribution for the ${}^2\text{H}(e, e'p)n$ reaction, but at large angles this cross section is too strong. Unfortunately, this has a big influence on the calculated radiative tail. Therefore, we have extended ENIGMA to use tabulated form factor calculations by Arenhövel *et al.* [Are98]. These calculations have been chosen as the “best guess to date” at these energies – the measurement of the actual cross section is one of the objectives of our experiment! A preliminary comparison with our experimental data has shown that the simulated cross section is already more realistic at large angles than the built-in cross section. The simulations cover the entire *energy* acceptance of the spectrometer, but only the centre of the *angular* acceptance, because the tabulated calculations are valid for those angles only.

Since ENIGMA cannot calculate *external Bremsstrahlung*, this is taken into account by relating it to the internal radiation. The amount of external radiation is

related to the thickness of the “external target”, i.e. the deuterium, in units of the radiation length:

$$t_{\text{external}} = t_{\text{before}} + t_{\text{after}} . \quad (4.53)$$

For our experimental setup the average values are

$$\begin{aligned} \langle t_{\text{before}} \rangle &= \frac{\ell/2}{X_0} = \frac{3 \text{ cm}}{X_0} \approx 0.4\% \\ \langle t_{\text{after}} \rangle &= \frac{r/\sin \Theta_{e'}}{X_0} = \frac{1.5 \text{ cm}/\sin 19^\circ}{X_0} \approx 0.6\% \end{aligned} \quad (4.54)$$

where ℓ is the target length, r is its radius, $\Theta_{e'}$ is the electron scattering angle and X_0 is the radiation length of Deuterium (754 cm [PDG96]). Estimating the amount of internal radiation in terms of an “equivalent target” [MTs69],

$$t_{\text{internal}}^{\text{equiv}} = \frac{\alpha}{\pi b} \left[\ln\left(\frac{-q_\mu^2}{m_e^2}\right) - 1 \right] \approx 2\% \quad (4.55)$$

where b is approximately $\frac{4}{3}$ for light nuclei, we see that the internal target is approximately twice as large as the external target. Therefore the (internal) radiative tail calculated by ENIGMA is increased by 50% to account for external radiation.

The *internal Bremsstrahlung* is calculated in the “peaking approximation”, i.e. the assumption that the photon is radiated in the same direction as the emitting electron. Photon emission *before* and *after* the actual ${}^2\text{H}(e, e'p)n$ interaction is treated independently. Higher order effects – more photons – are ignored since they are at least a factor α weaker. The radiative tail is calculated according to Borie and Drechsel [BDr71] or Ngoc and Jorba [NgP69]:

$$\begin{aligned} \frac{\text{tail}}{\text{peak}} &= \frac{\alpha}{\pi} \left((2\mathcal{E} - 1) \left(\log(k_m/k_c) - \frac{(k_m - k_c)}{E} \right) + \frac{\mathcal{E}}{E^2} \frac{(k_m^2 - k_c^2)}{2} \right) \\ \frac{df}{dk} &= \frac{(2\mathcal{E} - 1)}{k} - \frac{(2\mathcal{E} - 1)}{E} + \frac{\mathcal{E}}{E^2} k \end{aligned} \quad (4.56)$$

where $\mathcal{E} \equiv \log(2E/m)$. The first equation describes the fraction of the events scattered into the radiative tail, the second describes the distribution of these events within the tail as a function of the momentum k of the radiated photon. $k_m \equiv E - T_{\text{min}}$ is the maximum energy for a radiated photon, for which the emitting electron of energy E is still detected in the spectrometer with threshold T_{min} . For k_c , the cutoff of the tail at low photon energies, we use the experimental width of the quasielastic peak, because electrons emitting a photon with less energy are still seen as non-radiative in the analysis.

For every simulated event the *breakup parameter* B_{np} is calculated to see if the (possibly radiative) event would be identified as a ${}^2\text{H}(e, e'p)n$ event in our analysis. The TOF-wall segment or telescope for which the event is relevant is determined from the proton angles generated by ENIGMA and the geometry of the experimental setup.

no γ	photon emitted <i>before</i> interaction					photon emitted <i>after</i> interaction				
N_{none}	$N_{\text{bf,s}}^{\text{ok}}$	$N_{\text{bf,s}}^{\text{nok}}$	$N_{\text{bf,n}}^{\text{ok}}$	$N_{\text{bf,n}}^{\text{nok}}$	$N_{\text{bf,x}}^{\text{nok}}$	$N_{\text{af,s}}^{\text{ok}}$	$N_{\text{af,s}}^{\text{nok}}$	$N_{\text{af,n}}^{\text{ok}}$	$N_{\text{af,n}}^{\text{nok}}$	$N_{\text{af,x}}^{\text{nok}}$
60%	4%	1%	3%	5%	10%	4%	1%	3%	3%	6%

Table 4.6: Relative importance of the various kinds of radiative events for energy transfer bin E3. The numbers include both internal and external Bremsstrahlung.

Correction factor

For a particular energy transfer bin i the correction factor for radiative effects is

$$\eta_{\text{RAD}}(i) = \frac{N_{\text{meas}}(i)}{N_{\text{all}}(i)} \quad (4.57)$$

where $N_{\text{meas}}(i)$ represents the number of events which are correctly identified as “breakup” protons in bin i when radiation is taken into account, and $N_{\text{all}}(i)$ is the number of events populating this bin in the absence of radiative effects. The latter is easily found by switching off the photon emission in the simulations, but determining $N_{\text{meas}}(i)$ is less straightforward.

Several effects must be taken into account in determining which energy transfer bin the events eventually populate:

- For the majority of the events *no* radiative effects occur: N_{none} ,
- A photon may be emitted *before* the ${}^2\text{H}(e, e'p)n$ interaction: N_{bf} , or *after* the interaction: N_{af} ,
- After emitting a photon the electron may be assigned to the *same* energy transfer bin: N_{s} , the *next* (higher) bin: N_{n} , or one of the *other* bins: N_{x} ,
- Due to changes in the measured quantities the identification of “breakup” protons may still *succeed*: N^{ok} , or it may *fail*: N^{nok} .

These effects often occur simultaneously, especially when a high-energy photon is emitted. In the simulations all these situations can be identified individually and one observation is that events assigned to a different energy transfer bin, which is not the *next* bin, are also always rejected as “breakup” protons.

Thus the number of events populating a particular energy transfer bin in the *absence* of radiative effects, $N_{\text{all}}(i)$, can be written as:

$$\begin{aligned}
 N_{\text{all}} &= N_{\text{s}} + N_{\text{n}} + N_{\text{x}} & (4.58) \\
 N_{\text{s}} &= N_{\text{none}} + N_{\text{bf,s}}^{\text{ok}} + N_{\text{bf,s}}^{\text{nok}} + N_{\text{af,s}}^{\text{ok}} + N_{\text{af,s}}^{\text{nok}} \\
 N_{\text{n}} &= N_{\text{bf,n}}^{\text{ok}} + N_{\text{bf,n}}^{\text{nok}} + N_{\text{af,n}}^{\text{ok}} + N_{\text{af,n}}^{\text{nok}} \\
 N_{\text{x}} &= N_{\text{bf,x}}^{\text{nok}} + N_{\text{af,x}}^{\text{nok}}
 \end{aligned}$$

<i>bin</i>	η_{RAD}		<i>bin</i>	η_{RAD}	
	<i>TOF-walls</i>	<i>telescopes</i>		<i>TOF-walls</i>	<i>telescopes</i>
E1	0.70 ± 0.10	1.00 ± 0.01	E6	0.84 ± 0.07	0.95 ± 0.02
E2	0.79 ± 0.06	0.97 ± 0.01	E7	0.85 ± 0.10	0.98 ± 0.02
E3	0.90 ± 0.08	0.96 ± 0.02	E8	0.87 ± 0.10	0.99 ± 0.03
E4	0.87 ± 0.06	0.92 ± 0.02	E9	0.90 ± 0.10	1.04 ± 0.03
E5	0.84 ± 0.09	0.92 ± 0.02	E10	1.03 ± 0.10	1.14 ± 0.04

Table 4.7: The correction factor for radiative effects for the TOF-walls and the telescopes. The error of the TOF-wall factors is the standard deviation of the spread of the values for the individual segments.

where the division reflects the bins which the events populate in the *presence* of radiative effects, i.e. the $N_s(i)$ events remain in bin i , the $N_n(i)$ events end up in bin $i+1$ and the $N_x(i)$ events end up in bins $i+2, i+3, \dots$ Table 4.6 gives an example of the relative importance of the different contributions.

Therefore, when radiation is taken into account, the number of events in energy transfer bin i which are correctly identified as “breakup” protons is

$$N_{\text{meas}}(i) = N_{\text{none}}(i) + N_{\text{bf},s}^{\text{ok}}(i) + N_{\text{af},s}^{\text{ok}}(i) + N_{\text{bf},n}^{\text{ok}}(i-1) + N_{\text{af},n}^{\text{ok}}(i-1). \quad (4.59)$$

Note that this number includes events which would populate the previous bin ($i-1$) in the absence of radiative effects!

Table 4.7 shows the results for the correction factor η_{RAD} in the ten energy transfer bins for both TOF-walls and telescopes. When the value is larger than 1, more radiative events are moved *into* the bin than *out of* the bin. Note that the correction never exceeds 20%. The results in the highest energy transfer bins depend quite strongly on the (small!) value of the cross section in those bins, which is why we use Arenhövel’s calculations as a “reasonably accurate” guess.

The correction for the telescopes is in general closer to 1 than the corresponding TOF-wall correction. One reason might be that the telescope bars are much larger than the TOF-wall segments, so that the “edge effects” are less pronounced. Another cause could be the smaller variation of the cross section at large proton angles – where the telescopes are positioned – which leads to less difference in the number of radiative events moved into and out of the energy transfer bin.

Chapter 5

Results and interpretation

In this chapter the results of the analysis described in the previous chapter are presented. The representation chosen for the data points is discussed in section 5.1, together with two extrapolation methods needed to compare points with slightly different kinematics. The various contributions to the error and the criteria for discarding uncertain data points are discussed in section 5.2. An overview of the final results is given in section 5.3, whereas the complete data set is tabulated in the Appendix. In section 5.4 the internal consistency of the results is investigated. Also, our results are compared with two external references in order to explain the discrepancies encountered. The experimental results are compared with the model calculations from chapter 2 in section 5.5 and in section 5.6 the f_{LT} form factor is extracted from the data. Finally, in the last section some improvements are suggested for future ${}^2H(e, e'p)n$ experiments.

5.1 Data representation

The large amount of data points and the large kinematical range they cover make it difficult to show many results simultaneously or to compare (sets of) data points. This section presents our choice of kinematical variables and explains the methods used to overcome these problems.

5.1.1 Choice of variables

It has been shown in section 2.2 that there are several possibilities to represent the available degrees of freedom of the experiment. We have chosen the set $\{Q^2, \omega, \Theta_{pn}^{\text{CM}}\}$, because these observables – especially Θ_{pn}^{CM} – focus on the *whole* two-body system and not just on one of the components. Note that this is also the format in which the model calculations have been provided to us.

The results have been separated into ten bins of the energy transfer ω , each 50 MeV wide (see section 4.1.5). Each energy transfer bin corresponds to an approximately constant value of Q^2 , varying between -0.26 (GeV/c)^2 in bin E1 and -0.19 (GeV/c)^2 in bin E10. Separate plots will be shown for every energy transfer bin. Within the energy transfer bins one *physical* degree of freedom remains: the polar angle Θ_{pn}^{CM} of the relative momentum of the np -pair. So naturally the results will be shown as a function of this variable.

The differential cross section also has an explicit *kinematical* dependence on the azimuthal angle Φ_{pn}^{CM} , which is related to the contribution of the two interference form factors (equation 2.19). In order to show the measured Φ_{pn}^{CM} -dependence the results will be separated into several Θ_{pn}^{CM} -bins, because otherwise the dominating variation of the cross section due to change in the polar angle will obscure any Φ_{pn}^{CM} -dependent effects.

5.1.2 Integration over the electron quantities

Especially in the quasielastic region, the cross section varies strongly *within* one energy transfer bin and is dominated by the low energy transfer side of the bin. This must be taken into account when comparing data and model calculations.

A similar argument can be made for the variation of the cross section within the azimuthal angular acceptance $\Delta\Phi_{e'}$ of the electron spectrometer. That this is an important effect is perhaps surprising, because the cross section itself does not depend on this angle. It enters as an indirect effect, which is most pronounced for out-of-plane TOF-wall *segments*: For every segment the position of its centre is used to define the *polar* angle of the protons detected in the segment. The out-of-plane movement of the electron corresponds to a change in the vertical component of the momentum transfer and therefore the calculated proton angle w.r.t. this momentum transfer is also different. The cross section *does* depend strongly on this polar angle.

To take these two effects into account, the model calculations are integrated over the energy transfer and azimuthal angle bins simultaneously. The following five-point formula is used, based on a Taylor expansion of the cross section σ around the value at the center:

$$\sigma_{\text{int}} = (\sigma_{\omega_L, \phi_0} + \sigma_{\omega_U, \phi_0} + \sigma_{\omega_0, \phi_L} + \sigma_{\omega_0, \phi_U} + 2\sigma_{\omega_0, \phi_0})/6. \quad (5.1)$$

In this equation $\sigma_{\omega, \phi}$ is the cross section at a certain energy transfer ω and azimuthal angle ϕ . The subscripts 0, L and U indicate the centre of the bin and the lower and upper edges, respectively, as shown in Figure 5.1. The width of the energy transfer bin is the 50 MeV used in the analysis. The width of the azimuthal angle bin is 14 degrees, which corresponds to the range accepted by the ELAN spectrometer in our experiment.

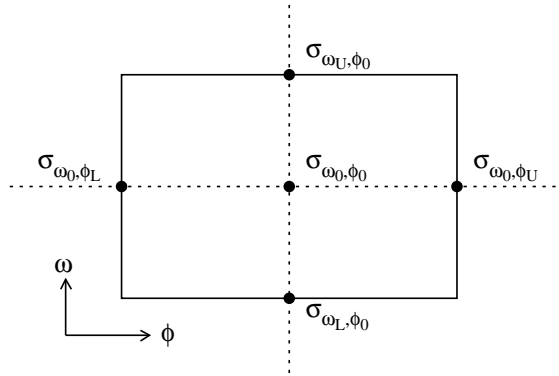


Figure 5.1: Nomenclature for the integration of the cross section over a energy transfer and azimuthal angle bin.

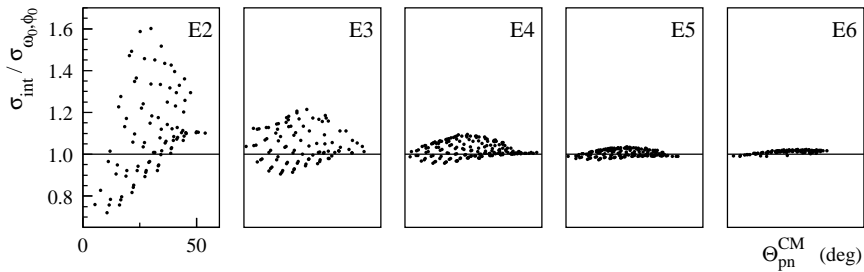


Figure 5.2: Ratio of the cross section integrated over the energy transfer and azimuthal angle bins σ_{int} and the value at the center $\sigma_{\omega_0, \phi_0}$. The values shown are for the TOF-wall segments for energy transfer bins E2 through E6.

The size of these effects is given in Figure 5.2, which shows the ratio of the integrated cross section σ_{int} and the central value $\sigma_{\omega_0, \phi_0}$. The effect is strongest in the quasielastic region and at small proton angles (w.r.t. the momentum transfer), because the cross section varies most strongly there. In energy transfer bins E4 and beyond the effect is less than our systematical error of 15%, but it will still be taken into account.

In a similar manner one can correct for the variation of the cross section over the range of the electron polar angle $\Theta_{e'}$, the position Y_{targ} of the interaction within the deuterium target, and the $20 \times 20 \text{ cm}^2$ surface of a TOF-wall segment. However, these corrections are all less than 2% for all energy transfer bins and are therefore ignored.

5.1.3 Extrapolation in the angles

The TOF-wall data points are on a rectangular grid defined by the vertical and horizontal bars, whereas they are to be represented in the spherical coordinates Θ_{pn}^{CM} and Φ_{pn}^{CM} . The transformation between the two systems is not linear, so that both the polar angle *and* the azimuthal angle vary from segment to segment. The influence of this difference in angles must be taken into account when comparing data points, even within one experimental data set.

Fortunately, as long as the change in angle is small, one can extrapolate a set of experimental data points to a common angle using model calculations. For this purpose we assume that a reasonable model – like that by Arenhövel *et al.* – in general will yield a reasonable description of the angular dependence of the cross section, where “reasonable” means: with an accuracy within the experimental error. Of course this method fails when the change in angle is large or when the cross section varies so strongly that one cannot be sure the model yields a reasonable description, but within a certain segment the assumption is valid.

In this thesis such an extrapolation (in the *polar* angle Θ_{pn}^{CM}) will be used in section 5.3.1, where the results are shown as a function of Φ_{pn}^{CM} for several bins of the proton polar angle Θ_{pn}^{CM} . The extrapolation factor is the ratio of the model calculations for the actual angle Θ_S^{CM} of the segment and the calculations for the angle Θ_0^{CM} of the bin. In both cases the actual Φ_{pn}^{CM} of the segment is used. The extrapolation factor is largest where the cross section varies strongly, i.e. in the lower energy transfer bins and close to the direction of the momentum transfer. In energy transfer bin E2 the correction is as large as 50% in a few extreme cases, but usually the extrapolation changes the result by only 10–20%, or even less in the higher energy transfer bins.

5.1.4 In-plane and out-of-plane

When comparing the results of the *jan96* and *feb97* measurements, and also when comparing the data to the model calculations, more effects than just changes in the angles play a role. In order to reduce the number of simultaneously varying parameters in a single figure, the following approach is taken – making use of the fact that the cross section depends more strongly on the energy transfer and the polar angle than on the azimuthal angle.

When we investigate the overall strength of the cross section, only in-plane data points are considered. These are segments located at beamheight (bar L43), both at $\Phi_{pn}^{\text{CM}} \approx 0^\circ$ and at $\Phi_{pn}^{\text{CM}} \approx 180^\circ$. The latter are included in order to have in-plane data points in energy transfer bin E6 of the *jan96* measurement too. In this way any out-of-plane (azimuthal) effects are eliminated from the figure, so that one can focus on the dependence on the energy transfer ω and/or the polar angle Θ_{pn}^{CM} . This approach is taken in most of section 5.4 and in section 5.5.1.

On the other hand, when we investigate the much smaller dependence of the cross section on the azimuthal angle Φ_{pn}^{CM} , a reduced cross section can be used:

$$d\sigma_{LT} \equiv d^5\sigma_{\text{exp}}(\theta, \phi) - d^5\sigma_{\text{exp}}(\theta, \phi = 0) . \quad (5.2)$$

In other words, only the deviation of the cross section from the in-plane value is considered. In terms of the form factors this means leaving out the f_L and f_T part and keeping only the f_{LT} and f_{TT} contributions (where the former is dominant). Thus the major part of any differences in e.g. the normalization is eliminated.

This second approach – applied in section 5.4.4 – still requires some finetuning: the individual segment results are extrapolated to the common polar angle Θ_0^{CM} of the corresponding in-plane segment, as described in section 5.1.3, and corrected for the variation over the $(\Delta\omega, \Delta\Phi_{e'})$ acceptance, see section 5.1.2.

5.2 Data selection

In this section we discuss the various contributions to the error in the data points and list the criteria applied to discard results.

5.2.1 Contributions to the error

At large angles and/or large energy transfers the important contributions to the final uncertainty are the error in the proton detection efficiency and the statistical error in the measured countrates. That these two occur together is no surprise, because the efficiency is determined from the actual data. Therefore, when the statistics are low, the efficiency determination is also not too accurate. The other contributions to the error only play a role at smaller angles and in the lower energy transfer bins. There the total error is dominated by the correction for radiative effects. The various contributions to the final error are summarized in Tabel 5.1.

The efficiency error is not included in the systematical error and is listed separately in the Appendix, as it is the only systematical part that varies strongly. However, for many plots in this chapter, showing all *three* errors for every data point may be confusing. Therefore in most cases only the *statistical* error is shown. At the bottom of plots with a *linear* scale an indication will be given of the *systematical* error including an average value for the *efficiency* error (see below). Only when the latter is very large, the full error will also be shown explicitly on the data point itself. Such data points can be recognized by the little line on the error bar, separating the statistical error from the systematical and efficiency error.

In order to quantify this discussion, Figure 5.3 shows the distribution of the efficiency errors per energy transfer bin. The (weighted) mean of these distributions is used as the approximate value for most points, while values more than one standard deviation larger than the mean are shown explicitly.

<i>source</i>		<i>TOF-walls</i>	<i>Telescopes</i>
statistics	$\delta N/N$	$\leq 40\%$	$\leq 40\%$
Total statistical error:		$\leq 40\%$	$\leq 40\%$
accumulated charge	$\delta Q/Q$	1.5 %	1.5 %
spectrometer	$\delta \eta_e/\eta_e$	1 %	1 %
electron energy	$\delta E_{e'}/E_{e'}$	6 %	6 %
electron solid angle	$\delta \Delta\Omega_{e'}/\Delta\Omega_{e'}$	4 %	4 %
target length	$\delta \ell/\ell$	1 %	1 %
target density	$\delta \rho/\rho$	3 %	3 %
radiative effects	$\delta \eta_{\text{RAD}}/\eta_{\text{RAD}}$	12 %	3 %
detection volume	$\delta \mathcal{V}_{\text{CM}}/\mathcal{V}_{\text{CM}}$	3 %	1 %
Total systematical error:		15 %	9 %
effi ciency (Wall 2)	$\delta \eta_2/\eta_2$	0 - 40 % (bin E2)... 15 - 100 % (bin E9)	25 %
(Wall 3)	$\delta \eta_3/\eta_3$	0 - 60 % (bin E2)... 25 - 100 % (bin E9)	
Total effi ciency error:		$\leq 100\%$	25 %

Table 5.1: Contributions to the final errors of the measured data points. The values mentioned for the statistical error are for the majority of the results, but there are also some points with errors up to 100%. In the analysis an upper limit is imposed on the statistical error (50%) and on the effi ciency error (35%).

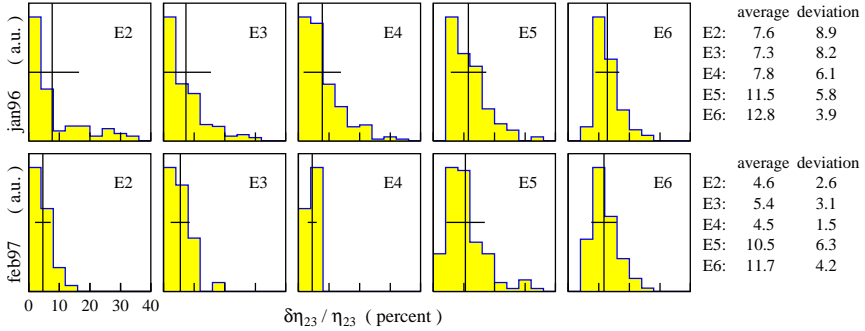


Figure 5.3: Distribution of the efficiency errors $\delta \eta_{23}/\eta_{23}$ for the TOF-wall results in the energy transfer bins E2 through E6. The weighted mean (vertical line) and deviation (horizontal line) of the distribution are indicated in each plot; the actual values are given on the right. The upper plots concern the jan96 measurement, the lower plots are for the feb97 measurement.

5.2.2 Selection criteria

It is clear from Table 5.1 and the discussion in previous sections, that some data points have very large uncertainties. Therefore several requirements are used to discard results, which do not contribute any useful information.

General criteria

The following general requirements are applied to all data points:

- All results from energy transfer bin E1 are discarded, because part of this 50 MeV wide energy bin is kinematically excluded – there can be no events below the quasielastic peak – and because in this energy range a large part of the protons cannot reach Wall 3 (or even Wall 2).
- A data point is discarded if a reliable fit of the PID-spectrum is not possible (with one exception, see section 5.2.3).
- A data point is discarded if the statistical error $\delta\sigma_{\text{stat}}$ is larger than 50%.
- A data point is discarded if the proton efficiency η_p is smaller than 30%.
- A data point is discarded if the relative error in the proton efficiency $\delta\eta_p/\eta_p$ is larger than 35%.

Naturally, these limits are arbitrary, based on our intent not to discard too many results (hence the high limit for the statistical error) and not to apply too large correction factors (a factor 3 due to the efficiency can already be considered large). No limit is required for the total systematical error (excluding the efficiency), because it is acceptable in all cases with $\delta\sigma_{\text{syst}} \approx 15\%$ for the TOF-walls and 9% for the telescopes.

As a consequence, no TOF-wall results will be given for energy transfer bins E7 through E10, especially due to the third and/or fourth criterion. Also, due to the limit on the statistical error, there are no results for energy transfer bin E4 in the *feb97* measurement – we spent very little time on those energies in that year. The second criterion affects individual data points at all energies, but of course mostly at energies where the statistics are also low.

Telescopes

For the five telescopes on the righthand side of the beam, only the results in energy transfer bin E1 need to be discarded based on the arguments above, but there are no significant countrates for the two telescopes at backward angles (*T2*, *T4*) in energy transfer bins E2 through E4, nor for telescope *S3* in energy transfer bin E2.

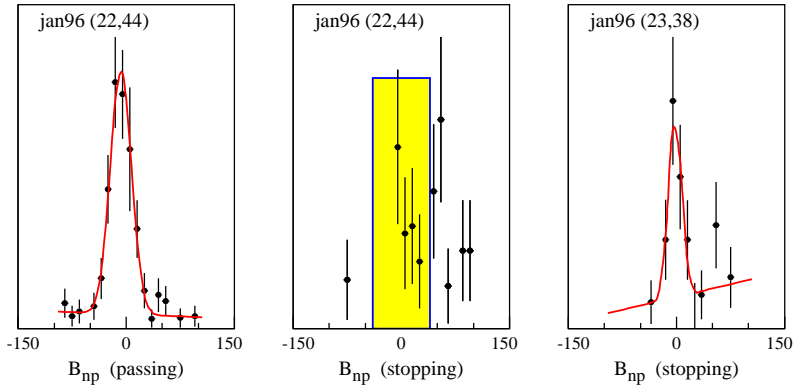


Figure 5.4: An example of a PID-spectrum for stopping protons, for which no reliable fit of the peak and background can be obtained (centre). The spectrum is for energy transfer bin E2 in the jan96 measurement. The box indicates the integration limits used for the upper limit of the countrate. As a comparison the corresponding PID-spectrum for passing protons is shown (left), as well as a stopping PID-spectrum for which the fit is possible (right).

TOF-walls

The following requirements are applied to the TOF-wall results only:

- All segments of the rightmost vertical bar (L31) are ignored. This bar is only partly in front of the TOF-wall behind it, so that it is impossible to obtain a reliable value for the efficiency and the detection volume for these segments.
- Individual segment results are discarded, when there is a substantial chance that the TOF-wall efficiencies are correlated (see section 4.2.5). This only affects a few segments.

5.2.3 Passing and stopping results

In the analysis of energy transfer bins E2 and E3 a distinction is made between protons *stopping* in Wall 3 and protons *passing* through Wall 3. Both countrates are determined separately and then added together to obtain the total rate for the segment (see section 4.2.4). However, it is not always possible to achieve a good fit of the PID-spectrum for the *stopping* protons, usually for statistical reasons. An example is given in Figure 5.4. According to the criteria from the previous section these data points should be discarded, but usually the situation is that the *passing* part is quite reliable and much stronger than the *stopping* part, so that it would be a pity to leave out the data point entirely. Simply ignoring the *stopping* part is not an option, because then the cross section would be underestimated. Therefore, in

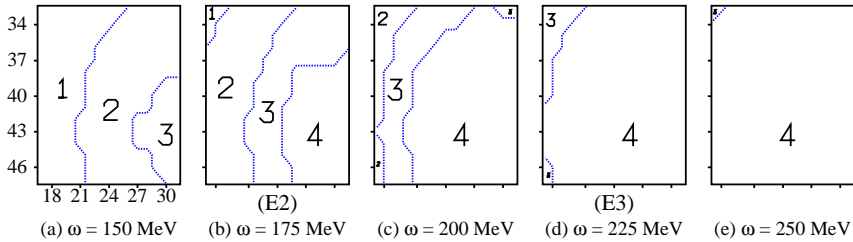


Figure 5.5: Front view of the TOF-walls indicating the Wall in which the proton is expected to be stopped, based on the proton energy in ${}^2\text{H}(e, e'p)n$ kinematics for the given value of the energy transfer. The region labeled 3 contains the stopping protons, the passing protons are in region 4. Events for which the proton cannot reach Wall 3 (regions 1 and 2) are ignored in this thesis. The bar numbers are given in the leftmost picture. The E2 energy range is $\omega = 150 \text{ MeV} - 200 \text{ MeV}$, the E3 range is $200 \text{ MeV} - 250 \text{ MeV}$.

such cases the *stopping* countrate is estimated by simply integrating between the limits indicated in Figure 5.4. These limits correspond to twice the width of the peak in a reliable PID-spectrum. Because this procedure completely ignores the possible contribution of the tail of the non- ${}^2\text{H}(e, e'p)n$ events (see section 4.2.4), the countrates obtained in this manner should be regarded as an upper limit.

Of course, this procedure is only necessary for segments in which *stopping* protons are expected. This is determined using the Bethe-Bloch formula and the known proton energy for every segment and energy transfer. The results are given in Figure 5.5 as the number of the TOF-wall (1...4) in which the proton is expected to stop. It is clear that most segments should contain both *passing* and *stopping* protons for energy transfer bin E2 (Figures 5.5a-c). It turns out that this is true for *all* data points which are not rejected on other grounds (see the previous section). For energy transfer bin E3 (Figures 5.5c-e) *stopping* protons are found only at large angles w.r.t. the momentum transfer, where the proton energy is lowest. These angles are not relevant in the *feb97* measurement due to low statistics, but they do contribute in the *jan96* measurement.

5.3 Result of the experiment

This section gives an overview of the experimental results after applying the criteria from the previous section. The data points from the *jan96* and *feb97* measurements will be shown separately.

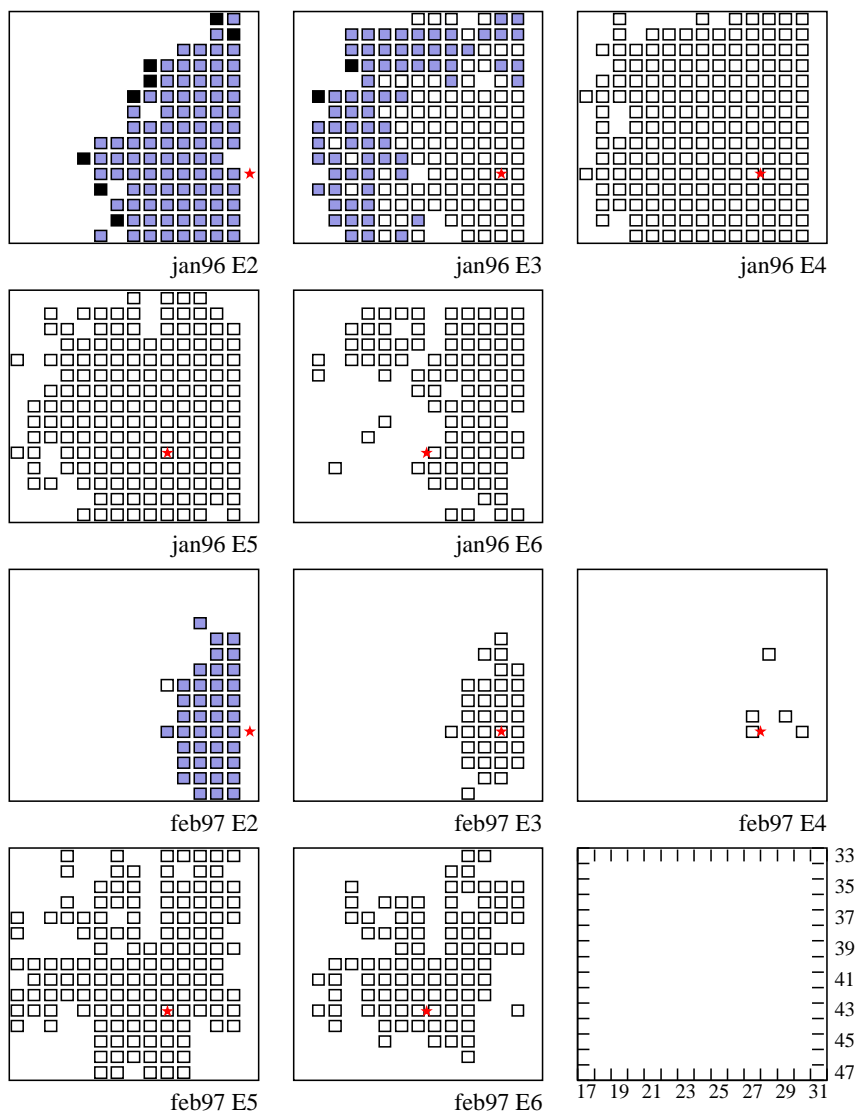


Figure 5.6: Distribution of the final results over the TOF-wall segments (front view) for all remaining energy transfer bins (E2 through E6). The first five plots are for the jan96 measurement, the others for the feb97 measurement. The direction of the momentum transfer is indicated by a star. See the text for a description of the segment shading.

5.3.1 TOF-walls

After applying the criteria from the previous section to the TOF-wall results about 550 data points remain from the *jan96* measurement and about 300 data points from the *feb97* measurement. These results are all in energy transfer bins E2 through E6. Figure 5.6 shows the distribution of these remaining data points over the TOF-walls. The white boxes indicate *passing* results, the darker boxes are results in which the *passing* and the *stopping* results have been added together and the black boxes indicate segments for which no reliable *stopping* result is available, although one is expected. In these cases the *stopping* contribution has been estimated as described in section 5.2.3.

The mixed (*stopping* and *passing*) results occur roughly in a circular band around the direction of the momentum transfer, reflecting the proton energy distribution, which is independent of the azimuthal angle Φ_{pn}^{CM} . The segments, for which no reliable *stopping* fit was found, are at the edges of the area containing results, where the statistics are poor. The irregularities at these edge are related to differences between the individual bars of the TOF-walls, e.g. in the thresholds or in the calibration. This is especially clear in energy transfer bin E5 of the *feb97* measurement, where there are no results for large parts of bars L25 (vertical) and L39 (horizontal) due to efficiency problems.

The complete set of results is given in the Appendix, one table for each energy transfer bin, separately for the two measurements.

Angular distribution

An example of the dependence of the TOF-wall results on the polar angle Θ_{pn}^{CM} is given in Figure 5.7a. In most cases the error bars indicate the statistical error only (see section 5.2.1). The variation between data points¹ at the same value of the polar angle Θ_{pn}^{CM} is predominantly due to the differences in the azimuthal angle Φ_{pn}^{CM} (see section 5.1.4). To illustrate this, only the in-plane results are shown in Figure 5.7b. These data points correspond to the lower edge of the data set in Figure 5.7a; a set of out-of-plane results with a different common azimuthal angle Φ_{pn}^{CM} are on a similar, somewhat higher, line (not shown in the figure). The same results are shown in Figure 5.8 as a function of Φ_{pn}^{CM} for several bins of the polar angle Θ_{pn}^{CM} . The central angle of each bin is indicated in the figure. The correction described in section 5.1.3 – extrapolating the data points to the common central value of Θ_{pn}^{CM} for the bin – has been applied. All other data points will be shown in section 5.5.2 in the comparison of the data to the model calculations.

¹Three types of data points are shown: segments in which all protons *pass* through Wall 3 (circles), segments in which some protons *stop* in Wall 3 and others *pass* (squares), and segments in which there should be *passing* and *stopping* protons, but for which the *stopping* contribution was estimated (stars).

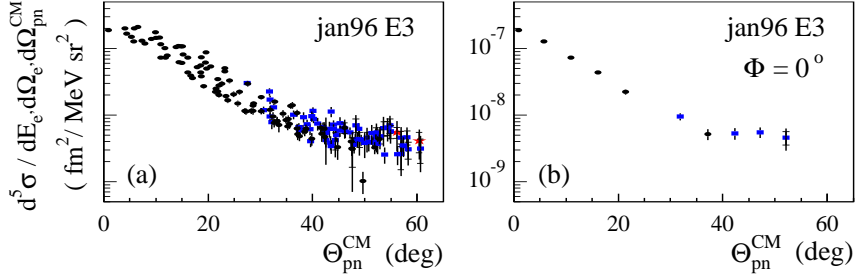


Figure 5.7: Some TOF-wall cross section results as a function of the polar angle Θ_{pn}^{CM} for energy transfer bin E3 of the jan96 measurement. (a) shows all data points for this bin, (b) shows only the in-plane results. For most points only the statistical error is shown, as discussed in section 5.2.1. Note the logarithmic scale.

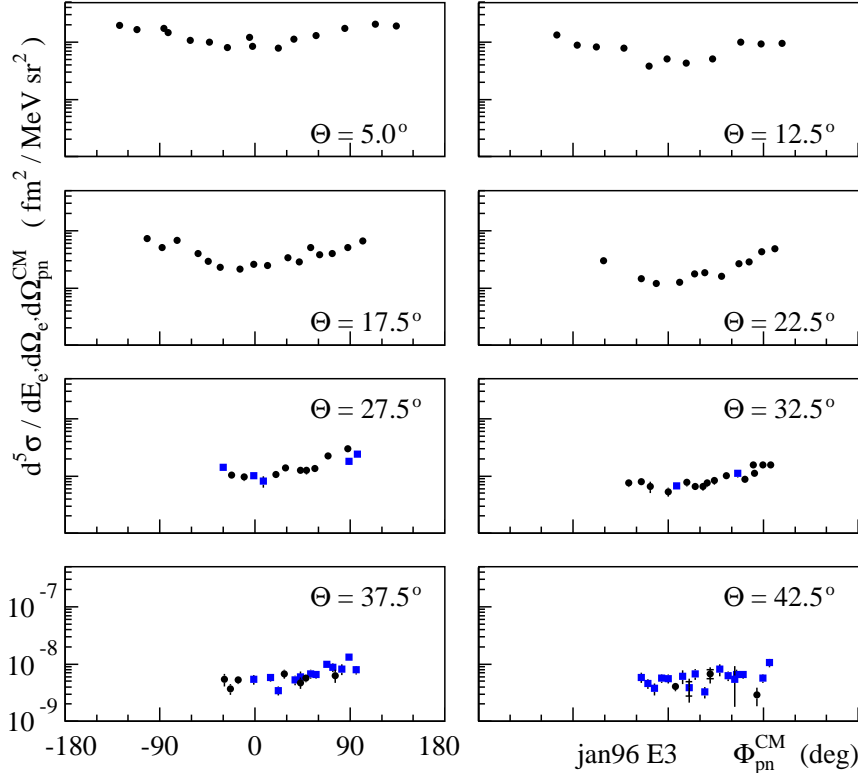


Figure 5.8: An example of the TOF-wall cross section results (bin E3 in the jan96 measurement) as a function of the azimuthal angle Φ_{pn}^{CM} . Again, for most data points only the statistical error is shown. All plots have the same logarithmic scale.

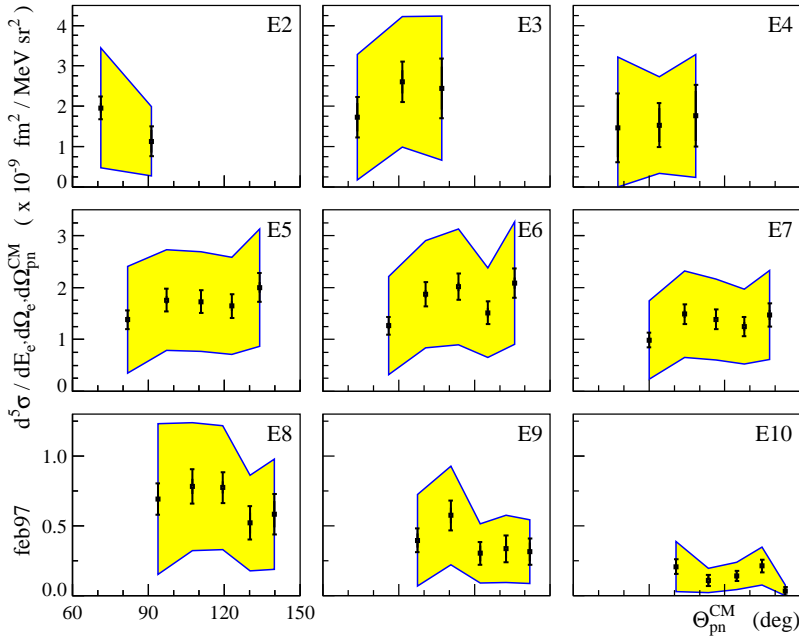


Figure 5.9: Telescope cross section results as a function of the polar angle Θ_{pn}^{CM} for nine energy transfer bins (E2...E10) in the feb97 measurement. The error bars represent the statistical and systematical errors; the shaded area indicates the total error including the estimated efficiency error. Note the different linear scales.

5.3.2 Telescopes

There are five telescope results for each energy transfer bin beyond E4, three results in bins E3 and E4, and two results in bin E2. The latter are for the two telescopes closest to the direction of the momentum transfer, where the countrate is highest. Figure 5.9 shows the results for all energy transfer bins. The statistical and systematical error bars are shown and the shaded area represents the total error including the estimated efficiency error. The complete set of telescope results is given in the Appendix.

5.4 Consistency of the results

In this section several checks of the experimental results are discussed. First, the internal consistency of the data is determined by comparing the telescope results to the TOF-wall data and by comparing the *jan96* and *feb97* measurements. Next, the results are compared to two external references, namely the ${}^2\text{H}(e, e'p)n$ experi-

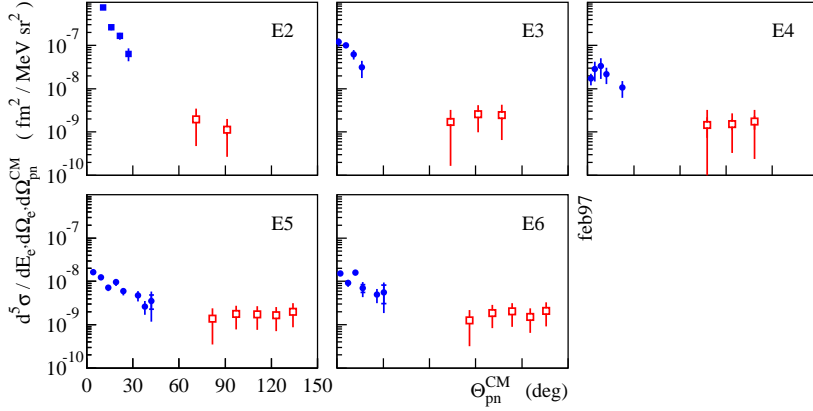


Figure 5.10: The cross section results for the feb97 measurement as a function of the polar angle Θ_{pn}^{CM} for both the TOF-walls (solid circles and squares) and the telescopes (open squares). Only in-plane data points are shown, except for energy transfer bin E4. In general only the statistical error is shown, as discussed in section 5.2.1. For the telescope results the error bar includes the efficiency error. All plots have the same logarithmic scale.

ment by Kasdorp [Kas97] and model calculations in the quasielastic region, where the ${}^2\text{H}(e, e'p)n$ reaction is thought to be well understood. These checks give an indication of the reliability of the results, specifically of the overall normalization. It turns out that discrepancies remain between the *jan96* and *feb97* measurements and an attempt is made to explain the differences.

5.4.1 Telescopes and TOF-walls

The telescope results are compared to some TOF-wall data points in Figure 5.10. Only the in-plane TOF-wall data points are shown for most energy transfer bins to avoid confusion by out-of-plane effects. The gap between the two sets is due to the concrete wall, which shields the TOF-walls from background radiation.

The two sets of results do not contradict each other, although it is difficult to extrapolate over two orders of magnitude. Also, the telescope data points are at $\Phi_{pn}^{\text{CM}} = 180^\circ$, whereas the TOF-wall values are for $\Phi_{pn}^{\text{CM}} = 0^\circ$. A more detailed discussion is given in section 5.5.1, the comparison with model calculations.

5.4.2 Two data sets

Since our experiment was performed as two separate measurements, *jan96* and *feb97*, which have been analyzed separately, we can compare the results of these two measurements. Figure 5.11 shows the ratio of the two data sets for the relevant energy transfer bins. The selection is again limited to in-plane segments to

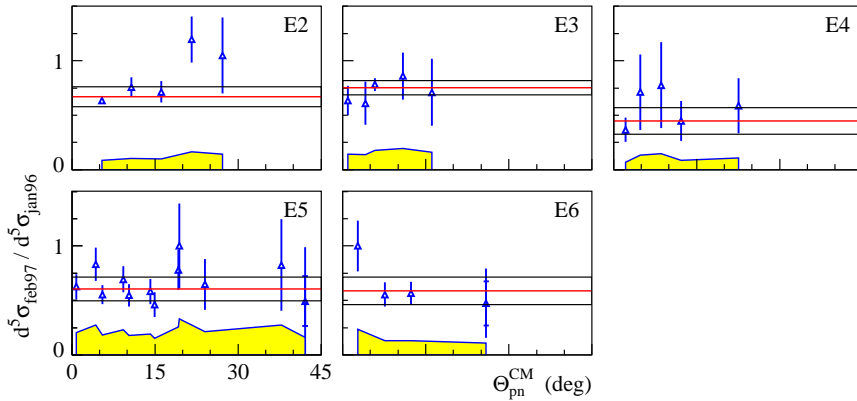


Figure 5.11: Ratio of the february 1997 and january 1996 in-plane data points for five energy transfer bins. On the horizontal axis the combined systematical and average efficiency error is shown, the error bars mostly indicate only the statistical error (see section 5.2.1). The lines represent the weighted mean and standard deviation of the data points shown.

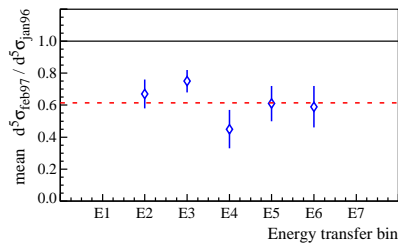


Figure 5.12: Weighted mean ratio of the february 1997 and january 1996 results. The five points are the mean values given by the lines in Figure 5.11. The dashed line is the average of these points.

avoid confusion by out-of-plane effects. The three lines in each picture indicate the weighted mean and standard deviation of the data points in the plot (only the *statistical* error is used to weigh the points). For most data points in the figure the ratio lies below unity, although there are several data points (with large errors) for which the ratio is much higher.

The weighted means from Figure 5.11 are shown as a function of the energy transfer bin in Figure 5.12. The ratio is around 0.6 in all energy transfer bins (indicated by the line). Such a reasonably constant factor may indicate a global correction factor that has not been taken into account correctly in one or both of the experiments. The next few sections are devoted to the question if one of the two experimental data sets is more reliable (or, if perhaps both are not reliable).

	<i>point 1</i>	<i>point 2</i>	
γ_{pq}	-8°	-12°	
p_m	-175	-194	(MeV/c)
Θ_{pn}^{CM}	12°	20°	($\Phi_{pn}^{\text{CM}} = 180^\circ$)

Table 5.2: Proton kinematics for Kasdorp’s two *in-plane* L02 data points.

5.4.3 Comparison with other experiments

Only one previous experiment has been done at (partially) comparable values of the physically relevant variables, namely that by Kasdorp [Kas97]. Specifically, his kinematics labeled L02 and H02 were measured at $Q^2 = 0.20 \text{ (GeV/c)}^2$ and $\omega = 224 \text{ MeV}$, which are close to the central values for energy transfer bin E3 of our experiment: $Q^2 = 0.24 \text{ (GeV/c)}^2$ and $\omega = 225 \text{ MeV}$. All other recent $^2H(e, e'p)n$ experiments have quite different kinematics – a completely different Q^2 and/or energy transfer – so that a comparison is not feasible due to the necessarily large extrapolations involved.

Like the results presented here, Kasdorp’s H02 data set was measured using a magnetic electron spectrometer and a segmented scintillator detector for the protons, so that the results can be compared easily. Both measurements have a fixed energy transfer ω on the electron side and the data points differ only in the proton kinematics (given in [Kas97] as the missing momentum p_m).

On the other hand, for Kasdorp’s L02 data set a magnetic spectrometer was used to detect the protons. Due to the much better resolution of a spectrometer w.r.t. scintillator bars, both the electron and proton kinematics could then be varied simultaneously. This means that Kasdorp’s data points correspond to a quite different set of “subkinematics” than our results, even though the central value of the energy transfer is nearly the same. Therefore, only the two *in-plane* data points from Kasdorp’s L02 data set are considered here (see Table 5.4.3 for the corresponding proton kinematics, in three equivalent notations). In the comparison we also consider only *in-plane* data points from our experiment.

In comparing the two experiments the kinematical differences must be taken into account. The following method has been used, which is essentially equivalent to extrapolating one set of data points to the kinematics of the other set, with the bonus that it also extrapolates the form factors themselves over the (slight) difference in Q^2 and ω .

From equations 2.19 and 2.20 the decomposition of the cross section into form factors and kinematical factors is known. For both experiments model calculations by Arenhövel are available for the form factors. Using these calculations as a “reasonable estimate” – which is defensible as long as the extrapolation is small – a reference cross section is calculated for both cases. The ratio of the experimental data and this reference cross section is what is actually compared in Figure 5.13.

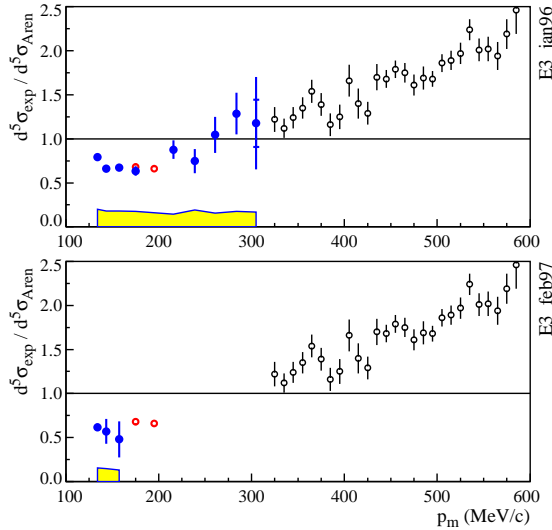


Figure 5.13: Comparison of our two experiments (solid circles) with that of Kasdorp [Kas97] (open circles). The two points just below $p_m = 200$ MeV/c are from his L02 data set, the points above $p_m = 300$ MeV/c represent the H02 data set. For the current experiment the in-plane results from energy transfer bin E3 are shown. In general only the statistical error is shown, the combined systematical and average efficiency error is indicated at the bottom of the plot (see section 5.2.1).

For the *jan96* measurement, the agreement with the L02 data is clear and our results nicely fill the gap between Kasdorp's L02 and H02 data sets. There are not enough data points from the *feb97* measurement to make a reliable comparison with Kasdorp's results. It seems as if the *feb97* data are too low but, given the large statistical errors for this measurement, the three points can just as well be in agreement with Kasdorp's L02 data.

Therefore, one cannot decide between the *jan96* and *feb97* measurements on the basis of this comparison, although the *jan96* results seem to be favoured. However, within the errors both our data sets agree with Kasdorp's results.

5.4.4 Comparison with quasielastic model calculations

Another possibility to determine which of the two measurements is more reliable, is to compare the results in the quasielastic region to the theory. In this region the reaction mechanism is well understood and the model calculations are known to reproduce the experimental results to within 10–15% (see discussions in e.g. [Ste92, Jor96, Böh01]).

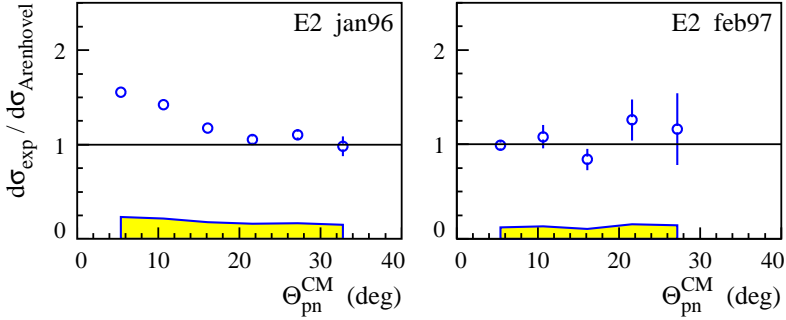


Figure 5.14: The in-plane experimental values for energy transfer bin E2 divided by Arenhövel’s ‘full’ calculations [Are98] integrated over the electron acceptance. Only the statistical error bar is shown, the combined systematical and average efficiency error is indicated at the bottom of the plots (see section 5.2.1).

Overall strength

The ratio of the experimental results and Arenhövel’s calculations for energy transfer bin E2 is shown in Figure 5.14. Only in-plane segments are used. Note that the model calculations have been integrated over the energy transfer and electron azimuthal angle bins, as described in section 5.1.2.

This comparison seems to favour the *feb97* results, since they agree quite well with Arenhövel’s model calculations, whereas the *jan96* data points are up to 50% too high at small angles – precisely where the model is expected to be most reliable. This difference is significant, because the (total) systematical error of the data is only about 25% here and the model calculations are supposed to be accurate to about 10–15%.

However, at larger angles both data sets agree with the calculations, so that still no definite choice can be made between the *jan96* and *feb97* results.

Out-of-plane effects

The out-of-plane behaviour in the same quasielastic energy domain might also help us choose between the two data sets. In Figure 5.15 the reduced cross section (defined in section 5.1.4) is shown as a function of the azimuthal angle Φ_{pn}^{CM} for several Θ_{pn}^{CM} -bins. By construction the value at $\Phi_{pn}^{\text{CM}} = 0^\circ$ is always exactly zero. The dashed line in the figure represents Arenhövel’s calculation for the central Θ_{pn}^{CM} of the bin. It is the following function of the two interference form factors:

$$d\sigma_{LT} = C \left\{ (\cos \phi - 1) \rho_{LT} f_{LT} + (\cos 2\phi - 1) \rho_{TT} f_{TT} \right\}. \quad (5.3)$$

Again, it seems that the *feb97* results agree with the model calculations in this

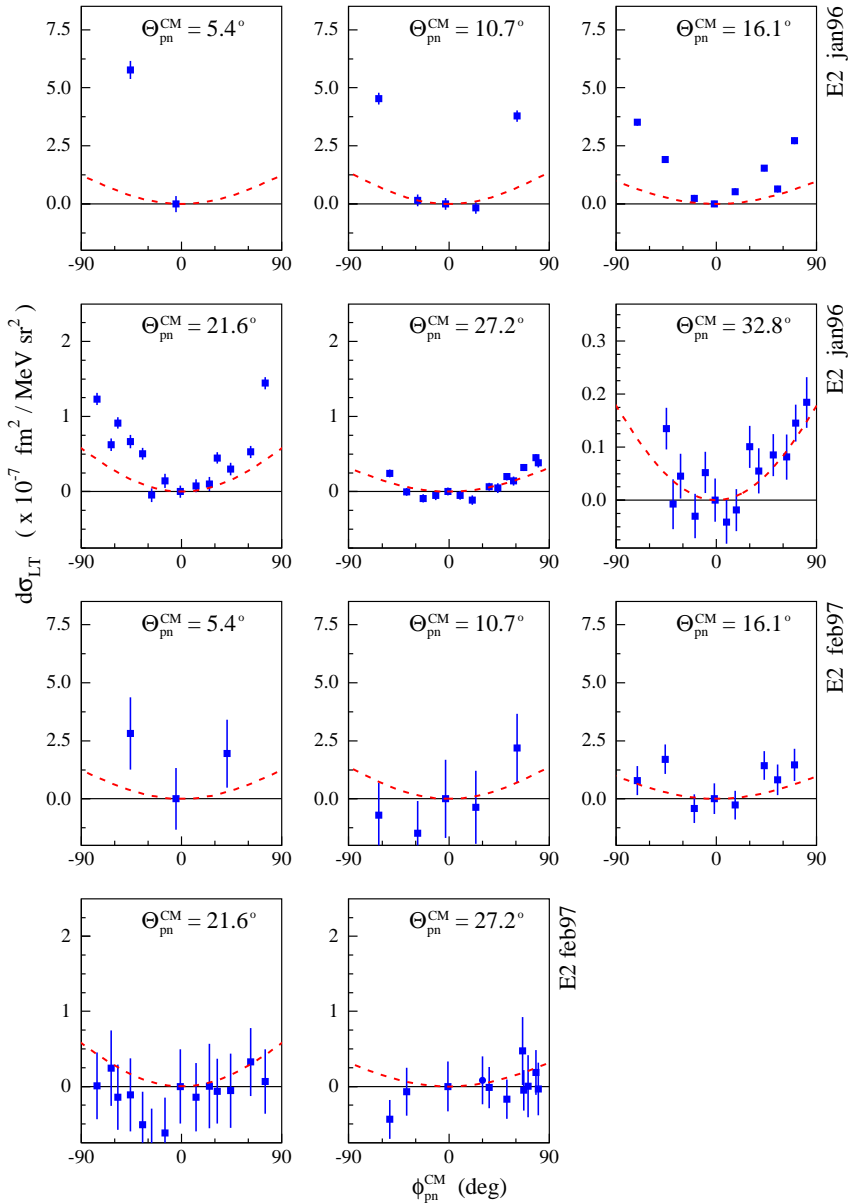


Figure 5.15: Comparison of the reduced cross section $d\sigma_{LT}$ for the two measurements (data points) with Arenhövel's "full" calculations [Are98] (dashed line). Only the first few angular bins, close to the direction of the momentum transfer, are shown. The error bars represent the statistical errors. Note the different linear scales.

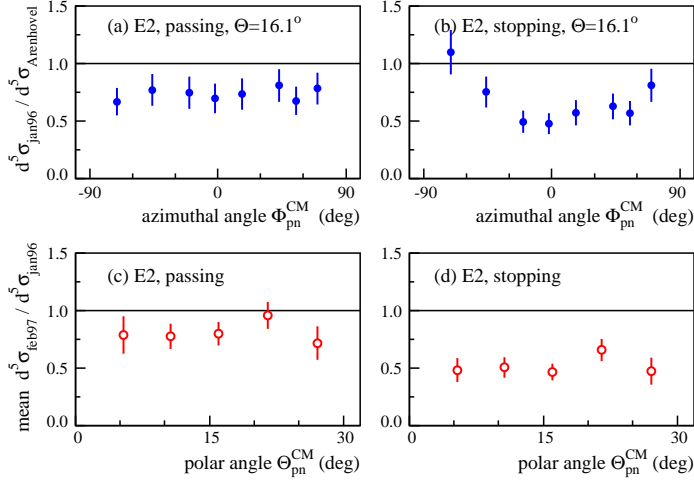


Figure 5.16: (a,b) Typical contribution of the passing and stopping parts of the cross section (scaled by the model calculations) in a particular $\Theta_{\text{pn}}^{\text{CM}}$ -bin for the *jan96* measurement. (c,d) Mean ratio of the two experimental strengths in the case of passing and stopping events, respectively (see text for details). The data are from energy transfer bin E2 and the total error is given.

energy transfer bin. The low points for the $\theta = 21.6^\circ$ bin of the *feb97* results indicate that the corresponding in-plane data point is most likely somewhat too high in comparison with its neighbours. This also means that the point should probably lay a little lower in Figure 5.14 as well, which even improves the agreement of the *feb97* results with the model calculations.

In contrast, the in-plane data points in the first four θ -bins of the *jan96* results do *not* disagree with their direct neighbours: the points seem to lay quite nicely on a curve. However, the out-of-plane effect in the *jan96* data is significantly stronger than in the model calculations. Just as the observation from Figure 5.14, that the in-plane data points themselves already exceed the model, this raises doubts about the *jan96* results for this energy transfer bin.

Passing and stopping results

There seems to be a correlation between the excess strength of the *jan96* results and the *stopping* contribution to the cross section. Like the excess strength, the *stopping* part varies with the azimuthal angle $\Phi_{\text{pn}}^{\text{CM}}$, while the *passing* part does not, as illustrated in Figure 5.16ab for a typical $\Theta_{\text{pn}}^{\text{CM}}$ -bin (compare Figure 5.16b to the third plot in Figure 5.15). Simultaneously, the *stopping* part is consistently stronger in the *jan96* data for these angles, see Figure 5.16cd. Each of the values in

these figures was determined by separately calculating the ratio for all data points in a particular Θ_{pn}^{CM} -bin and then taking the weighted mean of these ratios.

However, it is not clear what could have gone wrong in the *jan96 stopping* results to cause the excess strength. Some events may have been counted twice, i.e. both as *passing* and *stopping*, but far too few to account for the large effect.

5.4.5 Inclusive rates

The discrepancy between the two measurements might also be due to differences in the energy of the *incoming* electron. However, a comparison of the settings of the quadrupole magnets in the ELSA ring, as recorded in the logbook, indicates that the variation in the beam energy was less than 1 MeV, i.e. below 0.06%.

To check if there is a problem in the analysis of the *scattered* electron, the inclusive ${}^2\text{H}(e, e')$ spectra have been investigated (see Figure 4.33 in section 4.4.1). Clearly, the different kinematical settings within one experiment fit together nicely and the two experiments agree in the higher energy transfer bins. There might be a small shift (about 10 MeV) in the electron energy above $E_{e'} = 1.4$ GeV (i.e. in energy transfer bins E1 and E2). Such a shift could be an explanation for the differences seen in energy transfer bin E2, since the cross section changes rapidly with the scattered electron energy there. A crude estimate, based on the energy dependence of Arenhövel's calculations for small polar angles, indicates that a 10 MeV shift in the scattered electron energy corresponds to a factor 0.5 – 0.7 in the cross section, which is in the order of magnitude of the difference encountered. Of course, the actual effect would be more complex, because an energy shift changes the center-of-momentum angles of the segments too, which would also influence the cross section.

However, this possible shift in the scattered electron energy cannot explain the difference observed in the higher energy transfer bins. The energy dependence is not as strong there, so that a 10 MeV energy shift corresponds to a much smaller change in the cross section. Therefore, the conclusion must be that the electron analysis and the charge and target density corrections are correct and the discrepancy between the *jan96* and *feb97* data is related to the proton analysis.

5.4.6 Other possible explanantions

Several other factors, which could lead to differences between the *jan96* and *feb97* measurements, have also been ruled out:

- The hardware trigger for the data aquisition was the same in both measurements and there was no difference in the shielding of the TOF-walls.
- The absence of the downstream beampipe in the *feb97* measurement can only have influenced the background, which has been taken care of independently in both measurements.

- The magnet around the target in the *feb97* measurement changes the angle of the emerging protons, but the field of approximately 0.5 T with a range of (on average) 5 cm causes a shift of only 7 cm on Wall 2 for the slowest protons and much less for more energetic protons. Such a shift is too small to explain the difference between the two measurements.
- Likewise, the presence of the Vertex detector in the *feb97* measurement has increased the proton multiple scattering, but the shift on Wall 2 is estimated to be less than 2 cm for the slowest protons.
- The geometrical description of the TOF-walls used in the analysis has been doublechecked and the values used are almost certainly correct.
- Since the geometry is the same for both measurements, there can be no difference in the detection volume or the radiative effects.
- As described in chapter 4, all calibrations have been performed separately for the two measurements, so that any differences in the tuning of the various detector elements has been taken into account in the results. The same is true for the proton detection efficiency.
- The effects of not integrating the model calculations over the scattered electron polar angle $\Theta_{e'}$, the position of the interaction within the target Y_{targ} and the size of one segment on the TOF-walls are too small – only a few percent – to explain the differences. Since the geometry is the same for both measurements, the corrections are identical anyway!

5.4.7 Which data set should be chosen?

The results from the various consistency checks are ambiguous:

- There is a significant difference between the *jan96* and *feb97* results; the latter are approximately 40% lower at all energies (see section 5.4.2).
- The data for energy transfer bin E3 of the *jan96* measurement agree with the results of Kasdorp [Kas97], but for the *feb97* measurement the statistics do not allow a good comparison in this bin (see section 5.4.3).
- The *jan96* results in energy transfer bin E2 clearly deviate from the quasi-elastic model calculations, whereas the *feb97* results agree with the model (see section 5.4.4).
- The inclusive spectra shed some doubt on the *jan96* results: the scattered electron energy could possibly be a little too low (see section 5.4.5).

Unfortunately, there is no clear indication which experiment is wrong and no obvious mistake has been found in the analysis (although nearly all steps have been

doublechecked at least once), so that we cannot discard one of the data sets in favour of the other. Therefore, we have to average the results from *jan96* and *feb97* and add an extra systematical error of 20%, henceforth referred to as the *averaging error* $\delta\sigma_{\text{avg}}$.

In this thesis this average often will not be shown explicitly, because for many segments there is only a result in one of the two data sets and we do not want to ignore the information represented by such data points for lack of an average value. Therefore, usually the results will be shown separately for the two measurements with as many data points as possible for each case. For the interpretation it must be kept in mind that the real result is the average, i.e. higher than the *feb97* value and lower than the *jan96* value. Please note as well, that the statistical errors shown in the figures do *not* include the extra *averaging error* mentioned above.

5.5 Model calculations

In this section the experimental results are compared to model calculations by Arenhövel *et al.* [Are98]. The “full” calculations are used, i.e. including meson exchange currents (MEC), the Δ -isobar configuration (IC) and relativistic corrections (REL), see section 2.3. In order to illustrate the influence of the subnuclear degrees of freedom, the results of calculations *without* these effects – the “normal” (N) values – are also shown in the figures.

5.5.1 Overall strength

Figure 5.17 shows the in-plane results of the two measurements as a function of the polar angle Θ_{pn}^{CM} . These data points are all at $\Phi_{pn}^{\text{CM}} \approx 0^\circ$ (see section 5.1.4), so that we have a fair comparison to the model calculations, which are shown for $\Phi_{pn}^{\text{CM}} = 0^\circ$. There are no such TOF-wall data points in energy transfer bin E6 for the *jan96* measurement and only one in bin E4 for *feb97*. The telescope results are also included in the figure, together with the corresponding model calculations for $\Phi_{pn}^{\text{CM}} = 180^\circ$. The correction for the electron acceptance (see section 5.1.2) has been taken into account for all data points.

TOF-walls

The overall trend of the data is nicely reproduced by the model calculations, specifically the decrease in strength by up to three orders of magnitude with increasing energy transfer and polar angle. This observation confirms previous conclusions that Arenhövel’s model is quite reliable in the region where the influence of subnuclear degrees of freedom is small².

²i.e. the ‘full’ (solid line) and ‘normal’ calculations (dashed line) nearly coincide in Figure 5.17 – at the angles covered by the in-plane TOF-wall results.

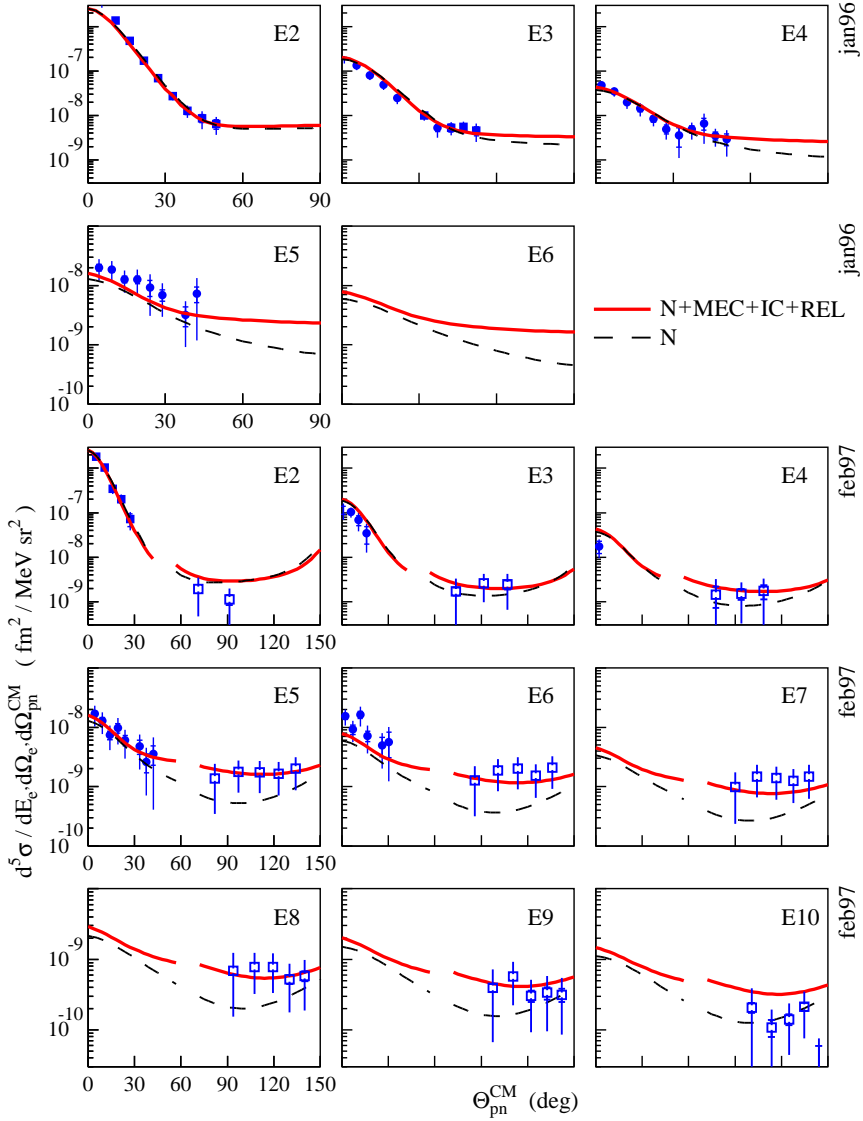


Figure 5.17: Results of the two measurements for the in-plane segments as a function of the polar angle Θ_{pn}^{CM} . For the feb97 measurement the telescope results are also included (open squares). The statistical error and the combined systematical and efficiency error are given for every data point. Note the different horizontal scale for the two measurements! The solid curves represent the ‘full’ calculations by Arenhövel, the dashed curves are his ‘normal’ results. For the TOF-wall data $\Phi_{pn}^{\text{CM}} = 0^\circ$, for the telescopes $\Phi_{pn}^{\text{CM}} = 180^\circ$.

However, looking in detail at the separate energy transfer bins, there are still some differences. In bins E2 and E4 the model calculations agree with the experimental results, certainly if one keeps in mind that the actual result is the *average* of the two measurements. Thus the slight underestimate by the model of the *jan96* results is compensated by the overestimate for *feb97*. In bin E3 the model exceeds the data in both cases. This is in agreement with Kasdorp's results, whose L02 data points are also overestimated by the corresponding calculations by Arenhövel, see section 5.4.3. In bins E5 and E6 the results seem to be slightly underestimated by the model, although there is still agreement within the errors. This is not unexpected since these bins are far from the quasielastic region and other experiments have also found that the models cannot yet fully describe the data there.

Telescopes

The telescope results seem to support the TOF-wall conclusions, although the uncertainty of these data points is larger. In the first few energy transfer bins the model nicely reproduces the data, whereas in bins E6 through E8 the results seem to be slightly underestimated (but still within the experimental errors). The strong decrease of the telescope data in the last (two) energy transfer bin(s) could be related to the fact that the edge of the energy acceptance of the spectrometer is reached – this possibility has not been investigated further. Or perhaps it is a consequence of the difficult fit of the “breakup proton selection parameter” B_{np} in these bins due to the dominating pion-production tail.

In any case, for high energies all our in-plane experimental results seem to substantiate the important role of subnuclear degrees of freedom: in Figure 5.17 the “normal” values (dashed line) often fail to describe the data, whereas the “full” values (solid line) agree better with the experimental results. It was shown in Figure 2.3 that this difference is predominantly due to the inclusion of the Δ -isobar configuration (IC).

5.5.2 Out-of-plane effects

In Figures 5.18 through 5.22 the out-of-plane behaviour of the data is investigated for energy transfer bins E2 through E6, respectively. In order to eliminate the dominant dependence on the polar angle Θ_{pn}^{CM} , the results are presented in several angular bins. All data points of a certain subset are extrapolated to the central Θ_{pn}^{CM} value of the bin, as discussed in section 5.1.3, and the correction for the electron acceptance is applied (see section 5.1.2). The “full” (N+MEC+IC+REL) and “normal” (N) model calculations are again represented by the solid and dashed lines, respectively.

The observations from the previous section on the overall strength of the model w.r.t. the results are of course reproduced here: on average the model agrees with the data in energy transfer bins E2 and E4, overestimates them in bin E3 and

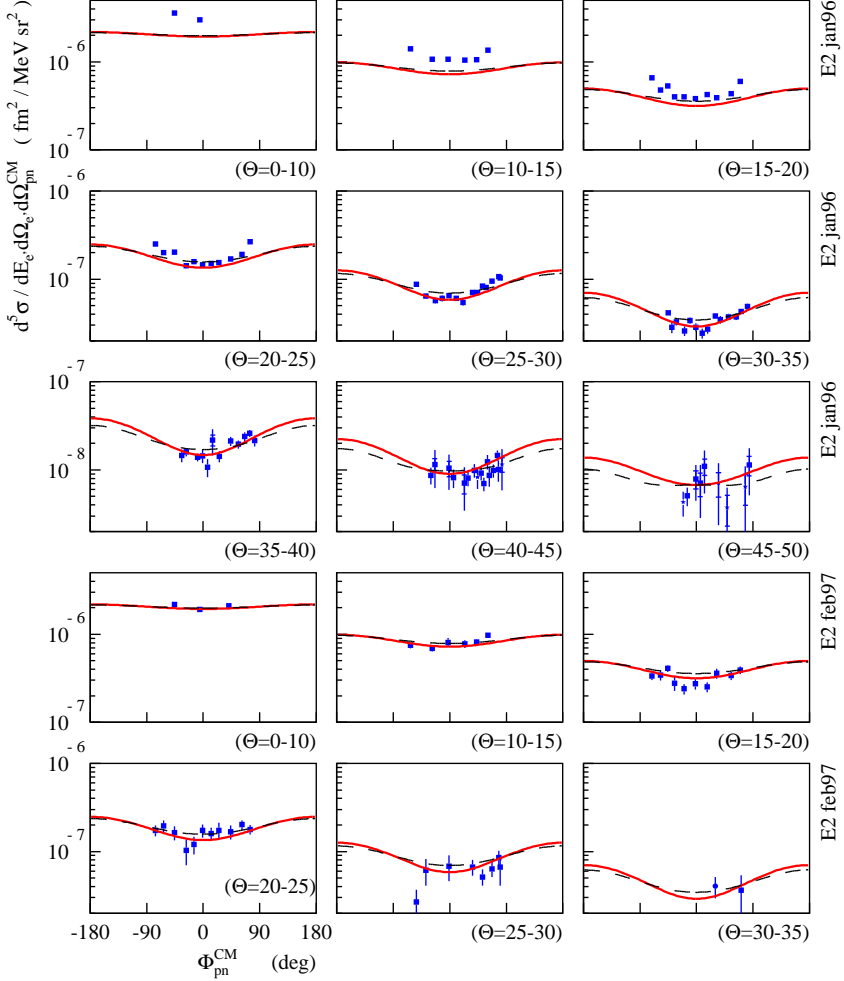


Figure 5.18: Results of the two measurements for energy transfer bin E2 as a function of the azimuthal angle Φ_{pn}^{CM} . The data points are presented in several Θ_{pn}^{CM} -bins and have been extrapolated to the central value of Θ_{pn}^{CM} for the relevant bin. For most data points only the statistical error is shown, as discussed in section 5.2.1. The curves represent model calculations by Arenhövel et al. [Are98] – the meaning is the same as in Figure 5.17. Note the different logarithmic scales.

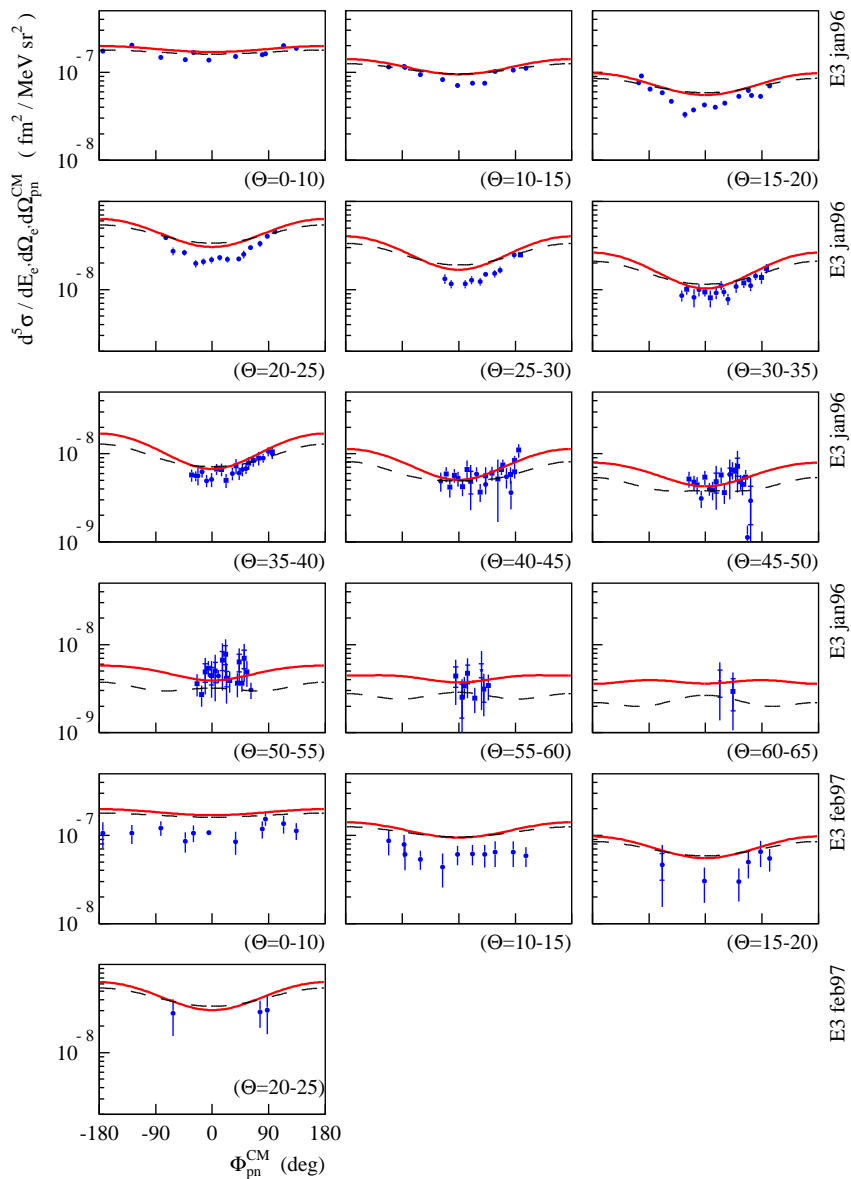


Figure 5.19: Results of the two measurements for energy transfer bin E3 as a function of the azimuthal angle Φ_{pn}^{CM} . See Figure 5.18 for details.

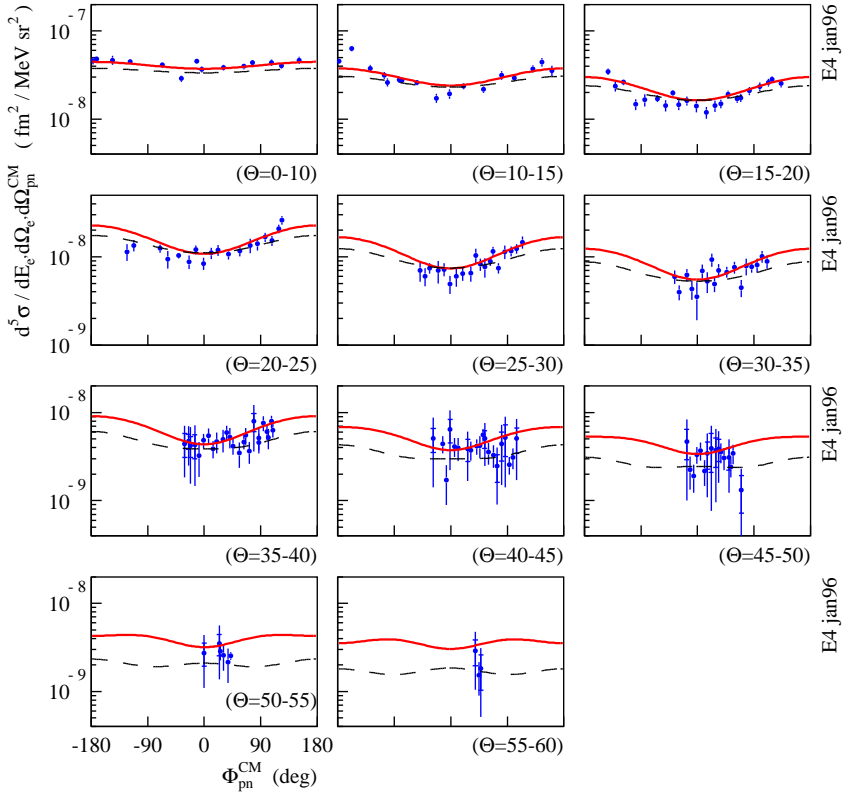


Figure 5.20: Results of the jan96 measurement for energy transfer bin E4 as a function of the azimuthal angle Φ_{pn}^{CM} . There are not enough data points in this energy transfer bin for the feb97 measurement to show a Φ_{pn}^{CM} -dependence. See Figure 5.18 for details.

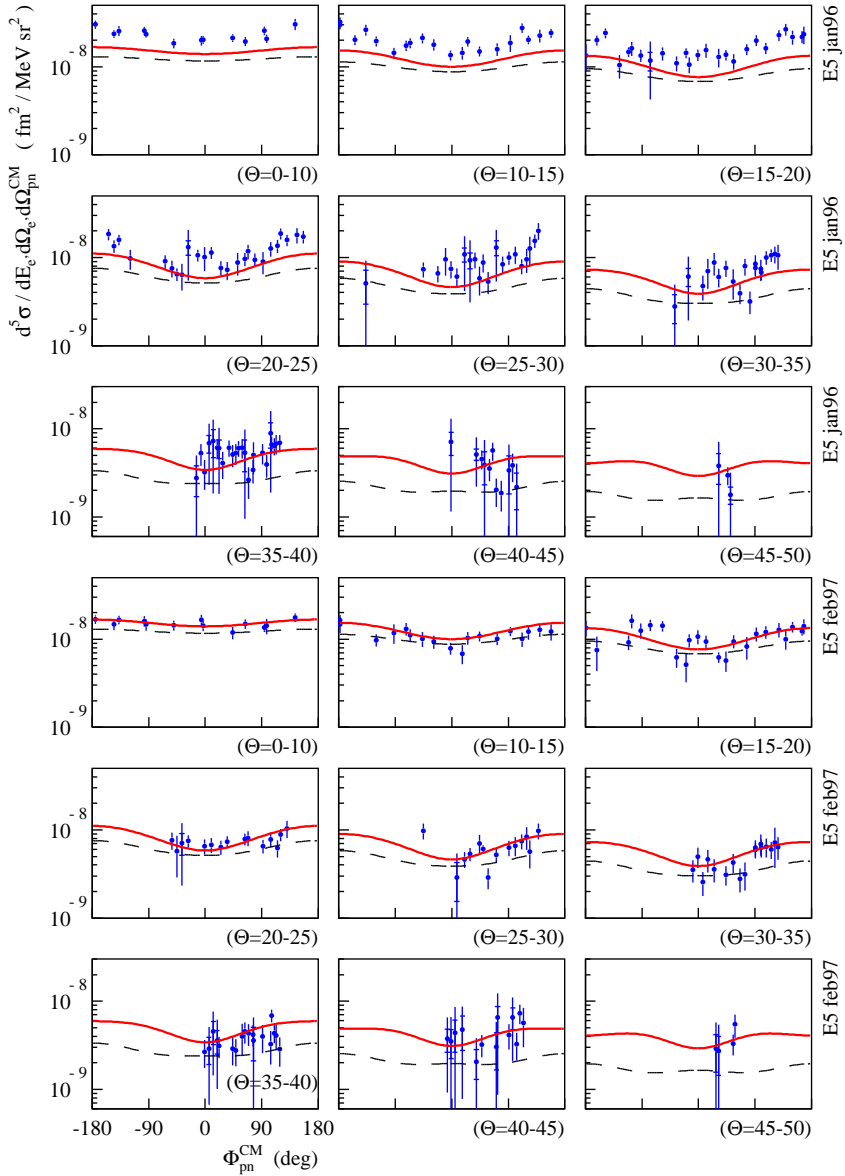


Figure 5.21: Results of the two measurements for energy transfer bin E5 as a function of the azimuthal angle Φ_{pn}^{CM} . See Figure 5.18 for details.

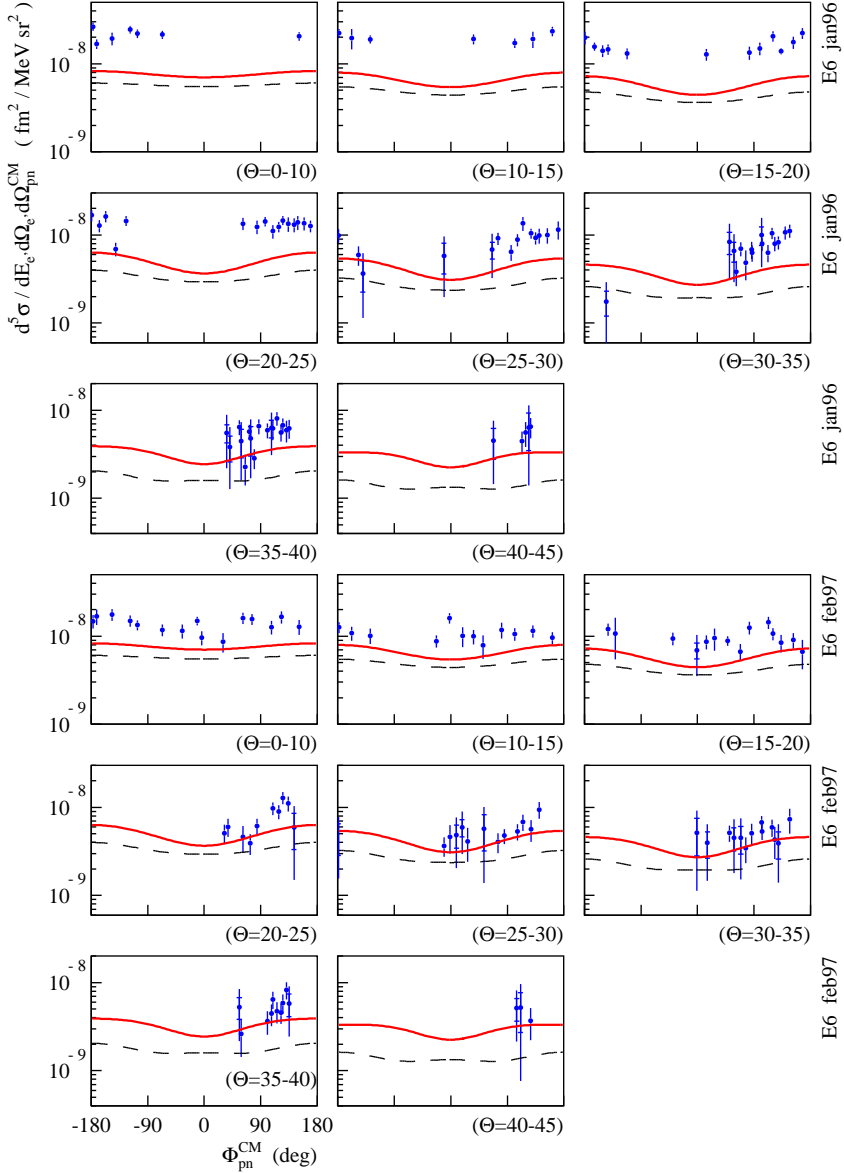


Figure 5.22: Results of the two measurements for energy transfer bin E6 as a function of the azimuthal angle Φ_{pn}^{CM} . See Figure 5.18 for details.

slightly underestimates them in E5 and E6. The expected cosine-like ϕ -dependent behaviour due to the f_{LT} form factor is clearly visible, especially in the first few θ -bins where the error bars are still small. At small energies and (polar) angles the calculations seem to underestimate this effect by up to 50%, but this difference disappears beyond (approximately) $\Theta_{pn}^{\text{CM}} = 30^\circ$. At large angles it is not possible to recognize the additional $\cos 2\phi$ variation because of the experimental errors, and at small angles this effect is expected to be too small to see.

In any case, the model calculations reproduce the shape of out-of-plane effects quite well, when the subnuclear degrees of freedom are taken into account. This is not only true in the direction of the momentum transfer, but over a wide range of proton angles. In order to further illustrate the last point, the experimental results are shown again in Figures 5.23 through 5.26, this time scaled by Arenhövel's "full" calculations. The model values have been determined separately for each segment with the correct angles ($\Theta_{pn}^{\text{CM}}, \Phi_{pn}^{\text{CM}}$) and integrated over the electron acceptance (see section 5.1.2). The *average* results of our two measurements are shown, and the error bars represent the statistical errors. The combined systematic and (average) efficiency errors are indicated on the horizontal axis, as well as the extra *averaging error* due to the unresolved difference between the two measurements (see section 5.4.7). There are no average results for energy transfer bin E4, because there are hardly any *feb97* data points for those energies.

From the observation that the ratio of the data and the "full" model is nearly constant (though not unity) over a very large angular range, we conclude that the difference between the model calculations and the experimental results is most likely due to some general factor and is not due to the details of the individual segments. However, the differences between the four energy transfer bins indicate that it is not just one constant global factor, but the result of an energy dependent effect.

On the experimental side, one might again consider a possible shift in the scattered electron energy determined in the spectrometer, see section 5.4.5. The result of such a shift could be that some of the reaction strength is moved from one energy transfer bin into another, depending on the relative average cross section in the two bins and thus depending on the energy.

On the theoretical side it is more difficult to imagine such a simple general factor, which should probably manifest itself predominantly in the f_L and f_T form factors since these govern the overall strength of the reaction.

5.6 Form factors

In order to extract form factors from the experimental results, the following function has been fitted to the experimental results:

$$f(\phi) = A + B \cos \phi \quad (5.4)$$

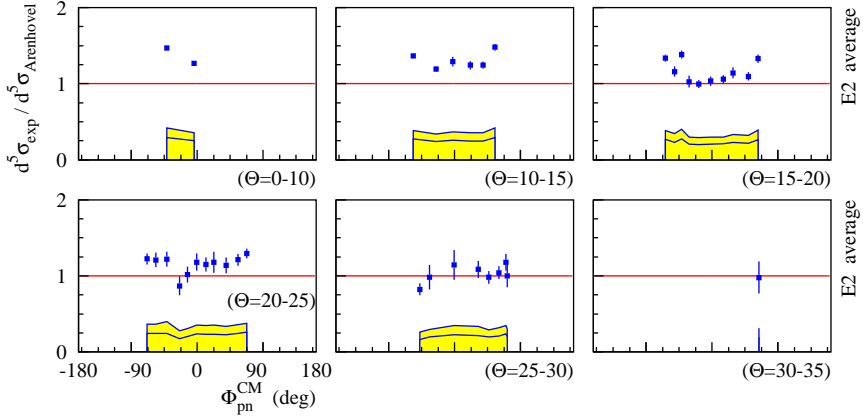


Figure 5.23: Average results of the two measurements for energy transfer bin E2 as a function of the azimuthal angle Φ_{pn}^{CM} . The experimental data have been divided by the “full” ($N+MEC+IC+REL$) model calculations by Arenhövel et al. [Are98] and are distributed over several Θ_{pn}^{CM} -bins. The error bars represent the statistical error; the combined systematical and efficiency error (top) and the extra averaging error of 20% (bottom) are given on the horizontal axis. All plots have the same linear scale.

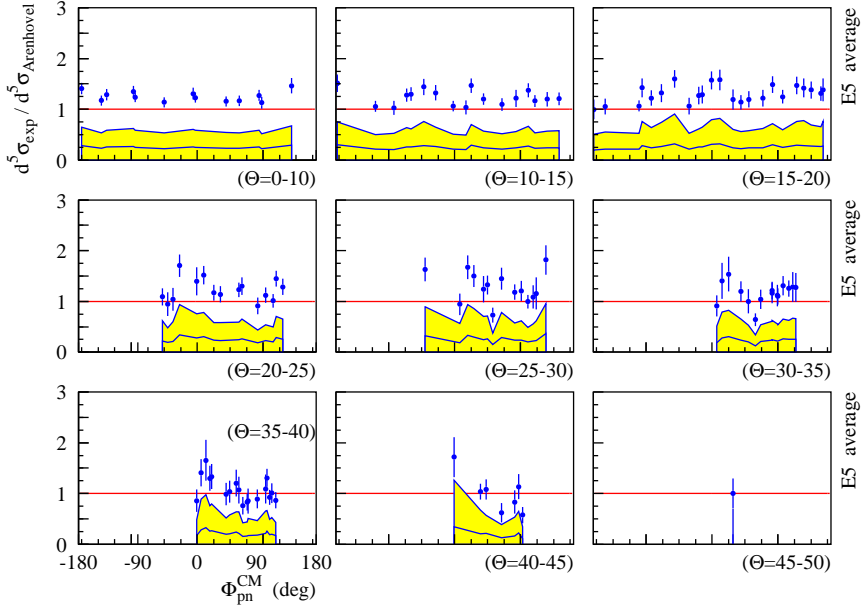


Figure 5.24: Average results of the two measurements divided by the “full” model calculations for energy transfer bin E5. See Figure 5.23 for details.

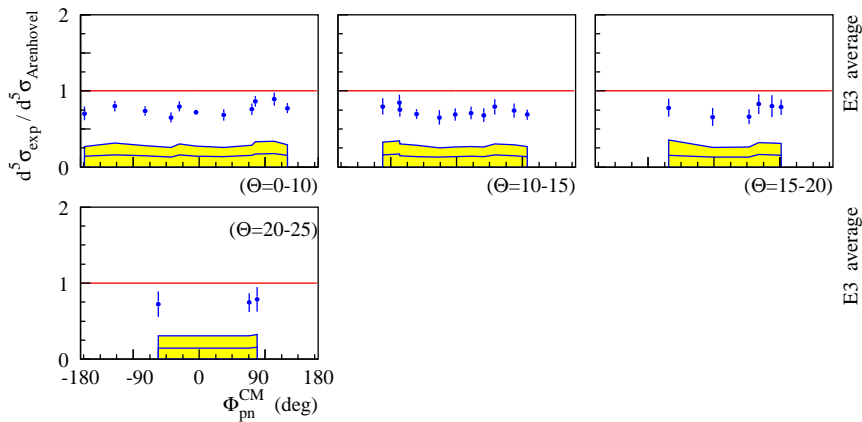


Figure 5.25: Average results of the two measurements divided by the ‘full’ model calculations for energy transfer bin E3. See Figure 5.23 for details.

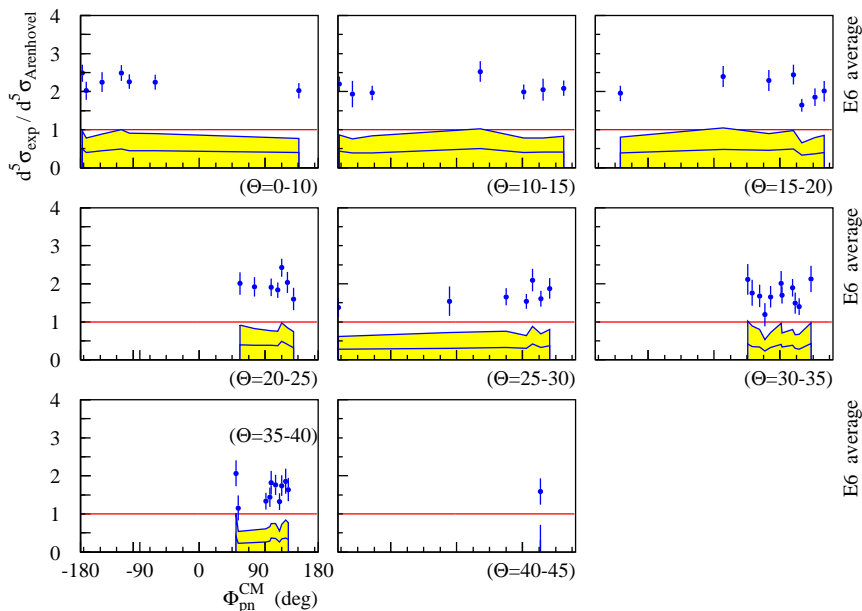


Figure 5.26: Average results of the two measurements divided by the ‘full’ model calculations for energy transfer bin E6. See Figure 5.23 for details.

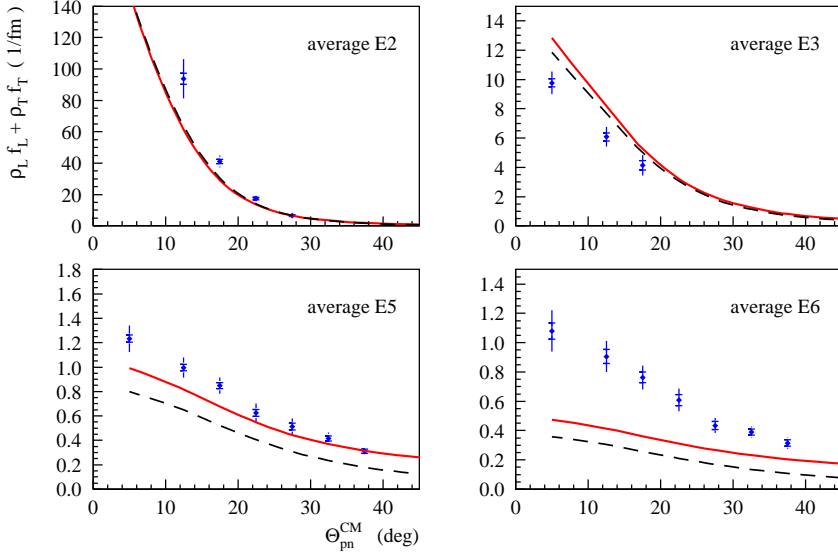


Figure 5.27: The combination of the two non-interference form factors, $\rho_L f_L + \rho_T f_T$, as a function of the polar angle of the proton for four energy transfer bins. The statistical error and the combined efficiency and systematical error are shown. The extra averaging error $\delta\sigma_{\text{avg}}$ has not been taken into account in the fit. The solid curves represent the ‘full’ model calculations by Arenhövel *et al.* [Are98], the dashed curves are his ‘normal’ results.

where A and B are the fitting parameters. Spectra like those in Figures 5.18 through 5.22 have been used, but then for the *average* of the *jan96* and *feb97* data. The $\cos 2\phi$ effect of the second interference form factor, f_{TT} , has been ignored because its influence is expected to be too weak to be observed within the experimental errors. This assumption is justified by the absence of a clear $\cos 2\phi$ dependence in the figures mentioned above.

The constant term A in the fitting function is related to the combination of the two non-interference form factors, $\rho_L f_L + \rho_T f_T$ (see equation 2.19). The fitted values for the *average* experimental results are shown in Figure 5.27 for the four energy transfer bins, in which there are enough data points in both measurements to investigate the ϕ -dependence of the average. The total error of the contributing data points is taken into account in the fit. The solid and dashed lines indicate the ‘full’ (N+MEC+IC+REL) and ‘normal’ (N) model calculations by Arenhövel *et al.* [Are98], respectively. The general features of the data are reproduced by the model, but in a more detailed view the differences mentioned in section 5.5.1 are again clear: the model calculations slightly overestimate the experimental results in bin E3 and yield too little strength in bins E5 and E6. Finally, in bin E2 the

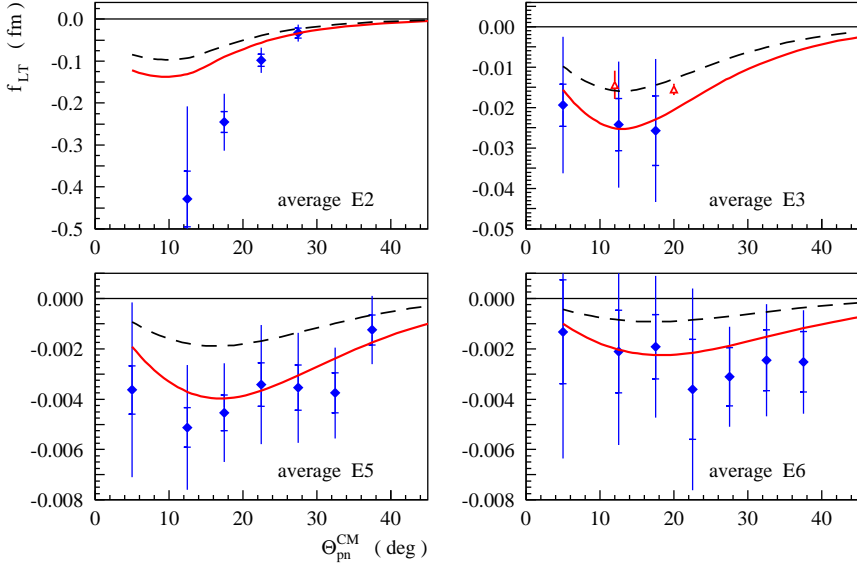


Figure 5.28: The f_{LT} form factor as a function of the polar angle of the proton for four energy transfer bins. The statistical error and the combined efficiency and systematical error are shown. The solid curves represent the ‘full’ model calculations by Arenhövel et al. [Are98], the dashed curves are his ‘normal’ results. The two triangles represent the L02 results from Kasdorp [Kas97].

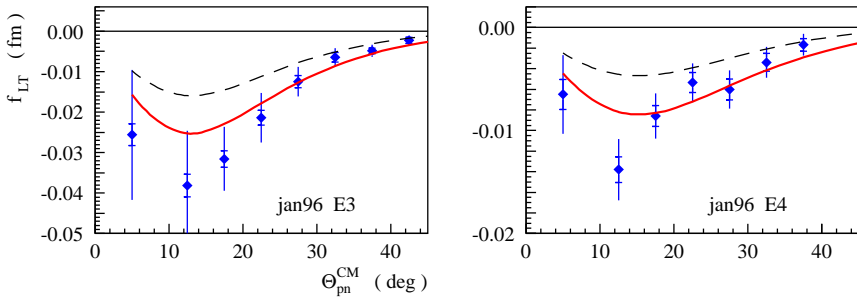


Figure 5.29: The f_{LT} form factor, extracted from the jan96 results only, for two energy transfer bins. The statistical error and the combined efficiency and systematical error are shown. The solid curves represent the ‘full’ model calculations by Arenhövel et al. [Are98], the dashed curves are his ‘normal’ results.

model is in agreement with the data, except at the smallest proton angles.

The strength B of the $\cos\phi$ term is directly proportional to the interference form factor f_{LT} . The values obtained in the fits are shown in Figure 5.28 for the same four energy transfer bins. The “full” (N+MEC+IC+REL) and “normal” (N) model calculations by Arenhövel are again represented by the solid and dashed lines, respectively. The two triangles represent f_{LT} results from the L02 kinematics of Kasdorp [Kas97] (see section 5.4.3), which are given as a comparison. The two results are in complete agreement within the experimental errors.

If we ignore energy transfer bin E2 for a moment, it is clear that the strength of the f_{LT} form factor is calculated in the “full” model is in agreement with the data. The difference between the “full” and “normal” calculations indicates the importance of the subnuclear degrees of freedom for this form factor. It was shown in Figure 2.4 that both the Δ -isobar configuration (IC) and the relativistic corrections (RC) play a role here.

In bin E2 there is a significant difference between the model calculations and the data, even when the total experimental error is taken into account. This is related to the unexpectedly high values we found for the cross section at small proton angles in the *jan96* measurement (see section 5.4.4 and Figure 5.15). There the difference between the two measurements is so large that this effect is still visible in the *average* results used to determine the form factors.

Since there are only a few *average* results in energy transfer bins E3 and E4, the f_{LT} form factor has also been extracted separately from the *jan96* data for these two bins, see Figure 5.29. Again, the total error of the data points has been taken into account. Comparison with the model calculations leads to the same conclusion for these two energy transfer bins as for bins E5 and E6.

5.7 Conclusions and outlook

We have obtained a large amount of data for energy transfers up to 400 MeV over a wide angular range, and some in-plane data points for energy transfers up to 600 MeV. Figure 5.30 illustrates the kinematics of our experimental results in the (E_{np}, Q^2) and $(\Theta_{pn}^{\text{CM}}, \Phi_{pn}^{\text{CM}})$ planes. These figures can be compared to Figures 1.1 and 1.2, which contain the same information for previous ${}^2H(e, e'p)n$ experiments. In the energy domain our results fill up the gap between the two data sets by Blomqvist *et al.* More importantly, we have extended the available data into a hitherto basically unmeasured out-of-plane region at energies well beyond the quasielastic values. In addition, our telescope results extend up to $\Theta_{pn}^{\text{CM}} = 145^\circ$, which corresponds to high missing momenta (up to $p_m = 1000$ MeV/c) and thus represents the short-range part of the NN-interaction. The clearly visible variation of the cross section with the azimuthal angle Φ_{pn}^{CM} has enabled us to extract values for the interference form factor f_{LT} and for a combination of the non-interference form factors f_L and f_T at these energies for proton (CM) angles up to 40° .

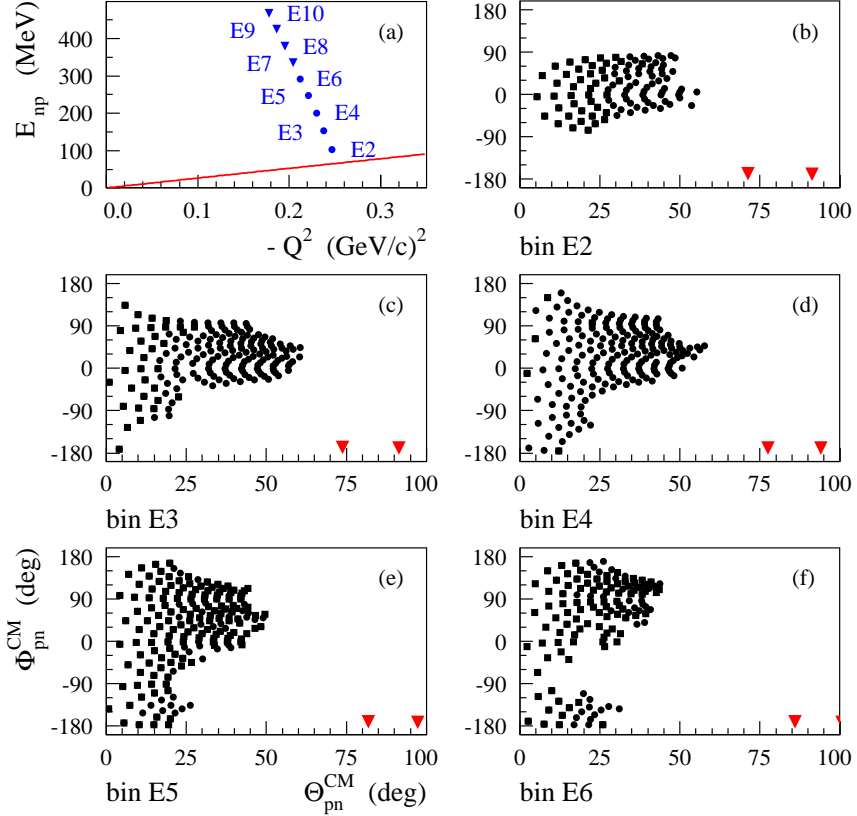


Figure 5.30: Kinematics of the current experiment: (a) The location of our energy transfer bins in the (E_{np}, Q^2) plane. The line corresponds to quasielastic kinematics. (b)–(f) The final data points in the $(\Theta_{pn}^{\text{CM}}, \Phi_{pn}^{\text{CM}})$ plane, separately for each energy transfer bin. The triangles represent the telescopes. Only the first two are shown; the other three telescopes are at even larger angles.

The *shape* of the cross section and of the extracted form factors is nicely reproduced by the “full” model calculations by Arenhövel *et al.* in the major part of the kinematical range, but some difference remains for the actual *strength*, especially in the higher energy transfer bins. This discrepancy indicates that the treatment of the subnuclear degrees of freedom in the model can still be improved.

The following suggestions can be made for future $^2H(e, e'p)n$ experiments:

- A separate efficiency measurement is necessary to improve the correction for proton losses in the complex proton identification and especially in the

separation of protons from the pion-production tail. An independent check of the absolute scale is also helpful – perhaps through a (nearly) simultaneous elastic measurement, cf. Kasdorp [Kas97] or Böhm [Böh01].

- To improve and/or check the electron part of the analysis, the response of the ELAN spectrometer along its focal plane should be investigated in detail. Some work on this subject is underway in Bonn [Ban99].
- On the proton side, one could use the “cone” formed by the simultaneously measured pion-production data to precisely determine the (average) direction of the momentum transfer, see e.g. Wacker [Wac98]. In our analysis the energy transfer bins are so wide that this direction varies too much within one bin to make this procedure feasible.
- If possible, one should try to eliminate – or reduce the influence of – the alinear transformation from energy deposit to proton kinetic energy in the analysis, since we suspect that part of the strong drop in proton efficiency we encountered is related to this alinearity. This would probably also improve the resolution of the “breakup” selection parameter, thereby allowing a better separation of actual ${}^2H(e, e' p)n$ protons from pion-production events.
- The major problem for the individual telescopes was the high background rate. To overcome this, more shielding is needed, perhaps not only in front of the detectors as in our setup, but on all sides (cf. the UTOF detector, which has operated very successfully in the ELAN area [Bru95b]).
- Higher beam intensities – at a different accelerator facility – and thus better statistics are of course helpful, especially at high energy transfers, as long as the background rates are kept under control. Better statistics would allow a smaller binning in the energy transfer, thereby reducing corrections due to the electron acceptance.
- By using polarization observables (e.g. asymmetries) to determine the interference form factors the measurement of the actual cross section is not always required, thereby eliminating the need for an absolute normalization of the data.

Although the setup used for our experiments is no longer available at the ELSA accelerator facility, the need for comparable measurements remains. A comprehensive experimental data set covering a large kinematical range represents the ultimate check of the theoretical models, hopefully one day including fully covariant versions. The main issue remains the description of the subnuclear degrees of freedom, isobar configurations and meson exchange currents, which are accessible through high proton energies and momenta and/or out-of-plane observables.

More precise measurements should be possible at electron accelerator facili-

ties like TJNAF or MAMI, where the luminosity is much higher than at ELSA and where more elaborate spectrometer systems are available. However, in order to make use of these advantages and improve on our accuracy, the proton solid angle measured simultaneously will probably have to be smaller. If it is feasible, however, it would be rewarding to reduce only the *energy* range, while still accepting as much of the proton *angular* range as possible, as we have done in the current experiment. In this respect the Out-Of-Plane Spectrometers (OOPS) at Bates could be an option, since they combine high accuracy and high luminosity with the possibility to sample several parts of the proton solid angle simultaneously.

Chapter 6

Summary

Scattering experiments on the deuteron are a useful tool to investigate the strong interaction between nucleons. Beyond the so-called quasielastic region, effects related to the subnuclear degrees of freedom of the deuteron become important, as has been established in several recent experiments.

The aim of the ${}^2\text{H}(e, e'p)n$ experiment described in this thesis is to measure the cross section over a large energy range and to add to the existing in-plane results by simultaneously covering a large out-of-plane solid angle. In this way we have obtained a broad experimental data set as a reference for model calculations and as a guide to identify interesting regions for future, more detailed, experiments.

The experiment was performed at the ELSA electron accelerator facility in Bonn, Germany, with a beam energy $E_0 = 1.600$ GeV and at four-momentum transfers around $Q^2 = -0.20$ (GeV/c) 2 . The scattered electrons were detected in the ELAN magnetic spectrometer; for the protons two segmented 3×3 m 2 scintillator “time-of-flight(TOF)-Walls” were used, together with several 1 m long scintillator “telescopes” at large proton angles.

The results are divided into ten energy transfer bins with a width of 50 MeV. Protons are identified by coincidences between two scintillator bars. At higher energy transfers, other reaction channels, in which an additional pion is created, start to dominate the proton countrate. Using a “breakup selection parameter”, which includes all the TDC and ADC information of an event and the kinematics of the ${}^2\text{H}(e, e'p)n$ reaction, the relevant “breakup” protons are separated from a tail of protons originating in a ${}^2\text{H}(e, e'N)N\pi$ reaction. Essentially, this is equivalent to a separation based on the missing mass, but it involves less non-linear transformations of the experimental values.

The correction for protons not detected in the apparatus and/or not identified as such in the analysis, has been determined from the experimental data set itself, because the separate efficiency measurement envisaged beforehand – involving the detection of the corresponding neutron in the telescopes – was not possible due to

the strong background in the detectors concerned. Consequently, this correction suffers from the low statistics in the higher energy transfer bins, so that the experimental error is dominated by the uncertainty in the efficiency. Results for which the calculated efficiency is very low or very uncertain have been ignored. In the end, we have TOF-wall results in five energy transfer bins, corresponding to energy transfers from 150 MeV to 400 MeV in the laboratory reference frame, i.e. from the quasielastic region to just below the Δ -resonance. For the telescopes the proton detection efficiency has been estimated, based on the background rates observed in the spectra, so that we have obtained results for all energy transfer bins, i.e. for energy transfers up to 600 MeV.

Although much effort has been invested in trying to explain the differences, a discrepancy remains between the two measurements we performed in consecutive years, where the second set of results is on average a factor 0.6 lower than the first. Since it is not possible to clearly mark one of the data sets as incorrect, the final result of our experiment is the average of the two data sets with a corresponding increase of the systematical error by 20%.

The final experimental cross section data set covers a considerable part of the out-of-plane region. For proton polar angles below $\Theta_{pn}^{\text{CM}} = 20^\circ\text{--}30^\circ$ nearly the full azimuthal angular range is sampled and for angles up to $\Theta_{pn}^{\text{CM}} = 50^\circ\text{--}60^\circ$ approximately half this range. In addition, with the telescopes we have measured the in-plane cross section at angles extending up to $\Theta_{pn}^{\text{CM}} = 145^\circ$, or $p_m = 1000$ MeV/c.

The clearly visible variation of the cross section with the azimuthal angle Φ_{pn}^{CM} has enabled us to extract values for the interference form factor f_{LT} and for a combination of the non-interference form factors f_L and f_T at proton (center-of-momentum) angles up to 40° .

The experimental results have been compared to the “full” model calculations by Arenhövel *et al.* For the major part of our kinematical range the *shape* of the cross section and of the form factors is reproduced by the model, but some differences remain in the *normalization* of the results, especially at higher energy transfers. This discrepancy indicates that the description of the subnuclear degrees of freedom in the model can still be improved. Thus our results corroborate the conclusions from other recent experiments concerning the importance of the subnuclear degrees of freedom for kinematics beyond the quasielastic region.

Future ${}^2\text{H}(e, e'p)n$ experiments at facilities like TJNAF or MAMI probably cannot simultaneously cover such a large kinematical range as we have in our experiment, but the increase in accuracy due to a higher luminosity and more accurate spectrometers will outweigh this disadvantage. Still, it would be rewarding to try to simultaneously span as much as possible of the out-of-plane angle in order to obtain a broad overview, for example using the OOPS detectors at Bates.

References

- [Are82] H. Arenhövel, Nucl.Phys. **A384** (1982) 287.
- [Are88] H. Arenhövel, W. Leidemann, E.L. Tomusiak, Z.Phys. **A331** (1988) 123.
- [Are92] H. Arenhövel, W. Leidemann, E.L. Tomusiak, Phys.Rev. **C46** (1992) 455.
- [Are93] H. Arenhövel, W. Leidemann, E.L. Tomusiak, Few-Body Systems **15** (1993) 109.
- [Are98] H. Arenhövel, *private communication* (1998, 1999).
- [Ban96] B. Bantes, Diplomarbeit, Universität Bonn, BONN-IB-96-18 (1996).
- [Ban98a] B. Bantes, *private communication* (1998).
- [Ban98b] B. Bantes, *private communication* (1998).
- [Ban99] B. Bantes, *private communication* (1999).
- [Ban03] B. Bantes, Ph.D. thesis, Universität Bonn, *expected* (2003).
- [Bec92] G. Beck, H. Arenhövel, Few-Body Systems **13** (1992) 165.
- [Ber81] M. Bernheim *et al.*, Phys.Rev.Lett. **46** (1981) 402.
- [Blo98] K.I. Blomqvist *et al.*, Phys.Lett. **B424** (1998) 33.
- [Bod90] B. Boden, Ph.D. thesis, Universität Bonn, BONN-IR-90-57 (1990).
- [Böh01] R. Böhm, Ph.D. thesis, Universität Mainz (2001).
- [BDr71] E. Borie, D. Drechsel, Nucl.Phys. **A167** (1971) 369.
- [Bre86] H. Breuker *et al.*, Nucl.Phys. **A455** (1986) 641.
- [Bru95a] E.E.W. Bruins, Ph.D. thesis, Utrecht University (1995).

- [Bru95b] E.E.W. Bruins *et al.*, Phys.Rev.Lett. **75** (1995) 21.
- [Bru01] H. Brunhöber, Ph.D. thesis, Universität Bonn, BONN-IR-2001-15 (2001).
- [Bul95] H.J. Bulten *et al.*, Phys.Rev.Lett. **74** (1995) 4775.
- [Don94] T.W. Donnelly, in: “Perspectives in the Structure of Hadronic Systems”, NATO ASI Series, Series B: Physics Vol. 333 (Plenum Press, 1994) 37-68.
- [Duc94] J.E. Ducret *et al.*, Phys.Rev. **C49** (1994) 1783.
- [Fab79] W. Fabian, H. Arenhövel, Nucl.Phys. **A314** (1979) 253.
- [Fro93] F. Frommberger, Ph.D. thesis, Universität Bonn, BONN-IR-93-63 (1993).
- [Fro94] F. Frommberger *et al.*, Phys.Lett. **B339** (1994) 17.
- [GEA93] “GEANT: Detector Description and Simulation Tool”, CERN Program Library W5013 (1993).
- [Got95] R. Gothe, *private communication* (1995).
- [Got98] R. Gothe, Habilitation thesis, Universität Bonn (1998).
- [Hai00] H. Hainer, Ph.D. thesis, Universität Bonn (2000).
- [Hal84] F. Halzen, A.D. Martin, “Quarks and Leptons” (John Wiley & Sons, 1984).
- [Ham89] R. Hamers, Ph.D. thesis, Vrije Universiteit Amsterdam (1989).
- [Hum94] E. Hummel, J.A. Tjon, Phys.Rev. **C49** (1994) 21.
- [Jak96] D. Jakob, Ph.D. thesis, Universität Bonn, BONN-IR-96-07 (1996).
- [Joo93] F.C.P. Joosse, Ph.D. thesis, Utrecht University (1993).
- [Jor96] D. Jordan *et al.*, Phys.Rev.Lett. **76** (1996) 1579.
- [Kas97] W.-J. Kasdorp, Ph.D. thesis, Utrecht University (1997).
- [Lan00] J. Langheinrich, Ph.D. thesis, Universität Münster (2000).
- [Lei87] W. Leidemann, H. Arenhövel, Nucl.Phys. **A465** (1987) 573.
- [Lei91] W. Leidemann, E.L. Tomusiak, H. Arenhövel, Phys.Rev. **C43** (1992) 1022.

- [Leo92] W.R. Leo, "Techniques for Nuclear and Particle Physics Experiments" (Springer Verlag, 1992).
- [Mas96] P. Maschke, Diplomarbeit, Universität Bonn, BONN-IB-96-17 (1996).
- [Mas01] P. Maschke, Ph.D. thesis, Universität Bonn, BONN-IR-2001-08 (2001).
- [MTs69] L.W. Mo, Y.S. Tsai, *Rev.Mod.Phys.* **41** (1969) 205.
- [NgP69] H. Nguyen-Ngoc, J.P. Perez-y-Jorba, *Phys.Rev.* **136** (1964) B1036.
- [Noe92] A. Noël, Diplomarbeit, Universität Bonn, BONN-IR-78-15 (1992).
- [Pap87] Z. Papandreou, TENERGY code, *unpublished* (1987).
- [Pel96] A. Pellegrino, Ph.D. thesis, Vrije Universiteit Amsterdam (1996).
- [Pel97] A. Pellegrino *et al.*, *Phys.Rev.Lett.* **78** (1997) 4011.
- [Rei93] H. Reike, Ph.D. thesis, Universität Bonn, BONN-IR-93-72 (1993).
- [PDG96] Particle Data Group, Review of Particle Physics, *Phys.Rev.* **D54** (1996) 1.
- [Rit74] K. Rith, Ph.D. thesis, Universität Bonn, PIB-1-239 (1974).
- [Sch91] M. van der Schaar *et al.*, *Phys.Rev.Lett.* **66** (1991) 2855.
- [Ste92] G. van der Steenhoven, *Few-Body Systems Suppl.* **5** (1992) 17.
- [Tam87] T. Tamae *et al.*, *Phys.Rev.Lett.* **59** (1987) 2919.
- [Tur84] S. Turck-Chieze *et al.*, *Phys.Lett.* **B142** (1984) 145.
- [Vis94] J.L. Visschers, Proceedings of MC93: International Conference on Monte Carlo Simulation in High Energy and Nuclear Physics, Tallahassee, Feb. 22-26 1993 (World Scientific Publishing Co., Singapore, 1994) 350.
- [Vri84] C. de Vries *et al.*, *Nucl.Instr.Meth.* **A223** (1984) 1.
- [Wac96] D. Wacker, *private communication* (1996).
- [Wac98] D. Wacker, Ph.D. thesis, Universität Bonn, BONN-IR-98-11 (1998).
- [Wil93] T. Wilbois, G. Beck, H. Arenhövel, *Few-Body Systems* **15** (1993) 39.
- [Wil88] P. Wilhelm, W. Leidemann, H. Arenhövel, *Few-Body Systems* **3** (1988) 111.
- [Zho01] Z.-L. Zhou *et al.*, *Phys.Rev.Lett.* **87** 172301 (2001).

Appendix – Numerical results

This appendix lists all TOF-wall results shown in Figures 5.23–5.26, a table for each energy transfer bin of the *jan96* and *feb97* measurements. The telescope results shown in Figure 5.9 are listed in a separate table at the end.

<i>bars</i>	Θ_{pn}^{CM}	Φ_{pn}^{CM}	T_{kin}	p_m	$d^5\sigma_{exp}$	$\pm \delta\sigma_{stat}$	$\pm \delta\sigma_{syst}$	$\pm \delta\sigma_{eff}$	η_{23}	
21,42	55.3	5	134	271	0.475E-08	0.147E-08	0.718E-09	0.786E-09	61 ± 13	*
22,41	50.6	12	140	250	0.806E-08	0.179E-08	0.608E-09	0.202E-08	47 ± 14	
22,42	49.9	6	141	247	0.633E-08	0.188E-08	0.490E-09	0.142E-08	50 ± 14	
22,43	49.7	-1	141	246	0.717E-08	0.169E-08	0.540E-09	0.874E-09	66 ± 11	
22,44	50.0	-7	141	248	0.486E-08	0.141E-08	0.739E-09	0.975E-09	62 ± 17	*
22,47	53.7	-24	136	264	0.477E-08	0.168E-08	0.362E-09	0.915E-09	69 ± 17	
23,41	45.2	13	146	226	0.144E-07	0.296E-08	0.108E-08	0.328E-08	42 ± 13	
23,42	44.4	6	147	223	0.709E-08	0.170E-08	0.537E-09	0.827E-09	65 ± 10	
23,43	44.1	-1	147	221	0.929E-08	0.183E-08	0.703E-09	0.147E-08	56 ± 11	
23,45	45.4	-15	146	228	0.657E-08	0.157E-08	0.498E-09	0.618E-09	70 ± 9	
23,46	46.9	-21	144	234	0.496E-08	0.157E-08	0.750E-09	0.445E-09	76 ± 9	*
24,38	45.9	35	145	229	0.898E-08	0.278E-08	0.136E-08	0.187E-08	56 ± 16	*
24,39	43.4	29	148	219	0.810E-08	0.159E-08	0.617E-09	0.492E-09	74 ± 6	
24,40	41.3	23	150	209	0.853E-08	0.209E-08	0.642E-09	0.164E-08	55 ± 15	
24,41	39.7	15	151	202	0.169E-07	0.236E-08	0.128E-08	0.198E-08	63 ± 10	
24,42	38.8	7	152	198	0.928E-08	0.214E-08	0.703E-09	0.100E-08	71 ± 10	
24,43	38.5	-1	152	197	0.127E-07	0.226E-08	0.960E-09	0.698E-09	79 ± 5	
24,44	38.9	-9	152	199	0.118E-07	0.118E-08	0.896E-09	0.383E-09	85 ± 3	
24,45	40.0	-17	151	204	0.158E-07	0.480E-08	0.119E-08	0.273E-08	51 ± 12	
24,46	41.7	-24	149	211	0.135E-07	0.213E-08	0.103E-08	0.310E-08	51 ± 16	
24,47	43.9	-30	147	220	0.825E-08	0.179E-08	0.624E-09	0.760E-09	78 ± 9	
25,36	47.8	49	143	238	0.418E-08	0.160E-08	0.635E-09	0.633E-09	66 ± 11	*
25,37	44.5	44	146	224	0.765E-08	0.201E-08	0.116E-08	0.507E-09	67 ± 8	*
25,38	41.4	39	150	209	0.125E-07	0.214E-08	0.946E-09	0.639E-09	73 ± 5	
25,40	36.2	26	154	186	0.174E-07	0.249E-08	0.132E-08	0.727E-09	74 ± 4	
25,41	34.3	18	156	178	0.204E-07	0.217E-08	0.155E-08	0.718E-09	80 ± 4	
	(deg)		(MeV)		(fm ² /MeVsr ²)				%	

Table A1: Results for energy transfer bin E2 of the *jan96* measurement. Central kinematics: $\omega = 175$ MeV, $\vec{q} = 527$ MeV/c, $Q^2 = -0.25$ (GeV/c)², $\Theta_q = 61^\circ$. The values marked with a star represent stopping values, the others are combined passing and stopping values.

<i>bars</i>	Θ_{pn}^{CM}	Φ_{pn}^{CM}	T_{kin}	p_m	$d^5\sigma_{exp}$	$\pm \delta\sigma_{stat}$	$\pm \delta\sigma_{syst}$	$\pm \delta\sigma_{eff}$	η_{23}
25,42	33.2	9	157	174	0.208E-07	0.263E-08	0.157E-08	0.841E-09	73 ± 4
25,43	32.8	-1	157	172	0.252E-07	0.267E-08	0.190E-08	0.490E-09	88 ± 2
25,44	33.3	-10	157	174	0.288E-07	0.230E-08	0.218E-08	0.729E-09	83 ± 2
25,45	34.6	-19	156	179	0.189E-07	0.235E-08	0.142E-08	0.682E-09	78 ± 3
25,46	36.6	-27	154	188	0.188E-07	0.208E-08	0.142E-08	0.106E-08	77 ± 6
25,47	39.1	-34	152	200	0.131E-07	0.209E-08	0.990E-09	0.728E-09	76 ± 6
26,36	44.2	54	147	222	0.687E-08	0.123E-08	0.522E-09	0.549E-09	77 ± 7
26,37	40.6	50	150	206	0.136E-07	0.237E-08	0.103E-08	0.633E-09	76 ± 4
26,38	37.1	44	154	191	0.254E-07	0.290E-08	0.193E-08	0.103E-08	72 ± 4
26,39	33.9	38	156	176	0.303E-07	0.292E-08	0.229E-08	0.107E-08	74 ± 3
26,40	31.1	30	158	164	0.461E-07	0.337E-08	0.350E-08	0.127E-08	77 ± 3
26,41	29.0	21	160	155	0.428E-07	0.381E-08	0.324E-08	0.910E-09	79 ± 2
26,42	27.6	10	161	148	0.544E-07	0.355E-08	0.412E-08	0.646E-09	89 ± 1
26,43	27.2	-1	161	146	0.612E-07	0.328E-08	0.463E-08	0.849E-09	87 ± 1
26,44	27.8	-12	161	149	0.536E-07	0.442E-08	0.405E-08	0.972E-09	82 ± 2
26,45	29.3	-23	160	157	0.430E-07	0.299E-08	0.326E-08	0.767E-09	87 ± 2
26,46	31.6	-32	158	166	0.372E-07	0.359E-08	0.283E-08	0.107E-08	78 ± 3
26,47	34.5	-39	156	179	0.231E-07	0.323E-08	0.176E-08	0.649E-09	83 ± 3
27,35	44.9	63	146	225	0.817E-08	0.208E-08	0.624E-09	0.442E-09	77 ± 5
27,36	41.0	60	150	208	0.186E-07	0.350E-08	0.142E-08	0.126E-08	69 ± 6
27,37	37.1	56	154	191	0.256E-07	0.266E-08	0.195E-08	0.763E-09	83 ± 3
27,38	33.2	51	157	174	0.399E-07	0.305E-08	0.302E-08	0.105E-08	78 ± 2
27,39	29.6	44	160	157	0.600E-07	0.425E-08	0.455E-08	0.127E-08	80 ± 2
27,40	26.4	36	162	144	0.878E-07	0.441E-08	0.665E-08	0.153E-08	81 ± 1
27,41	23.8	25	163	132	0.119E-06	0.491E-08	0.898E-08	0.141E-08	84 ± 1
27,42	22.1	13	164	125	0.137E-06	0.488E-08	0.103E-07	0.147E-08	86 ± 1
27,43	21.6	-1	165	123	0.138E-06	0.472E-08	0.105E-07	0.135E-08	87 ± 1
27,44	22.3	-15	164	126	0.139E-06	0.556E-08	0.105E-07	0.151E-08	85 ± 1
27,45	24.2	-27	163	134	0.105E-06	0.455E-08	0.793E-08	0.120E-08	87 ± 1
27,46	27.0	-38	161	146	0.745E-07	0.398E-08	0.564E-08	0.104E-08	86 ± 1
27,47	30.3	-45	159	160	0.641E-07	0.417E-08	0.486E-08	0.182E-08	74 ± 3
28,35	42.4	69	149	214	0.133E-07	0.229E-08	0.101E-08	0.121E-08	60 ± 7
28,36	38.2	66	153	196	0.290E-07	0.323E-08	0.222E-08	0.115E-08	77 ± 4
28,37	34.0	63	156	176	0.398E-07	0.351E-08	0.302E-08	0.102E-08	83 ± 3
28,38	29.8	58	159	158	0.764E-07	0.432E-08	0.580E-08	0.136E-08	84 ± 2
28,39	25.8	52	162	141	0.133E-06	0.488E-08	0.101E-07	0.189E-08	84 ± 1
28,40	22.0	44	164	124	0.197E-06	0.619E-08	0.149E-07	0.141E-08	89 ± 0
28,41	18.9	32	166	112	0.289E-06	0.690E-08	0.219E-07	0.185E-08	89 ± 0
28,42	16.7	17	167	104	0.381E-06	0.769E-08	0.288E-07	0.243E-08	89 ± 0
28,43	16.1	-2	167	100	0.364E-06	0.724E-08	0.276E-07	0.204E-08	89 ± 0
28,44	17.0	-20	167	104	0.349E-06	0.734E-08	0.265E-07	0.224E-08	89 ± 0
28,45	19.4	-35	166	114	0.282E-06	0.670E-08	0.214E-07	0.151E-08	92 ± 0
28,46	22.7	-46	164	128	0.216E-06	0.628E-08	0.163E-07	0.207E-08	88 ± 1
28,47	26.5	-53	162	145	0.129E-06	0.560E-08	0.977E-08	0.200E-08	81 ± 1
29,33	48.6	78	142	241	0.743E-08	0.287E-08	0.114E-08	0.119E-08	54 ± 10
29,34	44.6	77	146	224	0.107E-07	0.291E-08	0.816E-09	0.112E-08	61 ± 7
29,35	40.3	76	151	205	0.252E-07	0.348E-08	0.192E-08	0.146E-08	71 ± 5
29,36	36.0	74	155	186	0.442E-07	0.387E-08	0.336E-08	0.175E-08	79 ± 4
29,37	31.6	71	158	166	0.702E-07	0.322E-08	0.534E-08	0.174E-08	78 ± 2
	(deg)		(MeV)		(fm ² /MeVsr ²)				%

*

Table A1: Continued.

<i>bars</i>	Θ_{pn}^{CM}	Φ_{pn}^{CM}	T_{kin}	p_m	$d^5\sigma_{\text{exp}}$	$\pm \delta\sigma_{\text{stat}}$	$\pm \delta\sigma_{\text{syst}}$	$\pm \delta\sigma_{\text{eff}}$	η_{23}
29,38	27.1	67	161	146	0.149E-06	0.451E-08	0.113E-07	0.215E-08	84 ± 1
29,39	22.7	62	164	128	0.250E-06	0.655E-08	0.190E-07	0.178E-08	89 ± 0
29,40	18.4	55	166	110	0.434E-06	0.842E-08	0.329E-07	0.207E-08	89 ± 0
29,41	14.5	43	168	95	0.726E-06	0.106E-07	0.549E-07	0.286E-08	90 ± 0
29,42	11.6	24	169	85	0.907E-06	0.117E-07	0.688E-07	0.353E-08	91 ± 0
29,43	10.7	-3	169	82	0.987E-06	0.127E-07	0.748E-07	0.315E-08	90 ± 0
29,44	12.1	-28	169	87	0.894E-06	0.118E-07	0.678E-07	0.274E-08	92 ± 0
29,45	15.2	-46	168	98	0.720E-06	0.105E-07	0.545E-07	0.338E-08	90 ± 0
29,46	19.2	-57	166	113	0.439E-06	0.832E-08	0.333E-07	0.242E-08	90 ± 0
29,47	23.5	-63	164	131	0.237E-06	0.619E-08	0.179E-07	0.207E-08	89 ± 1
30,33	47.2	84	144	236	0.152E-07	0.382E-08	0.118E-08	0.335E-08	41 ± 10
30,34	43.1	83	148	217	0.150E-07	0.281E-08	0.231E-08	0.224E-08	54 ± 8 *
30,35	38.8	82	152	198	0.258E-07	0.368E-08	0.198E-08	0.156E-08	66 ± 5
30,36	34.4	81	156	178	0.548E-07	0.458E-08	0.418E-08	0.199E-08	71 ± 3
30,37	29.9	80	159	158	0.117E-06	0.555E-08	0.888E-08	0.240E-08	75 ± 2
30,38	25.2	78	163	138	0.240E-06	0.713E-08	0.182E-07	0.273E-08	81 ± 1
30,39	20.5	75	165	118	0.541E-06	0.100E-07	0.410E-07	0.429E-08	80 ± 0
30,40	15.7	70	167	99	0.976E-06	0.130E-07	0.740E-07	0.497E-08	83 ± 0
30,41	11.1	61	169	84	0.160E-05	0.159E-07	0.121E-06	0.526E-08	86 ± 0
30,43	5.4	-5	170	68	0.220E-05	0.185E-07	0.166E-06	0.524E-08	89 ± 0
30,44	7.8	-46	170	74	0.227E-05	0.197E-07	0.172E-06	0.736E-08	87 ± 0
30,45	12.0	-63	169	86	0.155E-05	0.159E-07	0.117E-06	0.362E-08	90 ± 0
30,46	16.6	-71	167	103	0.984E-06	0.129E-07	0.748E-07	0.486E-08	88 ± 0
30,47	21.4	-76	165	122	0.450E-06	0.884E-08	0.342E-07	0.349E-08	86 ± 0
	(deg)		(MeV)		(fm ² /MeVsr ²)				%

Table A1: Continued.

<i>bars</i>	Θ_{pn}^{CM}	Φ_{pn}^{CM}	T_{kin}	p_m	$d^5\sigma_{\text{exp}}$	$\pm \delta\sigma_{\text{stat}}$	$\pm \delta\sigma_{\text{syst}}$	$\pm \delta\sigma_{\text{eff}}$	η_{23}
18,40	58.1	14	166	332	0.467E-08	0.111E-08	0.381E-09	0.740E-09	64 ± 14 *
18,41	57.3	9	167	330	0.345E-08	0.960E-09	0.280E-09	0.320E-09	80 ± 9 *
18,42	56.9	5	167	327	0.261E-08	0.110E-08	0.212E-09	0.296E-09	77 ± 12 *
18,44	56.9	-5	167	327	0.457E-08	0.118E-08	0.374E-09	0.864E-09	66 ± 17 *
19,38	56.3	25	168	324	0.260E-08	0.824E-09	0.212E-09	0.223E-09	81 ± 9 *
19,39	54.8	21	170	317	0.703E-08	0.172E-08	0.571E-09	0.981E-09	65 ± 12 *
19,40	53.6	16	172	312	0.641E-08	0.156E-08	0.521E-09	0.145E-08	51 ± 16 *
19,41	52.8	10	173	308	0.438E-08	0.740E-09	0.711E-09	0.222E-09	86 ± 7 *
19,42	52.2	5	174	305	0.512E-08	0.134E-08	0.418E-09	0.104E-08	61 ± 16 *
19,43	52.1	-1	174	304	0.462E-08	0.105E-08	0.376E-09	0.634E-09	64 ± 12 *
19,44	52.3	-6	174	306	0.553E-08	0.113E-08	0.450E-09	0.583E-09	76 ± 11 *
19,45	52.9	-11	173	308	0.485E-08	0.115E-08	0.393E-09	0.614E-09	73 ± 13 *
19,46	53.8	-17	172	313	0.257E-08	0.695E-09	0.209E-09	0.212E-09	90 ± 10 *
20,34	60.6	44	162	344	0.314E-08	0.125E-08	0.257E-09	0.497E-09	76 ± 14 *
	(deg)		(MeV)		(fm ² /MeVsr ²)				%

Table A2: Results for energy transfer bin E3 in the jan96 measurement. Central kinematics: $\omega = 225$ MeV, $\vec{q} = 538$ MeV/c, $Q^2 = -0.24$ (GeV/c)², $\Theta_q = 56^\circ$. The values marked with a star represent combined passing and stopping values, the others are passing values.

<i>bars</i>	Θ_{pn}^{CM}	Φ_{pn}^{CM}	T_{kin}	p_m	$d^5\sigma_{exp}$	$\pm \delta\sigma_{stat}$	$\pm \delta\sigma_{syst}$	$\pm \delta\sigma_{eff}$	η_{23}	
20,35	58.3	40	165	334	0.307E-08	0.874E-09	0.251E-09	0.438E-09	81 ± 14	*
20,38	52.1	28	174	305	0.404E-08	0.109E-08	0.329E-09	0.331E-09	78 ± 9	*
20,39	50.4	23	177	298	0.461E-08	0.922E-09	0.373E-09	0.932E-09	63 ± 16	*
20,40	49.0	17	178	291	0.440E-08	0.112E-08	0.357E-09	0.797E-09	61 ± 14	*
20,41	48.0	11	180	287	0.380E-08	0.895E-09	0.308E-09	0.380E-09	76 ± 9	*
20,42	47.4	6	181	284	0.404E-08	0.672E-09	0.656E-09	0.290E-09	81 ± 7	*
20,43	47.2	-1	181	283	0.554E-08	0.101E-08	0.448E-09	0.315E-09	85 ± 6	*
20,44	47.5	-7	181	285	0.313E-08	0.694E-09	0.507E-09	0.186E-09	85 ± 7	*
20,45	48.2	-13	180	288	0.428E-08	0.928E-09	0.347E-09	0.458E-09	82 ± 11	*
20,46	49.3	-18	178	292	0.427E-08	0.807E-09	0.348E-09	0.393E-09	87 ± 9	*
20,47	50.7	-24	176	299	0.397E-08	0.112E-08	0.323E-09	0.296E-09	84 ± 8	*
21,34	57.4	47	167	330	0.350E-08	0.114E-08	0.287E-09	0.206E-09	88 ± 7	*
21,35	54.9	43	170	318	0.572E-08	0.128E-08	0.467E-09	0.726E-09	73 ± 13	*
21,36	52.4	40	174	306	0.370E-08	0.112E-08	0.303E-09	0.207E-09	88 ± 7	*
21,37	50.0	35	177	296	0.384E-08	0.156E-08	0.312E-09	0.205E-09	88 ± 6	*
21,38	47.9	30	180	286	0.360E-08	0.931E-09	0.292E-09	0.405E-09	79 ± 11	*
21,39	45.9	25	183	277	0.645E-08	0.133E-08	0.525E-09	0.374E-09	86 ± 6	*
21,40	44.4	19	185	271	0.422E-08	0.121E-08	0.342E-09	0.687E-09	63 ± 11	*
21,41	43.2	13	186	265	0.627E-08	0.170E-08	0.510E-09	0.573E-09	71 ± 7	*
21,42	42.5	6	187	261	0.420E-08	0.913E-09	0.341E-09	0.186E-09	87 ± 5	*
21,43	42.3	-1	187	260	0.532E-08	0.104E-08	0.431E-09	0.311E-09	83 ± 5	*
21,44	42.6	-7	187	262	0.567E-08	0.980E-09	0.461E-09	0.495E-09	79 ± 8	*
21,45	43.4	-14	186	266	0.389E-08	0.925E-09	0.315E-09	0.105E-09	97 ± 3	*
21,46	44.6	-20	184	271	0.498E-08	0.964E-09	0.405E-09	0.166E-09	94 ± 4	*
21,47	46.3	-26	182	278	0.568E-08	0.115E-08	0.462E-09	0.369E-09	81 ± 6	*
22,34	54.3	51	171	315	0.652E-08	0.155E-08	0.533E-09	0.926E-09	72 ± 14	*
22,35	51.5	47	175	302	0.389E-08	0.756E-09	0.317E-09	0.228E-09	88 ± 7	*
22,36	48.8	43	179	290	0.620E-08	0.138E-08	0.506E-09	0.417E-09	77 ± 7	*
22,37	46.1	39	182	277	0.648E-08	0.116E-08	0.106E-08	0.876E-09	62 ± 11	*
22,38	43.6	34	185	266	0.342E-08	0.800E-09	0.278E-09	0.148E-09	92 ± 4	*
22,39	41.5	28	188	257	0.649E-08	0.119E-08	0.105E-08	0.681E-09	76 ± 10	*
22,40	39.6	22	190	248	0.405E-08	0.753E-09	0.328E-09	0.191E-09	90 ± 4	*
22,41	38.2	15	192	243	0.613E-08	0.977E-09	0.497E-09	0.248E-09	88 ± 4	*
22,42	37.4	7	193	239	0.664E-08	0.910E-09	0.540E-09	0.390E-09	81 ± 5	*
22,43	37.1	-1	193	238	0.517E-08	0.952E-09	0.837E-09	0.257E-09	90 ± 4	*
22,44	37.5	-9	193	240	0.485E-08	0.763E-09	0.786E-09	0.374E-09	80 ± 6	*
22,45	38.5	-16	192	244	0.567E-08	0.831E-09	0.920E-09	0.320E-09	87 ± 5	*
22,46	39.9	-23	190	250	0.443E-08	0.972E-09	0.719E-09	0.153E-09	94 ± 3	*
22,47	41.8	-29	188	259	0.525E-08	0.129E-08	0.854E-09	0.426E-09	73 ± 7	*
23,34	51.3	55	175	302	0.536E-08	0.176E-08	0.437E-09	0.420E-09	78 ± 8	*
23,35	48.3	51	179	287	0.708E-08	0.165E-08	0.577E-09	0.131E-08	57 ± 14	*
23,36	45.2	48	183	274	0.754E-08	0.178E-08	0.612E-09	0.691E-09	70 ± 9	*
23,37	42.3	43	187	260	0.587E-08	0.154E-08	0.477E-09	0.418E-09	82 ± 7	*
23,38	39.5	38	190	248	0.616E-08	0.118E-08	0.501E-09	0.342E-09	86 ± 5	*
23,39	37.0	32	193	237	0.634E-08	0.102E-08	0.103E-08	0.346E-09	82 ± 5	*
23,40	34.9	25	195	228	0.850E-08	0.101E-08	0.138E-08	0.358E-09	86 ± 4	*
23,41	33.2	17	197	222	0.820E-08	0.124E-08	0.133E-08	0.637E-09	72 ± 6	*
23,42	32.2	8	198	217	0.784E-08	0.170E-08	0.634E-09	0.283E-09	89 ± 3	*
23,43	31.9	-1	198	215	0.953E-08	0.114E-08	0.773E-09	0.328E-09	87 ± 3	*
	(deg)		(MeV)		(fm ² /MeVsr ²)				%	

Table A2: Continued.

<i>bars</i>	Θ_{pn}^{CM}	Φ_{pn}^{CM}	T_{kin}	p_m	$d^5\sigma_{exp}$	$\pm \delta\sigma_{stat}$	$\pm \delta\sigma_{syst}$	$\pm \delta\sigma_{eff}$	η_{23}
23,44	32.4	-10	198	217	0.955E-08	0.153E-08	0.154E-08	0.511E-09	80 ± 4
23,45	33.5	-18	197	222	0.717E-08	0.166E-08	0.116E-08	0.211E-09	91 ± 2
23,46	35.2	-26	195	229	0.682E-08	0.911E-09	0.110E-08	0.205E-09	93 ± 3
23,47	37.5	-33	193	240	0.586E-08	0.939E-09	0.476E-09	0.384E-09	82 ± 6 *
24,33	51.9	62	175	304	0.325E-08	0.667E-09	0.533E-09	0.193E-09	83 ± 8
24,34	48.6	59	179	289	0.437E-08	0.111E-08	0.358E-09	0.170E-09	93 ± 5 *
24,35	45.3	56	183	274	0.585E-08	0.114E-08	0.477E-09	0.329E-09	91 ± 6 *
24,36	42.0	53	188	259	0.659E-08	0.119E-08	0.535E-09	0.534E-09	80 ± 8 *
24,37	38.7	48	191	245	0.621E-08	0.973E-09	0.101E-08	0.299E-09	89 ± 5
24,38	35.6	43	195	231	0.740E-08	0.118E-08	0.121E-08	0.499E-09	74 ± 5
24,39	32.7	36	198	219	0.770E-08	0.112E-08	0.125E-08	0.220E-09	90 ± 2
24,40	30.2	29	200	209	0.115E-07	0.127E-08	0.187E-08	0.720E-09	80 ± 5
24,41	28.3	20	202	201	0.116E-07	0.120E-08	0.189E-08	0.408E-09	90 ± 3
24,42	27.0	10	203	196	0.116E-07	0.123E-08	0.188E-08	0.372E-09	90 ± 2
24,44	27.2	-12	202	196	0.114E-07	0.123E-08	0.185E-08	0.220E-09	93 ± 1
24,45	28.6	-22	201	201	0.116E-07	0.145E-08	0.188E-08	0.721E-09	78 ± 4
24,46	30.6	-30	199	209	0.119E-07	0.155E-08	0.970E-09	0.103E-08	72 ± 6 *
24,47	33.2	-38	197	221	0.803E-08	0.116E-08	0.130E-08	0.429E-09	84 ± 4
25,33	49.6	67	178	294	0.103E-08	0.377E-09	0.171E-09	0.159E-09	72 ± 11
25,34	46.1	64	182	277	0.631E-08	0.136E-08	0.514E-09	0.400E-09	82 ± 7 *
25,35	42.6	62	187	262	0.548E-08	0.369E-08	0.447E-09	0.349E-09	77 ± 7 *
25,36	39.0	58	191	246	0.735E-08	0.120E-08	0.599E-09	0.254E-09	89 ± 4 *
25,37	35.4	54	195	230	0.882E-08	0.111E-08	0.143E-08	0.572E-09	78 ± 5
25,38	31.9	49	198	215	0.120E-07	0.184E-08	0.195E-08	0.399E-09	87 ± 2
25,39	28.6	43	201	201	0.139E-07	0.989E-09	0.225E-08	0.359E-09	89 ± 2
25,40	25.7	34	204	191	0.150E-07	0.155E-08	0.243E-08	0.312E-09	91 ± 1
25,41	23.4	24	205	181	0.193E-07	0.162E-08	0.314E-08	0.455E-09	89 ± 2
25,42	21.9	12	206	175	0.228E-07	0.185E-08	0.369E-08	0.492E-09	87 ± 1
25,43	21.4	-1	207	175	0.223E-07	0.191E-08	0.362E-08	0.314E-09	92 ± 1
25,44	22.1	-14	206	176	0.202E-07	0.177E-08	0.326E-08	0.333E-09	90 ± 1
25,45	23.8	-26	205	183	0.167E-07	0.160E-08	0.269E-08	0.292E-09	91 ± 1
26,33	47.6	72	180	284	0.310E-08	0.144E-08	0.507E-09	0.954E-09	44 ± 13
26,34	44.0	70	185	268	0.719E-08	0.112E-08	0.586E-09	0.467E-09	83 ± 7 *
26,35	40.2	68	190	252	0.873E-08	0.111E-08	0.713E-09	0.765E-09	71 ± 7 *
26,36	36.4	65	194	235	0.102E-07	0.154E-08	0.833E-09	0.766E-09	72 ± 5 *
26,37	32.5	61	198	218	0.131E-07	0.155E-08	0.107E-08	0.415E-09	86 ± 3 *
26,38	28.7	57	201	201	0.150E-07	0.142E-08	0.243E-08	0.315E-09	90 ± 1
26,39	24.9	50	204	187	0.207E-07	0.209E-08	0.336E-08	0.453E-09	86 ± 1
26,40	21.5	42	207	175	0.249E-07	0.130E-08	0.404E-08	0.415E-09	89 ± 1
26,41	18.7	31	208	164	0.383E-07	0.220E-08	0.620E-08	0.504E-09	91 ± 1
26,42	16.7	16	209	158	0.394E-07	0.244E-08	0.638E-08	0.427E-09	92 ± 0
26,43	16.1	-2	210	157	0.439E-07	0.246E-08	0.711E-08	0.590E-09	89 ± 1
26,44	17.0	-19	209	159	0.362E-07	0.231E-08	0.587E-08	0.439E-09	90 ± 1
26,45	19.1	-33	208	166	0.273E-07	0.220E-08	0.441E-08	0.393E-09	90 ± 1
26,46	22.1	-44	206	176	0.279E-07	0.213E-08	0.451E-08	0.584E-09	85 ± 1
27,34	42.2	76	187	260	0.623E-08	0.162E-08	0.102E-08	0.535E-09	77 ± 6
27,35	38.3	74	192	244	0.937E-08	0.164E-08	0.766E-09	0.549E-09	77 ± 5 *
27,36	34.3	72	196	226	0.105E-07	0.133E-08	0.171E-08	0.418E-09	85 ± 3
27,37	30.2	69	200	208	0.186E-07	0.152E-08	0.302E-08	0.482E-09	88 ± 2
	(deg)		(MeV)		(fm ² /MeVsr ²)				%

Table A2: Continued.

<i>bars</i>	Θ_{pn}^{CM}	Φ_{pn}^{CM}	T_{kin}	p_m	$d^5\sigma_{exp}$	$\pm \delta\sigma_{stat}$	$\pm \delta\sigma_{syst}$	$\pm \delta\sigma_{eff}$	η_{23}
27,38	26.0	66	203	191	0.223E-07	0.193E-08	0.363E-08	0.489E-09	86 ± 1
27,39	21.9	61	206	175	0.349E-07	0.226E-08	0.566E-08	0.602E-09	87 ± 1
27,40	17.9	53	209	163	0.529E-07	0.266E-08	0.858E-08	0.770E-09	89 ± 1
27,41	14.4	41	211	152	0.624E-07	0.316E-08	0.101E-07	0.615E-09	91 ± 0
27,42	11.8	22	212	146	0.735E-07	0.323E-08	0.119E-07	0.737E-09	89 ± 0
27,43	10.9	-2	212	143	0.730E-07	0.301E-08	0.118E-07	0.463E-09	94 ± 0
27,44	12.2	-26	211	145	0.790E-07	0.348E-08	0.128E-07	0.693E-09	91 ± 0
27,45	15.0	-43	210	153	0.608E-07	0.282E-08	0.986E-08	0.593E-09	92 ± 0
27,46	18.6	-54	208	164	0.439E-07	0.228E-08	0.711E-08	0.469E-09	93 ± 0
27,47	22.6	-62	206	179	0.297E-07	0.283E-08	0.482E-08	0.702E-09	80 ± 1
28,33	44.8	83	184	272	0.331E-08	0.117E-08	0.540E-09	0.386E-09	73 ± 8
28,34	41.0	82	189	255	0.745E-08	0.160E-08	0.608E-09	0.433E-09	79 ± 5 *
28,35	37.0	81	193	237	0.108E-07	0.126E-08	0.176E-08	0.361E-09	89 ± 2
28,36	32.8	80	197	219	0.160E-07	0.159E-08	0.260E-08	0.454E-09	88 ± 2
28,38	24.1	76	205	184	0.330E-07	0.282E-08	0.536E-08	0.612E-09	86 ± 1
28,39	19.7	73	208	168	0.499E-07	0.309E-08	0.811E-08	0.820E-09	85 ± 1
28,40	15.2	68	210	154	0.812E-07	0.344E-08	0.132E-07	0.909E-09	89 ± 1
28,41	10.9	58	212	143	0.116E-06	0.412E-08	0.189E-07	0.895E-09	90 ± 0
28,42	7.3	37	213	136	0.132E-06	0.414E-08	0.213E-07	0.862E-09	91 ± 0
28,43	5.8	-5	213	134	0.128E-06	0.479E-08	0.207E-07	0.840E-09	91 ± 0
28,44	7.9	-43	213	138	0.119E-06	0.422E-08	0.193E-07	0.913E-09	91 ± 0
28,45	11.7	-61	212	146	0.102E-06	0.375E-08	0.166E-07	0.914E-09	89 ± 0
28,46	16.1	-69	210	157	0.729E-07	0.358E-08	0.118E-07	0.633E-09	92 ± 0
28,47	20.5	-74	207	171	0.542E-07	0.336E-08	0.880E-08	0.975E-09	83 ± 1
29,33	44.0	89	185	268	0.622E-08	0.105E-08	0.512E-09	0.337E-09	82 ± 5 *
29,34	40.1	89	190	251	0.115E-07	0.150E-08	0.941E-09	0.682E-09	77 ± 5 *
29,36	31.9	89	198	215	0.172E-07	0.250E-08	0.140E-08	0.408E-09	89 ± 2 *
29,35	36.1	89	194	234	0.141E-07	0.165E-08	0.229E-08	0.611E-09	83 ± 3
29,37	27.6	88	202	197	0.298E-07	0.273E-08	0.486E-08	0.643E-09	87 ± 1
29,38	23.2	88	205	180	0.453E-07	0.264E-08	0.737E-08	0.775E-09	87 ± 1
29,39	18.6	88	208	164	0.557E-07	0.411E-08	0.904E-08	0.619E-09	90 ± 0
29,40	13.9	87	211	151	0.105E-06	0.410E-08	0.171E-07	0.111E-08	85 ± 0
29,41	9.2	85	212	139	0.139E-06	0.507E-08	0.226E-07	0.107E-08	90 ± 0
29,42	4.4	80	213	132	0.167E-06	0.510E-08	0.272E-07	0.111E-08	90 ± 0
29,43	0.9	-30	214	131	0.189E-06	0.541E-08	0.307E-07	0.126E-08	90 ± 0
29,44	5.3	-82	213	133	0.151E-06	0.506E-08	0.245E-07	0.997E-09	90 ± 0
29,45	10.1	-86	212	141	0.145E-06	0.500E-08	0.234E-07	0.157E-08	83 ± 0
29,46	14.8	-87	210	153	0.108E-06	0.443E-08	0.176E-07	0.826E-09	91 ± 0
29,47	19.5	-88	208	168	0.617E-07	0.368E-08	0.101E-07	0.778E-09	87 ± 1
30,33	43.6	95	186	267	0.113E-07	0.200E-08	0.930E-09	0.958E-09	66 ± 7 *
30,34	39.8	96	190	249	0.963E-08	0.164E-08	0.785E-09	0.363E-09	86 ± 4 *
30,35	35.8	96	194	232	0.138E-07	0.135E-08	0.226E-08	0.513E-09	86 ± 3
30,36	31.7	97	198	215	0.226E-07	0.287E-08	0.184E-08	0.480E-09	87 ± 2 *
30,37	27.5	98	202	197	0.303E-07	0.226E-08	0.247E-08	0.502E-09	88 ± 1 *
30,38	23.2	100	205	180	0.509E-07	0.307E-08	0.829E-08	0.835E-09	85 ± 1
30,39	18.7	102	208	165	0.741E-07	0.374E-08	0.121E-07	0.109E-08	81 ± 1
30,40	14.3	107	211	152	0.110E-06	0.514E-08	0.179E-07	0.132E-08	83 ± 0
30,41	9.9	114	212	140	0.175E-06	0.707E-08	0.285E-07	0.164E-08	85 ± 0
30,42	5.9	134	213	134	0.201E-06	0.622E-08	0.327E-07	0.112E-08	89 ± 0
	(deg)		(MeV)		(fm ² /MeVsr ²)				%

Table A2: Continued.

$bars$	Θ_{pn}^{CM}	Φ_{pn}^{CM}	T_{kin}	p_m	$d^5\sigma_{exp}$	$\pm \delta\sigma_{stat}$	$\pm \delta\sigma_{syst}$	$\pm \delta\sigma_{eff}$	η_{23}
30,43	4.1	-174	213	131	0.200E-06	0.611E-08	0.324E-07	0.134E-08	89 ± 0
30,44	6.6	-128	213	135	0.211E-06	0.675E-08	0.343E-07	0.250E-08	76 ± 0
30,45	10.7	-112	212	143	0.147E-06	0.592E-08	0.239E-07	0.116E-08	88 ± 0
30,46	15.1	-106	210	154	0.108E-06	0.575E-08	0.176E-07	0.112E-08	86 ± 0
30,47	19.6	-102	208	168	0.878E-07	0.408E-08	0.142E-07	0.124E-08	84 ± 1
	(deg)		(MeV)		(fm ² /MeVsr ²)				%

Table A2: Continued.

$bars$	Θ_{pn}^{CM}	Φ_{pn}^{CM}	T_{kin}	p_m	$d^5\sigma_{exp}$	$\pm \delta\sigma_{stat}$	$\pm \delta\sigma_{syst}$	$\pm \delta\sigma_{eff}$	η_{23}
17,38	54.4	24	205	362	0.321E-08	0.868E-09	0.412E-09	0.667E-09	63 ± 13
17,43	50.7	0	211	345	0.296E-08	0.877E-09	0.377E-09	0.526E-09	63 ± 11
18,35	56.2	39	202	370	0.306E-08	0.101E-08	0.392E-09	0.562E-09	69 ± 12
18,37	52.4	31	209	352	0.260E-08	0.860E-09	0.332E-09	0.224E-09	87 ± 7
18,38	50.7	26	211	344	0.309E-08	0.644E-09	0.390E-09	0.173E-09	92 ± 5
18,39	49.2	22	214	338	0.360E-08	0.169E-08	0.456E-09	0.753E-09	61 ± 12
18,40	48.0	16	216	332	0.338E-08	0.116E-08	0.425E-09	0.722E-09	65 ± 13
18,41	47.1	11	217	327	0.223E-08	0.725E-09	0.281E-09	0.161E-09	86 ± 6
18,42	46.6	5	218	325	0.389E-08	0.897E-09	0.492E-09	0.475E-09	78 ± 9
18,43	46.4	-1	218	325	0.353E-08	0.757E-09	0.447E-09	0.319E-09	81 ± 7
18,44	46.6	-6	218	325	0.199E-08	0.695E-09	0.251E-09	0.111E-09	92 ± 5
18,45	47.2	-12	217	328	0.229E-08	0.928E-09	0.292E-09	0.249E-09	77 ± 8
18,46	48.2	-17	215	332	0.451E-08	0.170E-08	0.575E-09	0.127E-08	49 ± 13
19,33	57.7	48	200	378	0.182E-08	0.781E-09	0.235E-09	0.291E-09	68 ± 10
19,34	55.4	45	204	367	0.165E-08	0.680E-09	0.211E-09	0.144E-09	89 ± 7
19,35	53.1	42	208	356	0.249E-08	0.260E-09	0.316E-09	0.309E-09	82 ± 10
19,36	50.9	38	211	346	0.233E-08	0.981E-09	0.296E-09	0.202E-09	87 ± 7
19,37	48.8	34	215	336	0.365E-08	0.104E-08	0.462E-09	0.649E-09	71 ± 12
19,38	46.8	29	217	326	0.391E-08	0.142E-08	0.488E-09	0.101E-08	60 ± 15
19,41	42.7	12	223	307	0.392E-08	0.114E-08	0.495E-09	0.455E-09	72 ± 8
19,42	42.0	6	224	304	0.425E-08	0.105E-08	0.535E-09	0.336E-09	81 ± 6
19,43	41.9	-1	225	304	0.663E-08	0.198E-08	0.840E-09	0.150E-08	53 ± 12
19,44	42.1	-7	224	305	0.175E-08	0.841E-09	0.219E-09	0.175E-09	77 ± 7
19,45	42.8	-13	223	308	0.432E-08	0.955E-09	0.543E-09	0.471E-09	75 ± 8
20,35	50.0	45	213	342	0.561E-08	0.176E-08	0.707E-09	0.190E-08	45 ± 15
20,36	47.5	42	216	329	0.309E-08	0.857E-09	0.392E-09	0.446E-09	71 ± 10
20,37	45.1	37	220	319	0.403E-08	0.102E-08	0.511E-09	0.563E-09	67 ± 9
20,38	42.9	32	223	309	0.368E-08	0.895E-09	0.466E-09	0.298E-09	82 ± 6
20,39	41.0	27	226	301	0.424E-08	0.120E-08	0.530E-09	0.678E-09	62 ± 9
20,40	39.4	20	228	293	0.413E-08	0.109E-08	0.523E-09	0.523E-09	73 ± 9
20,41	38.1	14	230	288	0.371E-08	0.812E-09	0.466E-09	0.261E-09	88 ± 6
20,42	37.4	7	231	285	0.545E-08	0.113E-08	0.689E-09	0.619E-09	66 ± 7
20,43	37.2	-1	231	284	0.491E-08	0.932E-09	0.619E-09	0.484E-09	74 ± 7
20,44	37.5	-8	230	284	0.322E-08	0.136E-08	0.404E-09	0.331E-09	75 ± 7
20,45	38.3	-15	229	288	0.405E-08	0.122E-08	0.511E-09	0.940E-09	57 ± 13
20,46	39.6	-22	228	294	0.364E-08	0.972E-09	0.454E-09	0.866E-09	62 ± 14
20,47	41.3	-28	225	301	0.545E-08	0.164E-08	0.687E-09	0.160E-08	45 ± 13
	(deg)		(MeV)		(fm ² /MeVsr ²)				%

Table A3: Results for energy transfer bin E4 in the jan96 measurement. Central kinematics: $\omega = 275$ MeV, $\vec{q} = 553$ MeV/c, $Q^2 = -0.23$ (GeV/c)², $\Theta_q = 51^\circ$.

<i>bars</i>	Θ_{pn}^{CM}	Φ_{pn}^{CM}	T_{kin}	p_m	$d^5\sigma_{exp}$	$\pm \delta\sigma_{stat}$	$\pm \delta\sigma_{syst}$	$\pm \delta\sigma_{eff}$	η_{23}
21,34	49.8	53	213	341	0.216E-08	0.514E-09	0.275E-09	0.171E-09	87 ± 6
21,35	47.0	50	217	327	0.320E-08	0.898E-09	0.411E-09	0.619E-09	64 ± 12
21,36	44.3	46	221	314	0.382E-08	0.107E-08	0.487E-09	0.297E-09	82 ± 6
21,37	41.6	41	225	303	0.443E-08	0.871E-09	0.561E-09	0.415E-09	76 ± 7
21,38	39.1	36	228	291	0.538E-08	0.975E-09	0.679E-09	0.563E-09	74 ± 7
21,39	36.8	30	231	282	0.519E-08	0.147E-08	0.649E-09	0.465E-09	73 ± 6
21,40	34.9	23	234	274	0.773E-08	0.135E-08	0.975E-09	0.814E-09	74 ± 7
21,41	33.5	16	235	268	0.486E-08	0.129E-08	0.611E-09	0.613E-09	63 ± 8
21,42	32.6	8	236	264	0.672E-08	0.122E-08	0.846E-09	0.523E-09	73 ± 5
21,43	32.3	-1	236	263	0.352E-08	0.163E-08	0.443E-09	0.355E-09	68 ± 6
21,44	32.7	-9	236	264	0.416E-08	0.101E-08	0.523E-09	0.242E-09	87 ± 5
21,45	33.7	-17	235	268	0.566E-08	0.951E-09	0.714E-09	0.556E-09	74 ± 7
21,46	35.3	-25	233	275	0.547E-08	0.105E-08	0.692E-09	0.829E-09	62 ± 9
21,47	37.2	-31	231	284	0.455E-08	0.136E-08	0.574E-09	0.742E-09	61 ± 10
22,34	47.3	57	217	329	0.353E-08	0.870E-09	0.448E-09	0.214E-09	90 ± 5
22,35	44.2	54	221	314	0.465E-08	0.105E-08	0.591E-09	0.735E-09	61 ± 9
22,36	41.2	51	226	301	0.611E-08	0.100E-08	0.775E-09	0.575E-09	75 ± 7
22,37	38.2	46	230	288	0.404E-08	0.832E-09	0.509E-09	0.209E-09	90 ± 4
22,38	35.3	41	233	275	0.616E-08	0.162E-08	0.776E-09	0.610E-09	71 ± 7
22,39	32.7	34	236	264	0.695E-08	0.122E-08	0.868E-09	0.554E-09	75 ± 5
22,40	30.5	27	238	255	0.559E-08	0.107E-08	0.701E-09	0.400E-09	81 ± 5
22,41	28.8	19	240	249	0.585E-08	0.104E-08	0.733E-09	0.300E-09	81 ± 4
22,42	27.7	9	241	244	0.579E-08	0.136E-08	0.725E-09	0.525E-09	70 ± 6
22,43	27.4	-1	242	244	0.488E-08	0.112E-08	0.612E-09	0.303E-09	78 ± 4
22,44	27.9	-11	241	245	0.691E-08	0.117E-08	0.868E-09	0.328E-09	84 ± 3
22,45	29.1	-20	240	250	0.620E-08	0.178E-08	0.777E-09	0.750E-09	59 ± 7
22,46	30.9	-29	238	257	0.440E-08	0.832E-09	0.552E-09	0.295E-09	83 ± 5
22,47	33.2	-36	236	267	0.567E-08	0.984E-09	0.715E-09	0.327E-09	83 ± 4
23,34	45.0	62	220	318	0.499E-08	0.105E-08	0.634E-09	0.457E-09	77 ± 7
23,35	41.6	60	225	303	0.383E-08	0.106E-08	0.483E-09	0.469E-09	71 ± 8
23,36	38.3	56	229	288	0.338E-08	0.109E-08	0.425E-09	0.283E-09	80 ± 6
23,37	35.0	52	233	273	0.589E-08	0.108E-08	0.743E-09	0.414E-09	78 ± 5
23,38	31.8	47	237	261	0.716E-08	0.100E-08	0.905E-09	0.449E-09	81 ± 5
23,39	28.8	40	240	249	0.959E-08	0.189E-08	0.121E-08	0.670E-09	74 ± 5
23,40	26.2	32	243	239	0.720E-08	0.142E-08	0.903E-09	0.230E-09	90 ± 2
23,41	24.1	22	245	232	0.104E-07	0.150E-08	0.130E-08	0.661E-09	72 ± 4
23,42	22.8	11	246	227	0.105E-07	0.153E-08	0.132E-08	0.363E-09	86 ± 3
23,43	22.4	-1	246	226	0.820E-08	0.131E-08	0.103E-08	0.325E-09	85 ± 3
23,44	23.0	-13	245	227	0.113E-07	0.131E-08	0.143E-08	0.812E-09	72 ± 5
23,45	24.4	-24	244	232	0.753E-08	0.131E-08	0.944E-09	0.226E-09	90 ± 2
23,46	26.6	-34	242	241	0.800E-08	0.108E-08	0.100E-08	0.404E-09	81 ± 4
23,47	29.3	-41	240	251	0.540E-08	0.124E-08	0.679E-09	0.356E-09	77 ± 5
24,33	46.4	70	218	325	0.144E-08	0.651E-09	0.182E-09	0.220E-09	68 ± 10
24,34	42.9	68	223	309	0.332E-08	0.949E-09	0.419E-09	0.390E-09	75 ± 8
24,35	39.4	66	228	293	0.500E-08	0.110E-08	0.636E-09	0.623E-09	75 ± 9
24,36	35.8	63	233	278	0.538E-08	0.950E-09	0.682E-09	0.396E-09	78 ± 5
24,37	32.2	59	237	263	0.803E-08	0.125E-08	0.101E-08	0.481E-09	83 ± 5
24,38	28.6	54	240	248	0.737E-08	0.183E-08	0.933E-09	0.524E-09	73 ± 5
24,39	25.2	47	244	236	0.101E-07	0.160E-08	0.127E-08	0.488E-09	78 ± 3
	(deg)		(MeV)		(fm ² /MeVsr ²)				%

Table A3: Continued.

<i>bars</i>	Θ_{pn}^{CM}	Φ_{pn}^{CM}	T_{kin}	p_m	$d^5\sigma_{exp}$	$\pm \delta\sigma_{stat}$	$\pm \delta\sigma_{syst}$	$\pm \delta\sigma_{eff}$	η_{23}
24,40	22.1	-39	246	224	0.111E-07	0.146E-08	0.139E-08	0.567E-09	80 ± 4
24,41	19.5	28	248	216	0.121E-07	0.180E-08	0.152E-08	0.435E-09	86 ± 3
24,42	17.8	14	249	211	0.113E-07	0.174E-08	0.142E-08	0.599E-09	73 ± 3
24,43	17.3	-2	249	209	0.137E-07	0.221E-08	0.171E-08	0.581E-09	77 ± 3
24,44	18.1	-17	249	212	0.150E-07	0.180E-08	0.188E-08	0.584E-09	77 ± 3
24,45	19.9	-30	248	218	0.121E-07	0.161E-08	0.153E-08	0.812E-09	69 ± 4
24,46	22.6	-41	246	227	0.103E-07	0.786E-09	0.128E-08	0.916E-09	64 ± 5
24,47	25.8	-49	243	238	0.821E-08	0.212E-08	0.103E-08	0.619E-09	71 ± 5
25,34	41.3	74	225	300	0.276E-08	0.959E-09	0.349E-09	0.437E-09	72 ± 11
25,35	37.5	72	230	284	0.380E-08	0.105E-08	0.481E-09	0.550E-09	73 ± 10
25,36	33.7	70	235	268	0.430E-08	0.959E-09	0.544E-09	0.225E-09	85 ± 4
25,37	29.8	67	239	252	0.103E-07	0.137E-08	0.129E-08	0.543E-09	77 ± 4
25,38	25.9	63	243	238	0.106E-07	0.121E-08	0.133E-08	0.427E-09	81 ± 3
25,39	22.0	57	246	224	0.125E-07	0.173E-08	0.157E-08	0.423E-09	82 ± 2
25,40	18.4	49	249	213	0.182E-07	0.170E-08	0.228E-08	0.434E-09	88 ± 2
25,41	15.2	37	250	205	0.170E-07	0.190E-08	0.213E-08	0.439E-09	85 ± 2
25,42	13.0	20	252	199	0.223E-07	0.188E-08	0.280E-08	0.603E-09	81 ± 2
25,43	12.2	-2	252	197	0.188E-07	0.235E-08	0.237E-08	0.508E-09	81 ± 2
25,44	13.3	-23	252	200	0.160E-07	0.183E-08	0.200E-08	0.601E-09	74 ± 2
25,45	15.8	-39	250	205	0.218E-07	0.174E-08	0.274E-08	0.542E-09	84 ± 2
25,46	19.0	-51	248	214	0.130E-07	0.195E-08	0.163E-08	0.482E-09	80 ± 3
25,47	22.7	-58	246	227	0.966E-08	0.219E-08	0.121E-08	0.781E-09	60 ± 4
26,33	43.7	81	222	312	0.425E-08	0.154E-08	0.544E-09	0.717E-09	56 ± 9
26,34	40.0	80	227	296	0.429E-08	0.119E-08	0.546E-09	0.377E-09	80 ± 7
26,35	36.2	79	232	279	0.915E-08	0.216E-08	0.116E-08	0.165E-08	51 ± 9
26,36	32.2	78	237	263	0.853E-08	0.188E-08	0.108E-08	0.538E-09	77 ± 4
26,37	28.1	76	241	247	0.768E-08	0.105E-08	0.965E-09	0.330E-09	83 ± 3
26,38	23.9	73	245	231	0.130E-07	0.238E-08	0.164E-08	0.442E-09	82 ± 2
26,39	19.6	69	248	217	0.158E-07	0.167E-08	0.198E-08	0.457E-09	82 ± 2
26,40	15.5	63	250	206	0.196E-07	0.199E-08	0.245E-08	0.493E-09	83 ± 2
26,41	11.5	52	252	195	0.227E-07	0.206E-08	0.283E-08	0.450E-09	85 ± 1
26,42	8.4	31	254	191	0.336E-07	0.263E-08	0.421E-08	0.587E-09	85 ± 1
26,43	7.2	-4	254	189	0.335E-07	0.266E-08	0.419E-08	0.852E-09	78 ± 1
26,44	8.9	-36	252	190	0.249E-07	0.204E-08	0.313E-08	0.468E-09	85 ± 1
26,45	12.2	-54	252	197	0.264E-07	0.201E-08	0.331E-08	0.524E-09	85 ± 1
26,46	16.2	-64	250	207	0.190E-07	0.167E-08	0.238E-08	0.501E-09	83 ± 2
26,47	20.4	-70	247	219	0.152E-07	0.164E-08	0.190E-08	0.611E-09	74 ± 3
27,33	42.9	87	223	309	0.532E-08	0.208E-08	0.674E-09	0.111E-08	46 ± 9
27,34	39.2	87	228	292	0.484E-08	0.133E-08	0.615E-09	0.297E-09	84 ± 5
27,35	35.3	87	233	275	0.564E-08	0.139E-08	0.712E-09	0.283E-09	85 ± 4
27,36	31.3	86	238	259	0.903E-08	0.128E-08	0.114E-08	0.437E-09	80 ± 3
27,37	27.1	86	242	243	0.128E-07	0.228E-08	0.162E-08	0.536E-09	81 ± 3
27,38	22.7	85	246	227	0.149E-07	0.236E-08	0.188E-08	0.528E-09	79 ± 2
27,39	18.3	83	249	213	0.210E-07	0.224E-08	0.264E-08	0.608E-09	79 ± 2
27,40	13.8	81	250	200	0.303E-07	0.326E-08	0.381E-08	0.112E-08	70 ± 2
27,41	9.2	77	252	191	0.385E-07	0.300E-08	0.482E-08	0.739E-09	83 ± 1
27,42	4.8	63	254	185	0.398E-07	0.300E-08	0.500E-08	0.840E-09	80 ± 1
27,43	2.2	-12	255	185	0.469E-07	0.307E-08	0.589E-08	0.780E-09	84 ± 1
27,44	5.6	-67	254	186	0.402E-07	0.284E-08	0.504E-08	0.661E-09	85 ± 1
	(deg)		(MeV)		(fm ² /MeVsr ²)				%

Table A3: Continued.

<i>bars</i>	Θ_{pn}^{CM}	Φ_{pn}^{CM}	T_{kin}	p_m	$d^5\sigma_{exp}$	$\pm \delta\sigma_{stat}$	$\pm \delta\sigma_{syst}$	$\pm \delta\sigma_{eff}$	η_{23}
27,45	10.1	-78	252	193	0.315E-07	0.249E-08	0.395E-08	0.589E-09	85 ± 1
27,46	14.6	-82	250	203	0.258E-07	0.220E-08	0.324E-08	0.635E-09	81 ± 2
27,47	19.2	-84	248	215	0.157E-07	0.249E-08	0.198E-08	0.678E-09	71 ± 3
28,33	42.6	93	224	308	0.267E-08	0.595E-09	0.336E-09	0.397E-09	61 ± 9
28,34	38.9	94	229	292	0.734E-08	0.142E-08	0.928E-09	0.422E-09	83 ± 4
28,35	35.0	94	233	274	0.816E-08	0.182E-08	0.104E-08	0.400E-09	83 ± 4
28,36	31.0	95	238	258	0.969E-08	0.176E-08	0.122E-08	0.578E-09	77 ± 4
28,37	26.9	96	242	241	0.133E-07	0.167E-08	0.169E-08	0.411E-09	87 ± 2
28,38	22.6	97	246	227	0.181E-07	0.216E-08	0.228E-08	0.526E-09	82 ± 2
28,39	18.2	99	249	212	0.238E-07	0.265E-08	0.300E-08	0.781E-09	76 ± 2
28,40	13.8	101	250	200	0.289E-07	0.224E-08	0.362E-08	0.715E-09	80 ± 1
28,41	9.3	107	252	191	0.394E-07	0.342E-08	0.495E-08	0.605E-09	84 ± 1
28,42	5.0	123	254	185	0.410E-07	0.322E-08	0.513E-08	0.770E-09	79 ± 1
28,43	2.8	-171	255	185	0.505E-07	0.338E-08	0.634E-08	0.787E-09	83 ± 1
28,44	5.8	-118	254	186	0.446E-07	0.300E-08	0.559E-08	0.839E-09	79 ± 1
28,45	10.1	-106	252	193	0.363E-07	0.321E-08	0.456E-08	0.923E-09	74 ± 1
28,46	14.6	-101	250	202	0.245E-07	0.246E-08	0.309E-08	0.523E-09	84 ± 1
28,47	19.0	-98	248	214	0.143E-07	0.200E-08	0.180E-08	0.472E-09	78 ± 2
29,33	42.6	99	224	308	0.325E-08	0.863E-09	0.413E-09	0.284E-09	76 ± 6
29,34	39.0	100	228	291	0.581E-08	0.110E-08	0.742E-09	0.327E-09	86 ± 4
29,35	35.3	102	233	275	0.640E-08	0.165E-08	0.816E-09	0.288E-09	86 ± 3
29,36	31.4	103	238	260	0.119E-07	0.184E-08	0.151E-08	0.673E-09	74 ± 4
29,37	27.4	105	242	245	0.137E-07	0.169E-08	0.172E-08	0.408E-09	87 ± 2
29,38	23.4	108	245	229	0.157E-07	0.206E-08	0.197E-08	0.471E-09	83 ± 2
29,39	19.3	113	248	215	0.248E-07	0.255E-08	0.313E-08	0.719E-09	79 ± 2
29,40	15.3	119	250	205	0.346E-07	0.313E-08	0.436E-08	0.125E-08	69 ± 2
29,41	11.6	131	252	195	0.410E-07	0.396E-08	0.515E-08	0.921E-09	75 ± 1
29,42	8.6	151	254	191	0.432E-07	0.411E-08	0.546E-08	0.842E-09	77 ± 1
29,43	7.6	-177	254	189	0.444E-07	0.405E-08	0.558E-08	0.845E-09	78 ± 1
29,44	9.1	-146	252	191	0.425E-07	0.495E-08	0.533E-08	0.102E-08	74 ± 1
29,45	12.2	-128	252	197	0.402E-07	0.379E-08	0.506E-08	0.156E-08	61 ± 2
29,46	16.0	-118	250	206	0.309E-07	0.237E-08	0.388E-08	0.877E-09	74 ± 2
29,47	20.1	-112	248	219	0.173E-07	0.247E-08	0.218E-08	0.541E-09	80 ± 2
30,33	43.1	105	223	310	0.517E-08	0.166E-08	0.665E-09	0.111E-08	50 ± 10
30,34	39.6	107	228	294	0.732E-08	0.115E-08	0.933E-09	0.543E-09	76 ± 5
30,35	36.0	109	232	278	0.746E-08	0.131E-08	0.957E-09	0.432E-09	79 ± 4
30,36	32.4	111	236	263	0.968E-08	0.168E-08	0.123E-08	0.529E-09	76 ± 4
30,37	28.6	114	240	248	0.147E-07	0.232E-08	0.186E-08	0.591E-09	79 ± 3
30,38	24.9	119	244	234	0.189E-07	0.208E-08	0.239E-08	0.621E-09	79 ± 2
30,39	21.3	124	247	222	0.309E-07	0.359E-08	0.390E-08	0.156E-08	61 ± 3
30,40	17.9	133	249	211	0.266E-07	0.268E-08	0.335E-08	0.933E-09	68 ± 2
30,41	14.9	145	250	204	0.411E-07	0.458E-08	0.517E-08	0.134E-08	67 ± 2
30,42	12.9	161	252	199	0.368E-07	0.503E-08	0.463E-08	0.837E-09	74 ± 1
30,43	12.2	-178	252	197	0.485E-07	0.331E-08	0.610E-08	0.118E-08	73 ± 1
30,44	13.2	-158	252	200	0.647E-07	0.490E-08	0.814E-08	0.324E-08	51 ± 2
30,45	15.4	-142	250	205	0.420E-07	0.356E-08	0.528E-08	0.131E-08	67 ± 2
30,46	18.5	-131	249	214	0.237E-07	0.315E-08	0.299E-08	0.832E-09	68 ± 2
30,47	22.0	-123	246	224	0.129E-07	0.281E-08	0.163E-08	0.573E-09	69 ± 3
	(deg)		(MeV)		(fm ² /MeVsr ²)				%

Table A3: Continued.

<i>bars</i>	Θ_{pn}^{CM}	Φ_{pn}^{CM}	T_{kin}	p_m	$d^5\sigma_{\text{exp}}$	$\pm \delta\sigma_{\text{stat}}$	$\pm \delta\sigma_{\text{syst}}$	$\pm \delta\sigma_{\text{eff}}$	η_{23}
17,37	48.2	32	250	375	0.364E-08	0.139E-08	0.809E-09	0.953E-09	47 ± 12
17,43	42.1	-1	261	347	0.716E-08	0.210E-08	0.159E-08	0.231E-08	35 ± 11
18,40	39.8	19	264	336	0.537E-08	0.130E-08	0.118E-08	0.729E-09	61 ± 8
18,41	38.7	13	266	331	0.674E-08	0.237E-08	0.148E-08	0.117E-08	57 ± 9
18,42	38.0	6	267	329	0.660E-08	0.152E-08	0.145E-08	0.139E-08	45 ± 9
18,43	37.8	-1	267	328	0.315E-08	0.117E-08	0.693E-09	0.377E-09	70 ± 8
18,44	38.1	-7	267	330	0.505E-08	0.139E-08	0.111E-08	0.699E-09	67 ± 9
18,45	38.9	-14	266	332	0.253E-08	0.971E-09	0.562E-09	0.513E-09	57 ± 11
19,34	49.1	51	249	379	0.164E-08	0.369E-09	0.363E-09	0.557E-09	55 ± 18
19,35	46.5	47	252	366	0.306E-08	0.713E-09	0.678E-09	0.465E-09	75 ± 11
19,37	41.6	39	262	345	0.529E-08	0.768E-09	0.116E-08	0.107E-08	51 ± 10
19,39	37.3	28	268	325	0.410E-08	0.139E-08	0.908E-09	0.566E-09	63 ± 8
19,40	35.6	22	270	318	0.659E-08	0.159E-08	0.145E-08	0.156E-08	44 ± 10
19,41	34.4	15	272	313	0.627E-08	0.234E-08	0.139E-08	0.915E-09	56 ± 8
19,42	33.6	7	273	310	0.440E-08	0.138E-08	0.968E-09	0.726E-09	57 ± 9
19,45	34.6	-16	272	314	0.536E-08	0.125E-08	0.118E-08	0.123E-08	49 ± 11
20,35	43.9	52	258	355	0.360E-08	0.147E-08	0.803E-09	0.984E-09	51 ± 14
20,36	41.1	48	262	342	0.484E-08	0.119E-08	0.107E-08	0.612E-09	71 ± 9
20,37	38.3	44	266	329	0.486E-08	0.137E-08	0.107E-08	0.607E-09	69 ± 8
20,38	35.8	38	270	319	0.664E-08	0.139E-08	0.145E-08	0.975E-09	54 ± 7
20,39	33.4	32	273	309	0.564E-08	0.134E-08	0.124E-08	0.865E-09	58 ± 9
20,40	31.5	25	276	301	0.915E-08	0.265E-08	0.201E-08	0.133E-08	56 ± 8
20,41	30.0	17	277	294	0.788E-08	0.284E-08	0.173E-08	0.187E-08	42 ± 10
20,42	29.0	8	278	291	0.554E-08	0.135E-08	0.122E-08	0.938E-09	50 ± 8
20,43	28.8	-1	279	291	0.686E-08	0.152E-08	0.151E-08	0.909E-09	56 ± 7
20,44	29.2	-10	278	291	0.860E-08	0.296E-08	0.189E-08	0.138E-08	50 ± 8
21,34	44.5	60	257	358	0.317E-08	0.888E-09	0.699E-09	0.337E-09	78 ± 8
21,36	38.3	53	266	329	0.577E-08	0.119E-08	0.128E-08	0.881E-09	60 ± 9
21,37	35.3	49	271	317	0.591E-08	0.155E-08	0.130E-08	0.701E-09	64 ± 7
21,38	32.3	44	274	304	0.766E-08	0.163E-08	0.168E-08	0.112E-08	56 ± 8
21,39	29.6	37	278	294	0.844E-08	0.173E-08	0.186E-08	0.104E-08	63 ± 7
21,40	27.3	29	280	285	0.945E-08	0.195E-08	0.207E-08	0.230E-08	45 ± 11
21,41	25.5	20	282	278	0.120E-07	0.213E-08	0.262E-08	0.264E-08	36 ± 7
21,42	24.3	10	283	274	0.102E-07	0.157E-08	0.224E-08	0.104E-08	58 ± 6
21,43	24.0	-1	284	274	0.914E-08	0.276E-08	0.202E-08	0.132E-08	48 ± 7
21,44	24.5	-12	283	275	0.939E-08	0.148E-08	0.206E-08	0.977E-09	61 ± 6
21,45	25.8	-22	282	280	0.718E-08	0.151E-08	0.158E-08	0.754E-09	65 ± 6
21,47	30.1	-38	277	296	0.315E-08	0.113E-08	0.692E-09	0.577E-09	57 ± 10
22,34	42.5	65	260	348	0.562E-08	0.132E-08	0.124E-08	0.823E-09	69 ± 10
22,35	39.2	63	265	333	0.489E-08	0.192E-08	0.108E-08	0.102E-08	53 ± 11
22,36	35.8	59	270	319	0.666E-08	0.166E-08	0.147E-08	0.658E-09	70 ± 7
22,37	32.4	55	274	304	0.535E-08	0.202E-08	0.118E-08	0.610E-09	62 ± 7
22,38	29.1	50	278	291	0.810E-08	0.188E-08	0.178E-08	0.108E-08	54 ± 7
22,39	26.0	44	282	281	0.629E-08	0.227E-08	0.139E-08	0.108E-08	47 ± 8
22,40	23.3	35	284	270	0.690E-08	0.161E-08	0.152E-08	0.740E-09	61 ± 6
22,41	21.0	25	286	263	0.816E-08	0.152E-08	0.179E-08	0.795E-09	61 ± 5
	(deg)		(MeV)		(fm ² /MeVsr ²)				%

Table A4: Results for energy transfer bin E5 in the jan96 measurement. Central kinematics: $\omega = 325$ MeV, $\bar{q} = 572$ MeV/c, $Q^2 = -0.22$ (GeV/c)², $\Theta_q = 46^\circ$.

<i>bars</i>	Θ_{pn}^{CM}	Φ_{pn}^{CM}	T_{kin}	p_m	$d^5\sigma_{\text{exp}}$	$\pm \delta\sigma_{\text{stat}}$	$\pm \delta\sigma_{\text{syst}}$	$\pm \delta\sigma_{\text{eff}}$	η_{23}
22,42	19.6	12	287	259	0.136E-07	0.247E-08	0.299E-08	0.181E-08	51 ± 6
22,43	19.2	-1	288	258	0.123E-07	0.177E-08	0.272E-08	0.127E-08	60 ± 6
22,44	19.8	-15	287	259	0.928E-08	0.191E-08	0.204E-08	0.876E-09	62 ± 5
22,45	21.4	-27	286	264	0.137E-07	0.253E-08	0.304E-08	0.239E-08	43 ± 7
22,46	23.8	-37	284	272	0.590E-08	0.197E-08	0.129E-08	0.739E-09	57 ± 7
22,47	26.6	-45	281	282	0.776E-08	0.146E-08	0.170E-08	0.818E-09	60 ± 6
23,34	40.8	71	263	341	0.219E-08	0.784E-09	0.482E-09	0.340E-09	63 ± 9
23,35	37.3	69	268	325	0.266E-08	0.104E-08	0.588E-09	0.447E-09	69 ± 11
23,36	33.7	66	273	310	0.372E-08	0.947E-09	0.817E-09	0.420E-09	73 ± 8
23,37	30.0	63	277	295	0.845E-08	0.159E-08	0.187E-08	0.110E-08	60 ± 7
23,38	26.3	58	281	281	0.578E-08	0.160E-08	0.127E-08	0.541E-09	69 ± 6
23,39	22.8	52	285	269	0.868E-08	0.253E-08	0.191E-08	0.115E-08	55 ± 7
23,40	19.5	44	288	260	0.123E-07	0.167E-08	0.272E-08	0.925E-09	66 ± 4
23,41	16.7	32	290	252	0.132E-07	0.314E-08	0.292E-08	0.143E-08	53 ± 5
23,42	14.8	17	291	247	0.128E-07	0.210E-08	0.282E-08	0.774E-09	69 ± 4
23,43	14.2	-2	291	245	0.123E-07	0.156E-08	0.270E-08	0.744E-09	72 ± 4
23,44	15.1	-20	291	248	0.157E-07	0.205E-08	0.345E-08	0.109E-08	66 ± 4
23,45	17.2	-35	289	252	0.110E-07	0.214E-08	0.241E-08	0.721E-09	70 ± 4
23,46	20.1	-45	287	261	0.734E-08	0.123E-08	0.162E-08	0.557E-09	72 ± 5
23,47	23.5	-53	284	271	0.723E-08	0.155E-08	0.159E-08	0.113E-08	55 ± 8
24,33	43.1	79	259	351	0.180E-08	0.692E-09	0.396E-09	0.303E-09	68 ± 11
24,34	39.6	77	265	336	0.454E-08	0.179E-08	0.997E-09	0.685E-09	60 ± 9
24,35	35.9	76	270	319	0.374E-08	0.110E-08	0.825E-09	0.376E-09	77 ± 7
24,36	32.0	74	275	304	0.829E-08	0.180E-08	0.182E-08	0.109E-08	60 ± 7
24,37	28.1	71	279	288	0.128E-07	0.246E-08	0.282E-08	0.222E-08	46 ± 8
24,38	24.1	68	284	275	0.110E-07	0.205E-08	0.242E-08	0.119E-08	61 ± 6
24,39	20.2	63	287	261	0.110E-07	0.186E-08	0.243E-08	0.667E-09	72 ± 4
24,40	16.3	56	290	250	0.122E-07	0.244E-08	0.267E-08	0.115E-08	60 ± 5
24,41	12.8	44	292	242	0.146E-07	0.192E-08	0.321E-08	0.116E-08	63 ± 4
24,42	10.2	25	293	237	0.206E-07	0.253E-08	0.452E-08	0.145E-08	61 ± 4
24,43	9.3	-3	293	235	0.180E-07	0.190E-08	0.395E-08	0.121E-08	65 ± 4
24,44	10.6	-29	293	238	0.187E-07	0.274E-08	0.410E-08	0.139E-08	59 ± 4
24,45	13.4	-47	292	244	0.202E-07	0.270E-08	0.445E-08	0.289E-08	44 ± 6
24,46	17.0	-57	289	252	0.146E-07	0.248E-08	0.321E-08	0.238E-08	41 ± 6
24,47	20.9	-64	286	262	0.100E-07	0.175E-08	0.222E-08	0.149E-08	49 ± 7
25,36	31.0	82	276	299	0.353E-08	0.101E-08	0.777E-09	0.576E-09	65 ± 10
25,37	26.9	81	281	284	0.894E-08	0.191E-08	0.197E-08	0.716E-09	69 ± 5
25,38	22.7	79	285	269	0.961E-08	0.172E-08	0.212E-08	0.512E-09	77 ± 4
25,39	18.4	77	288	256	0.153E-07	0.213E-08	0.335E-08	0.899E-09	69 ± 4
25,40	14.1	72	291	245	0.150E-07	0.245E-08	0.329E-08	0.994E-09	64 ± 4
25,41	9.8	64	293	236	0.173E-07	0.205E-08	0.379E-08	0.711E-09	75 ± 3
25,42	6.0	44	295	232	0.205E-07	0.200E-08	0.449E-08	0.119E-08	61 ± 3
25,43	4.3	-6	295	230	0.197E-07	0.243E-08	0.435E-08	0.942E-09	69 ± 3
25,44	6.7	-50	294	232	0.176E-07	0.213E-08	0.388E-08	0.981E-09	66 ± 3
25,45	10.6	-66	293	238	0.199E-07	0.259E-08	0.438E-08	0.110E-08	64 ± 3
25,46	14.9	-73	291	247	0.159E-07	0.208E-08	0.350E-08	0.134E-08	57 ± 4
25,47	19.2	-77	288	259	0.110E-07	0.265E-08	0.242E-08	0.196E-08	37 ± 6
	(deg)		(MeV)		(fm ² /MeVsr ²)				%

Table A4: Continued.

<i>bars</i>	Θ_{pn}^{CM}	Φ_{pn}^{CM}	T_{kin}	p_m	$d^5\sigma_{\text{exp}}$	$\pm \delta\sigma_{\text{stat}}$	$\pm \delta\sigma_{\text{syst}}$	$\pm \delta\sigma_{\text{eff}}$	η_{23}
26,33	42.0	91	261	347	0.348E-08	0.161E-08	0.774E-09	0.969E-09	46 ± 12
26,34	38.3	91	266	329	0.519E-08	0.135E-08	0.115E-08	0.513E-09	71 ± 7
26,35	34.5	91	272	314	0.767E-08	0.200E-08	0.169E-08	0.101E-08	59 ± 7
26,36	30.6	91	277	298	0.862E-08	0.170E-08	0.190E-08	0.105E-08	57 ± 7
26,37	26.5	91	281	281	0.109E-07	0.185E-08	0.240E-08	0.777E-09	70 ± 5
26,38	22.2	92	285	267	0.940E-08	0.262E-08	0.207E-08	0.533E-09	74 ± 4
26,39	17.8	92	289	255	0.200E-07	0.282E-08	0.440E-08	0.136E-08	63 ± 4
26,40	13.4	93	292	244	0.183E-07	0.401E-08	0.403E-08	0.768E-09	73 ± 3
26,41	8.8	94	294	236	0.237E-07	0.273E-08	0.522E-08	0.108E-08	68 ± 3
26,42	4.2	98	295	230	0.209E-07	0.220E-08	0.460E-08	0.861E-09	72 ± 2
26,43	0.8	-145	295	228	0.243E-07	0.251E-08	0.535E-08	0.117E-08	66 ± 3
26,44	5.1	-97	295	231	0.254E-07	0.258E-08	0.558E-08	0.118E-08	66 ± 3
26,45	9.7	-94	293	236	0.211E-07	0.173E-08	0.464E-08	0.111E-08	66 ± 3
26,46	14.2	-92	291	245	0.137E-07	0.182E-08	0.302E-08	0.811E-09	65 ± 3
26,47	18.7	-92	288	256	0.130E-07	0.203E-08	0.287E-08	0.813E-09	65 ± 4
27,33	42.0	97	261	347	0.399E-08	0.142E-08	0.881E-09	0.473E-09	68 ± 8
27,34	38.4	98	266	330	0.378E-08	0.109E-08	0.835E-09	0.396E-09	70 ± 7
27,35	34.7	99	271	314	0.666E-08	0.178E-08	0.147E-08	0.488E-09	80 ± 5
27,36	30.8	100	276	298	0.764E-08	0.138E-08	0.168E-08	0.484E-09	77 ± 4
27,37	26.8	101	281	283	0.117E-07	0.259E-08	0.258E-08	0.107E-08	65 ± 6
27,38	22.7	104	285	269	0.129E-07	0.242E-08	0.284E-08	0.710E-09	72 ± 4
27,39	18.5	107	288	256	0.159E-07	0.234E-08	0.350E-08	0.918E-09	69 ± 4
27,40	14.3	112	291	245	0.262E-07	0.320E-08	0.576E-08	0.195E-08	55 ± 4
27,41	10.3	122	293	237	0.221E-07	0.259E-08	0.487E-08	0.899E-09	71 ± 2
27,42	6.9	143	294	232	0.294E-07	0.437E-08	0.646E-08	0.152E-08	63 ± 3
27,43	5.5	-175	295	232	0.299E-07	0.314E-08	0.657E-08	0.120E-08	67 ± 2
27,44	7.4	-137	294	233	0.244E-07	0.313E-08	0.536E-08	0.106E-08	66 ± 2
27,45	11.0	-120	293	239	0.208E-07	0.267E-08	0.458E-08	0.111E-08	63 ± 3
27,46	15.1	-111	291	248	0.168E-07	0.198E-08	0.370E-08	0.122E-08	59 ± 4
27,47	19.3	-106	288	259	0.153E-07	0.280E-08	0.335E-08	0.174E-08	49 ± 5
28,33	42.4	103	260	348	0.220E-08	0.973E-09	0.490E-09	0.428E-09	56 ± 10
28,34	39.0	104	265	332	0.831E-08	0.269E-08	0.183E-08	0.202E-08	42 ± 10
28,35	35.4	106	271	318	0.753E-08	0.164E-08	0.166E-08	0.687E-09	71 ± 6
28,36	31.7	108	275	301	0.108E-07	0.193E-08	0.238E-08	0.750E-09	74 ± 5
28,37	27.9	111	280	287	0.809E-08	0.159E-08	0.179E-08	0.438E-09	79 ± 4
28,38	24.0	115	284	274	0.129E-07	0.214E-08	0.283E-08	0.751E-09	70 ± 4
28,39	20.2	120	287	261	0.218E-07	0.314E-08	0.481E-08	0.159E-08	60 ± 4
28,40	16.6	128	290	251	0.243E-07	0.354E-08	0.535E-08	0.198E-08	55 ± 4
28,41	13.4	140	292	244	0.221E-07	0.360E-08	0.485E-08	0.120E-08	62 ± 3
28,42	11.1	158	293	239	0.257E-07	0.298E-08	0.564E-08	0.116E-08	66 ± 2
28,43	10.3	-178	293	237	0.325E-07	0.364E-08	0.717E-08	0.150E-08	62 ± 2
28,44	11.4	-154	293	240	0.213E-07	0.274E-08	0.468E-08	0.967E-09	66 ± 3
28,45	14.0	-137	291	244	0.252E-07	0.349E-08	0.555E-08	0.185E-08	55 ± 4
28,46	17.3	-126	289	253	0.108E-07	0.324E-08	0.239E-08	0.843E-09	61 ± 4
28,47	21.0	-119	286	263	0.109E-07	0.279E-08	0.240E-08	0.165E-08	47 ± 7
29,34	39.9	110	264	336	0.570E-08	0.127E-08	0.126E-08	0.601E-09	72 ± 7
29,35	36.5	113	269	322	0.730E-08	0.180E-08	0.161E-08	0.864E-09	63 ± 7
	(deg)		(MeV)		(fm ² /MeVsr ²)				%

Table A4: Continued.

<i>bars</i>	Θ_{pn}^{CM}	Φ_{pn}^{CM}	T_{kin}	p_m	$d^5\sigma_{exp}$	$\pm \delta\sigma_{stat}$	$\pm \delta\sigma_{syst}$	$\pm \delta\sigma_{eff}$	η_{23}
29,36	33.0	116	274	308	0.106E-07	0.171E-08	0.233E-08	0.757E-09	72 ± 5
29,37	29.5	119	278	294	0.886E-08	0.271E-08	0.196E-08	0.668E-09	70 ± 5
29,38	26.1	124	282	281	0.143E-07	0.510E-08	0.314E-08	0.872E-09	70 ± 4
29,39	22.7	130	285	269	0.161E-07	0.244E-08	0.353E-08	0.140E-08	60 ± 5
29,40	19.7	139	287	259	0.244E-07	0.375E-08	0.538E-08	0.229E-08	49 ± 4
29,41	17.1	150	289	252	0.227E-07	0.410E-08	0.502E-08	0.145E-08	57 ± 3
29,42	15.4	165	290	247	0.245E-07	0.382E-08	0.540E-08	0.176E-08	52 ± 3
29,43	14.9	-178	291	247	0.295E-07	0.403E-08	0.651E-08	0.186E-08	55 ± 3
29,44	15.7	-162	290	249	0.221E-07	0.289E-08	0.486E-08	0.155E-08	56 ± 4
29,45	17.6	-148	289	253	0.246E-07	0.319E-08	0.539E-08	0.278E-08	45 ± 5
29,46	20.2	-137	287	261	0.184E-07	0.252E-08	0.404E-08	0.156E-08	56 ± 4
30,35	38.0	119	267	329	0.693E-08	0.148E-08	0.152E-08	0.632E-09	71 ± 6
30,36	34.8	122	271	314	0.984E-08	0.210E-08	0.218E-08	0.833E-09	68 ± 5
30,37	31.6	127	275	301	0.114E-07	0.363E-08	0.252E-08	0.117E-08	59 ± 6
30,38	28.6	132	279	290	0.151E-07	0.268E-08	0.332E-08	0.141E-08	62 ± 5
30,39	25.7	138	282	279	0.231E-07	0.499E-08	0.509E-08	0.280E-08	44 ± 5
30,40	23.1	146	284	270	0.179E-07	0.350E-08	0.396E-08	0.218E-08	45 ± 5
30,41	21.1	156	286	264	0.190E-07	0.312E-08	0.420E-08	0.237E-08	43 ± 5
30,42	19.8	168	287	259	0.212E-07	0.488E-08	0.468E-08	0.208E-08	45 ± 4
30,43	19.4	-179	288	259	0.125E-07	0.415E-08	0.275E-08	0.106E-08	51 ± 4
30,44	20.0	-166	287	261	0.316E-07	0.418E-08	0.698E-08	0.550E-08	34 ± 6
30,45	21.4	-154	286	265	0.200E-07	0.292E-08	0.441E-08	0.209E-08	44 ± 4
30,46	23.6	-145	284	272	0.130E-07	0.215E-08	0.287E-08	0.175E-08	46 ± 6
30,47	26.2	-137	281	281	0.563E-08	0.235E-08	0.124E-08	0.102E-08	44 ± 8
	(deg)		(MeV)		(fm ² /MeVsr ²)				%

Table A4: Continued.

<i>bars</i>	Θ_{pn}^{CM}	Φ_{pn}^{CM}	T_{kin}	p_m	$d^5\sigma_{exp}$	$\pm \delta\sigma_{stat}$	$\pm \delta\sigma_{syst}$	$\pm \delta\sigma_{eff}$	η_{23}
18,37	38.9	41	302	369	0.362E-08	0.117E-08	0.414E-09	0.834E-09	35 ± 8
18,38	36.6	36	306	359	0.578E-08	0.133E-08	0.633E-09	0.152E-08	33 ± 8
19,44	26.4	-11	320	319	0.610E-08	0.230E-08	0.689E-09	0.106E-08	31 ± 5
20,35	39.3	59	302	372	0.417E-08	0.150E-08	0.473E-09	0.717E-09	47 ± 8
20,36	36.2	56	307	358	0.687E-08	0.133E-08	0.775E-09	0.108E-08	46 ± 7
20,37	33.1	51	311	344	0.818E-08	0.229E-08	0.880E-09	0.184E-08	31 ± 7
21,34	40.8	68	299	377	0.490E-08	0.189E-08	0.545E-09	0.886E-09	43 ± 7
21,35	37.4	65	305	363	0.231E-08	0.883E-09	0.258E-09	0.296E-09	59 ± 7
21,36	34.0	62	310	348	0.362E-08	0.116E-08	0.404E-09	0.438E-09	53 ± 6
21,37	30.6	58	315	335	0.723E-08	0.187E-08	0.827E-09	0.132E-08	32 ± 6
21,42	17.2	14	329	290	0.128E-07	0.194E-08	0.143E-08	0.172E-08	34 ± 4
22,34	39.4	74	302	372	0.442E-08	0.162E-08	0.496E-09	0.737E-09	47 ± 7
22,35	35.9	72	307	356	0.622E-08	0.117E-08	0.691E-09	0.103E-08	42 ± 7
22,36	32.2	69	313	342	0.720E-08	0.132E-08	0.796E-09	0.898E-09	48 ± 6
22,37	28.5	66	317	327	0.659E-08	0.145E-08	0.755E-09	0.124E-08	32 ± 6
	(deg)		(MeV)		(fm ² /MeVsr ²)				%

Table A5: Results for energy transfer bin E6 in the jan96 measurement. Central kinematics: $\omega = 375$ MeV, $\vec{q} = 594$ MeV/c, $Q^2 = -0.21$ (GeV/c)², $\Theta_q = 42^\circ$.

<i>bars</i>	Θ_{pn}^{CM}	Φ_{pn}^{CM}	T_{kin}	p_m	$d^5\sigma_{\text{exp}}$	$\pm \delta\sigma_{\text{stat}}$	$\pm \delta\sigma_{\text{syst}}$	$\pm \delta\sigma_{\text{eff}}$	η_{23}
22,38	24.8	62	322	314	0.123E-07	0.194E-08	0.138E-08	0.185E-08	32 ± 4
22,41	14.7	36	331	284	0.176E-07	0.232E-08	0.194E-08	0.193E-08	34 ± 3
23,34	38.5	80	303	367	0.278E-08	0.706E-09	0.310E-09	0.301E-09	64 ± 6
23,36	31.0	77	314	336	0.528E-08	0.196E-08	0.581E-09	0.811E-09	43 ± 6
23,37	27.0	75	319	321	0.951E-08	0.153E-08	0.108E-08	0.155E-08	39 ± 6
24,34	38.0	87	304	366	0.656E-08	0.126E-08	0.745E-09	0.103E-08	44 ± 6
24,35	34.2	87	310	349	0.587E-08	0.122E-08	0.661E-09	0.719E-09	51 ± 6
24,36	30.3	86	315	333	0.769E-08	0.168E-08	0.859E-09	0.976E-09	45 ± 5
24,38	22.1	84	325	305	0.128E-07	0.221E-08	0.138E-08	0.174E-08	35 ± 4
24,39	17.8	83	328	291	0.134E-07	0.226E-08	0.148E-08	0.122E-08	42 ± 3
24,44	5.5	-67	335	269	0.211E-07	0.220E-08	0.231E-08	0.207E-08	34 ± 3
25,37	26.2	96	320	318	0.695E-08	0.142E-08	0.771E-09	0.798E-09	44 ± 5
25,38	22.1	97	325	305	0.147E-07	0.182E-08	0.163E-08	0.141E-08	44 ± 4
25,39	17.8	99	328	291	0.149E-07	0.248E-08	0.163E-08	0.160E-08	37 ± 3
25,40	13.5	102	331	281	0.167E-07	0.206E-08	0.185E-08	0.156E-08	38 ± 3
25,43	2.7	-171	335	267	0.169E-07	0.208E-08	0.189E-08	0.128E-08	42 ± 3
25,44	5.7	-118	335	270	0.242E-07	0.245E-08	0.271E-08	0.264E-08	32 ± 3
25,45	9.9	-106	333	274	0.204E-07	0.226E-08	0.228E-08	0.201E-08	35 ± 3
26,34	38.3	101	303	366	0.584E-08	0.111E-08	0.655E-09	0.711E-09	55 ± 6
26,35	34.7	102	309	352	0.920E-08	0.217E-08	0.106E-08	0.199E-08	30 ± 6
26,36	30.9	103	314	336	0.870E-08	0.144E-08	0.979E-09	0.100E-08	47 ± 5
26,37	27.0	106	319	321	0.925E-08	0.146E-08	0.103E-08	0.871E-09	51 ± 4
26,38	23.0	109	324	308	0.110E-07	0.193E-08	0.122E-08	0.103E-08	47 ± 4
26,40	15.1	120	330	285	0.226E-07	0.317E-08	0.252E-08	0.247E-08	34 ± 3
26,41	11.5	131	333	278	0.197E-07	0.405E-08	0.221E-08	0.154E-08	39 ± 3
26,42	8.6	151	334	273	0.194E-07	0.207E-08	0.215E-08	0.133E-08	43 ± 3
26,43	7.6	-177	334	271	0.254E-07	0.263E-08	0.283E-08	0.260E-08	32 ± 3
26,44	9.0	-147	334	274	0.182E-07	0.308E-08	0.200E-08	0.140E-08	41 ± 3
26,45	12.1	-128	332	278	0.193E-07	0.208E-08	0.212E-08	0.188E-08	36 ± 3
26,47	19.8	-112	327	298	0.122E-07	0.173E-08	0.136E-08	0.144E-08	37 ± 4
27,34	39.2	107	302	371	0.592E-08	0.135E-08	0.659E-09	0.991E-09	43 ± 7
27,35	35.7	109	307	355	0.683E-08	0.180E-08	0.761E-09	0.766E-09	51 ± 5
27,36	32.1	112	313	341	0.651E-08	0.144E-08	0.730E-09	0.698E-09	52 ± 5
27,37	28.5	115	317	326	0.133E-07	0.242E-08	0.147E-08	0.165E-08	40 ± 5
27,38	24.8	119	322	314	0.114E-07	0.154E-08	0.126E-08	0.119E-08	43 ± 4
27,39	21.2	125	325	301	0.157E-07	0.185E-08	0.175E-08	0.167E-08	38 ± 4
27,40	17.9	133	328	291	0.138E-07	0.109E-08	0.153E-08	0.119E-08	44 ± 3
27,41	15.0	145	330	284	0.209E-07	0.231E-08	0.229E-08	0.194E-08	37 ± 3
27,42	13.0	162	332	281	0.231E-07	0.281E-08	0.256E-08	0.230E-08	34 ± 3
27,43	12.3	-178	332	279	0.224E-07	0.261E-08	0.248E-08	0.188E-08	39 ± 3
27,44	13.3	-158	332	282	0.192E-07	0.502E-08	0.210E-08	0.184E-08	36 ± 3
27,45	15.5	-142	330	286	0.158E-07	0.211E-08	0.175E-08	0.134E-08	42 ± 3
27,47	21.9	-124	325	304	0.151E-07	0.196E-08	0.166E-08	0.220E-08	32 ± 4
28,34	40.4	113	300	377	0.499E-08	0.138E-08	0.564E-09	0.777E-09	48 ± 7
28,35	37.1	116	305	362	0.839E-08	0.147E-08	0.947E-09	0.100E-08	48 ± 5
28,36	33.8	119	310	348	0.101E-07	0.146E-08	0.113E-08	0.135E-08	42 ± 5
28,37	30.5	123	315	334	0.892E-08	0.170E-08	0.100E-08	0.917E-09	50 ± 5
	(deg)		(MeV)		(fm ² /MeVsr ²)				%

Table A5: Continued.

<i>bars</i>	Θ_{pn}^{CM}	Φ_{pn}^{CM}	T_{kin}	p_m	$d^5\sigma_{\text{exp}}$	$\pm \delta\sigma_{\text{stat}}$	$\pm \delta\sigma_{\text{syst}}$	$\pm \delta\sigma_{\text{eff}}$	η_{23}
28,38	27.2	128	319	322	0.108E-07	0.141E-08	0.120E-08	0.106E-08	46 ± 4
28,39	24.1	134	323	311	0.127E-07	0.238E-08	0.142E-08	0.147E-08	37 ± 4
28,40	21.2	143	325	301	0.140E-07	0.248E-08	0.153E-08	0.156E-08	39 ± 4
28,41	19.0	153	327	294	0.167E-07	0.259E-08	0.186E-08	0.169E-08	37 ± 3
28,42	17.5	167	329	291	0.224E-07	0.308E-08	0.250E-08	0.223E-08	38 ± 3
28,43	17.0	-179	329	290	0.203E-07	0.328E-08	0.227E-08	0.208E-08	35 ± 3
28,44	17.7	-164	328	291	0.157E-07	0.167E-08	0.176E-08	0.117E-08	45 ± 3
28,45	19.3	-151	327	296	0.132E-07	0.205E-08	0.146E-08	0.126E-08	44 ± 4
28,46	21.7	-141	325	303	0.728E-08	0.127E-08	0.801E-09	0.101E-08	39 ± 5
29,34	42.0	119	297	383	0.582E-08	0.185E-08	0.660E-09	0.804E-09	51 ± 7
29,35	38.9	122	302	369	0.536E-08	0.116E-08	0.601E-09	0.510E-09	60 ± 5
29,36	35.9	125	307	356	0.743E-08	0.145E-08	0.839E-09	0.830E-09	53 ± 6
29,37	32.9	129	312	345	0.829E-08	0.141E-08	0.930E-09	0.119E-08	42 ± 6
29,38	29.9	135	316	333	0.847E-08	0.134E-08	0.941E-09	0.882E-09	47 ± 4
29,39	27.3	141	319	322	0.102E-07	0.196E-08	0.114E-08	0.113E-08	44 ± 4
29,40	24.9	149	322	314	0.127E-07	0.234E-08	0.143E-08	0.193E-08	34 ± 5
29,41	23.1	159	324	308	0.134E-07	0.228E-08	0.149E-08	0.152E-08	38 ± 4
29,42	21.9	169	325	304	0.131E-07	0.203E-08	0.145E-08	0.133E-08	39 ± 3
29,43	21.5	-179	325	303	0.176E-07	0.258E-08	0.198E-08	0.178E-08	34 ± 3
29,44	22.1	-167	325	305	0.131E-07	0.212E-08	0.144E-08	0.125E-08	44 ± 4
29,45	23.4	-157	323	308	0.159E-07	0.239E-08	0.174E-08	0.234E-08	31 ± 4
29,46	25.3	-147	321	315	0.663E-08	0.165E-08	0.743E-09	0.825E-09	40 ± 4
29,47	27.7	-140	318	323	0.370E-08	0.143E-08	0.410E-09	0.699E-09	36 ± 6
30,34	43.8	124	294	392	0.614E-08	0.281E-08	0.675E-09	0.131E-08	39 ± 8
30,35	41.0	127	299	379	0.703E-08	0.182E-08	0.799E-09	0.962E-09	51 ± 7
30,36	38.2	131	304	368	0.588E-08	0.164E-08	0.652E-09	0.772E-09	48 ± 6
30,37	35.5	135	308	355	0.692E-08	0.169E-08	0.786E-09	0.933E-09	45 ± 6
30,38	33.0	140	312	345	0.106E-07	0.176E-08	0.120E-08	0.143E-08	42 ± 5
30,39	30.6	147	315	335	0.123E-07	0.210E-08	0.140E-08	0.200E-08	33 ± 5
30,40	28.7	154	317	327	0.955E-08	0.189E-08	0.108E-08	0.148E-08	35 ± 5
30,42	26.2	171	320	318	0.124E-07	0.287E-08	0.139E-08	0.188E-08	34 ± 5
30,43	25.9	-179	320	317	0.107E-07	0.187E-08	0.119E-08	0.110E-08	44 ± 4
30,47	31.1	-145	314	336	0.189E-08	0.590E-09	0.211E-09	0.462E-09	32 ± 7
	(deg)		(MeV)		(fm ² /MeVsr ²)				%

Table A5: Continued.

<i>bars</i>	Θ_{pn}^{CM}	Φ_{pn}^{CM}	T_{kin}	p_m	$d^5\sigma_{exp}$	$\pm \delta\sigma_{stat}$	$\pm \delta\sigma_{syst}$	$\pm \delta\sigma_{eff}$	η_{23}	*
26,40	31.1	30	158	164	0.485E-07	0.131E-07	0.735E-08	0.265E-08	84 ± 7	*
26,43	27.2	-1	161	146	0.643E-07	0.211E-07	0.487E-08	0.257E-08	95 ± 5	
27,40	26.4	36	162	144	0.829E-07	0.167E-07	0.629E-08	0.431E-08	86 ± 5	
27,41	23.8	25	163	132	0.134E-06	0.293E-07	0.101E-07	0.548E-08	87 ± 4	
27,42	22.1	13	164	125	0.145E-06	0.226E-07	0.110E-07	0.587E-08	86 ± 4	
27,43	21.6	-1	165	123	0.165E-06	0.285E-07	0.124E-07	0.551E-08	86 ± 3	
27,44	22.3	-15	164	126	0.106E-06	0.239E-07	0.804E-08	0.407E-08	89 ± 4	
27,45	24.2	-27	163	134	0.763E-07	0.250E-07	0.578E-08	0.568E-08	80 ± 8	
27,46	27.0	-38	161	146	0.709E-07	0.236E-07	0.537E-08	0.231E-08	95 ± 4	
28,36	38.2	66	153	196	0.395E-07	0.128E-07	0.300E-08	0.257E-08	87 ± 8	
28,39	25.8	52	162	141	0.826E-07	0.174E-07	0.625E-08	0.201E-08	94 ± 3	
28,40	22.0	44	164	124	0.194E-06	0.351E-07	0.147E-07	0.665E-08	85 ± 3	
28,41	18.9	32	166	112	0.264E-06	0.346E-07	0.200E-07	0.598E-08	91 ± 2	
28,42	16.7	17	167	104	0.226E-06	0.290E-07	0.171E-07	0.271E-08	96 ± 1	
28,43	16.1	-2	167	100	0.260E-06	0.353E-07	0.197E-07	0.547E-08	91 ± 2	
28,44	17.0	-20	167	104	0.208E-06	0.279E-07	0.158E-07	0.605E-08	89 ± 3	
28,45	19.4	-35	166	114	0.194E-06	0.349E-07	0.147E-07	0.553E-08	90 ± 3	
28,46	22.7	-46	164	128	0.175E-06	0.312E-07	0.132E-07	0.157E-07	65 ± 8	
28,47	26.5	-53	162	145	0.391E-07	0.149E-07	0.296E-08	0.271E-08	76 ± 7	
29,37	31.6	71	158	166	0.594E-07	0.277E-07	0.451E-08	0.345E-08	85 ± 7	
29,38	27.1	67	161	146	0.992E-07	0.194E-07	0.753E-08	0.447E-08	85 ± 5	
29,39	22.7	62	164	128	0.264E-06	0.324E-07	0.201E-07	0.903E-08	83 ± 3	
29,40	18.4	55	166	110	0.339E-06	0.365E-07	0.256E-07	0.950E-08	84 ± 3	
29,41	14.5	43	168	95	0.557E-06	0.454E-07	0.422E-07	0.874E-08	92 ± 1	
29,42	11.6	24	169	85	0.673E-06	0.688E-07	0.510E-07	0.122E-07	89 ± 2	
29,43	10.7	-3	169	82	0.749E-06	0.860E-07	0.567E-07	0.142E-07	89 ± 2	
29,44	12.1	-28	169	87	0.575E-06	0.457E-07	0.435E-07	0.991E-08	90 ± 2	
29,45	15.2	-46	168	98	0.551E-06	0.467E-07	0.417E-07	0.134E-07	87 ± 2	
29,46	19.2	-57	166	113	0.316E-06	0.434E-07	0.239E-07	0.120E-07	82 ± 4	
29,47	23.5	-63	164	131	0.232E-06	0.371E-07	0.175E-07	0.102E-07	79 ± 4	
30,37	29.9	80	159	158	0.746E-07	0.283E-07	0.569E-08	0.270E-08	90 ± 4	
30,38	25.2	78	163	138	0.191E-06	0.391E-07	0.145E-07	0.504E-08	91 ± 3	
30,39	20.5	75	165	118	0.360E-06	0.431E-07	0.273E-07	0.898E-08	88 ± 3	
30,40	15.7	70	167	99	0.635E-06	0.654E-07	0.481E-07	0.180E-07	81 ± 3	
30,41	11.1	61	169	84	0.115E-05	0.791E-07	0.873E-07	0.167E-07	88 ± 1	
30,42	7.1	41	170	72	0.139E-05	0.768E-07	0.106E-06	0.175E-07	90 ± 1	
30,43	5.4	-5	170	68	0.140E-05	0.713E-07	0.106E-06	0.179E-07	89 ± 1	
30,44	7.8	-46	170	74	0.139E-05	0.809E-07	0.105E-06	0.175E-07	90 ± 1	
30,45	12.0	-63	169	86	0.821E-06	0.614E-07	0.622E-07	0.108E-07	92 ± 1	
30,46	16.6	-71	167	103	0.499E-06	0.503E-07	0.380E-07	0.110E-07	86 ± 2	
30,47	21.4	-76	165	122	0.312E-06	0.430E-07	0.237E-07	0.116E-07	82 ± 4	
	(deg)		(MeV)		(fm ² /MeVsr ²)				%	

Table A6: Results for energy transfer bin E2 in the feb97 measurement. Central kinematics: $\omega = 175$ MeV, $\vec{q} = 527$ MeV/c, $Q^2 = -0.25$ (GeV/c)², $\Theta_q = 61^\circ$. The data point marked with a star is a passing value, all others are combined passing and stopping values.

<i>bars</i>	Θ_{pn}^{CM}	Φ_{pn}^{CM}	T_{kin}	p_m	$d^5\sigma_{exp}$	$\pm \delta\sigma_{stat}$	$\pm \delta\sigma_{syst}$	$\pm \delta\sigma_{eff}$	η_{23}
26,43	16.1	-2	210	157	0.312E-07	0.134E-07	0.506E-08	0.128E-08	92 ± 3
27,40	17.9	53	209	163	0.299E-07	0.122E-07	0.486E-08	0.151E-08	89 ± 4
27,41	14.4	41	211	152	0.508E-07	0.147E-07	0.824E-08	0.203E-08	92 ± 3
27,42	11.8	22	212	146	0.608E-07	0.156E-07	0.985E-08	0.126E-08	96 ± 2
27,43	10.9	-2	212	143	0.628E-07	0.156E-07	0.101E-07	0.179E-08	94 ± 2
27,44	12.2	-26	211	145	0.422E-07	0.176E-07	0.685E-08	0.155E-08	92 ± 3
27,45	15.0	-43	210	153	0.366E-07	0.122E-07	0.594E-08	0.134E-08	93 ± 3
27,47	22.6	-62	206	179	0.305E-07	0.136E-07	0.495E-08	0.320E-08	77 ± 8
28,38	24.1	76	205	184	0.290E-07	0.988E-08	0.471E-08	0.236E-08	84 ± 6
28,40	15.2	68	210	154	0.650E-07	0.225E-07	0.105E-07	0.288E-08	87 ± 3
28,41	10.9	58	212	143	0.732E-07	0.237E-07	0.119E-07	0.237E-08	92 ± 3
28,42	7.3	37	213	136	0.750E-07	0.218E-07	0.122E-07	0.182E-08	94 ± 2
28,43	5.8	-5	213	134	0.100E-06	0.666E-08	0.162E-07	0.295E-08	91 ± 2
28,44	7.9	-43	213	138	0.739E-07	0.195E-07	0.120E-07	0.426E-08	81 ± 4
28,45	11.7	-61	212	146	0.581E-07	0.140E-07	0.948E-08	0.496E-08	73 ± 6
28,46	16.1	-69	210	157	0.576E-07	0.191E-07	0.935E-08	0.102E-07	55 ± 9
29,37	27.6	88	202	197	0.107E-07	0.318E-08	0.175E-08	0.948E-09	86 ± 7
29,38	23.2	88	205	180	0.341E-07	0.160E-07	0.556E-08	0.261E-08	86 ± 6
29,39	18.6	88	208	164	0.678E-07	0.221E-07	0.110E-07	0.392E-08	84 ± 4
29,40	13.9	87	211	151	0.639E-07	0.208E-07	0.103E-07	0.346E-08	83 ± 4
29,41	9.2	85	212	139	0.133E-06	0.214E-07	0.215E-07	0.467E-08	88 ± 3
29,42	4.4	80	213	132	0.125E-06	0.279E-07	0.204E-07	0.318E-08	94 ± 2
29,43	0.9	-30	214	131	0.120E-06	0.256E-07	0.195E-07	0.422E-08	88 ± 3
29,44	5.3	-82	213	133	0.125E-06	0.236E-07	0.203E-07	0.424E-08	88 ± 3
29,45	10.1	-86	212	141	0.774E-07	0.259E-07	0.126E-07	0.505E-08	78 ± 5
29,46	14.8	-87	210	153	0.731E-07	0.209E-07	0.119E-07	0.622E-08	72 ± 6
30,39	18.7	102	208	165	0.574E-07	0.164E-07	0.931E-08	0.245E-08	91 ± 3
30,40	14.3	107	211	152	0.582E-07	0.148E-07	0.945E-08	0.298E-08	83 ± 4
30,41	9.9	114	212	140	0.119E-06	0.274E-07	0.193E-07	0.351E-08	91 ± 2
30,42	5.9	134	213	134	0.122E-06	0.265E-07	0.199E-07	0.345E-08	91 ± 2
30,43	4.1	-174	213	131	0.122E-06	0.397E-07	0.199E-07	0.364E-08	90 ± 2
30,44	6.6	-128	213	135	0.111E-06	0.273E-07	0.180E-07	0.562E-08	81 ± 4
30,45	10.7	-112	212	143	0.111E-06	0.342E-07	0.179E-07	0.951E-08	68 ± 5
	(deg)		(MeV)		(fm ² /MeVsr ²)				%

Table A7: Results for energy transfer bin E3 in the feb97 measurement. Central kinematics: $\omega = 225$ MeV, $\vec{q} = 538$ MeV/c, $Q^2 = -0.24$ (GeV/c)², $\Theta_q = 56^\circ$.

<i>bars</i>	Θ_{pn}^{CM}	Φ_{pn}^{CM}	T_{kin}	p_m	$d^5\sigma_{exp}$	$\pm \delta\sigma_{stat}$	$\pm \delta\sigma_{syst}$	$\pm \delta\sigma_{eff}$	η_{23}
27,42	4.8	63	254	185	0.283E-07	0.137E-07	0.355E-08	0.649E-09	87 ± 2
27,43	2.2	-12	255	185	0.172E-07	0.516E-08	0.217E-08	0.527E-09	81 ± 2
28,38	22.6	97	246	227	0.106E-07	0.440E-08	0.133E-08	0.650E-09	79 ± 4
29,42	8.6	151	254	191	0.335E-07	0.167E-07	0.423E-08	0.182E-08	66 ± 3
30,43	12.2	-178	252	197	0.217E-07	0.880E-08	0.273E-08	0.125E-08	65 ± 3
	(deg)		(MeV)		(fm ² /MeVsr ²)				%

Table A8: Results for energy transfer bin E4 in the feb97 measurement. Central kinematics: $\omega = 275$ MeV, $\vec{q} = 553$ MeV/c, $Q^2 = -0.23$ (GeV/c)², $\Theta_q = 51^\circ$.

<i>bars</i>	Θ_{pn}^{CM}	Φ_{pn}^{CM}	T_{kin}	p_m	$d^5\sigma_{\text{exp}}$	$\pm \delta\sigma_{\text{stat}}$	$\pm \delta\sigma_{\text{syst}}$	$\pm \delta\sigma_{\text{eff}}$	η_{23}
17,37	48.2	32	250	375	0.260E-08	0.122E-08	0.578E-09	0.776E-09	42 ± 12
17,38	46.5	28	254	367	0.297E-08	0.136E-08	0.668E-09	0.924E-09	40 ± 12
17,40	43.8	17	258	354	0.442E-08	0.185E-08	0.981E-09	0.868E-09	49 ± 9
17,42	42.3	5	260	347	0.437E-08	0.174E-08	0.968E-09	0.149E-08	35 ± 12
17,43	42.1	-1	261	347	0.354E-08	0.128E-08	0.770E-09	0.108E-08	39 ± 12
17,44	42.4	-7	260	347	0.372E-08	0.110E-08	0.817E-09	0.892E-09	42 ± 10
18,40	39.8	19	264	336	0.313E-08	0.945E-09	0.689E-09	0.613E-09	52 ± 10
18,41	38.7	13	266	331	0.422E-08	0.124E-08	0.930E-09	0.710E-09	49 ± 8
18,42	38.0	6	267	329	0.279E-08	0.948E-09	0.614E-09	0.588E-09	45 ± 9
18,43	37.8	-1	267	328	0.260E-08	0.909E-09	0.573E-09	0.412E-09	51 ± 8
19,37	41.6	39	262	345	0.213E-08	0.800E-09	0.473E-09	0.530E-09	41 ± 10
19,40	35.6	22	270	318	0.337E-08	0.912E-09	0.741E-09	0.385E-09	61 ± 6
19,41	34.4	15	272	313	0.410E-08	0.116E-08	0.900E-09	0.579E-09	57 ± 8
19,42	33.6	7	273	310	0.237E-08	0.715E-09	0.522E-09	0.277E-09	63 ± 7
19,43	33.4	-1	273	308	0.470E-08	0.124E-08	0.103E-08	0.505E-09	62 ± 6
19,44	33.7	-9	273	310	0.325E-08	0.912E-09	0.717E-09	0.275E-09	74 ± 6
20,33	49.5	58	248	381	0.491E-08	0.143E-08	0.109E-08	0.628E-09	64 ± 8
20,34	46.7	55	252	367	0.339E-08	0.908E-09	0.751E-09	0.375E-09	74 ± 8
20,36	41.1	48	262	342	0.341E-08	0.948E-09	0.752E-09	0.273E-09	77 ± 6
20,37	38.3	44	266	329	0.274E-08	0.957E-09	0.604E-09	0.233E-09	75 ± 6
20,40	31.5	25	276	301	0.374E-08	0.111E-08	0.824E-09	0.318E-09	71 ± 6
20,41	30.0	17	277	294	0.417E-08	0.920E-09	0.917E-09	0.353E-09	69 ± 5
20,42	29.0	8	278	291	0.264E-08	0.124E-08	0.582E-09	0.479E-09	44 ± 8
21,37	35.3	49	271	317	0.309E-08	0.105E-08	0.681E-09	0.497E-09	54 ± 8
21,38	32.3	44	274	304	0.311E-08	0.767E-09	0.686E-09	0.322E-09	70 ± 7
21,40	27.3	29	280	285	0.536E-08	0.885E-09	0.118E-08	0.379E-09	73 ± 5
21,41	25.5	20	282	278	0.514E-08	0.103E-08	0.113E-08	0.328E-09	76 ± 4
21,42	24.3	10	283	274	0.603E-08	0.117E-08	0.132E-08	0.572E-09	62 ± 5
21,43	24.0	-1	284	274	0.592E-08	0.115E-08	0.130E-08	0.591E-09	58 ± 5
22,35	39.2	63	265	333	0.413E-08	0.112E-08	0.911E-09	0.617E-09	55 ± 8
22,36	35.8	59	270	319	0.435E-08	0.173E-08	0.963E-09	0.553E-09	55 ± 7
22,37	32.4	55	274	304	0.430E-08	0.107E-08	0.942E-09	0.485E-09	64 ± 7
22,38	29.1	50	278	291	0.559E-08	0.556E-09	0.122E-08	0.591E-09	58 ± 6
22,39	26.0	44	282	281	0.766E-08	0.187E-08	0.169E-08	0.979E-09	49 ± 6
22,40	23.3	35	284	270	0.697E-08	0.111E-08	0.153E-08	0.475E-09	73 ± 4
22,41	21.0	25	286	263	0.681E-08	0.123E-08	0.150E-08	0.392E-09	72 ± 4
22,42	19.6	12	287	259	0.826E-08	0.137E-08	0.181E-08	0.567E-09	65 ± 4
22,43	19.2	-1	288	258	0.959E-08	0.175E-08	0.211E-08	0.671E-09	64 ± 4
22,44	19.8	-15	287	259	0.852E-08	0.146E-08	0.187E-08	0.607E-09	67 ± 4
22,45	21.4	-27	286	264	0.786E-08	0.124E-08	0.173E-08	0.665E-09	61 ± 5
22,46	23.8	-37	284	272	0.663E-08	0.182E-08	0.146E-08	0.119E-08	36 ± 6
22,47	26.6	-45	281	282	0.103E-07	0.211E-08	0.228E-08	0.156E-08	37 ± 5
23,33	44.3	73	257	356	0.597E-08	0.198E-08	0.132E-08	0.189E-08	30 ± 9
23,34	40.8	71	263	341	0.328E-08	0.148E-08	0.730E-09	0.782E-09	43 ± 10
	(deg)		(MeV)		(fm ² /MeVsr ²)				%

Table A9: Results for energy transfer bin E5 in the feb97 measurement. Central kinematics: $\omega = 325$ MeV, $\vec{q} = 572$ MeV/c, $Q^2 = -0.22$ (GeV/c)², $\Theta_q = 46^\circ$.

<i>bars</i>	Θ_{pn}^{CM}	Φ_{pn}^{CM}	T_{kin}	p_m	$d^5\sigma_{\text{exp}}$	$\pm \delta\sigma_{\text{stat}}$	$\pm \delta\sigma_{\text{syst}}$	$\pm \delta\sigma_{\text{eff}}$	η_{23}
23,35	37.3	69	268	325	0.436E-08	0.120E-08	0.969E-09	0.406E-09	68 ± 6
23,36	33.7	66	273	310	0.264E-08	0.802E-09	0.582E-09	0.262E-09	65 ± 6
23,38	26.3	58	281	281	0.312E-08	0.825E-09	0.685E-09	0.326E-09	59 ± 6
23,40	19.5	44	288	260	0.516E-08	0.136E-08	0.114E-08	0.345E-09	67 ± 4
23,41	16.7	32	290	252	0.637E-08	0.887E-09	0.140E-08	0.344E-09	74 ± 4
23,42	14.8	17	291	247	0.610E-08	0.147E-08	0.134E-08	0.293E-09	72 ± 3
23,43	14.2	-2	291	245	0.716E-08	0.112E-08	0.157E-08	0.464E-09	64 ± 4
23,44	15.1	-20	291	248	0.560E-08	0.206E-08	0.123E-08	0.307E-09	69 ± 3
23,45	17.2	-35	289	252	0.624E-08	0.149E-08	0.137E-08	0.497E-09	57 ± 4
23,46	20.1	-45	287	261	0.649E-08	0.322E-08	0.143E-08	0.682E-09	49 ± 5
23,47	23.5	-53	284	271	0.729E-08	0.160E-08	0.161E-08	0.105E-08	38 ± 5
24,34	39.6	77	265	336	0.320E-08	0.131E-08	0.707E-09	0.633E-09	48 ± 9
24,35	35.9	76	270	319	0.460E-08	0.124E-08	0.102E-08	0.540E-09	58 ± 6
24,36	32.0	74	275	304	0.328E-08	0.115E-08	0.722E-09	0.224E-09	79 ± 5
24,37	28.1	71	279	288	0.512E-08	0.977E-09	0.113E-08	0.306E-09	78 ± 4
24,38	24.1	68	284	275	0.752E-08	0.143E-08	0.165E-08	0.438E-09	73 ± 4
24,39	20.2	63	287	261	0.900E-08	0.138E-08	0.199E-08	0.509E-09	74 ± 4
24,40	16.3	56	290	250	0.997E-08	0.169E-08	0.219E-08	0.379E-09	78 ± 2
24,41	12.8	44	292	242	0.105E-07	0.131E-08	0.232E-08	0.359E-09	79 ± 2
24,42	10.2	25	293	237	0.110E-07	0.178E-08	0.242E-08	0.487E-09	72 ± 3
24,43	9.3	-3	293	235	0.125E-07	0.167E-08	0.276E-08	0.552E-09	72 ± 3
24,44	10.6	-29	293	238	0.981E-08	0.167E-08	0.215E-08	0.574E-09	63 ± 3
24,45	13.4	-47	292	244	0.959E-08	0.186E-08	0.211E-08	0.722E-09	55 ± 4
24,46	17.0	-57	289	252	0.145E-07	0.200E-08	0.319E-08	0.185E-08	37 ± 4
25,39	18.4	77	288	256	0.799E-08	0.231E-08	0.175E-08	0.102E-08	41 ± 5
25,40	14.1	72	291	245	0.949E-08	0.143E-08	0.208E-08	0.393E-09	74 ± 3
25,41	9.8	64	293	236	0.132E-07	0.169E-08	0.291E-08	0.468E-09	76 ± 2
25,42	6.0	44	295	232	0.114E-07	0.185E-08	0.251E-08	0.418E-09	73 ± 2
25,43	4.3	-6	295	230	0.164E-07	0.219E-08	0.360E-08	0.555E-09	73 ± 2
25,44	6.7	-50	294	232	0.137E-07	0.179E-08	0.300E-08	0.534E-09	74 ± 2
25,45	10.6	-66	293	238	0.118E-07	0.191E-08	0.260E-08	0.523E-09	69 ± 3
25,46	14.9	-73	291	247	0.120E-07	0.196E-08	0.262E-08	0.976E-09	50 ± 4
25,47	19.2	-77	288	259	0.135E-07	0.194E-08	0.297E-08	0.144E-08	41 ± 4
26,33	42.0	91	261	347	0.426E-08	0.136E-08	0.948E-09	0.686E-09	50 ± 8
26,34	38.3	91	266	329	0.385E-08	0.136E-08	0.850E-09	0.360E-09	69 ± 6
26,35	34.5	91	272	314	0.538E-08	0.108E-08	0.119E-08	0.354E-09	79 ± 5
26,36	30.6	91	277	298	0.713E-08	0.147E-08	0.157E-08	0.469E-09	72 ± 4
26,37	26.5	91	281	281	0.689E-08	0.137E-08	0.152E-08	0.428E-09	70 ± 4
26,38	22.2	92	285	267	0.684E-08	0.123E-08	0.150E-08	0.338E-09	77 ± 3
26,39	17.8	92	289	255	0.115E-07	0.211E-08	0.253E-08	0.722E-09	60 ± 3
26,40	13.4	93	292	244	0.120E-07	0.141E-08	0.263E-08	0.509E-09	73 ± 3
26,41	8.8	94	294	236	0.124E-07	0.138E-08	0.273E-08	0.390E-09	79 ± 2
26,42	4.2	98	295	230	0.142E-07	0.289E-08	0.312E-08	0.555E-09	71 ± 2
26,43	0.8	-145	295	228	0.152E-07	0.229E-08	0.334E-08	0.475E-09	76 ± 2
26,44	5.1	-97	295	231	0.159E-07	0.216E-08	0.349E-08	0.542E-09	73 ± 2
26,45	9.7	-94	293	236	0.131E-07	0.189E-08	0.289E-08	0.725E-09	59 ± 3
26,46	14.2	-92	291	245	0.112E-07	0.281E-08	0.246E-08	0.133E-08	35 ± 4
	(deg)		(MeV)		(fm ² /MeVsr ²)				%

Table A9: Continued.

<i>bars</i>	Θ_{pn}^{CM}	Φ_{pn}^{CM}	T_{kin}	p_m	$d^5\sigma_{\text{exp}}$	$\pm \delta\sigma_{\text{stat}}$	$\pm \delta\sigma_{\text{syst}}$	$\pm \delta\sigma_{\text{eff}}$	η_{23}
26,47	18.7	-92	288	256	0.121E-07	0.240E-08	0.267E-08	0.171E-08	31 ± 4
27,33	42.0	97	261	347	0.679E-08	0.187E-08	0.150E-08	0.125E-08	47 ± 8
27,35	34.7	99	271	314	0.626E-08	0.171E-08	0.139E-08	0.490E-09	71 ± 5
27,36	30.8	100	276	298	0.711E-08	0.165E-08	0.157E-08	0.551E-09	70 ± 5
27,37	26.8	101	281	283	0.716E-08	0.171E-08	0.158E-08	0.682E-09	59 ± 5
27,38	22.7	104	285	269	0.799E-08	0.146E-08	0.176E-08	0.528E-09	68 ± 4
27,39	18.5	107	288	256	0.118E-07	0.189E-08	0.261E-08	0.580E-09	71 ± 3
27,40	14.3	112	291	245	0.950E-08	0.174E-08	0.210E-08	0.524E-09	65 ± 3
27,41	10.3	122	293	237	0.132E-07	0.245E-08	0.291E-08	0.468E-09	73 ± 2
27,42	6.9	143	294	232	0.170E-07	0.187E-08	0.375E-08	0.557E-09	73 ± 2
27,43	5.5	-175	295	232	0.166E-07	0.194E-08	0.367E-08	0.736E-09	65 ± 2
27,44	7.4	-137	294	233	0.158E-07	0.176E-08	0.347E-08	0.552E-09	71 ± 2
27,45	11.0	-120	293	239	0.104E-07	0.168E-08	0.230E-08	0.622E-09	60 ± 3
27,46	15.1	-111	291	248	0.105E-07	0.195E-08	0.232E-08	0.798E-09	50 ± 3
27,47	19.3	-106	288	259	0.152E-07	0.278E-08	0.336E-08	0.167E-08	37 ± 4
28,33	42.4	103	260	348	0.328E-08	0.114E-08	0.727E-09	0.519E-09	51 ± 8
28,34	39.0	104	265	332	0.305E-08	0.125E-08	0.674E-09	0.379E-09	65 ± 8
28,35	35.4	106	271	318	0.783E-08	0.130E-08	0.173E-08	0.632E-09	70 ± 5
28,36	31.7	108	275	301	0.693E-08	0.170E-08	0.153E-08	0.523E-09	70 ± 5
28,37	27.9	111	280	287	0.753E-08	0.144E-08	0.166E-08	0.698E-09	61 ± 5
28,38	24.0	115	284	274	0.592E-08	0.129E-08	0.130E-08	0.482E-09	60 ± 4
28,39	20.2	120	287	261	0.103E-07	0.162E-08	0.228E-08	0.561E-09	69 ± 3
28,40	16.6	128	290	251	0.137E-07	0.259E-08	0.303E-08	0.153E-08	43 ± 4
28,41	13.4	140	292	244	0.125E-07	0.218E-08	0.275E-08	0.728E-09	61 ± 3
28,42	11.1	158	293	239	0.129E-07	0.270E-08	0.284E-08	0.969E-09	50 ± 3
28,43	10.3	-178	293	237	0.178E-07	0.270E-08	0.391E-08	0.165E-08	41 ± 3
29,33	43.2	108	259	352	0.708E-08	0.176E-08	0.157E-08	0.117E-08	47 ± 7
29,34	39.9	110	264	336	0.387E-08	0.891E-09	0.856E-09	0.419E-09	72 ± 7
29,35	36.5	113	269	322	0.438E-08	0.140E-08	0.968E-09	0.379E-09	69 ± 6
29,36	33.0	116	274	308	0.598E-08	0.129E-08	0.131E-08	0.540E-09	67 ± 6
29,37	29.5	119	278	294	0.772E-08	0.221E-08	0.170E-08	0.780E-09	57 ± 5
29,38	26.1	124	282	281	0.633E-08	0.224E-08	0.140E-08	0.100E-08	45 ± 7
29,39	22.7	130	285	269	0.106E-07	0.232E-08	0.234E-08	0.874E-09	54 ± 4
29,40	19.7	139	287	259	0.916E-08	0.221E-08	0.203E-08	0.150E-08	34 ± 5
29,41	17.1	150	289	252	0.143E-07	0.198E-08	0.315E-08	0.133E-08	46 ± 4
29,42	15.4	165	290	247	0.138E-07	0.150E-08	0.304E-08	0.116E-08	48 ± 4
29,43	14.9	-178	291	247	0.136E-07	0.279E-08	0.301E-08	0.123E-08	39 ± 3
29,44	15.7	-162	290	249	0.834E-08	0.350E-08	0.183E-08	0.115E-08	31 ± 4
30,33	44.3	114	257	357	0.524E-08	0.247E-08	0.116E-08	0.856E-09	48 ± 7
30,35	38.0	119	267	329	0.283E-08	0.104E-08	0.623E-09	0.193E-09	82 ± 5
30,36	34.8	122	271	314	0.643E-08	0.312E-08	0.142E-08	0.733E-09	57 ± 6
30,37	31.6	127	275	301	0.687E-08	0.196E-08	0.151E-08	0.683E-09	62 ± 6
30,39	25.7	138	282	279	0.112E-07	0.226E-08	0.247E-08	0.103E-08	52 ± 4
30,42	19.8	168	287	259	0.128E-07	0.250E-08	0.281E-08	0.207E-08	37 ± 5
30,43	19.4	-179	288	259	0.125E-07	0.259E-08	0.274E-08	0.118E-08	46 ± 4
30,44	20.0	-166	287	261	0.112E-07	0.302E-08	0.247E-08	0.160E-08	37 ± 5
	(deg)		(MeV)		(fm ² /MeVsr ²)				%

Table A9: Continued.

bars	Θ_{pn}^{CM}	Φ_{pn}^{CM}	T_{kin}	p_m	$d^5\sigma_{\text{exp}}$	$\pm \delta\sigma_{\text{stat}}$	$\pm \delta\sigma_{\text{syst}}$	$\pm \delta\sigma_{\text{eff}}$	η_{23}
18,41	31.5	16	314	339	0.411E-08	0.136E-08	0.461E-09	0.765E-09	42 ± 8
18,43	30.4	-1	315	334	0.563E-08	0.256E-08	0.610E-09	0.123E-08	35 ± 7
19,40	28.8	27	317	328	0.389E-08	0.161E-08	0.430E-09	0.535E-09	53 ± 7
19,41	27.3	18	319	322	0.598E-08	0.133E-08	0.663E-09	0.102E-08	43 ± 7
19,42	26.3	9	320	318	0.513E-08	0.151E-08	0.568E-09	0.895E-09	42 ± 7
19,43	26.0	-1	320	317	0.494E-08	0.178E-08	0.549E-09	0.623E-09	52 ± 6
19,44	26.4	-11	320	319	0.382E-08	0.937E-09	0.421E-09	0.494E-09	52 ± 6
20,35	39.3	59	302	372	0.244E-08	0.111E-08	0.274E-09	0.330E-09	62 ± 8
20,36	36.2	56	307	358	0.564E-08	0.155E-08	0.635E-09	0.115E-08	44 ± 8
20,37	33.1	51	311	344	0.504E-08	0.105E-08	0.558E-09	0.584E-09	59 ± 6
20,40	24.9	32	322	314	0.459E-08	0.115E-08	0.508E-09	0.450E-09	63 ± 6
21,37	30.6	58	315	335	0.498E-08	0.148E-08	0.560E-09	0.982E-09	41 ± 8
21,38	27.2	53	319	322	0.588E-08	0.260E-08	0.664E-09	0.121E-08	38 ± 7
21,40	21.1	38	325	301	0.638E-08	0.147E-08	0.709E-09	0.625E-09	60 ± 5
21,41	18.8	27	328	295	0.899E-08	0.252E-08	0.999E-09	0.126E-08	41 ± 5
21,42	17.2	14	329	290	0.862E-08	0.157E-08	0.952E-09	0.104E-08	48 ± 5
21,43	16.7	-1	329	289	0.704E-08	0.143E-08	0.771E-09	0.125E-08	35 ± 6
22,36	32.2	69	313	342	0.461E-08	0.160E-08	0.526E-09	0.932E-09	38 ± 7
22,38	24.8	62	322	314	0.421E-08	0.141E-08	0.470E-09	0.599E-09	46 ± 6
22,40	17.7	48	328	291	0.881E-08	0.111E-08	0.980E-09	0.776E-09	57 ± 5
22,41	14.7	36	331	284	0.918E-08	0.169E-08	0.101E-08	0.738E-09	58 ± 4
22,42	12.6	19	332	280	0.993E-08	0.257E-08	0.110E-08	0.105E-08	47 ± 5
22,43	11.9	-2	332	278	0.161E-07	0.224E-08	0.179E-08	0.190E-08	36 ± 4
22,44	12.9	-23	332	281	0.857E-08	0.137E-08	0.953E-09	0.111E-08	42 ± 5
22,45	15.2	-39	330	285	0.101E-07	0.164E-08	0.114E-08	0.133E-08	40 ± 5
23,36	31.0	77	314	336	0.375E-08	0.123E-08	0.419E-09	0.452E-09	53 ± 6
23,37	27.0	75	319	321	0.421E-08	0.108E-08	0.472E-09	0.491E-09	54 ± 6
23,38	23.0	73	324	308	0.389E-08	0.103E-08	0.431E-09	0.430E-09	54 ± 5
23,39	19.0	68	327	294	0.638E-08	0.138E-08	0.697E-09	0.877E-09	45 ± 6
23,40	15.0	62	330	284	0.834E-08	0.146E-08	0.917E-09	0.879E-09	48 ± 5
23,41	11.2	51	333	277	0.808E-08	0.242E-08	0.900E-09	0.732E-09	50 ± 4
23,42	8.2	30	334	272	0.808E-08	0.200E-08	0.910E-09	0.767E-09	45 ± 4
23,43	7.1	-4	334	270	0.914E-08	0.165E-08	0.102E-08	0.935E-09	44 ± 4
23,44	8.7	-35	334	273	0.106E-07	0.188E-08	0.119E-08	0.105E-08	42 ± 4
24,36	30.3	86	315	333	0.570E-08	0.158E-08	0.638E-09	0.666E-09	56 ± 6
24,37	26.3	85	320	318	0.514E-08	0.990E-09	0.574E-09	0.431E-09	64 ± 5
24,38	22.1	84	325	305	0.638E-08	0.128E-08	0.712E-09	0.643E-09	54 ± 5
24,39	17.8	83	328	291	0.125E-07	0.207E-08	0.138E-08	0.902E-09	58 ± 4
24,40	13.4	81	331	281	0.115E-07	0.234E-08	0.128E-08	0.106E-08	50 ± 4
24,41	9.0	76	334	274	0.144E-07	0.206E-08	0.159E-08	0.125E-08	45 ± 3
24,42	4.7	62	335	269	0.159E-07	0.230E-08	0.175E-08	0.130E-08	46 ± 3
24,43	2.2	-11	335	267	0.151E-07	0.173E-08	0.167E-08	0.117E-08	52 ± 4
24,44	5.5	-67	335	269	0.116E-07	0.177E-08	0.129E-08	0.963E-09	49 ± 4
25,40	13.5	102	331	281	0.103E-07	0.167E-08	0.114E-08	0.759E-09	54 ± 4
25,41	9.1	107	334	274	0.117E-07	0.204E-08	0.129E-08	0.860E-09	51 ± 3
25,42	4.9	123	335	269	0.164E-07	0.256E-08	0.182E-08	0.111E-08	48 ± 3
	(deg)		(MeV)		(fm ² /MeVsr ²)				%

Table A10: Results for energy transfer bin E6 in the feb97 measurement. Central kinematics: $\omega = 375$ MeV, $\vec{q} = 594$ MeV/c, $Q^2 = -0.21$ (GeV/c)², $\Theta_q = 42^\circ$.

<i>bars</i>	Θ_{pn}^{CM}	Φ_{pn}^{CM}	T_{kin}	p_m	$d^5\sigma_{exp}$	$\pm \delta\sigma_{stat}$	$\pm \delta\sigma_{syst}$	$\pm \delta\sigma_{eff}$	η_{23}
25,43	2.7	-171	335	267	0.169E-07	0.337E-08	0.188E-08	0.120E-08	47 ± 3
25,44	5.7	-118	335	270	0.147E-07	0.219E-08	0.163E-08	0.111E-08	54 ± 4
25,45	9.9	-106	333	274	0.122E-07	0.158E-08	0.134E-08	0.102E-08	51 ± 4
26,34	38.3	101	303	366	0.357E-08	0.107E-08	0.404E-09	0.561E-09	51 ± 8
26,35	34.7	102	309	352	0.624E-08	0.109E-08	0.699E-09	0.670E-09	62 ± 6
26,36	30.9	103	314	336	0.588E-08	0.121E-08	0.657E-09	0.555E-09	62 ± 5
26,37	27.0	106	319	321	0.556E-08	0.116E-08	0.623E-09	0.598E-09	57 ± 6
26,38	23.0	109	324	308	0.972E-08	0.161E-08	0.108E-08	0.859E-09	56 ± 4
26,39	19.0	113	327	295	0.137E-07	0.221E-08	0.153E-08	0.113E-08	49 ± 4
26,40	15.1	120	330	285	0.117E-07	0.184E-08	0.129E-08	0.820E-09	58 ± 4
26,41	11.5	131	333	278	0.118E-07	0.192E-08	0.130E-08	0.703E-09	63 ± 3
26,42	8.6	151	334	273	0.120E-07	0.233E-08	0.133E-08	0.799E-09	60 ± 4
26,43	7.6	-177	334	271	0.141E-07	0.240E-08	0.156E-08	0.812E-09	60 ± 3
26,44	9.0	-147	334	274	0.163E-07	0.250E-08	0.180E-08	0.142E-08	43 ± 3
26,45	12.1	-128	332	278	0.103E-07	0.205E-08	0.113E-08	0.140E-08	36 ± 4
27,33	42.6	105	296	386	0.520E-08	0.152E-08	0.600E-09	0.910E-09	43 ± 7
27,34	39.2	107	302	371	0.419E-08	0.116E-08	0.472E-09	0.574E-09	58 ± 7
27,35	35.7	109	307	355	0.711E-08	0.155E-08	0.797E-09	0.594E-09	68 ± 5
27,37	28.5	115	317	326	0.663E-08	0.139E-08	0.743E-09	0.617E-09	63 ± 5
27,38	24.8	119	322	314	0.828E-08	0.153E-08	0.926E-09	0.731E-09	60 ± 5
27,39	21.2	125	325	301	0.138E-07	0.223E-08	0.152E-08	0.106E-08	58 ± 4
27,40	17.9	133	328	291	0.840E-08	0.194E-08	0.934E-09	0.753E-09	52 ± 4
27,41	15.0	145	330	284	0.127E-07	0.232E-08	0.140E-08	0.886E-09	55 ± 3
27,42	13.0	162	332	281	0.944E-08	0.145E-08	0.105E-08	0.628E-09	58 ± 3
27,43	12.3	-178	332	279	0.127E-07	0.175E-08	0.142E-08	0.102E-08	54 ± 4
27,44	13.3	-158	332	282	0.106E-07	0.198E-08	0.118E-08	0.690E-09	58 ± 3
27,45	15.5	-142	330	286	0.130E-07	0.207E-08	0.144E-08	0.149E-08	44 ± 5
27,46	18.5	-131	328	294	0.105E-07	0.521E-08	0.119E-08	0.149E-08	35 ± 5
28,33	43.6	111	294	391	0.503E-08	0.240E-08	0.581E-09	0.131E-08	30 ± 8
28,35	37.1	116	305	362	0.489E-08	0.134E-08	0.545E-09	0.508E-09	65 ± 6
28,36	33.8	119	310	348	0.569E-08	0.123E-08	0.638E-09	0.507E-09	65 ± 5
28,37	30.5	123	315	334	0.477E-08	0.189E-08	0.533E-09	0.738E-09	48 ± 7
28,38	27.2	128	319	322	0.581E-08	0.161E-08	0.641E-09	0.746E-09	50 ± 6
28,39	24.1	134	323	311	0.106E-07	0.207E-08	0.119E-08	0.997E-09	55 ± 5
28,40	21.2	143	325	301	0.635E-08	0.281E-08	0.722E-09	0.121E-08	34 ± 6
28,41	19.0	153	327	294	0.862E-08	0.174E-08	0.953E-09	0.111E-08	42 ± 5
28,42	17.5	167	329	291	0.668E-08	0.245E-08	0.739E-09	0.815E-09	41 ± 5
29,35	38.9	122	302	369	0.435E-08	0.109E-08	0.488E-09	0.513E-09	58 ± 6
29,36	35.9	125	307	356	0.640E-08	0.158E-08	0.721E-09	0.598E-09	64 ± 6
29,37	32.9	129	312	345	0.394E-08	0.134E-08	0.444E-09	0.748E-09	41 ± 7
29,39	27.3	141	319	322	0.970E-08	0.208E-08	0.107E-08	0.122E-08	45 ± 5
30,35	41.0	127	299	379	0.400E-08	0.159E-08	0.453E-09	0.521E-09	58 ± 7
30,36	38.2	131	304	368	0.816E-08	0.184E-08	0.927E-09	0.118E-08	50 ± 7
30,37	35.5	135	308	355	0.639E-08	0.181E-08	0.717E-09	0.114E-08	44 ± 8
30,39	30.6	147	315	335	0.807E-08	0.252E-08	0.902E-09	0.104E-08	45 ± 5
30,43	25.9	-179	320	317	0.507E-08	0.197E-08	0.557E-09	0.854E-09	36 ± 6
	(deg)		(MeV)		(fm ² /MeVsr ²)				%

Table A10: Continued.

<i>bin</i>	<i>name</i>	Θ_{pn}^{CM}	Φ_{pn}^{CM}	T_{kin}	p_m	$d^5\sigma_{\text{exp}}$	$\pm \delta\sigma_{\text{stat}}$	$\pm \delta\sigma_{\text{syst}}$	$\pm \delta\sigma_{\text{eff}}$
E2	<i>D4</i>	71.2	-169	114	339	0.195E-08	0.122E-09	0.160E-09	0.488E-09
	<i>S4</i>	91.3	-171	85	416	0.113E-08	0.283E-09	0.926E-10	0.282E-09
E3	<i>D4</i>	73.7	-170	140	403	0.172E-08	0.355E-09	0.143E-09	0.431E-09
	<i>S4</i>	91.5	-172	109	476	0.260E-08	0.289E-09	0.216E-09	0.650E-09
	<i>S3</i>	107.0	-174	81	535	0.244E-08	0.534E-09	0.203E-09	0.611E-09
E4	<i>D4</i>	77.6	-171	162	469	0.146E-08	0.729E-09	0.123E-09	0.365E-09
	<i>S4</i>	94.0	-172	128	540	0.153E-08	0.417E-09	0.129E-09	0.382E-09
	<i>S3</i>	108.5	-173	99	598	0.176E-08	0.617E-09	0.149E-09	0.439E-09
E5	<i>D4</i>	81.8	-172	181	536	0.138E-08	0.658E-10	0.116E-09	0.345E-09
	<i>S4</i>	97.2	-173	145	605	0.176E-08	0.693E-10	0.149E-09	0.439E-09
	<i>S3</i>	110.9	-173	114	661	0.173E-08	0.739E-10	0.146E-09	0.432E-09
	<i>T4</i>	123.1	-174	88	703	0.164E-08	0.920E-10	0.139E-09	0.411E-09
	<i>T2</i>	134.0	-174	68	735	0.200E-08	0.105E-09	0.170E-09	0.500E-09
E6	<i>D4</i>	86.0	-172	197	601	0.126E-08	0.631E-10	0.106E-09	0.315E-09
	<i>S4</i>	100.7	-173	159	669	0.187E-08	0.721E-10	0.159E-09	0.468E-09
	<i>S3</i>	113.7	-173	126	722	0.201E-08	0.831E-10	0.169E-09	0.504E-09
	<i>T4</i>	125.3	-174	100	764	0.151E-08	0.880E-10	0.127E-09	0.379E-09
	<i>T2</i>	135.8	-174	80	798	0.209E-08	0.109E-09	0.176E-09	0.521E-09
E7	<i>D4</i>	90.0	-172	211	664	0.988E-09	0.618E-10	0.828E-10	0.247E-09
	<i>S4</i>	104.1	-173	171	731	0.149E-08	0.697E-10	0.124E-09	0.371E-09
	<i>S3</i>	116.6	-173	138	785	0.138E-08	0.724E-10	0.116E-09	0.346E-09
	<i>T4</i>	127.7	-174	111	827	0.125E-08	0.811E-10	0.105E-09	0.312E-09
	<i>T2</i>	137.8	-174	90	859	0.147E-08	0.100E-09	0.124E-09	0.368E-09
E8	<i>D4</i>	93.8	-173	224	726	0.692E-09	0.529E-10	0.602E-10	0.173E-09
	<i>S4</i>	107.4	-173	182	793	0.781E-09	0.546E-10	0.679E-10	0.195E-09
	<i>S3</i>	119.5	-173	148	846	0.774E-09	0.437E-10	0.674E-10	0.194E-09
	<i>T4</i>	130.2	-174	120	887	0.520E-09	0.744E-10	0.453E-10	0.130E-09
	<i>T2</i>	139.9	-174	98	917	0.584E-09	0.939E-10	0.510E-10	0.146E-09
E9	<i>D4</i>	97.4	-173	236	787	0.395E-09	0.506E-10	0.342E-10	0.988E-10
	<i>S4</i>	110.6	-173	192	854	0.574E-09	0.559E-10	0.496E-10	0.144E-09
	<i>S3</i>	122.2	-173	157	907	0.303E-09	0.550E-10	0.261E-10	0.757E-10
	<i>T4</i>	132.5	-174	129	947	0.336E-09	0.677E-10	0.290E-10	0.839E-10
	<i>T2</i>	142.0	-174	107	978	0.314E-09	0.669E-10	0.271E-10	0.786E-10
E10	<i>D4</i>	100.7	-173	247	847	0.208E-09	0.338E-10	0.185E-10	0.519E-10
	<i>S4</i>	113.5	-173	201	913	0.109E-09	0.296E-10	0.957E-11	0.271E-10
	<i>S3</i>	124.8	-173	165	965	0.141E-09	0.240E-10	0.126E-10	0.354E-10
	<i>T4</i>	134.8	-174	136	1005	0.213E-09	0.263E-10	0.190E-10	0.532E-10
	<i>T2</i>	144.0	-173	114	1036	0.317E-10	0.277E-10	0.286E-11	0.793E-11
		(deg)		(MeV)		(fm ² /MeVsr ²)			

Table A11: Results for the telescopes in the feb97 measurement. The values for the angles, proton energy and missing momentum refer to the centre of the telescope bar.

Samenvatting

In dit proefschrift worden de resultaten beschreven van een ${}^2H(e, e'p)n$ experiment, d.w.z. een meting waarbij een deuteriumkern door middel van elektronen wordt opgebroken in een proton en een neutron en waarbij naast het verstrooide elektron ook het verstrooide proton wordt gedetecteerd.

Dergelijke verstrooiingsexperimenten bieden een goede mogelijkheid om de zogenaamde *sterke wisselwerking* tussen de bouwstenen van een atoomkern te onderzoeken. Deze wisselwerking is een van de vier fundamentele natuurkrachten en wordt theoretisch beschreven door de quantumchromodynamica (QCD). Op dit moment is het echter nog niet mogelijk om vanuit de elementaire beschrijving in termen van quarks en gluonen rechtstreeks de resultaten van een dergelijk experiment te berekenen. Daarom maakt men veelal gebruik van “effectieve” modellen, die gebaseerd zijn op een empirische wisselwerking tussen de kerndeeltjes (protonen en neutronen). Het effect van de onderliggende (quark-)structuur van deze *nucleonen* wordt in dergelijke modellen verdisconteerd door het toevoegen van tijdelijk aangeslagen toestanden van de nucleonen (*isobar configurations*, IC) en van de uitwisseling van virtuele deeltjes tussen de nucleonen (*meson exchange currents*, MEC). In diverse experimenten uit de afgelopen jaren is vastgesteld, dat dergelijke effecten met name belangrijk zijn in het energiebereik voorbij het zogenaamde *quasi-elastische* gebied.

Het doel van ons experiment was het meten van de differentiële werkzame doorsnede over een groot energiebereik. Hierbij wilden we een zo groot mogelijke ruimtehoek bestrijken als aanvulling op de bestaande experimentele gegevens in het verstrooiingsvlak. Zo'n brede experimentele gegevensverzameling is een ijkpunt voor de hierboven genoemde modelberekeningen en helpt bij het bepalen van interessante gebieden voor toekomstige (precisie-)metingen.

Het experiment is uitgevoerd met de ELSA elektronenversneller van de Universiteit van Bonn, Duitsland, bij een bundelenergie $E_0 = 1.600$ GeV en een vier-impulsoverdracht rond $Q^2 = -0.20$ (GeV/c) 2 . De verstrooide elektronen zijn gedetecteerd in de magnetische spectrometer, ELAN, de protonen in gesegmenteerde scintillatiedetectoren, *TOF-walls*, met ieder een oppervlakte van 3×3 m 2 . Tevens zijn nog enkele, 1 m lange, scintillatoren gebruikt. Deze *telescopes*

waren geplaatst op grote protonhoeken.

De resultaten zijn op grond van de energie van het verstrooide elektron in tien delen (*bins*) verdeeld, waarbij elke *bin* een breedte had van 50 MeV. De protonen zijn geïdentificeerd aan de hand van gelijktijdige signalen in twee achter elkaar gelegen scintillatoren. Bij hogere energieën worden er echter ook steeds meer protonen gemeten van reacties, waarin ook nog een pion wordt gecreëerd. Met behulp van een *breakup-selectieparameter* – samengesteld uit alle ADC- en TDC-informatie van een gebeurtenis en de behoudswetten voor de ${}^2H(e, e'p)n$ reactie – zijn de gewenste “breakup” protonen gescheiden van de achtergrond van protonen uit dergelijke ${}^2H(e, e'N)N\pi$ reacties. In wezen is dit equivalent aan een scheiding op basis van de *ontbrekende massa*, maar op deze manier zijn er minder (niet-lineaire) omrekeningen nodig van de gemeten grootheden.

Het uiteindelijke aantal gedetecteerde gebeurtenissen is gecorrigeerd voor protonen die geen signaal hebben gegeven in de detectoren, of die niet als (relevant) proton zijn herkend in één van de analysestappen. De correctiefactor is bepaald aan de hand van de meetwaarden zelf, omdat de geplande onafhankelijke bepaling van de waarde in een aparte meting niet haalbaar bleek. Hiervoor zou namelijk het bij een gemeten proton behorende neutron in één van de *telescopes* gedetecteerd moeten worden, maar daarvoor was de achtergrond in de *telescopes* te sterk. Het gevolg is wel, dat de correctie in de hoogste *bins* statistisch niet erg nauwkeurig kan zijn. Daar wordt de totale meetfout dan ook gedomineerd door de onzekerheid in deze *efficiency* correctiefactor. Meetpunten, waarvoor de berekende *efficiency* heel erg klein en/of heel erg onzeker is, zijn in het eindresultaat buiten beschouwing gelaten. Met name hierdoor houden we ten slotte voor de *TOF-walls* meetresultaten over in slechts vijf *bins*. Deze *bins* komen overeen met een energieoverdracht tussen 150 MeV en 400 MeV (gemeten in het laboratoriumstelsel), oftewel vanaf het quasi-elastische gebied tot net onder de $\Delta(1232)$ -resonantie. In het geval van de *telescopes* hebben we de *efficiency* voor protonen geschat aan de hand van de achtergrond in de gemeten spectra. Hierdoor zijn er voor de *telescopes* wel meetresultaten in alle *bins*, oftewel voor waarden van de energieoverdracht tot 600 MeV.

Ons experiment omvatte twee meetperioden (in opeenvolgende jaren), die afzonderlijk zijn geanalyseerd. Helaas komen de twee deelresultaten niet helemaal overeen, hoewel we ons veel moeite hebben getroost om de verschillen te verklaren. De meetresultaten van de tweede periode liggen gemiddeld een factor 0,6 lager dan die van de eerste periode. Aangezien het niet mogelijk bleek om een van beide deelresultaten als onjuist terzijde te schuiven, is het eindresultaat van het experiment het gemiddelde van de twee metingen. Om de gevonden spreiding te verdisconteren hebben we de systematische fout met 20% verhoogd.

De uiteindelijke meetresultaten voor de werkzame doorsnede bestrijken een aanzienlijk gebied buiten het verstrooiingsvlak van de elektronen. Voor protonhoeken tussen $\Theta_{pn}^{\text{CM}} = 20^\circ$ en $\Theta_{pn}^{\text{CM}} = 30^\circ$ hebben we bijna het volledige azimu-

tale hoekbereik afgetast, terwijl voor protonhoeken tot 50° à 60° bijna de helft van dit bereik is gemeten. Tevens hebben we met behulp van de *telescopes* nog meetresultaten verkregen voor de werkzame doorsnede in het verstrooiingsvlak tot $\Theta_{pn}^{\text{CM}} = 145^\circ$. Dit laatste komt overeen met een *ontbrekende impuls* $p_m = 1000 \text{ MeV}/c$.

De afhankelijkheid van de werkzame doorsnede van de azimutale protonhoek Φ_{pn}^{CM} is duidelijk zichtbaar in de meetgegevens. Uit deze afhankelijkheid is de interferentie-structuurfunctie f_{LT} bepaald voor protonhoeken tot 40° (in het zwaartepuntstelsel). Bovendien is in hetzelfde hoekbereik een combinatie van de twee dominante structuurfuncties f_L en f_T bepaald.

De meetresultaten zijn vergeleken met berekeningen van het “volledige” model van Arenhövel *et al.* In het grootste deel van het door ons gemeten gebied wordt de *vorm* van de werkzame doorsnede en van de structuurfuncties goed beschreven door het model, maar er blijven verschillen in de *ijking*, met name bij de hogere energieën. Dit duidt erop dat het model de subnucleaire vrijheidsgraden nog niet volledig onder de knie heeft. Zo bevestigen onze resultaten de conclusies van eerdere metingen, dat die subnucleaire vrijheidsgraden van groot belang zijn zodra men zich begeeft buiten het quasi-elastische gebied.

Bij toekomstige $^2H(e, e'p)n$ metingen, bijvoorbeeld bij de versnellers van TJNAF of MAMI, zal het waarschijnlijk niet mogelijk zijn om in één keer een vergelijkbaar groot kinematisch bereik te omvatten als in ons experiment. De verhoogde nauwkeurigheid, ten gevolge van de hogere luminositeit en de meer precieze detectoren, zal dit nadeel echter ruimschoots compenseren. Desondanks zou men nog steeds kunnen proberen een zo groot mogelijke ruimtehoek ineens te bestrijken, om zo een brede overzichtsmeting uit te voeren, bijvoorbeeld met behulp van de OOPS detectoren van Bates.

Nawoord

*Het enige wat overblijft is te genieten
van wat je met gezwog bereikt hebt.*
Prediker 2:24a (Groot Nieuws vertaling)

Hoewel ik bovenstaande tekst wel enigszins uit zijn verband heb gerukt – want in tegenstelling tot de Prediker ervaar ik mijn proefschrift toch niet echt als enkel *lucht en leegte* – geeft hij mijn gevoel op dit moment vrij goed weer. Het voorbereiden en schrijven van dit proefschrift heeft erg lang geduurd. In elk geval veel langer dan ik verwachtte, toen ik er eind 1992 vol enthousiasme aan begon. En ook nog veel langer dan ik hoopte, toen ik me in 1998 alvast op een nieuwe baan stortte. Het grootste probleem – het verschil tussen de twee metingen – kwam pas enkele maanden daarna aan het licht, op het moment dat ik eigenlijk dacht het eindresultaat al in handen te hebben. Daarom mag er wat mij betreft best van gezwog worden gesproken, maar omdat *all's well that ends well* is het nu tijd om te genieten van het feit dat de eindstreep is gehaald.

Door de lange doorlooptijd zijn er extra veel mensen, die op de een of andere manier een bijdrage hebben geleverd aan de totstandkoming van dit boekwerk.

Mijn promotor, Peter de Witt Huberts, wil ik bedanken voor zijn geduld. Zeker toen ik nog druk zocht naar de verschillen tussen de twee metingen, duurde het vaak erg lang voordat je weer iets van mij hoorde. Pas in de laatste fase, het schrijven, kon ons contact intensiever zijn – relatief gezien dan, vanwege mijn 40-urige werkweek elders. Bedankt voor je input op het manuscript, met name ook voor je bredere blik op de context van mijn onderzoek.

Daarnaast wil ik Denise en Prisca bedanken voor de ontelbare uren, dagen en zelfs enkele weken, die ze hun echtgenoot / vader aan mij hebben uitgeleend: voor overleg in Utrecht of op het NIKHEF, voor het steeds weer zoeken naar een nieuwe ingang, waardoor ik weer gemotiveerd verder kon speuren, voor reizen naar Bonn, voor het corrigeren van teksten en nog veel meer. En dan heb ik de “sociale” bezoeken aan Amstelveen en de wijnimport nog niet eens genoemd¹.

Bei Prof. Dr. B. Schoch und Dr. Ralf Gothe möchte ich mich gerne bedanken für die Möglichkeit teil zu nehmen an den Experimenten mit dem Flugzeitspektrometer. Besonders will ich auch die relativ kurzfristig geplante neue ²H(e, e'p)n Messung erwähnen, nachdem meine erste Messung nicht völlig gelungen war.

¹ en iets anders ook niet...

Danke auch dafür! Der gesamten Bedienungsmannschaft von ELSA danke ich für ihren Einsatz beim Betrieb der Beschleunigeranlage während meines Experiments. Sie haben mir immer wieder einen guten Elektronenstrahl geliefert! Und dann gibt es noch die ELANi's – Detlef, Dirk, Helmut, Henning, Patrick, Tina und Rene, Jörn: ihr habt mich ganz freundlich geholfen und in euere Gruppe aufgenommen, und das nicht nur *während* der Arbeitszeit. Dadurch habt ihr mir eine sehr schöne Zeit in Bonn besorgt! Tina möchte ich auch noch speziell danken, weil sie nachdem so oft und so schnell meine Fragen beantwortet hat (schau mal nach in meinem Literaturverzeichnis).

De tijd dat ik dagelijks rondliep binnen de vakgroep subatomaire fysica van de Universiteit Utrecht ligt al weer ruim achter me, maar ik heb er goede herinneringen aan overgehouden. Daarbij springen met name de cryptogrammen uit de diverse zaterdagkranten in het oog, omdat we die iedere maandagochtend toch echt tijdens de koffie moesten oplossen! Edward, Wim, Frank (ook voor het wijzen op de PAW-versie voor de PC), Raimond, Erik en alle andere AIO's, OIO's, studenten, secretaresses, stafleden en technici: bedankt voor dat alles.

In de kleinere kring rond de UUTOF en HARP detectoren en mijn eigen experiment waren de contacten logischerwijs intensiever. Eppo (en Marlies), bedankt voor de jarenlange vriendschap. Andrzej, it was good to have you as roommate in the Ornstein building; thanks for your assistance during the experiments and afterwards. Mark, thanks for your help and your calmness. Zizis, unfortunately we never found a good substitute for those video nights! Thanks for your inspiration during my student days. Henk, David, Ernst-Paul, Daniël, Eelco, Guillermo en de overige promovendi en studenten in de voormalige *leptongroep*: bedankt voor jullie bijdrage aan de metingen en/of aan het geheel.

In mijn OIO-tijd had ik veel te maken met het NIKHEF, in het kader van HARP maar ook bij de (nacht-)shifts van diverse experimenten. Marco, Gerard, Willem K., Antonio, Jeff, Chiara, Eddy en de overige collega-OIO's en stafleden: bedankt voor de prettige samenwerking.

Sinds 1998 bevind ik me echter in heel andere omgevingen, namelijk die van de gedetacheerde automatiseerder. Ik wil mijn werkgever, *CENTRIC*, en dan in het bijzonder mijn twee fieldmanagers, Jos van Ginkel en Bert Poort, hartelijk bedanken voor de rust die ze me hebben gegund om naast mijn werk het promotieonderzoek af te maken. Jullie zullen af en toe wel gedacht hebben: "Verschuift die planning nu alweer?"... Gelukkig staat de einddatum nu wel vast!

Bij de "klanten" ontkwamen mijn collega's evenmin aan de proefschriftverhalen. Gelukkig kan ik ze nu eindelijk het resultaat laten zien. René, Ruud, Bert en anderen bij *Abz*, Roelof, Pasquale, Alexander, René, Gerard (2x), Klaas (2x), Albert, Marc en de overige (voornamelijk) PRL 25.0 teamleden bij *Holland Railconsult*: dit is het dan, waar het allemaal om draaide.

Al ben ik dan zelf jaren met hetzelfde bezig geweest, dat betekent niet dat de wereld om mij heen stilstond. Dat blijkt ook wanneer ik bedenk wie er in mijn

persoonlijke omgeving met me meeleeften. Er kwamen mensen bij, er verhuisden velen naar elders, en weer anderen bleven gewoon. Allemaal hebben ze op hun tijd belangstellend geïnformeerd, me gestimuleerd vol te houden, voor me gebeden, of geluisterd naar mijn zoveelste melding dat het langzaam vooruitging (of niet). Ze hielden het contact gaande, ook als ik hen soms verwaarloosde vanwege een onbewust – en waarschijnlijk onterecht – gevoel “dat ik toch eigenlijk eerst met het proefschrift aan de gang moest...”

Ivo en Marian, Dries en Henriëtte, Annie en Reinout: ik hoop dat we binnenkort weer bij kunnen praten, want dat heb ik inmiddels veel te lang uitgesteld! En beste ooms, tantes, neven en nichten: op de eerstvolgende familiereünie hoeven jullie niet meer te vragen hoe het gaat, want dat is toch op het promotiefeest?

Ik zou bijna de hele *SoW-gemeente Utrecht-West* hier vermelden, want er waren veel gemeenteleden die hun warme belangstelling niet onder stoelen of (kerk-)banken staken. Zoals Joke en Theo, Arjan en Wieke, Heim en Jody, Theo en Marjon, Margo, Lilian, Ad en Greet, Martin S., Franciska, Wytze, Astrid en Ronald, enz. En natuurlijk kan ook de naam van Mark Smits hier niet ontbreken. Of de leden van de twee bijbelkringen, waartoe ik behoort(de): Bert en Gerdien, Cees en Gerdien, Ellen, Linda, Mariëlle en Arjan; Peter en Janet, Hendrik Jan en Christine, Niek en Bernice, Jan Floor, Jenny, Jeroen.

Ik wil jullie allemaal heel erg bedanken en ik hoop dat jullie het eindresultaat met mij komen vieren!

Tenslotte kom ik bij degenen, die er eigenlijk altijd waren. Frank en Henny, Martin T., Dirk, Hinko en Petra, ik weet niet of ik dit proefschrift wel af had gekregen zonder jullie steun en de nodige ontspanning in de vorm van spelletjes, maaltijden, toneelvoorstellingen, films of zomaar een pilsje tussendoor. Datzelfde geldt zeker ook voor mijn ouders en Hella! Laat ik het maar houden bij de woorden van de Prediker. Genieten jullie mee?

Levensloop

Ἄνδρα μοι ἔννεπε, Μοῦσα . . .
Homerus, Odyssee

Ik ben op 21 juli 1968 geboren in Groningen, maar al snel verhuisde ons gezin naar Limerick, Ierland, zodat mijn eerste schoolervaringen vooral Engelstalig waren. Terug in Nederland ben ik verder gevormd aan de Immanuëlschool in Oudewater en het Coornhert Gymnasium te Gouda, waar ik ook kennismaatte met de alfa's, bèta's, gamma's en Delta's, die u in dit boek veelvuldig tegenkomt.

Na het eindexamen in 1986 studeerde ik een jaar in de Verenigde Staten aan Denison University in Granville, Ohio. In de beste *liberal arts* traditie heb ik daar zeer diverse colleges gevolgd: van natuur- en sterrenkunde tot theologie, van moderne en klassieke geschiedenis tot informatica, dit alles aangevuld met ski- en orgellessen en activiteiten in de vereniging van buitenlandse studenten.

Tijdens mijn studie experimentele natuurkunde aan de Universiteit Utrecht heb ik ook diverse keuzevakken informatica gevolgd. Mijn afstudeeronderzoek in de vakgroep subatomaire fysica sloot daarop aan: simuleren en optimaliseren van de nieuw te bouwen HARP neutronendetector. Naast de studie was er ruim plaats voor "vorming en gezelligheid" in de christelijke studentengezelligheidsvereniging S.S.R.-N.U. Ik maakte in het academisch jaar 1991-1992 als *fiscus* deel uit van het Bestuur der Afdeling.

Na het *cum laude* behalen van mijn doctoraal in 1992 begon ik als OIO van de Stichting F.O.M. aan een promotieonderzoek in bovengenoemde vakgroep. In dit kader heb ik o.a. een half jaar aan de Universität Bonn doorgebracht om onze metingen voor te bereiden, aan diverse andere experimenten meegewerkt in Bonn en op het NIKHEF, enkele conferenties bezocht en het practicum begeleid van studenten natuurwetenschappen. Voor mijn algemene ontwikkeling waren ook de colleges Reformatorische Wijsbegeerte van belang, waarin werd nagedacht over de relatie tussen (christelijk) geloof en moderne (natuur-)wetenschap.

Helaas kende mijn promotieonderzoek veel tegenslag en uitloop, zodat ik mij begin 1998 op de arbeidsmarkt begaf en in dienst trad bij *CCE Technische Software*, later opgegaan in *Centric Information Engineering*. Deze baan bood (en biedt) mij goede mogelijkheden om mijn interesse voor software te combineren met mijn vaardigheden en plezier in het analyseren van complexe systemen.

Uiteindelijk is het ook gelukt om in de avonden en weekenden het promotieonderzoek af te ronden, resulterend in dit boekwerk.

